Causes of Color in Corundum

Chinese Jade Carving

Characteristics of Blue to Yellow Beryl

History of the Chivor Mine, Part I

p. 3

p. 35

p. 92

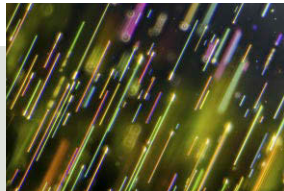p. 143

p. 174

GEMS & GEMOLOGY®

About the Cover

Distinguished gem carver Michael Dyber created "Flora" from a 3,070 ct Ukrainian heliodor found in the Volodarsk-Volynskii mine. The carving weighs 1,754.70 ct and measures 165 mm tall, 50 mm wide, and 37 mm deep. It was photographed during the 2020 Tucson gem shows, which are featured in the Gem News International section of this issue. Photo by Robert Weldon/GIA; courtesy of Michael M. Dyber.

Investigations into Corundum and Beryl Color, Jade Artistry, the Chivor Emerald Mine's History, and Swiss Rhodonite...

Welcome to the Spring *Gems & Gemology*! Publication was significantly delayed by the COVID-19 pandemic, but we're very proud to present this issue, which offers a blend of science, art, and history. In our lead article, authors Emily Dubinsky, Jennifer Stone-Sundberg, and John Emmett illuminate the chemistry behind gem corundum's rich array of colors to reveal the influence of the concentrations of the six identified chromophores found in natural corundum on the depth of color. The authors use quantitative visible absorption spectroscopy and chemical analysis by secondary-ion mass spectrometry (SIMS) to study specially chosen

> *"This article provides insight for the practicing gemologist on the influence of six specific chromophores and their concentrations on depth of color in corundum."*

synthetic and natural corundum samples to calculate each chromophore's absorption cross section. This information is presented as spectra and color-circle arrays, which we hope practicing gemologists will find informative.

In our second paper, Mingying Wang and Guanghai Shi of the China University of Geosciences (Beijing) present a study of Chinese jade carving artistry ranging from time-honored, traditional techniques to state-of-the-art computer numerical control and 3D replicate engraving. Using data from almost 2,500 contemporary pieces, the authors demonstrate the art's rich heritage and its continuing innovation.

Next, two more authors from the China University of Geosciences (Wuhan), Yang Hu and Ren Lu, examine the chromophores in blue and yellow beryl using quantitative spectroscopy and trace-element analysis to explore their color-causing characteristics. The authors show that different concentrations of iron ions with various valences and occupancies are most responsible for the gem's blue to green to yellow colors.

Our following paper offers a change of topic. Karl Schmetzer, Gérard Martayan, and Jose Guillermo Ortiz provide the first of two installments detailing the checkered history of Colombia's Chivor emerald mine: its abandonment, rediscovery, and intermittent operations by a fascinating cast of characters, including German gem merchant Fritz Klein.

In our final feature article, a team of Italian researchers led by Dr. Franca Caucia offers a study of the chemical, physical, and gemological properties of attractive rhodonite-rich rocks from Switzerland's Tanatz Alp.

Our regular sections have much to offer, too. In *Lab Notes*, we describe diamonds with graphitic cavities and corundum inclusions, a clarity-enhanced glass imitating emerald, a large grandidierite, and curious pearls. *Micro-World* also provides intriguing curiosities, including a diamond with a mobile green diamond inclusion and a pallasitic peridot with iridescent needles. In *Diamonds from the Deep*, regular contributors Karen Smit and Steve Shirey demonstrate that diamonds are not necessarily forever with an exploration of the dissolution many diamond crystals suffer during transport in kimberlite magma. Our *Gem News International* section surveys gem materials and events from the 2020 Tucson gem shows, including star peridot, demantoid garnet, emerald, sapphire, trapiche gems, Tucson's first ethical gem fair, and the results of the 2019 Buccellati jewelry design competition. Please also see the winners of our Dr. Edward J. Gübelin Most Valuable Article Award and this year's *G&G* Challenge quiz.

Finally, do make sure you visit our new *G&G* Facebook group at www.facebook.com/groups/giagemsgemology. Since our February 2020 launch, over 7,000 of you have joined, so if you haven't seen it yet, please check it out. Thank you all for your support and interest!

Duncan Pay | Editor-in-Chief | dpay@gia.edu

A Quantitative Description of the Causes of Color in Corundum

Emily V. Dubinsky, Jennifer Stone-Sundberg, and John L. Emmett

The color of a gemstone is inextricably linked to its chemical composition, yet the quantitative relationship between color and chemistry is poorly understood in most cases. Here we use corundum to present a comprehensive quantitative description of the causes of color in a gem material and illustrate its predictive power. Natural corundum has six major chromophores that cause color: Cr^{3+}, $h^{\bullet}$-Cr^{3+}, Fe^{3+}, $h^{\bullet}$-Fe^{3+}, Fe^{2+}-Ti^{4+}, and V^{3+}. We use synthetic samples doped with a single chromophore to study their light absorption behavior in isolation. Natural samples are used as well to study single chromophores, and we can subtract out the absorption of additional chromophores that might be present. Combining quantitative visible absorption spectroscopy with chemical analysis by SIMS, we are able to calculate the absorption cross section of each chromophore. The absorption cross section information is used to determine the depth of color that would occur in corundum of a given size (optical path length) containing a specific chromophore of a given concentration.

Gemstones are valued for their beauty, rarity, and durability, and what typically captures our attention is their magnificent array of colors. Corundum exhibits an extremely wide range of colors in nature (figure 1). From pigeon's blood red ruby to cornflower blue and lemon yellow sapphire, nearly every color is represented. The only corundum color not represented in nature is a saturated intense emerald green. However, less intense olive green to teal green stones are often found in basalt-hosted corundum deposits.

Corundum's broad range of colors is related to its detailed chemistry. Some minerals possess inherent color because the chromophore is one of the basic chemical components of its makeup. Such stones are termed *idiochromatic*, meaning self-colored. For example, turquoise, whose chemical formula is $CuAl_6(PO_4)_4(OH)_8 \cdot 4H_2O$, is colored by copper, a primary component of its structure.

Other minerals such as corundum are, when very pure, completely colorless. In fact, pure corundum, with the chemical formula Al_2O_3, is absolutely transparent from the deep ultraviolet region into the infrared. Such minerals are termed *allochromatic*. Their colors in nature are caused by minor impurities, referred to as trace elements, or other point defects in the crystal lattice that have been incorporated during growth or later equilibration in nature. The causes of color in corundum are many and have been primarily addressed in a non-quantitative way for many years (see, for example, Fritsch and Rossman, 1987, 1988; Häger, 2001; Emmett et al., 2003). Trace elements themselves can be the direct cause of color. Cr^{3+}, for example, creates pink and red coloration in corundum. Trace elements can also interact with each other, creating a new chromophore. The Fe^{2+}-Ti^{4+} pair is such an example, strongly absorbing in the yellow and red regions of the spectrum and thus creating magnificent blue sapphires.

When beryllium-diffused corundum entered the marketplace, we were surprised by the wide range of colors that were produced, seemingly by a single element (Emmett et al., 2003). Measurements of the beryllium levels showed that the concentrations were generally from a few to a few tens of parts per million atomic (ppma), yet the colors produced were often intense. For comparison, red coloration in corundum requires several hundred to a few thousand ppma of Cr^{3+}, a concentration at least two orders of magnitude greater than Be^{2+}, to produce strong color.

Our studies of the beryllium-diffused stones (Emmett et al., 2003) demonstrated that the Be^{2+} ion itself was not the cause of color. However, replacing a trivalent aluminum ion with a divalent beryllium ion required the creation of a trapped hole ($h^{\bullet}$) for

Figure 1. Gem corundum is rarely colored only by a single chromophore; the vast majority are colored by a combination of two or three chromophores. This composite photo illustrates the colors of single chromophores as they would appear in a faceted stone. We searched through a few thousand photos, courtesy of Lotus Gemology, to find these few that closely matched the single-chromophore color circles in this article. These gems represent (clockwise from top left) V^{3+} (first two stones), Cr^{3+}, $h^{\bullet}$-Cr^{3+}, $h^{\bullet}$-Fe^{3+}, Fe^{2+}-Ti^{4+}, and Fe^{3+}. Photos by Lotus Gemology.

charge compensation. A trapped hole is an oxygen ion with a valence of –1 rather than –2. It is this O^{-1} ion that is the strong absorber of light (Kvapil et al., 1973). In natural stones, this trapped hole associating with either iron or chromium creates intense golden yellow or intense orange colors, respectively.

In natural corundum, beryllium only rarely, if ever, exists in solution in the corundum lattice and thus does not produce these colors. Instead, natural corundum usually contains some amount of magnesium. Magnesium, like beryllium, is divalent (Mg^{2+}, Be^{2+}) when it replaces Al^{3+} in corundum and thus requires charge compensation. If the stone is acceptor-dominated[1] with [Mg + Ni] > [Si + Ti + H] (square brackets denote concentrations in ions/cm^3), and formed in conditions of relatively high oxygen fugacity, the charge compensation is by a trapped hole (h$^\bullet$). Since it is the trapped hole in association with iron or chromium and not the beryllium or magnesium that produces color, the colors produced naturally by magnesium or by diffusion of beryllium are very similar (Emmett et al., 2003, 2017b; Kröger, 1984).

Having identified the h$^\bullet$-Fe^{3+} and the h$^\bullet$-Cr^{3+} as two additional chromophores in natural corundum, we have six major chromophores that are responsible for the multitude of colors in natural corundum: Fe^{3+}, Cr^{3+}, V^{3+}, Fe^{2+}-Ti^{4+}, h$^\bullet$-Fe^{3+}, and h$^\bullet$-Cr^{3+}. Individually, their colors in corundum are as follows:

Pink, Red: Cr^{3+}
Orange: h$^\bullet$-Cr^{3+}
Yellow: Fe^{3+}, h$^\bullet$-Fe^{3+}
Blue: Fe^{2+}-Ti^{4+}, V^{3+}
Green, Purple: V^{3+}

These chromophores can occur singly in a corundum sample (again, see figure 1), though it is common for natural corundum to contain more than one color-causing agent, as all natural corundum generally contains measureable levels of trace elements Mg, Si, Ti, V, Cr, Fe, and Ga that have been incorporated into the lattice. When multiple chromophores are present, the apparent color of the corundum sample results from the sum of the light absorption by each of the chromophores present (Emmett et al., 2017a).

---

[1]We use the terms "acceptor-dominated" and "donor-dominated" and also refer to chemical reactions among trace elements here without detailed explanations. These matters are discussed in detail in Emmett et al. (2003), with corrections and extensions in Emmett et al. (2017a,b). Rather than repeat these discussions, we refer the reader to these references and the extensive references therein. Furthermore, we will not repeatedly restate these references throughout this text.

To determine the visual color of a corundum sample from the chemical analyses, we need to know four additional factors: the absorption spectrum of each of the chromophores, the absorption "strengths" of the chromophores, the thickness and crystallographic orientation of the sample, and the color temperature of the illumination.

All of these factors are well known in gemology with the exception of the absorption "strength." The term for the absorption "strength" in physics is the absorption cross section (see box A on pp. 6–9; we strongly advise reading box A before proceeding). The absorption cross section quantitatively determines the effectiveness of a single ion or ion pair in a particular host material (such as corundum) in absorbing light of a given wavelength. The larger the absorption cross section, the stronger the chromophore. The unit of the absorption cross section is centimeters squared (cm^2), which represents an area. One can conceptually visualize this as the size of the absorbing area that a single chromophore particle presents to the light beam. However, note that it is *not* the actual physical size of an ion or an ion pair.

In Brief

- Natural corundum has six major color-causing chromophores: Cr^{3+}, h·-Cr^{3+}, Fe^{3+}, h·-Fe^{3+}, Fe^{2+}-Ti^{4+}, and V^{3+}.

- The depth of color produced by each chromophore depends on three factors: the size of the gem, the concentration of the chromophore in the gem, and the absorption strength of the chromophore.

- The absorption strength of each chromophore is expressed by its absorption cross section. The cross sections of the various chromophores in corundum vary by a factor of approximately 500, meaning they range from weak to strong colorants.

- Using the cross section data provided in this paper, the color produced in a sample of any specified size and chromophore concentration can be calculated.

Knowing the absorption cross sections is absolutely critical to determining the origin of color of a given sample. Before detailed chemical analyses were available, it was often assumed that iron was primarily responsible for yellow color in sapphire. However, we now know that there are yellow sapphires with 3000 ppma Fe and yellow sapphires with 200 ppma Fe with similar depth or intensity of color, so clearly these are not colored by the same chromophore.

Figure 2. Shown are some of the many crystallographically oriented samples used in this study. Clockwise from top left, they represent the following chromophores: $h^\bullet$-Cr^{3+}, $h^\bullet$-Fe^{3+}, Fe^{3+}, Cr^{3+}, V^{3+}, and Fe^{2+}-Ti^{4+} (the two blue samples at lower left). The sample in the far lower left corner is a natural blue sapphire from Yogo Gulch, Montana, and the sample in the upper right corner is a natural yellow sapphire from the Subera deposit in Queensland, Australia; the rest are Czochralski grown. Sample numbers clockwise from upper left are 991, 992, 1121, 1110, 1102, 1065, and 1014; detailed information on the samples can be found in Appendix 1.

The objective of this paper is to present the results of our efforts over more than a decade to determine both the $E \perp c$ (O-ray) and $E \| c$ (E-ray) (see box B) absorption cross sections for all six chromophores in corundum and to describe how they were determined. We also illustrate the range of colors these chromophores produce. Finally, the digital files at 1.5 nm resolution and 1 nm wavelength intervals from 200 to 1100 nm for each of these chromophores are available to the reader to download for their own use (see https://www.gia.edu/doc/sp20-corundum-chromophores-absorption-cross-section-data.xlsx).

Determining the absorption cross sections relies upon accurate determination of the chromophore concentrations in the samples. These determinations were made possible by secondary ion mass spectrometry (SIMS) analysis at the California Institute of Technology (Caltech). SIMS was calibrated with single-element ion implants in sapphire standards, eliminating any matrix effects. The calibration of SIMS, a major effort in itself, is described in detail in Stone-Sundberg et al. (2017).

The chromophore concentrations in this paper have largely been determined by SIMS analyses from synthetic corundum crystals grown doped only with a single chromophore. This is true of Cr^{3+}, V^{3+}, $h^\bullet$-Fe^{3+}, and $h^\bullet$-Cr^{3+}. The Fe^{3+} chromophore and Fe^{2+}-Ti^{4+} chromophore data were determined using both natural and single-doped synthetic crystals grown by the Czochralski method (figure 2). Unlike many other minerals, corundum contains only a single small cation site. Additionally, the energy required to force a cation into an interstitial site is very high (Matsunaga et al., 2004). These facts, together with the fact that the crystal must be rigorously electrically neutral, very strongly constrain what trace elements and what valence states of these trace elements can exist in corundum. For example, iron in corundum by itself will be Fe^{3+} because the crystal must be electrically neutral. That is, the valence of Fe must equal the valence of Al^{3+}. Unless there is a tetravalent donor such as Si^{4+} or Ti^{4+} or an H^+ interstitial (El-Aiat and Kröger, 1982; Norby, 1989; Beran and Rossman, 2006; Li and Robertson, 2014) to charge compensate it, Fe^{2+} will not exist. If there is such a donor, the Fe^{2+}-Si^{4+} and Fe^{2+}-Ti^{4+} pairs will form. Thus the concentration of Fe^{2+} is limited by the concentrations of H^+, Si^{4+}, and Ti^{4+}. This is why we thoroughly analyze even the singly doped synthetic crystals.

If a very high-purity synthetic crystal doped only with Fe^{3+} is processed at high temperature in a highly reducing atmosphere, oxygen vacancies with a charge of +2 with regard to the lattice may form and thus charge compensate two Fe^{2+} ions. It is for this reason that we process at high temperature in a pure oxygen atmosphere many of the synthetic crystals

Highly pure allochromatic gem materials are colorless. Color in these gems results from the incorporation of a variety of trace elements and other point defects into the lattice. Unlike idiochromatic gems, whose chromophores are part of the fundamental composition of the mineral, the concentration of trace elements incorporated in allochromatic gems can vary widely. Corundum, an allochromatic gem, displays a very wide range of coloration: Nearly every color with the exception of emerald green is available. In what follows, we identify and quantify the six chromophores that produce this wide range of coloration in natural corundum by incorporating either singly or in combination in the corundum lattice.

Three of these chromophores are single transition metals (Fe^{3+}, Cr^{3+}, and V^{3+}), one is a pair of metals (Fe^{2+}-Ti^{4+}), and two are comprised of a lattice defect and a transition metal ($h^{\bullet}$-Cr^{3+} and $h^{\bullet}$-Fe^{3+}). As we demonstrate in this article, the effectiveness of each of these chromophores in producing color varies greatly because of their very different electronic structures. For example, nearly 2000 ppma of Fe^{3+} in a 1 cm thick sample is needed to produce a saturated yellow, while only 1.5 ppma of the $h^{\bullet}$-Fe^{3+} will produce a similar depth of color.

In gemology we are familiar with the absorption spectra of the majority of these chromophores as single entities in corundum, but we do not have a simple methodology for characterizing their "strength." The strength determines the concentration of a chromophore (in ppma) required to produce a given level of color saturation. Knowing the strength of the chromophores and the chemical composition determined by SIMS or LA-ICP-MS analysis, we can correctly identify the sources of color in a sample. In physics the strength of an absorber of light or X-rays or neutrons is often referred to as an absorption cross section. We can use this simple concept to establish relative strengths of our chromophores. This paper presents our determination of the absorption cross sections for each of the six chromophores.

To define the terms we will use, consider a transparent material of thickness t, as shown in figure A-1.

If an incident beam of light with intensity I_0 strikes a sample that absorbs light, the intensity of the light transmitted through it is I, *assuming no reflection from the surfaces*. Now the transmission, T, of the sample is:

$$T = I/I_0$$

Or, if expressed as a percentage:

$$T\,(\%) = 100\,I/I_0$$

The decadic absorbance, A, of the sample is then:

$$10^{-A} = I/I_0$$

or

$$A = -Log_{10}(I/I_0).$$
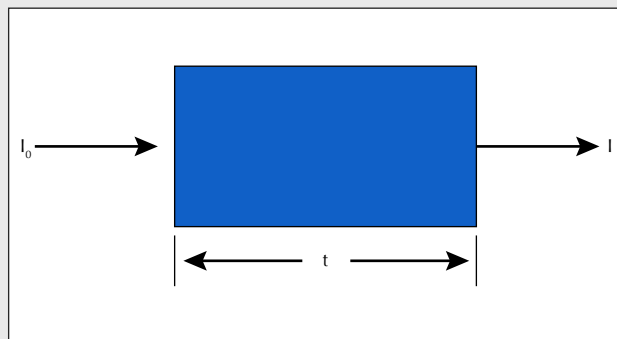
Figure A-1. This simple diagram represents a transparent material of thickness t. Light with intensity I_0 strikes its surface at left. Some of the light is absorbed as it travels through the material, so the beam has intensity I as it exits at right. The light transmission T of the sample is represented by the ratio of the exiting beam intensity to the entering beam intensity, I/I_0.

All real samples have a portion of the probe beam reflected from their surfaces. Thus a spectrophotometer does not directly measure the true absorbance, A, but rather $A^{\star}$.

To determine the true absorbance A, the measured absorbance $A^{\star}$ must first be corrected for the loss from multiple reflections between the two polished surfaces of the sample. This is done by summing (T.S. Hemphill, pers. comm., 2011) all the reflections between the two surfaces and using a three-term Sellmeier equation for corundum to determine the sample's refractive index as a function of wavelength (Tatian, 1984). The index input data to the Sellmeier equation is a combination of all relatively recent data from the suppliers of high-purity synthetic corundum material for the fabrication of high-purity optical elements. The Sellmeier equation fit to these data was performed for us by John Trenholme using TableCurve 2D software. Correcting for this loss we have the true absorbance, A. This correction is important because it is greatest where the absorption is least, and it is just this region of the absorption spectrum that transmits the most intense light and thus contributes most to the color. This reflection correction has been made for all spectra presented in this paper and for all spectra used in deriving these results.

The true absorbance, A, for E⊥c of a synthetic sapphire 6.26 mm thick containing 116 ppma V^{3+} is shown in figure A-2. Note that the vertical axis is unitless because absorbance is simply a ratio.

The true absorbance A depends in turn on the thickness of the sample, t, the concentration of the chromophore, c, and its absorption cross section, σ. With the true absorbance, A, we can write:

V³⁺ E⊥c

ABSORBANCE vs WAVELENGTH (nm)
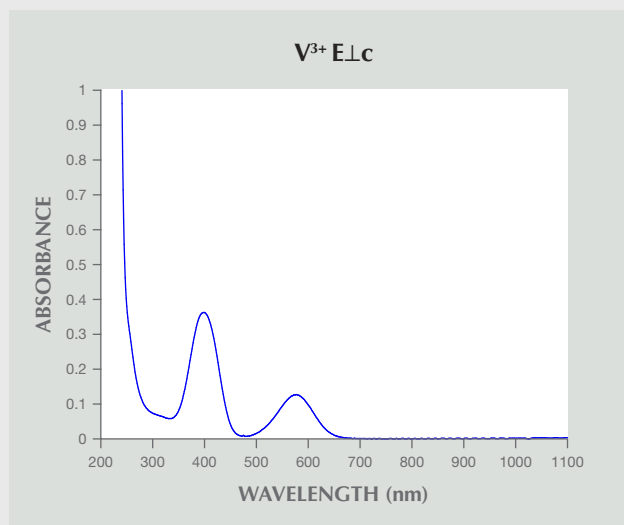
Figure A-2. UV/visible/near-infrared (UV-Vis-NIR) absorption spectrum of synthetic sapphire 6.26 mm thick containing 116 ppma V³⁺, as measured by a spectrophotometer and corrected for internal reflections. Note that the spectrophotometer measures light absorption in absorbance units, which are dimensionless.

V³⁺ E⊥c

ABSORPTION COEFFICIENT (cm⁻¹) vs WAVELENGTH (nm)
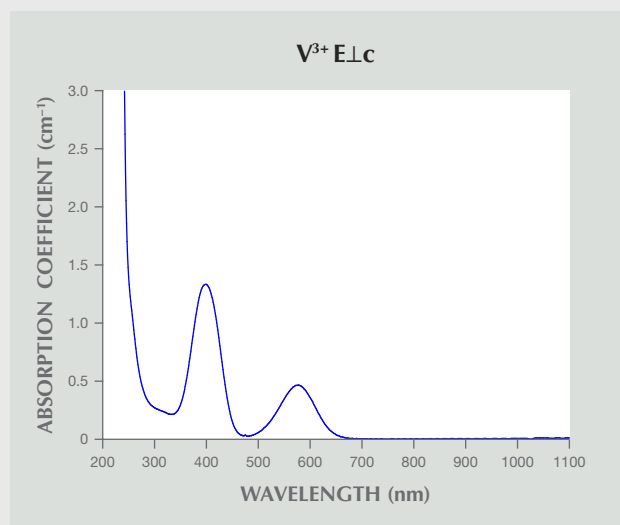
Figure A-3. UV-Vis-NIR infrared absorption coefficient spectrum of the V³⁺-doped synthetic sapphire, produced by dividing the spectrum in figure A-2 by sample thickness (0.626 cm) and multiplying by 2.303. Note that the shape of the curve is the same but the y-axis units are cm⁻¹.

$$I/I_0 = T = 10^{-A} = e^{-\alpha t} = e^{-\sigma ct}$$

Where I/I_0 and T are here associated only with the actual absorption, and

> T = transmittance
> A = decadic true absorbance (dimensionless)
> t = thickness of the sample in cm
> α = naperian true absorption coefficient in cm⁻¹
> c = chromophore concentration in ions/cm³
> σ = true absorption cross section in cm²
> e = base of the natural logarithm = 2.71828…

The reflection-corrected absorption coefficient is simply

$$\alpha = 2.303A/t$$

(In gemology publications, the uncorrected absorbance A* or an absorption coefficient derived from A* is usually presented.)

The absorption coefficient of the V³⁺-doped sapphire sample above is shown in figure A-3. Because A, a unitless ratio, is divided by the dimension t in cm, the units of absorption coefficient are cm⁻¹. The absorption coefficient is independent of the sample thickness, making it useful for comparing samples.

The absorption coefficient is, of course, dependent on the concentration of the chromophore. If we want to compare two different chromophores but the samples have different chromophore concentrations, we can divide the absorption coefficient of each chromophore by its concentration in absorbers/cm³ (note that 1 ppma in corundum is a concentration of 1.178×10^{17} ions/cm³):

$$\sigma = \alpha/c$$

The result, σ, is termed the absorption cross section. Figure A-4 shows the absorption cross section for the same vanadium-doped sapphire sample.

With absorption coefficient units of cm⁻¹ and concentration units of ions/cm³, the units of the cross section are cm²/ion, or just cm², which is an "area" per absorber. One can conceptualize this as the size of the absorbing area that a single chromophore particle presents to the light beam. In other words, imagine that the light beam is an arrow and the absorption cross section is a target; a larger absorption cross section means the target's area is larger. However, note that it is *not* the physical size of an ion or an ion pair. The vertical axis in figure A-4 is labeled "absorption cross section × 10¹⁹ cm²." This means that the actual values plotted are from 0 to 2 times 10⁻¹⁹ cm². It is important to observe that the spectra in figures A-2, A-3, and A-4 are exactly the same. Only the vertical axis values and units are different.

Each chromophore has its own absorption cross section that is unique to that particular absorber. A sample with multiple chromophores of different concentrations is best characterized by an absorption coefficient, as we

V³⁺ E⊥c
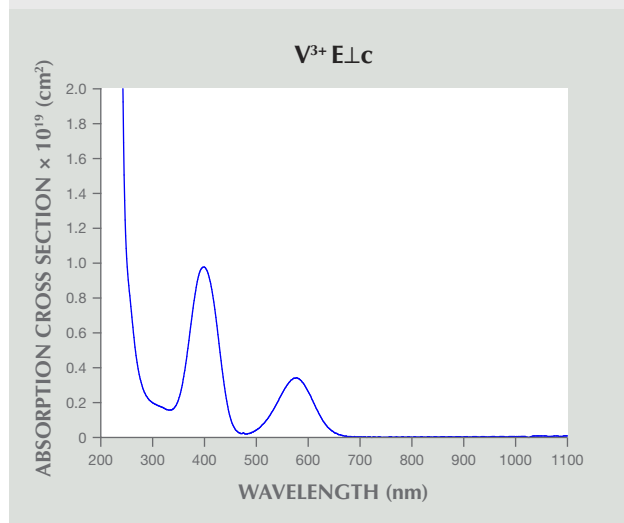
Figure A-4. UV-Vis-NIR cross section spectrum of the V^{3+}-doped synthetic sapphire, produced by dividing the spectrum in figure A-3 by the V^{3+} concentration of the sample. Note that the shape of the curve is the same but the y-axis units are cm^2.

do with all natural samples. This absorption coefficient is the summation of each chromophore's cross section multiplied by its concentration. For example, a sample containing three chromophores of three different concentrations has an absorption coefficient of

$$\alpha = \sigma_1 c_1 + \sigma_2 c_2 + \sigma_3 c_3$$

The magnitude of the absorption cross section of the chromophore, and the portion of the visible spectrum that its absorption spectrum covers, taken together provide a rough indication of chromophore strength. The portion of the visible spectrum is estimated by the full width half maximum (FWHM) of the absorption bands in the visible region, divided by 300 nm (the 400–700 nm approximate visible range). Table A-1 compares these values for the E⊥c absorption of the various chromophores in order of increasing absorption cross section.

Examining the peak absorption cross sections first, note that the values span a factor of about 500. This is a huge difference. Next, examining the portion of the visible spectrum spanned by each chromophore, note that they are within a factor of two and a half with the exception of Fe^{3+}, which is about one-fifth of the average of the other five. Taking into consideration the very low absorption cross section and the very narrow absorption band, the conclusion is that Fe^{3+} is a very weak chromophore in corundum. Figure 16 presents a visual method of comparing the strength of the six chromophores.

The concept of absorption cross section is very useful in understanding the types of optical transitions involved with the individual chromophores. It is also useful in comparing similar chromophores in different environments. Mattson and Rossman (1988) used this concept in comparing the strength of the Fe^{2+}-Ti^{4+} absorption bands in different minerals. Their absorption cross section was in units of $(moles)^{-1}$ cm^{-1}, which is simply a different system of units but the same concept.

This paper presents the color calculations for a range of concentrations of each of the six chromophores. The color coordinates were calculated using Thermo Scientific's GRAMS/AI spectroscopy software. To calculate the color coordinates with Grams/AI, the spectral data is input as the single-pass transmission spectrum, T. T is related to the single-chromophore absorption cross section and concentration as follows:

$$T = 10^{-A} = 10^{-(ct\sigma/2.303)}$$

where the product, ct, is termed the areal density in units of ions/cm^2. Under the color circles in this paper, we present the areal density in ppma-cm. This factor is

$$\text{ppma-cm} = ct/(1.178 \times 10^{17} \text{ ions/cm}^3)$$

where 1.178×10^{17} is the number of ions in 1 cubic centimeter of Al_2O_3 determined by

$$1 \text{ ppma} = 5A\rho/M = 1.178 \times 10^{17} \text{ ions/cm}^3$$

where A is Avogadro's number (6.022×10^{23} molecules/mole), ρ is the density of corundum (taken as 3.99 grams/cm^3), and M is the molecular weight of corundum (101.961 grams/mole).

Finally, it should be stated that presenting the definitions and units of A, α, and σ is very important, as there are multiple definitions in use in the scientific literature.

TABLE A-1. Comparison of various chromophores' E⊥c absorption values.

Chromophore	Peak absorption cross section in the 400–700 nm range, cm² E⊥c	Approximate fraction of the 400–700 nm range at chromophore FWHM
Fe^{3+}	$2.3 \times 10^{-20} \pm 8.0\%$	0.09
V^{3+}	$1.0 \times 10^{-19} \pm 8.9\%$	0.37
Cr^{3+}	$1.6 \times 10^{-19} \pm 7.6\%$	0.40
Fe^{2+}-Ti^{4+}	$1.9 \times 10^{-18} \pm 25\%$	0.66
h•-Fe^{3+}	$1.3 \times 10^{-17} \pm 12.0\%$	0.28
h•-Cr^{3+}	$1.3 \times 10^{-17} \pm 12.5\%$	0.44

we have grown. This eliminates any oxygen vacancies, assuring a valence of +3. Additional possibilities for alternate valences of other ions, or interferences from different pair absorption spectra, have been addressed using the variety of synthetic crystals indicated in Appendix 1 at https://www.gia.edu/doc/SP20-corundum-chromophores-appendix1.

Such considerations, plus the processing of synthetic crystals in a high-temperature oxygen atmosphere and thorough analyses for other trace elements, assure that the chromophore concentrations equal the SIMS-determined concentrations.

In the following sections, we will first describe the Cr^{3+} chromophore and how its cross section was determined. Much of this same detail will apply for the other five chromophores and thus will not be repeated. We present the origin of the samples (again, see figure 2), their crystallographic orientation, the absorption cross sections determined for both E⊥c and E||c, color circle arrays for different areal densities of the chromophore, viewing directions, and illumination sources. Detailed information on these samples can be found in Appendix 1.

THE Cr^{3+} CHROMOPHORE

Cr^{3+} is the trace element primarily responsible for coloring ruby red and sapphire pink (McClure, 1962) and in doing so creates some of the most beautiful gems in the world. This coloration results from Cr^{3+} ions replacing some of the Al^{3+} ions in the corundum lattice.

High-purity synthetic sapphire doped with Cr^{3+} has been available since the invention of the laser in 1960. The very first laser employed synthetic ruby as the active element (Maiman et al., 1961). Interest in ruby lasers for many applications drove the development of large, exceedingly high-optical-quality and high-purity synthetic ruby crystals. Our samples were from excess material salvaged from several different laser-quality single-crystal ingots (boules) grown by St. Gobain Crystals and Detectors in Washougal, Washington.

Wafer samples cut from these boules were crystallographically oriented to an accuracy of approximately 1.5° using an optical instrument (Thomas et al., 2014) with the c-axis in the plane of the wafer. The absorption spectra were measured with a resolution of 1.5 nm using a Hitachi Model 2910 spectrophotometer modified by Tim Thomas at GIA to enable rotation of the polarization plane of the probe beam, thus allowing the separate recording of both E⊥c and E||c spectra. The spectra were corrected for the multiple reflections between the two polished surfaces of the wafer by summing all the reflections (see box A). Wafers from four different boules were fabricated and measured, and the one with the lowest absorption at approximately 226 nm was chosen as the most pure. 226 nm is between the two highest-energy absorption bands of Cr^{3+} yet below the first Cr^{3+} charge transfer band. However, at this wavelength the charge transfer bands of Fe, Ti, and other metals are very strong (Tippins, 1970), and thus minimal absorption at this wavelength is a good relative indicator of crystal purity.

Quantitative data on this sample with the minimum 226 nm absorption (and all of the other samples characterized in this study) were obtained using a Cameca IMS 7f-GEO SIMS instrument. SIMS is a highly precise analytical technique that can detect all elemental masses to the sub-ppma level. To achieve accuracy, however, relative sensitivity factors (RSF) need to be developed to correctly convert the secondary ion signal for each trace element in the matrix of interest into concentration. This is best done by creating ion implant standards. For each trace element we wish to quantify, a chosen isotope of this trace element is implanted in a high-purity wafer of the intended matrix. Our developed RSF values were based upon multiple measurements validating the "dose" of each of these ion implants, and upon multiple SIMS depth profiles of these same implants (Stone-Sundberg et al., 2017). The calculated RSF values account for all of the identified and quantifiable sources of uncertainty; for the final SIMS-generated concentration values for all of the subsequently measured samples, we report a total uncertainty that is equal to the square root of the sum of the squares of the error associated with each source. In total, there are four separately quantified sources of error: the ion implant standard dose measurement, determination of the peak depths for the ion implants, differences between the multiple depth profiles for each ion implant, and the set of measurements of the trace element of interest in the sample. For the Cr^{3+} chromophore, the concentration and total combined error is 134 ppma ± 7.6%. The determined detection limit for Cr^{3+} in corundum to the 95% confidence level using our conditions was 0.002 ppma (2 parts per billion atomic, ppba).

The absorption cross sections thus determined over the 200–1100 nm range are shown in figure 3. The data range includes the visible region of the electromagnetic spectrum, which extends from 400 nm (violet) to 700 nm (red). The vertical axis is labeled "absorption cross section $\times 10^{19}$ cm^2." This means that
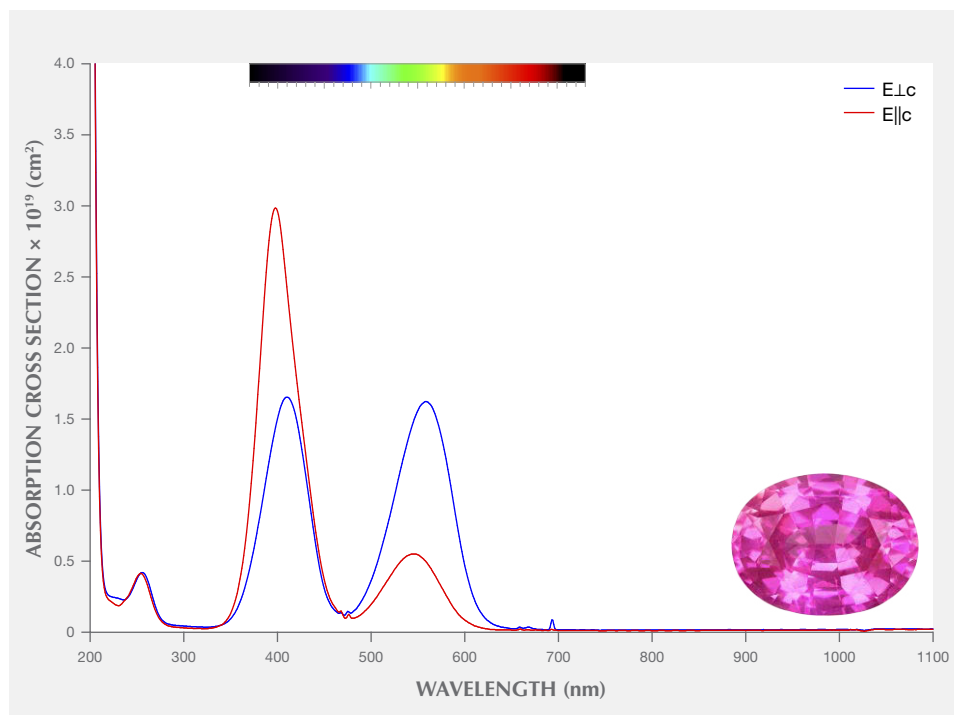
Figure 3. Cross section spectra of the Cr^{3+} chromophore measured from a synthetic ruby grown by the Czochralski method. The color band shown along the top of these spectra and those in following figures is the visible spectrum that would be observed through an optical spectroscope, shown for reference. Also shown is a 1.30 ct unheated Mozambique pink sapphire, representative of the color that would be produced by the Cr^{3+} chromophore in isolation. Photo by Lotus Gemology; courtesy of Nomad's Ltd.

the actual values plotted are from 0 to 4×10^{-19} cm²; we will use the same labeling convention for subsequent cross section spectra presented in this article. Figure 3 shows the absolute absorption cross section spectra for both the E⊥c (ordinary) and E‖c (extraordinary) rays for Cr^{3+} in the high-purity synthetic ruby. These two spectra fully characterize, at 1.5 nm resolution, the absorption characteristics of Cr^{3+} in corundum over the range from 200 to 1100 nm. Whether in a high-purity synthetic crystal containing only Cr^{3+}, a natural ruby containing Cr^{3+} and iron, or a purple sapphire containing Fe^{2+}-Ti^{4+} pairs and Cr^{3+}, the absorption cross section of Cr^{3+} is the same. The broad bands near 560 nm are termed the U bands, while the two near 400 nm are designated the Y bands. At a wavelength of 694 nm, there is a weak, narrow absorption feature. This is known as the R-line. In actuality, the R-line is two weak lines, R1 and R2, which are separated by 1.4 nm. Since our instrumental resolution is 1.5 nm, these two lines appear as a single weak feature. The weak lines near 660 nm most clearly observable in the E⊥c spectrum are called the S-lines, while the weak lines in both spectra near 470 nm are referred to as the B-lines (Powell, 1998). Shown along with the spectra is an image of a faceted sapphire we selected as representative of a stone that is very close to being colored by only the Cr^{3+} chromophore. In the following sections, we show a representative faceted stone alongside the spectra for each chromophore, selected as representa-

tive of the color that would be produced by that chromophore in isolation.

Note that the E⊥c peak cross section of 1.62×10^{-19} cm² ± 7.6% we determined for the 560 nm U band represents a moderately strong absorber, and thus Cr^{3+} is a moderately strong chromophore. It is the magnitude of this cross section in the visible region of the spectrum, and to a lesser extent the width and position of the bands, that determines the "strength" of the chromophore (see box A). The position and width of the absorption bands determine the color. Approximately speaking, the larger the cross section and the wider the bands in the visible region, the more color produced.

It is interesting to note that apparently the first determination of Cr^{3+} cross section was published in 1961 in the seminal paper reporting the achievement of the first laser—the ruby laser (Maiman et al., 1961). His value of the peak cross section for the E⊥c U band was approximately 1.8×10^{-19} cm². The small difference between his value and ours probably reflects the improved analytical instrumentation for determining Cr^{3+} concentration available to us today. Subsequently, the absorption and emission spectrum of ruby has been extensively studied by many researchers; see, for example, Powell (1966, 1998) and Henderson and Bartram (2000).

While the absorption cross section provides the definitive characterization of a chromophore, it is not

easy to guess the color from simply examining the spectra. It is, however, straightforward to calculate the color from these spectra. The color coordinates (Berns, 2000) are usually calculated from the sample's transmission spectrum and the characteristics of the light source. Calculation of the color coordinates for a given color temperature was performed via Thermo Scientific's GRAMS/AI spectroscopy software, a general-purpose spectra manipulation code that includes color coordinate calculations. There are many color coordinate systems, and we chose the CIE 1976 $L^{*}a^{*}b^{*}$ system for its approximately uniform color space. We used color temperatures of 6500 K (D65 illuminant) and 2856 K (A illuminant) in order to maximize the color temperature difference and the color difference, thereby maximizing the visual effects of different light

sources for the reader. Having determined the color coordinates for a particular sample thickness and chromophore concentration, a color circle is then created by specifying the color coordinates to the drawing program. We have used Photoshop, EasyDraw, and other graphics programs to produce the color circles. Visualizing the color from the absorption spectrum of the sample has broad application in gemology. We first used this technique to determine the amount of diffused beryllium that would cause a visible reduction in the depth of color of a dark blue sapphire.

Figure 4 (left) shows an array of color circles corresponding to a range of Cr^{3+} areal densities. Presented are the E⊥c color, the E||c color, and a color representing equal proportions of E⊥c and E||c (we will call this E⊥c + E||c), as viewed with illuminant

Figure 4. Left: Areal density color circles of the Cr^{3+} chromophore under illuminant D65. Right: Illuminant comparison color circles of the Cr^{3+} chromophore.
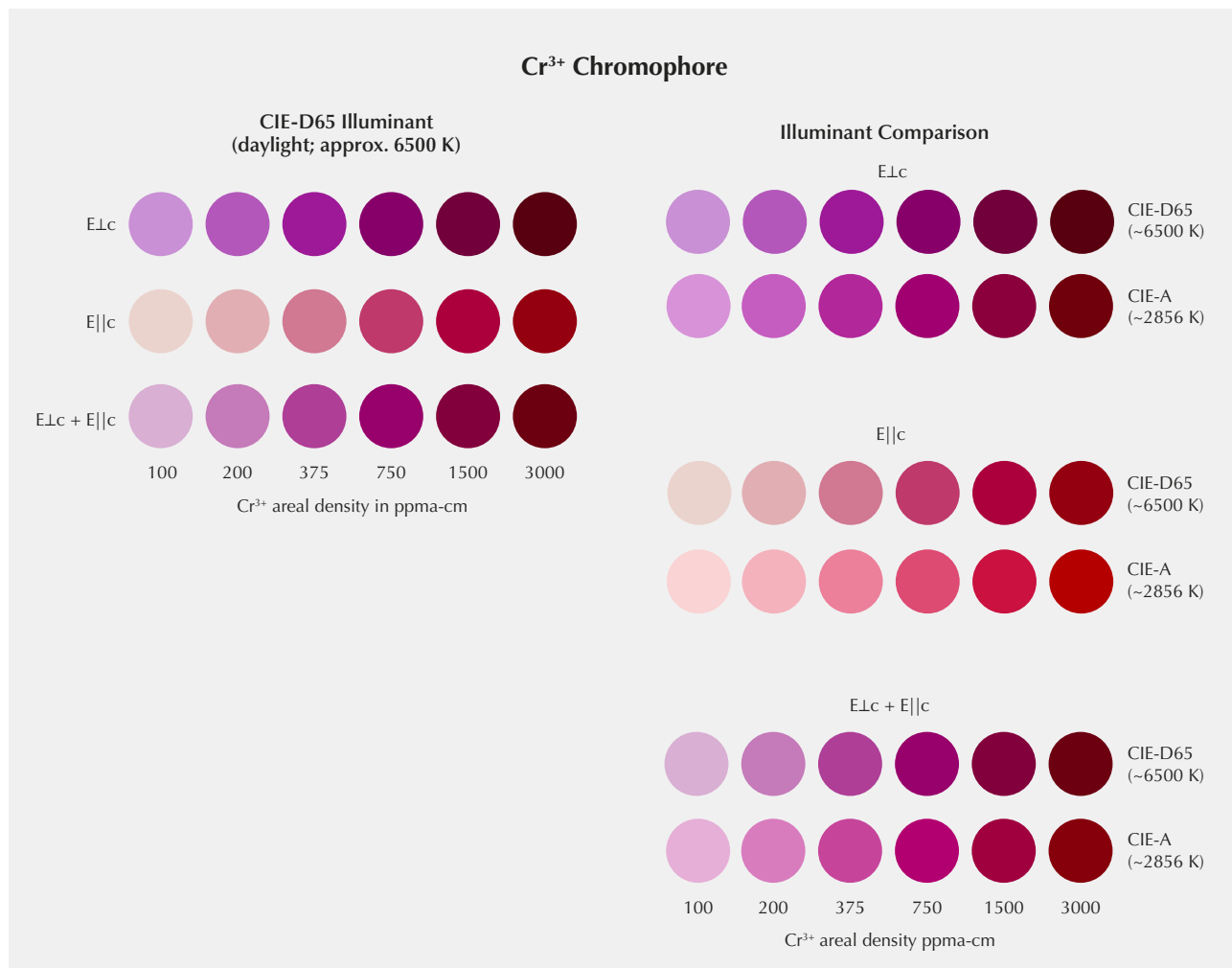
Box B: Crystal Optics of Uniaxial Minerals

Glass is an optically *isotropic* material, meaning its physical properties such as absorption coefficient spectrum and refractive index are the same in any measured direction within the glass, regardless of the polarization of the measurement beam. Consequently, light traveling in any direction in an isotropic medium behaves the same way. Many crystals are not optically isotropic—they are *anisotropic*, which means their optical properties vary with direction in the crystal. Corundum crystals are anisotropic, and they are termed optically *uniaxial*: The optical properties measured in two of the three spatial directions (*x* and *y*) are the same, but properties in the *z* direction are different. We refer to the unique *z* direction of a uniaxial crystal as the *c-axis*, also called the *optic axis*. The other two directions, *x* and *y*, are identical and are termed the *a-axes* (see figure B-1).

Light is a combination of electric and magnetic fields that oscillate perpendicular to the direction of the light propagation as shown in figure B-2.

Linear polarized light is light whose *electric field*, *E*, oscillates in a single direction perpendicular to the direction of propagation, as shown in figure B-3. By convention the direction of E is the *polarization direction*.

A light beam from a thermal source (such as the sun or a heated filament light bulb) comprises light rays whose electrical fields oscillate in all directions perpendicular to the direction of propagation (figure B-4). Such

Figure B-2. Light is a combination of electric and magnetic components that oscillate perpendicular to each other and to the direction of propagation.

a light beam is termed *unpolarized* and is necessarily perpendicular to the propagation direction.

For optical measurements of uniaxial crystals, there are two unique geometries for a light beam passing through a crystal that yield two different absorption spectra. This property is termed *dichroism*. It is this dichroism that accounts for the different colors we see looking through crystals in different directions. The first of these geometries is termed the *ordinary ray*; its polarization direction, E, is perpendicular to the c-axis. This is often designated by E⊥c. Thus a beam of light traveling along the c-axis, polarized in any direction or unpolarized, is E⊥c. A linearly polarized light beam traveling at any direction through the crystal is also an ordinary ray as long as the polarization direction E is perpendicular to the c-axis (E⊥c). It is called ordinary because this holds true for any propagation direction through the crystal.

The second unique geometry is where the polarization direction E of the light beam traveling through the

Figure B-1. Corundum is a uniaxial mineral, meaning it has one unique crystallographic axis out of three. This drawing shows the three axes of a uniaxial crystal. The two a-axes are the same while the c-axis is different. Properties of uniaxial crystals are different when measured along the c-axis rather than perpendicular to it. Optical absorption, and thus color, are different when viewed with light propagating along the c-axis rather than along either a-axis.

Figure B-3. A light ray's electric field direction, which is also called the polarization direction, is perpendicular to its propagation direction. In this diagram, the light ray is propagating toward the right side of the page and its electric field is oscillating up and down in the plane of the page.
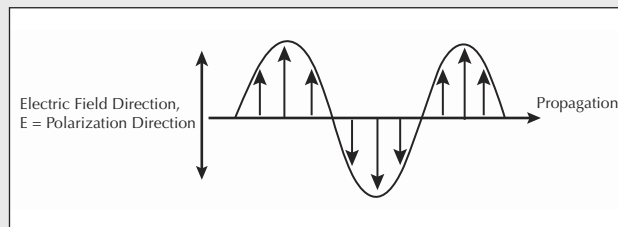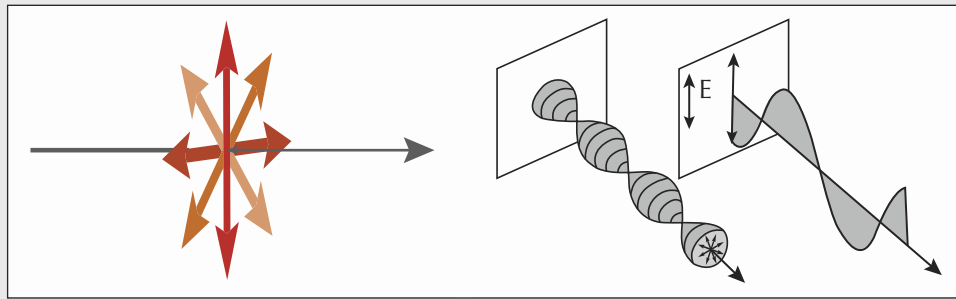
Figure B-4. Unpolarized light is composed of rays whose electrical fields oscillate in all directions perpendicular to the propagation direction (left and center). Polarized light has an electric field E that is constrained to oscillate in a single direction (right).

crystal is parallel to the c-axis. Visualizing this geometry, it is clearly a much greater restriction in that the light beam must be both linearly polarized and propagating perpendicular to the c-axis. Thus it is termed the *extraordinary ray* and designated E||c.

For any other combinations of propagation and polarization directions, what is measured is some combination of these unique spectra or indices of refraction.

When we view a corundum crystal down the c-axis, the color we see is determined by the E⊥c absorption spectrum (figure B-5, top row). This is because all polarization directions of that light beam are E⊥c.

When we view a corundum crystal along any a-axis, the situation is more complex. The light incident on the crystal is unpolarized. When entering the crystal, it is split into two colinear beams—one E⊥c and one E||c. Each of these sees the corresponding absorption spectrum, and thus when the beam emerges we see a color that is the average of the colors produced by the two absorption spectra, E⊥c and E||c (figure B-5, bottom row).

Figure B-5. Shown at left are the ruby crystal from figure B-1 and two crystallographically oriented ruby wafers with polished parallel surfaces corresponding to the shaded crystal faces. One wafer has the c-axis perpendicular to its surfaces (top), and one contains the c-axis in the plane of the wafer (bottom). A beam of unpolarized light contains rays that are polarized in all directions perpendicular to the direction of propagation. Unpolarized incident light striking the left side of the top wafer passes through unaltered except for absorption by the E⊥c absorption spectrum shown at the right. Thus only E⊥c color is observed, and the dichroscope also shows only E⊥c color (both top and bottom dichroscope views regardless of dichroscope rotation). Unpolarized light striking the bottom wafer is split into two beams polarized at 90° to one another. One beam is polarized parallel to the c-axis (E||c) and one is polarized perpendicular to the c-axis (E⊥c). The different absorptions of these two orthogonal beams are shown to the right. The observed color is equal proportions of E⊥c and E||c. When the wafer is viewed with a dichroscope that is rotated to maximum color difference, the E⊥c and E||c colors are resolved individually (bottom dichroscope view).
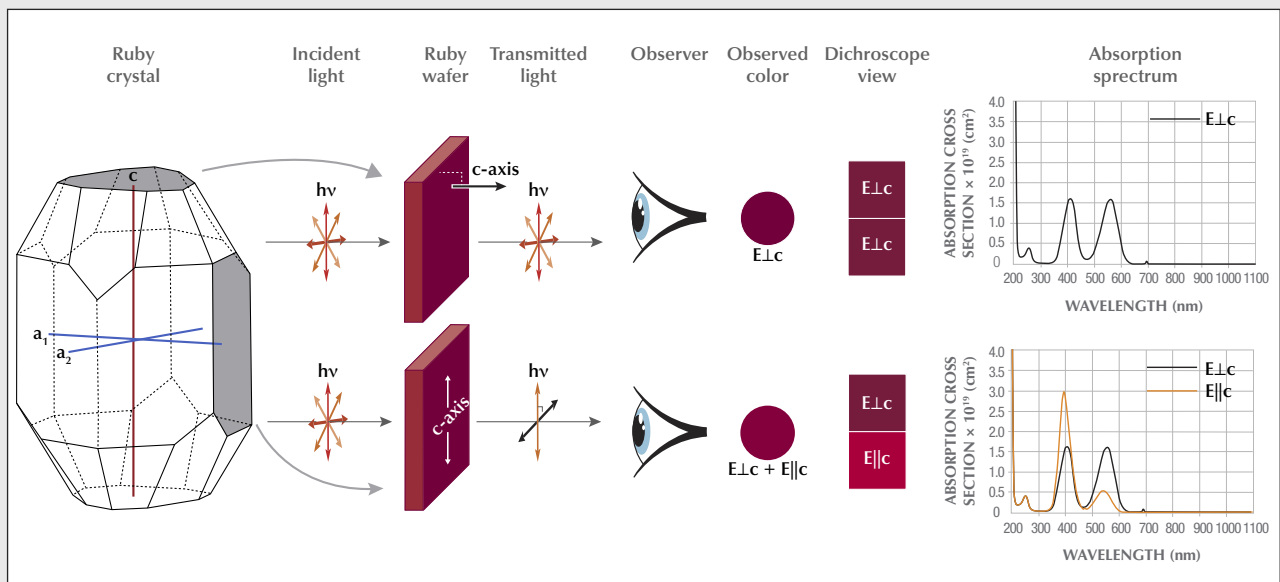
A calcite dichroscope is simply an instrument that splits a beam into two rays whose polarization directions are at 90° to each other. If we observe through a dichroscope a beam of light that has propagated along an a-axis of the crystal and rotate the dichroscope so that the color difference between the two sides is at a maximum, we have found the orientation where its two polarization directions match the two directions of the crystal. We are observing both a pure E⊥c color and pure E||c color (figure B-5 bottom, dichroscope view). If we view the crystal in this orientation *without* the dichroscope, we see a single color that is equal proportions of E⊥c and E||c color, which we call E⊥c + E||c (figure B-2 bottom, observed color). If instead we view the crystal with the dichroscope along the c-axis, we observe the same color on each side, and the color stays the same as we rotate the dichroscope. In this case we are observing pure E⊥c color (figure B-2 top, dichroscope view). In this paper we present absorption cross section spectra for E⊥c and E||c, and color circles for E⊥c, E||c, and E⊥c + E||c.

Crystal optics is a venerable field of study, and there are many different designations in use for E⊥c and E||c.

We have chosen to use these two designations for simplicity, because they say exactly what they are and we don't have to remember what they mean. The same designation issues arise with the two indices of refraction. In table B-1 we have listed the more commonly used designations for both rays and indices of refraction.

TABLE B-1. Alternative designations for rays and indices of refraction.

Rays	
E⊥c	E||c
Ordinary ray	Extraordinary ray
O-ray	E-ray
σ or sigma	Π or pi
ω	ε
Indices of Refraction	
$n_\perp$	$n_{||}$
n_o	n_e
n_σ or n_s	n_π or n_p
n_ω	n_ε

D65 (daylight equivalent). The E⊥c colors are seen looking through a stone along the c-axis. The E⊥c + E||c colors are what is seen looking through a stone perpendicular to the c-axis. With a properly aligned dichroscope viewing in this same direction, we see the pure E⊥c and E||c colors separated (see box B for a basic introduction to uniaxial crystal optics). L*a*b* color coordinates for these color circles and all subsequent color circles presented in this article are available in Appendix 2 at https://www.gia.edu/doc/SP20-corundum-chromophores-appendix2.

Along the horizontal axis of the color circle array is the areal density of the Cr^{3+} in units of ppma-cm. Areal density is the product of the chromophore concentration in ions per cm^3, times the path length through the stone in cm. The concentration of chromophore ions is 1.178×10^{17} ions/cm^3 times the concentration in ppma (see box A). For a 1 cm thick sample, the numbers under the color circles are the Cr^{3+} concentration in ppma. For a 2 cm thick sample showing the same color, the concentration is one half the numerical ppma-cm value. For a 1/2 cm thick stone, the concentration is twice the ppma-cm value. Thus the numbers under the color circles can be

viewed as presenting a stone of fixed concentration of increasing thickness, or of fixed thickness with increasing Cr^{3+} concentration, or any combination of the two.

The color we perceive also changes with the type of light source. Figure 4 (right) shows the three sets of color circles—E⊥c, E||c, and E⊥c + E||c—but also for each of two illuminants—D65 (daylight) and A (tungsten bulb). We have chosen these two light sources to maximize the observable color difference. Thus we can see a substantial change in the perceived color with a change in light source. While this color change is significant, ruby is not described as a color-change gem. A color-change gem is usually thought of as one where the hue changes significantly (more than one adjacent hue position), such as blue to red or green to red.

THE V^{3+} CHROMOPHORE

Vanadium (V^{3+}) commonly occurs in trace element analyses of natural corundum, particularly ruby. Generally, the vanadium concentration is not high enough (<20 ppma) to have a significant impact on the color. However, recently published analyses of

corundum from the Mogok Stone Tract in Myanmar (Harlow and Bender, 2013; Zaw et al., 2015) have shown concentrations as high as 2000 ppma and reported sapphire colors of "slate" (grayish blue to gray-blue) to purple as well as color-change in some cases. For concentrations at or considerably less than this extreme, vanadium will indeed impact the color of ruby and sapphire. V^{3+} spectra in corundum have been studied for decades (Pryce and Runciman, 1958; McClure, 1962; MacFarlane, 1964).

Several decades ago, the former Union Carbide Corporation crystal growth facility in Washougal, Washington, grew a large vanadium-doped sapphire crystal by the Czochralski technique for research purposes. A slice of this unique crystal was provided for our research. SIMS analysis showed a vanadium concentration of 116 ppma with a total combined uncertainty of ± 8.9%. The detection limit determined for V^{3+} in corundum at the 95% confidence level was 0.016 ppma. Wafers were fabricated from this boule with the c-axis in the plane of the wafer so that both E⊥c and E∥c absorption spectra could be recorded. Since vanadium can exist in multiple valences, the wafers were heated at 1750°C in oxygen for 10 hours to assure that all of the vanadium was in the 3+ va-

lence state, as previously discussed. Previous multiple heat treatment experiments on this material had shown these conditions were effective.

Figure 5 shows the absorption cross section for both the E⊥c and E∥c for V^{3+} in sapphire. It is interesting to note that the V^{3+} spectra in the visible range show two absorption bands with similar positions and widths to those of Cr^{3+}. However, their relative magnitudes are very different, leading to very different colors. Vanadium is a weak chromophore in corundum since its absorption band, centered at 580 nm, is much weaker than that of Cr^{3+} at 560 nm. We determined that vanadium's E⊥c peak cross section for the 580 nm band is 1.0×10^{-19} cm^2 ± 8.9%.

Figure 6 (left) shows the three sets of color circles for E⊥c, E∥c, and E⊥c + E∥c under D65 illumination for V^{3+}. There is a significant hue difference between the E⊥c color, which is a grayish blue, and the E∥c color, which is distinctly green at the lower concentrations. Nearly the same amount of color difference also exists between the E⊥c color and the E⊥c + E∥c color. The color of a faceted stone can therefore be quite different depending on the orientation of the cut. While the hue differences between the E⊥c color and E∥c color for Cr^{3+} illustrated in the previous
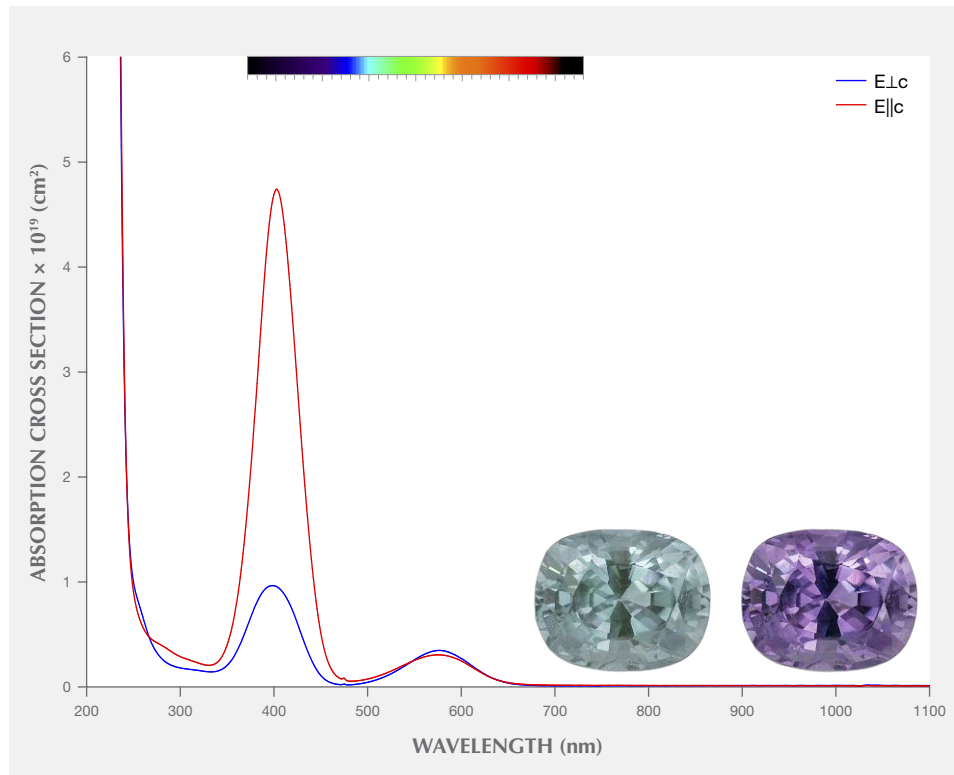
Figure 5. Cross section spectra of the V^{3+} chromophore, measured from a synthetic color-change sapphire grown by the Czochralski method. Also shown is a 1.17 ct color-change sapphire in daylight (left) and incandescent light (right), representative of the color that would be produced by the V^{3+} chromophore in isolation. Photo by Wimon Manorotkul; courtesy of Lotus Gemology collection.

V³⁺ Chromophore

CIE-D65 Illuminant
(daylight; approx. 6500 K)

Illuminant Comparison
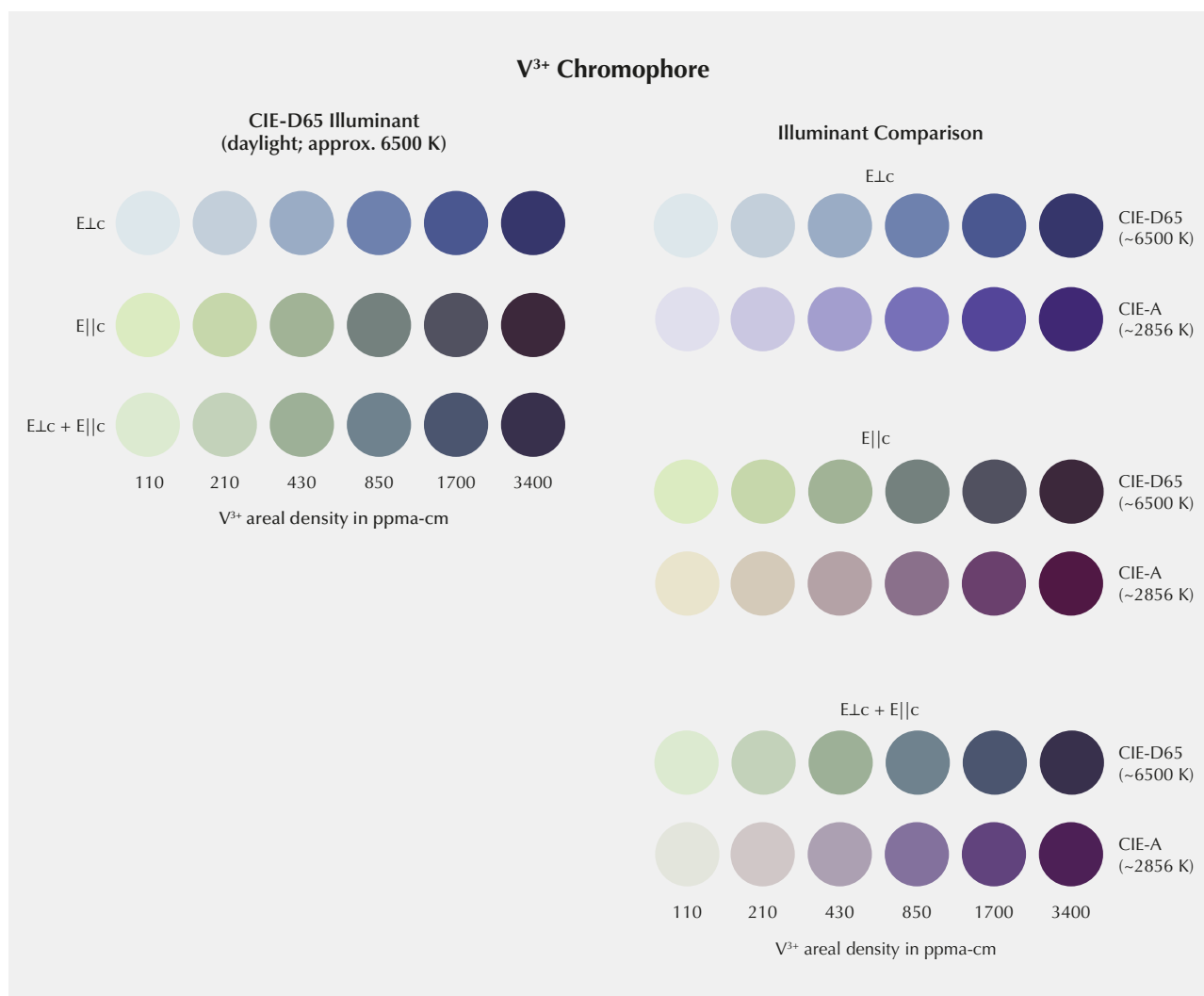
Figure 6. Left: Areal density color circles of the V^{3+} chromophore under illuminant D65. Note the significant color difference between the E⊥c color, which is grayish blue, and the E∥c color, which is quite green at lower concentrations. As with Cr^{3+}, the E⊥c and E∥c color difference is significant. Right: Illuminant comparison color circles of the V^{3+} chromophore for illuminants A and D65. For two of the orientations (E∥c and E⊥c + E∥c), the hue difference under A and D65 and illuminants certainly appears substantial enough to qualify it as a color-change gem.

section are certainly noticeable, the hue difference for V^{3+} illustrated in this section is very substantial.

Figure 6 (right) presents the E⊥c, E∥c, and E⊥c + E∥c data for illuminants A and D65. While all three orientations show a noticeable hue difference for the two illuminants, the E∥c color and E⊥c + E∥c color show a very strong hue difference, which would certainly qualify as a color-change gem when properly cut. The hue difference in these orientations is produced because the D65 light source is richer in blue to green wavelengths than the A light source. Consequently, the stone transmits more green light under D65 illumination, giving the stone a greener

hue. The A light source is richer in orange to red wavelengths, so the stone transmits proportionally more of these wavelengths, giving the stone a purplish color. Given the hue differences, it would be interesting to cut some faceted stones from this synthetic crystal, and to search for unusually colored natural high-V pieces from Myanmar.

Fe³⁺: MULTIPLE CHROMOPHORES

Iron is nearly ubiquitous in gem corundum, present over a very wide range of concentrations from less than a few ppma to nearly 5000 ppma. While this

makes it difficult to characterize, the fact that Fe^{3+} can exist as single ions replacing aluminum, Fe^{3+} ion pairs, and perhaps larger Fe^{3+} clusters pose yet greater problems. Because the Fe^{3+} spectrum is composed of all of these species whose individual concentrations depend in a nonlinear way upon the total iron concentration in the sample, the spectrum's dependence on concentration can be quite complex (Ferguson and Fielding, 1971 and 1972; Krebs and Maisch, 1971). In addition to these problems, the Fe^{3+} chromophore is the weakest chromophore in natural corundum. Its peak absorption cross section at 450 nm in the visible region does not exceed 2.5×10^{-20} cm^2 ± 8.0%, and it is quite narrow. Thus a variety of samples with a wide range of total Fe^{3+} concentrations is required to characterize the spectra.

Directly growing synthetic sapphire at its melt temperature (~2050°C) doped with iron is limited by the fact that iron and its oxides all have very high vapor pressures at this temperature and thus vaporize from the melt. This imposes a practical limit of a few hundred ppma of iron for crystals grown this way. Flux growth at temperatures of 900–1300°C would seem to be an attractive alternative, and it has been tried (Ferguson and Fielding, 1972), yet the spectroscopy applied still employed only natural crystals. Another problem is that the fraction of pairs and larger clusters would certainly be dependent on the thermal history of the crystal, which would not necessarily mimic nature. For these reasons we too are constrained to using natural crystals for part of our characterization.

Figure 7 shows the absorption cross section spectra of a natural corundum sample with a very high iron concentration determined with SIMS of 4730 ppma, with a total combined uncertainty of 8.0%, the highest concentration among our samples. The detection limit to the 95% confidence level for Fe was 0.003 ppma. The highest concentration was chosen as the cross sections will most easily be measured. At such a high iron concentration, one can easily observe and compare the weak broad features of both the E⊥c and E∥c absorptions. This sample is from the Subera deposit in Queensland, Australia. Yellow sapphires of similar iron concentrations are found in the Garba Tula deposit in Kenya, the Chanthaburi area of Thailand, and other alkali basalt-hosted deposits, but they are not common. Usually such sapphires also include a few ppma of Fe^{2+}-Ti^{4+} pairs, which shifts the yellow to a greenish yellow, or they contain a few tenths of a ppma of h•-Fe^{3+} pairs, which adds some golden yellow coloration.

The spectra of Fe^{3+} containing corundum is quite
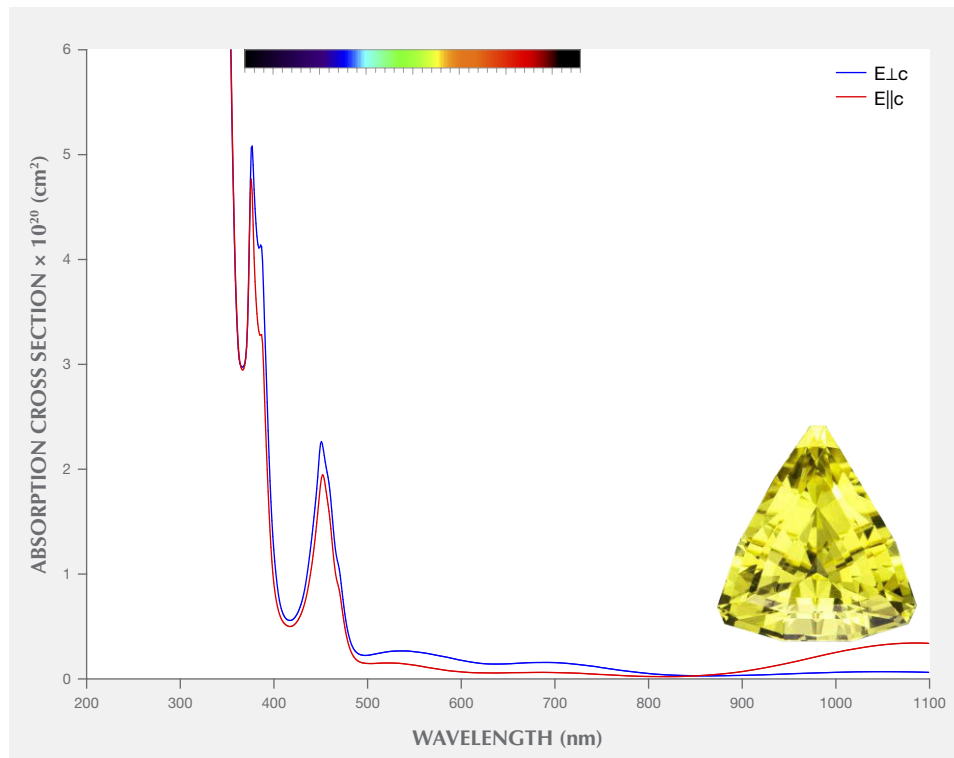
Figure 7. Cross section spectra of Fe^{3+} and Fe^{3+}-Fe^{3+} pairs measured in a natural yellow sapphire from the Subera deposit in Queensland, Australia, with a remarkably high Fe^{3+} concentration of 4730 ppma. Also shown is a 2.33 ct unheated Australian yellow sapphire, representative of the color that would be produced by this chromophore in isolation. Photo by Lotus Gemology; courtesy of Terry Coldham/Intogems PL.

complex. In figure 7, the narrow peaks at 377 and 450 nm are attributed to Fe^{3+}-Fe^{3+} pairs, as is the weak but broad band at 540 nm. The narrow peak at 388 nm is attributed to single Fe^{3+} ions. The weak but broad bands at 700, 1050, and 1085 nm are only really quantifiable at high Fe^{3+} concentrations. The lack of temperature dependence in the absorption coefficient of these bands implies that they arise from single Fe^{3+} ions (Ferguson and Fielding, 1972). There is also a broad band at 330 nm that is identified as an Fe^{3+}-Fe^{3+} pair band, but it is not visible in this spectrum. It can be seen in two of the spectra presented in figure 8. The relatively narrow spectral features at 377, 388, and 450 nm are observable in the spectra of most corundum samples with a Fe concentration of 150 ppma or higher. This is because the absorbance, absorption coefficient, and absorption cross section of different species are additive, and thus a weak narrow feature can be easily seen on top of a much stronger wide band.

The ratio of the peaks of the 388 nm band to the 377 nm band changes dramatically with concentration. This is because the 388 peak is primarily a single Fe^{3+} ion, while the 377 nm peak is a pair of Fe^{3+} ions. Our earlier studies of about 40 different natural samples with widely varying Fe^{3+} concentrations indicate that the peak absorption coefficient at 450 nm, which is a pair of ions, increases very approximately with $C^{1.5}$, where C is the total Fe^{3+} concentration. This implies that the absorption cross section of the 450 nm band increases approximately with the square root of C. If there was not a concentration dependence of this cross section, there would be a single curve for $E \perp c$ in figure 8, just as we see for Cr^{3+} and V^{3+}. This dependence of the cross section on concentration is currently under study by the authors with over 100 natural samples analyzed by laser ablation–inductively coupled plasma–mass spectrometry (LA-ICP-MS).

Because the absorption cross section is not independent of the iron concentration, our usual presentation of color circles as a function of the areal density, ppma-cm, is not a valid characterization. Thus we present some $E \perp c$ color circles at a few fixed concentrations and as a function of the path length through the sample. Figure 9 (left) compares the $E \perp c$ color circles for D65 illumination. Figure 9 (right) also shows the same color circles but under illuminant A. Fe^{3+} exists in natural gem corundum over a much wider concentration range than any other chromophore. At a few thousand ppma, Fe does indeed cause strongly colored yellow sapphire. However, it is such a weak chromophore that only at these higher concentrations does it contribute much color to a gem. Presenting a more detailed discussion of the color contributed by iron will require a much better
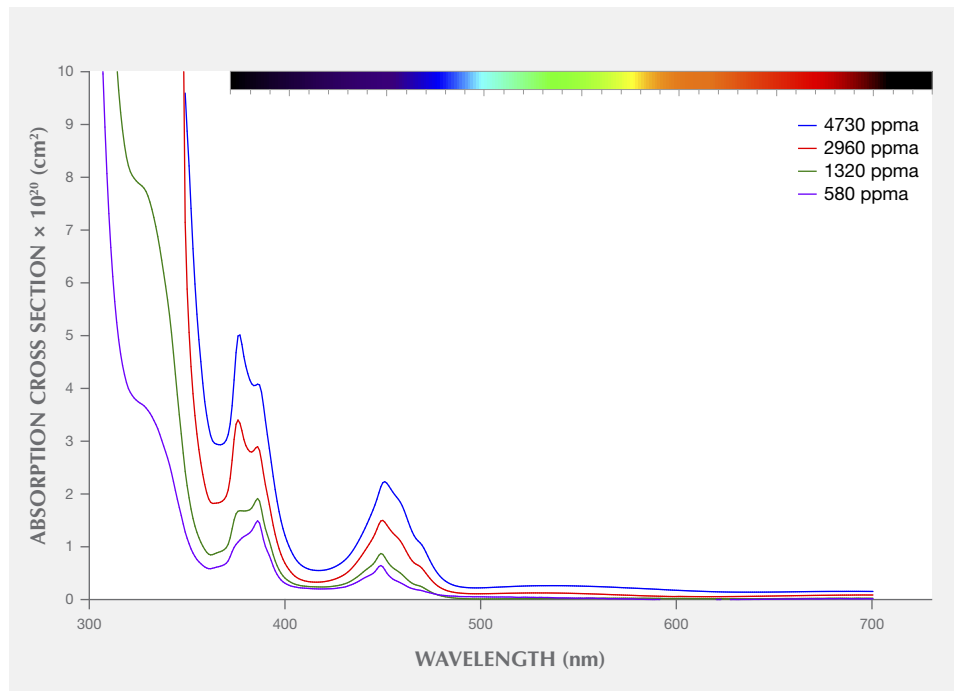
Figure 8. Unlike the other corundum chromophores, the cross section of the iron chromophore is dependent on the iron concentration. Shown here are the $E \perp c$ cross sections for four different Fe^{3+} concentrations: 4730 ppma, 2960 ppma, 1320 ppma, and 580 ppma.

Fe³⁺ Chromophore Comparison
E⊥c

	CIE-D65 Illuminant (daylight; approx. 6500 K)					CIE-A Illuminant (incandescent; approx. 2856 K)				
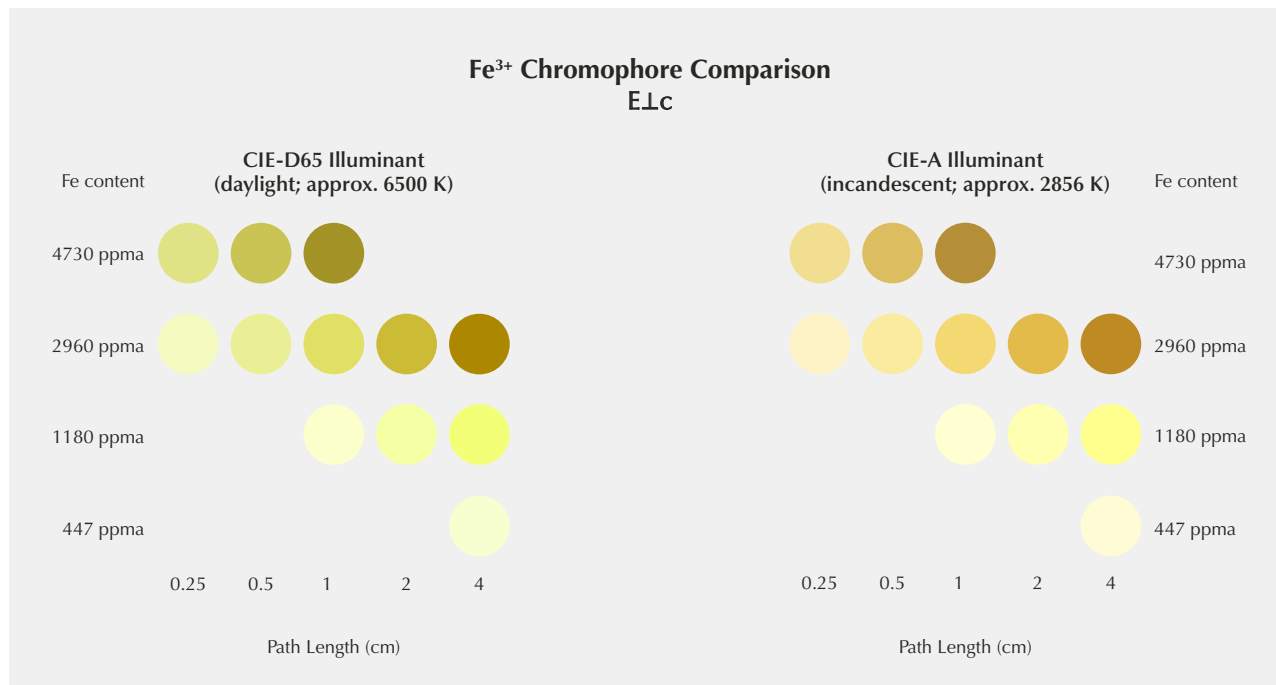
Figure 9. The color produced by various iron concentrations and path lengths through the stone. The iron chromophore is very weak, so high concentrations are needed to produce significant color. There is also a quite noticeable color difference between illuminants D65 and A.

physical model of iron in the corundum crystal, as the pair or larger cluster concentrations will also be dependent on the thermal histories of the samples. We encourage our colleagues to study this matter.

THE Fe²⁺-Ti⁴⁺ CHROMOPHORE

Fe²⁺-Ti⁴⁺ pairs are the primary chromophore of blue sapphire (Townsend, 1968; Mattson and Rossman, 1988; Moon and Phillips, 1994). The defect chemistry that creates this pair is interesting. Titanium in corundum is a donor, and iron in corundum can be an acceptor. They electrostatically attract each other and locate on adjacent Al^{3+} sites in the crystal, creating a donor-acceptor pair. Neither Fe^{2+} nor Ti^{4+} alone has absorption features in the visible region. Ti^{4+} is a closed-shell electron configuration, and Fe^{2+} is expected to absorb only in the near infrared, but that absorption has not yet been observed. Yet when these two ions are located on neighboring aluminum sites, strong absorption bands arise across the visible and near infrared region of the spectrum. For E⊥c the band peaks at 580 nm, while for E||c the peak is at 700 nm. While the theory of the energy levels of a single transition metal ion in a crystal is quite well developed, the theory for ion pairs or clusters in a crystal is not.

The most commonly proposed explanation for the absorption spectra of blue sapphires is that of intervalence charge transfer (IVCT) between the two cations as follows:

$$Fe^{2+} + Ti^{4+} \xrightarrow{\ h\nu\ } Fe^{3+} + Ti^{3+}$$
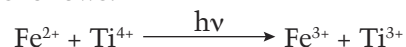
where hν is Planck's constant, h, times the optical frequency, ν. This a common way to indicate that a photon has been absorbed to enable the chemical reaction.

It would seem straightforward to determine the absorption cross sections of this transition by just analyzing a fairly uniform piece of natural blue sapphire and measuring the Fe and Ti concentrations to determine the concentration of Fe^{2+}-Ti^{4+} pairs. However, as discussed elsewhere (Emmett et al., 2017b), it is difficult to accurately determine the amount of titanium available, $[Ti]_{available}$, to pair with Fe^{2+} creating the blue color. Since the Si donor state lies above the Ti donor state in the corundum band gap, it will preferentially pair with acceptors such as Mg and Ni. Thus the Ti available to pair with Fe can be expressed as:

$$[Ti]_{available} = [Ti] + [Si - Mg - Ni] \text{ for } [Si - Mg - Ni] < 0$$
$$[Ti]_{available} = [Ti] \text{ for } [Si - Mg - Ni] \geq 0$$

Note that the square brackets around ions denote

atomic concentrations. The standard deviation (SD) of $[Ti]_{available}$ is the square root of the sum of the squares of SDs of Ti, Mg, Ni, and Si. Thus the standard deviation of $[Ti]_{available}$ can be very large, often exceeding the value itself, making accurate estimates of $[Ti]_{available}$ difficult.

It would also seem straightforward to just grow a synthetic crystal doped only with Fe and Ti, measure the concentrations, and calculate the Fe^{2+}-Ti^{4+} pair concentration. Such crystals were grown by Milan Kokta at the Union Carbide Corporation crystal growth factory in the 1980s for synthetic gem material. However, two problems arose with the use of synthetic crystals. First, at the Czochralski growth temperature of sapphire (~2050°C), the Fe^{2+}-Ti^{4+} pairs are largely dissociated. They only partially re-form as the stone cools over a day or two from growth temperature. Thus there are fewer pairs than the concentrations of [Fe] and [Ti] would imply, and we could not determine what fraction of the possible pairs were indeed present.

In nature the growth temperature is much lower, so there is less dissociation, and the cooldown is presumably extremely slow, so the pairs should more fully form. If so, the concentration of pairs should be determined by the ion concentrations.

To re-form the pairs, we heated the synthetic crystals in air for a few thousand hours. The temperature of 750°C was chosen to be low enough that many of the pairs would re-form, yet high enough that the diffusion coefficients of the ions were still large enough that clustering would take place at some finite rate. The absorption coefficients were re-measured at intervals of 50 and 100 hours to track the increase. This process was carried on until no further increase with time was noted, and thus equilibrium was reached. For our samples with the highest Ti concentration, equilibrium was reached in 1500 hours, with the absorption coefficient at 580 nm being 2–2.5 times higher than before heat treatment. It is likely that some additional pairs would form if the temperature were lowered further and the time greatly increased. Just what percentage we have achieved of the low-temperature equilibrium pair concentration is difficult to estimate.

Another problem with the growth of synthetic crystals doped with Fe^{2+}-Ti^{4+} is determining what fraction of iron in the crystal is actually in solution rather than present as microscopic iron particles. Under the oxygen partial pressure of Czochralski growth from an iridium crucible, all the iron present may not be trivalent and thus soluble in the melt.

We have observed microscopic iron crystals in some synthetic Fe-Ti doped crystals. Presently we have no reliable way to determine what portion of the iron in the crystal is actually in solution as Fe^{3+}. The synthetic crystals did, however, give us very high-quality E⊥c and E||c spectra without the interference from high concentrations of iron and other trace elements (Si, Cr, V, and Ni).

To achieve reasonably good approximation of the cross sections of the Fe^{2+}-Ti^{4+} pair, we have chosen a combination of both synthetic crystals and natural crystals. After examining a wide variety of natural crystals, we have chosen Yogo sapphires for their rather extreme optical and chemical uniformity, which far exceeds all other natural crystals we have studied, and for the fact that there is no 880 nm absorption band in this material. Since the synthetic crystals have no interference to the shape of the spectrum from other chromophores, they have been used to accurately determine the shape of the Fe^{2+}-Ti^{4+} pair absorption spectra.

We have carefully measured the trace element composition of 14 Yogo sapphires by SIMS at Caltech. The SIMS technique gives the smallest SDs of our current measurement techniques, and only SIMS can quantify Si. These analyses provided accurate determinations of Fe, Ti, Mg, Si, Ni, Cr, and V. The detection limits for Cr, V, and Fe were previously given, and the determined detection limits for Ti, Mg, Si, and Ni were 0.039, 0.001, 0.552, and 0.030 ppma, respectively. The higher detection limit for Si is partially due to its larger RSF value, but mainly due to the difficulty of removing all traces of Si from the chamber and mass spectrometer. Because [Si – Mg – Ni] is always negative for Yogo sapphires due to their high Mg concentrations (~100 ppma), the $[Ti]_{available}$ as noted above was calculated as

$$[Ti]_{available} = [Ti] + [Si] - [Mg] - [Ni]$$

The absorption spectra of the 14 Yogo samples were measured and the contributions from Cr^{3+} and V^{3+} subtracted from each using the absorption cross sections of Cr^{3+} and V^{3+} previously determined. The shape of the remaining Fe^{2+}-Ti^{4+} absorption band closely matched the shape determined from the synthetic crystals. The resulting absorption cross sections are shown in figure 10. The band shapes are from the synthetic crystals, and the band peak values are determined from the averages of the 14 Yogo crystals studied. The peak E⊥c absorption cross section at 580 nm thus determined is 1.94×10^{-18} cm^2 ± 25%.
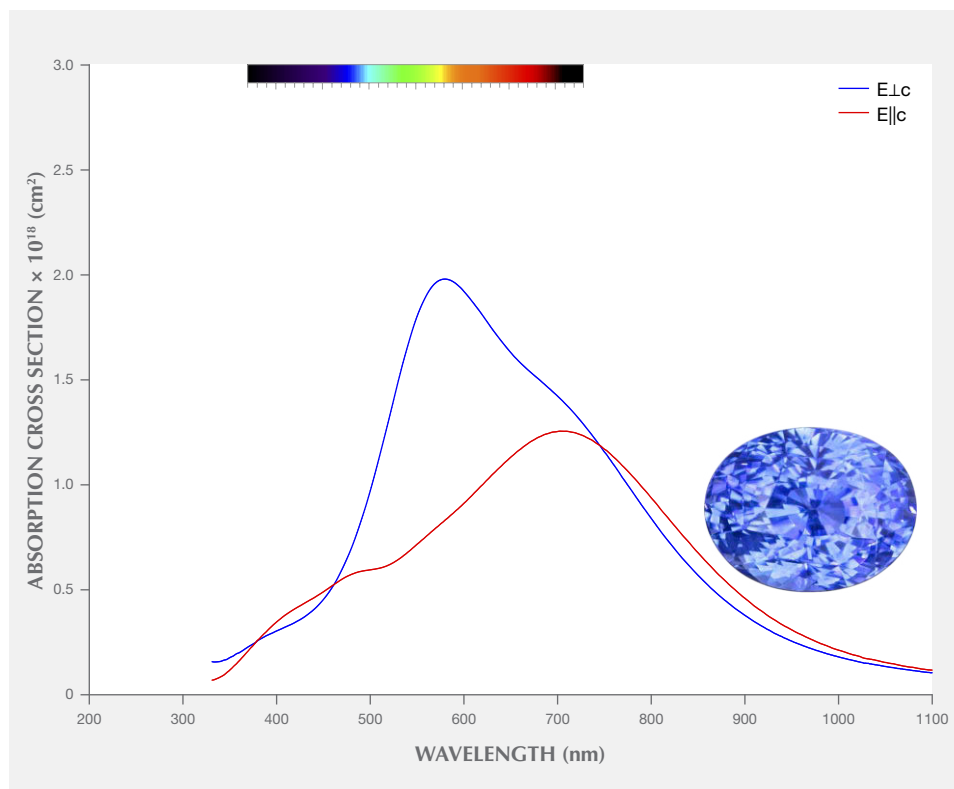
Figure 10. Cross section spectra of the Fe^{2+}-Ti^{4+} chromophore measured from a synthetic blue sapphire grown by the Czochralski method. Also shown is a fine 4.10 ct unheated Sri Lankan blue sapphire, representative of the color that would be produced by the Fe^{2+}-Ti^{4+} chromophore in isolation. Photo by Lotus Gemology; courtesy of Ruby N' Sapphire.

These spectra have been terminated at 330 nm in the UV. This was necessary because the first $O \rightarrow Fe^{3+}$ charge transfer band (Tippins, 1970) peaks at 259 nm. We have determined the peak cross section for this transition as 1.66×10^{-17} cm^2, which is extremely large. The sloping band edge on the long-wavelength side of this band mixes with the short-wavelength side of the Fe^{2+}-Ti^{4+} pair and rapidly exceeds the dynamic range of the spectrophotometer. Thus we terminated the Fe^{2+}-Ti^{4+} spectra before the charge transfer absorption became significant.

In the course of our study of the Fe^{2+}-Ti^{4+} band in many natural sapphires from many locations, we have found some whose Fe^{2+}-Ti^{4+} cross sections appear much larger (by factors of two or three) than those determined here using synthetic and Yogo sapphires. Nearly all of these non-Yogo samples contain very high iron content and substantial OH, as revealed by FTIR measurements. We do not know if this is a correct determination and thus represents an enhanced Fe^{2+}-Ti^{4+} cross section due to the presence of iron pairs or clusters with the Ti^{4+}, or whether it results from the fact that our chemical analyses only measure a very thin layer on the stone's surface rather than the bulk composition. Many of these samples demonstrating anomalous Fe^{2+}-Ti^{4+} cross sections are strongly color zoned, mean-ing that the concentration of Fe^{2+}-Ti^{4+} pairs along the optical path can vary substantially, something our surface-level measurements would not be able to capture. Additional research on this topic is definitely needed.

It is interesting to note that in the synthetic and Yogo crystals, the peak of the E⊥c cross section at 580 nm of 1.94×10^{-18} cm^2 ± 25% is about 12 times larger than that of Cr^{3+} at 560 nm. The large cross section and the width of the band in the visible region make the Fe^{2+}-Ti^{4+} pair a strong chromophore. Less than one-tenth the amount of it relative to Cr^{3+} is needed to produce strong coloration.

Figure 11 presents the color circles calculated from the cross section determinations. As in the discussion of the Cr^{3+} chromophore, we have used the areal density in ppma-cm to present the data. Figure 11 (left) shows the three sets of color circles for E⊥c, E||c, and E⊥c + E||c under illuminant D65. As we saw with the Cr^{3+} chromophore, the E⊥c and E||c colors are quite distinct. This is because the E⊥c absorption spectrum is more effective at blocking the blue-green and green portions of the spectrum than the E||c spectrum, thus transmitting a purer blue color.

Figure 11 (right) compares the color observed under illuminants A and D65. While the color differences shown between illuminants D65 (daylight) and
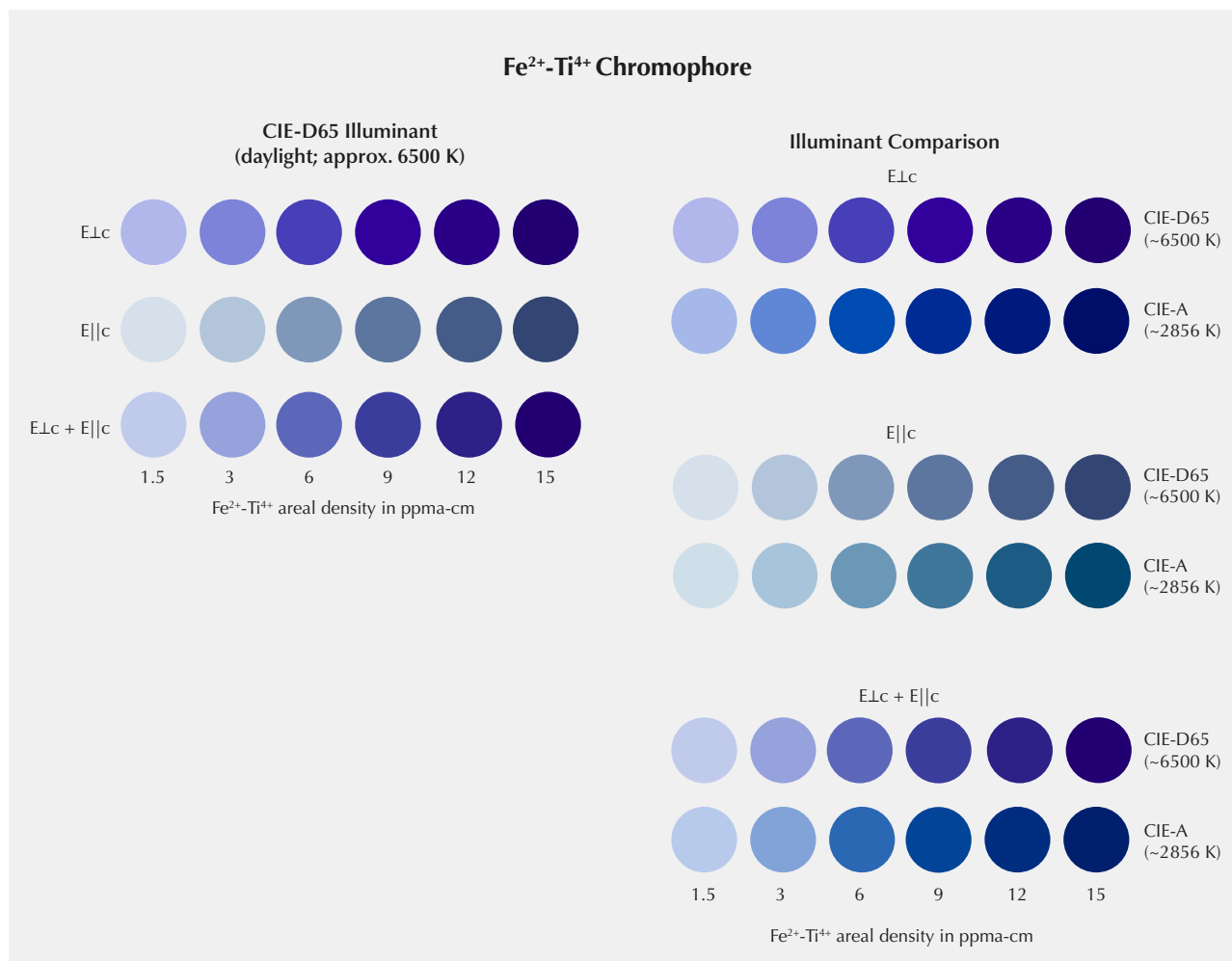
Figure 11. Left: Areal density color circles under illuminant D65 of the Fe^{2+}-Ti^{4+} chromophore. As with the Cr^{3+} chromophore, the E⊥c and E||c colors are quite distinct. This is because the E⊥c absorption spectrum is more effective at blocking the blue-green and green portions of the spectrum than the E||c spectrum, thus transmitting a purer blue color. Right: Illuminant comparison color circles of the Fe^{2+}-Ti^{4+} chromophore. While the color differences shown between illuminants D65 (daylight) and A (tungsten lamp) are not dramatic, the color circles for the D65 illuminant exhibit a lighter, brighter blue resulting from a greater portion of blue light in the D65 spectrum.

A (tungsten lamp) are not dramatic, the color circles for the D65 illuminant exhibit a brighter blue resulting from the greater portion of blue light in the D65 spectrum.

CHROMOPHORES INVOLVING TRAPPED HOLES

When the concentration of magnesium and nickel exceeds the sum of the concentrations of silicon, titanium, and hydrogen, the corundum sample is acceptor dominated. If this occurs in a relatively oxidizing natural environment, or if the stone is heat treated in air or oxygen, the excess acceptors will be charge compensated by trapped holes.

$$h^{•} = [acceptors] - [donors] = [Mg + Ni] - [Si + Ti + H]$$

If the sample also contains iron but not chromium, the $h^{•}$-Fe^{3+} pair can form, producing a strong yellow coloration. If instead the sample contains only chromium, the $h^{•}$-Cr^{3+} pair can form, producing a strong orange coloration. If the sample contains both Fe^{3+} and Cr^{3+}, the hole will preferentially pair with the Cr^{3+}. The association of the hole with Fe^{3+} or Cr^{3+} is unusual, as both are isoelectronic with Al^{3+} in the corundum lattice. However, isoelectronic dopants

Figure 12. Cross section spectra of the h•-Fe³⁺ chromophore measured from a synthetic yellow sapphire grown by the Czochralski method. Also shown is an 11.41 ct unheated Sri Lankan yellow sapphire, representative of the color that would be produced by the h•-Fe³⁺ chromophore in isolation. Photo by Lotus Gemology; courtesy of F.M. Gems.

that trap electrons, holes, or excitons are well known in wide gap semiconductors (Pajot and Clerjaud, 2013). Isoelectronic traps in wide-band-gap oxides have received some study as exciton traps that can greatly increase the fluorescence from UV excitation (Shtepliuk et al., 2011; Zorenko et al., 2011).

To study the chromophores composed of trapped holes paired with either Fe^{3+} or Cr^{3+}, two crystals were grown by the Czochralski technique at St. Gobain Crystals and Detectors; one was doped only with iron and magnesium, while the other was doped only with chromium and magnesium. As grown, the crystal containing iron and magnesium had a bright orangy yellow color, and the crystal containing chromium and magnesium had a bright orange color. The concentrations with total combined uncertainty for the h•-Fe^{3+} crystal were Fe = 180 ± 7.7% and Mg = 2.13 ± 9.2%. If quantifiable concentrations of Si and Ti were present in this crystal, the total available Mg and its associated total combined error would have to be adjusted to account for these ions. However, both Si and Ti were below the quantification limits, eliminating the need to account for these trace elements. For the h•-Cr^{3+} crystal, the Cr concentration with total combined uncertainty was 12.6 ± 7.7%, and the Mg concentration with total combined uncertainty was 0.813 ± 9.8% Similarly, the crystal pu-

rity was high enough that we did not need to account for Ti and Si that would scavenge available Mg. Following growth, the crystals were annealed in oxygen at 1750°C for 10 hours to assure that all magnesium was charge compensated by holes. Previous experiments under a variety of conditions indicated that this annealing condition maximizes the hole concentration. The resulting crystals were a deeper yellow, almost golden color (iron and magnesium), and a deeper orange color (chromium and magnesium).

The cross sections presented for these two chromophores are determined from the absorption spectra recorded on these double-doped samples. Since the h•-Fe^{3+} sample also contains the Fe^{3+} chromophore by itself, that spectrum was subtracted before calculating the h•-Fe^{3+} cross section. Since the Fe^{3+} chromophore is so weak, it only modifies the color produced by the h•-Fe^{3+} chromophore at high Fe^{3+} concentrations. Similarly, since the h•-Cr^{3+} sample also contains the Cr^{3+} chromophore by itself, that spectrum was subtracted before calculating the h•-Cr^{3+} cross section. However, Cr^{3+} is a moderately strong chromophore, and thus any gemstone containing the h•-Cr^{3+} chromophore will also exhibit a pink to red component from Cr^{3+} alone. It is these two chromophores together that create the magnificent pinkish orange *padparadscha* sapphire.
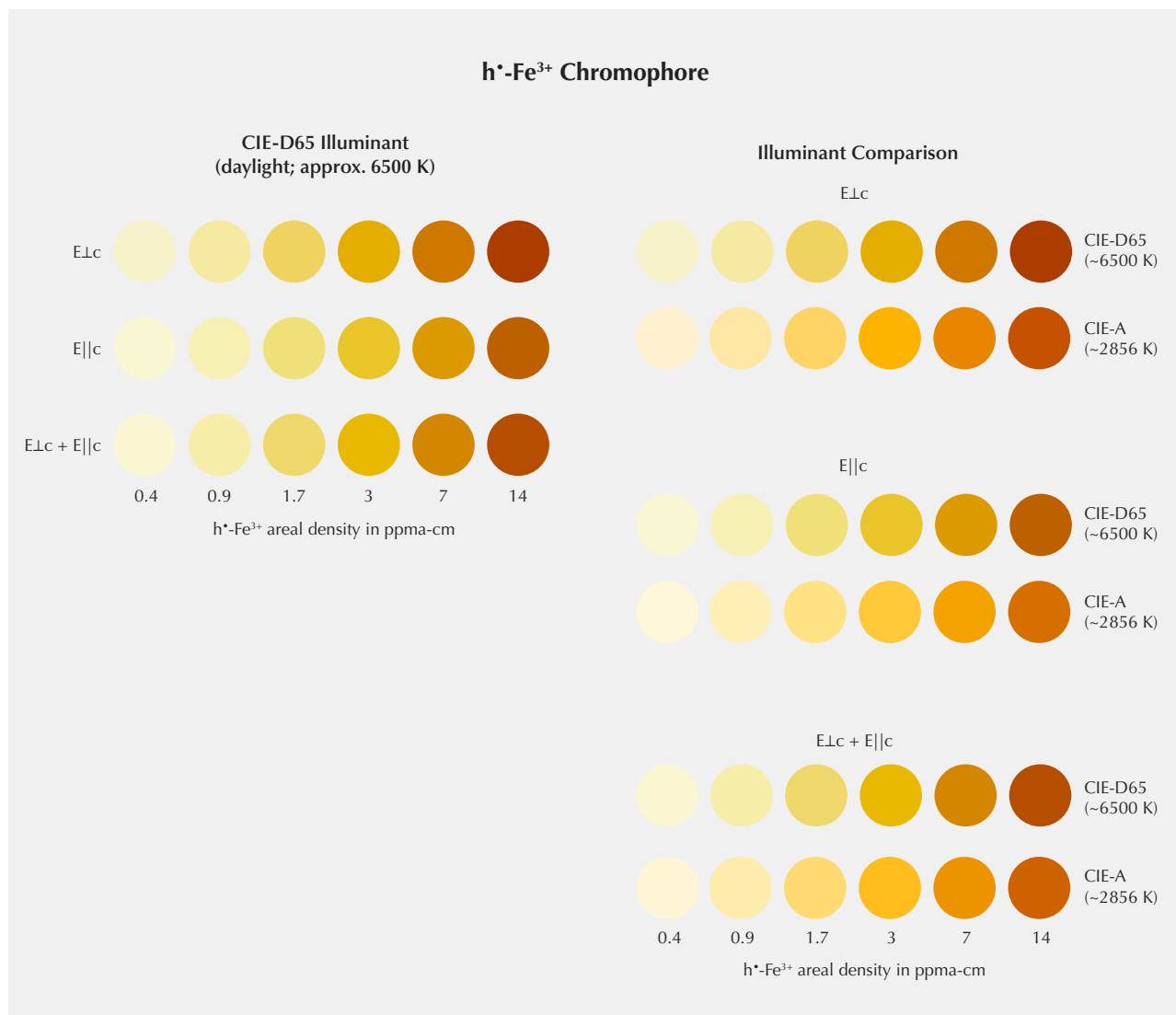
Figure 13. Left: Areal density color circles for the h•-Fe³⁺ chromophore. Right: Illuminant comparison of the h•-Fe³⁺ chromophore. Little color change is observed with the change in illuminant for all orientations.

The spectrum in figure 12 shows the absorption cross sections for E⊥c and E||c of a sample cut from the crystal containing iron and magnesium. Note the extremely large cross section of the h•-Fe³⁺ chromophore, 1.3×10^{-17} cm² ± 12.0%, which is about 6.8 times that measured for the Fe^{2+}-Ti^{4+} pair or about 80 times larger than that of Cr^{3+}. It is thus a very strong chromophore in corundum. The h•-Fe³⁺ and the h•-Cr³⁺ are the strongest chromophores in the visible region of the spectrum for corundum. As discussed in the section on the Fe^{2+}-Ti^{4+} pair chromophore, the spectrum of the h•-Fe³⁺ chromophore has been termi-nated at 330 nm to avoid interference by the O → Fe^{3+} charge transfer band. This is not necessary for the h•-Cr³⁺ spectra, as the first O → Cr^{3+} band is well below 200 nm (Tippins, 1970).

Figure 13 presents the color circles for the h•-Fe³⁺ pairs. The E⊥c and E||c spectra are quite similar. Thus the E⊥c, E||c, and E⊥c + E||c color circles under D65 illumination shown in figure 13 (left) are also similar, unlike some of the other chromophores we have studied. What is interesting to note here is the extremely small amount of h•-Fe³⁺ pairs required to create a strong color. Only a few ppma are necessary

in a 1 cm thick sample to produce strong coloration, whereas nearly 3000 ppma of Fe^{3+} alone would be required to produce similar coloration (see figure 9). Examining the color circles in figure 13 (right) for the two different illuminants, D65 and A, we see that the color differences for the two illuminants are greater than the E⊥c and E||c color differences.

The h•-Fe^{3+} chromophore is the primary cause of color for yellow sapphires from Sri Lanka and other sources where the iron content is not extremely high. It also occasionally occurs in some high-iron sapphires from Thailand, where stones with the combination of the two chromophores are referred to as "Mekong Whisky" color sapphires.

Figure 14 shows the E⊥c and E||c absorption cross sections of the h•-Cr^{3+} pair system. Again, note the extremely large cross sections (1.3×10^{-17} cm^2 ± 12.5%), which are similar in magnitude to those of the h•-Fe^{3+} pair. These two systems are by far the strongest chromophores in corundum.

Figure 15 illustrates the color circles for h•-Cr^{3+} pairs. At left are shown the color circles for E⊥c, E||c, and E⊥c + E||c under D65 illumination. From the color circles we can see that this chromophore exhibits little dichroism, as the E⊥c and E||c circles are very similar in appearance. This results from the fact

that strong absorption is present below 560 nm for both E⊥c and E||c. Figure 15 (right) shows the color circles for both D65 and A illuminants. There is little chromatic difference resulting from the two illuminants. The color circles for illuminant A, which contains proportionally more yellow and red light, may be slightly brighter than their D65 counterparts.

The cross sections and color circles presented for the h•-Cr^{3+} chromophore are for the chromophore itself and do not include a contribution from the Cr^{3+}. Since Cr^{3+} is a moderately strong chromophore, very little is required to shift these hues toward a more pure orange. Concentrations of only 20–40 ppma Cr^{3+} are sufficient to cause a noticeable color shift.

COMPARING THE CHROMOPHORES

Looking closely at the absorption cross section spectra for the various chromophores, one can observe a wide range of values in the visible region of the spectrum of a factor of about 500. However, the variability of the "strength" of the chromophore is even greater because the width (full width half maximum, FWHM) of the cross section features in the visible range varies from ~25 nm for Fe^{3+} to ~250 nm for the Fe^{2+}-Ti^{4+} pair (see box A). Figure 16 shows the approximate concentrations of the six chro-
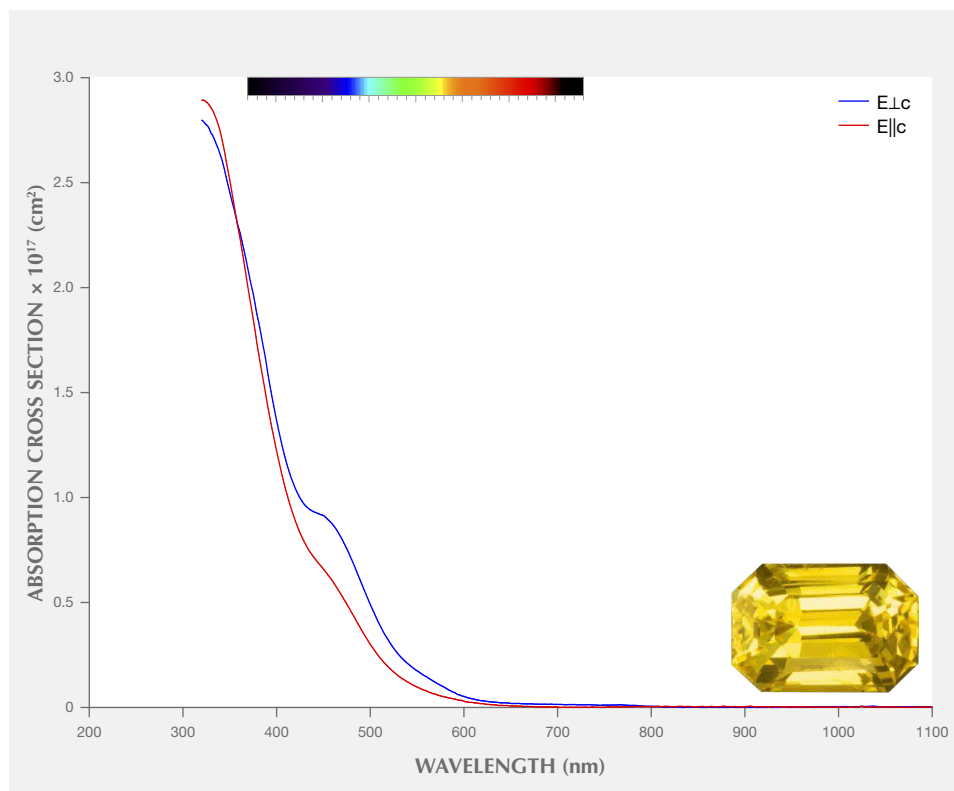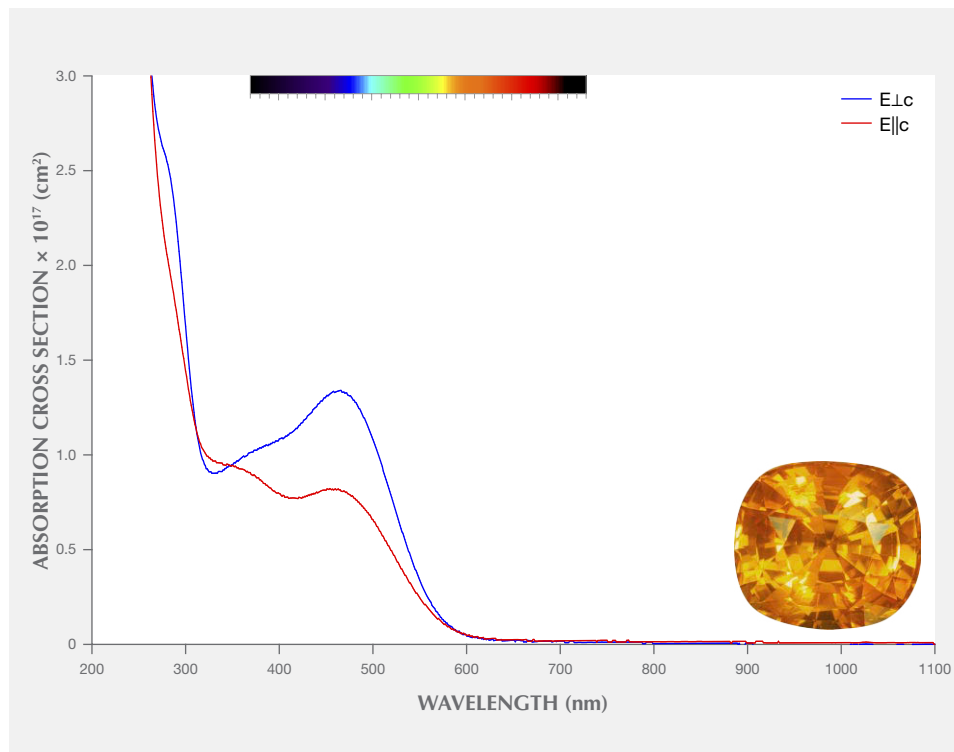

Figure 14. Cross section spectra of the h•-Cr^{3+} chromophore measured from a synthetic orange sapphire grown by the Czochralski method. Also shown is a 14.62 ct heated Sri Lankan orange sapphire, representative of the color that would be produced by the h•-Cr^{3+} chromophore in isolation. Photo by Lotus Gemology; courtesy of Ceylon Fine Gems.
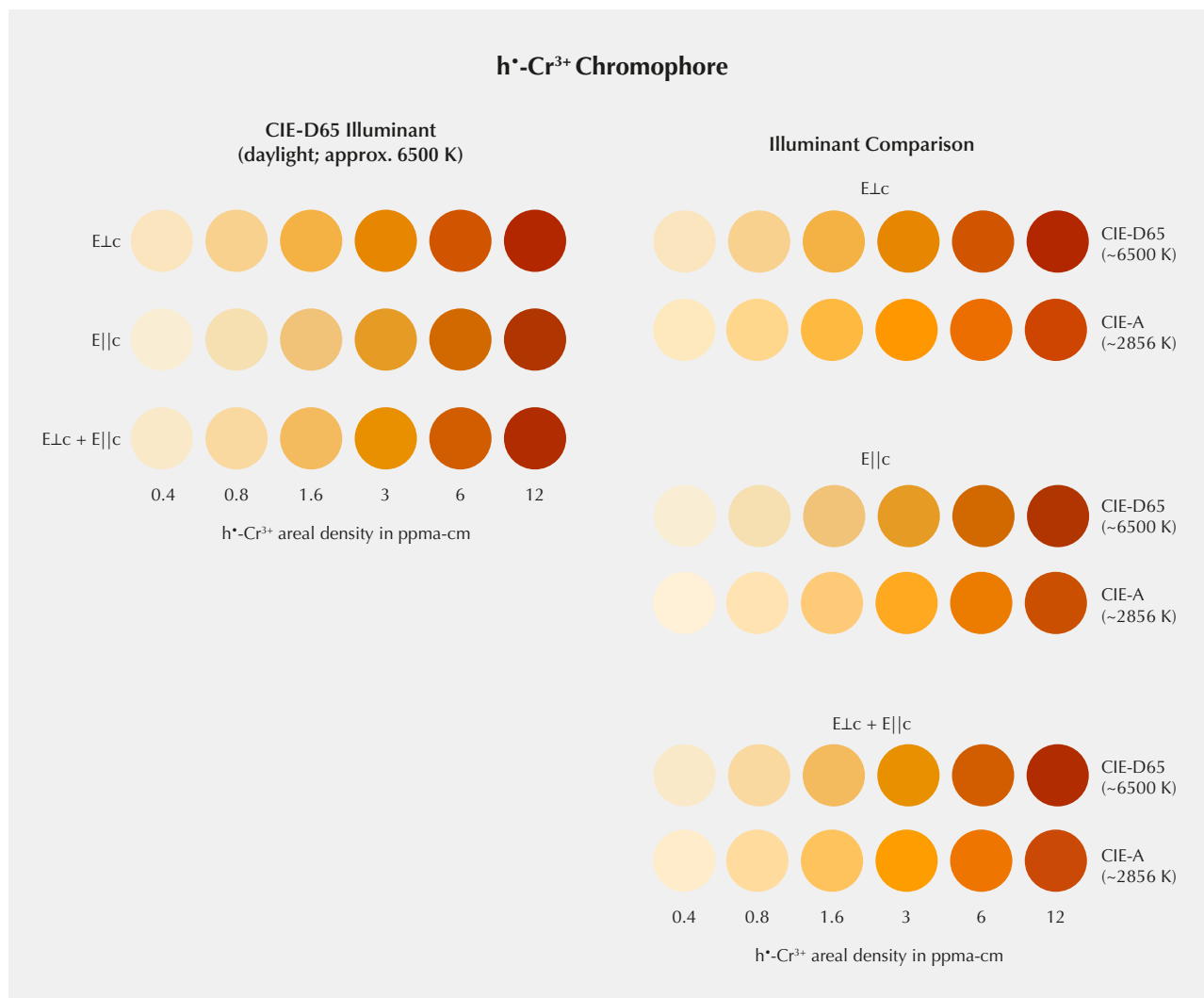
Figure 15. Left: Areal density color circles for the h•-Cr³⁺ chromophore. Right: Illuminant comparison of the h•-Cr³⁺ chromophore. As with the h•-Fe³⁺ chromophore, little color change is observed with the change in illuminant for all orientations.

mophores required to create roughly similar levels of color saturation for E⊥c in samples 1 cm thick. Concentrations for the chromophores were selected by visually comparing color circles and forming a consensus opinion among the authors about which circles appeared to have similar saturation levels. Comparing the chromophore concentrations in ppma under each circle emphasizes the rather extreme range in "strength," which is greater than a factor of 1000.

The belief that yellow sapphires were colored only by iron with or without some undefined "color center" (Schmetzer et al., 1983; Nassau, 1991) was

engendered by the fact that the existence of, strength, and absorption spectrum of the h•-Fe³⁺ chromophore was unknown. Additionally, the analytical techniques available before SIMS and SIMS-calibrated LA-ICP-MS with matrix-matched standards were incapable of measurements down to the ppma level. Another key to our current understanding of chromophores in corundum was the capability of growing synthetic sapphire containing only one of the chromophores we wished to study. This allowed us to confirm what we observed in natural samples.

Determining the absorption cross sections is a powerful technique in the study of color in allochro-
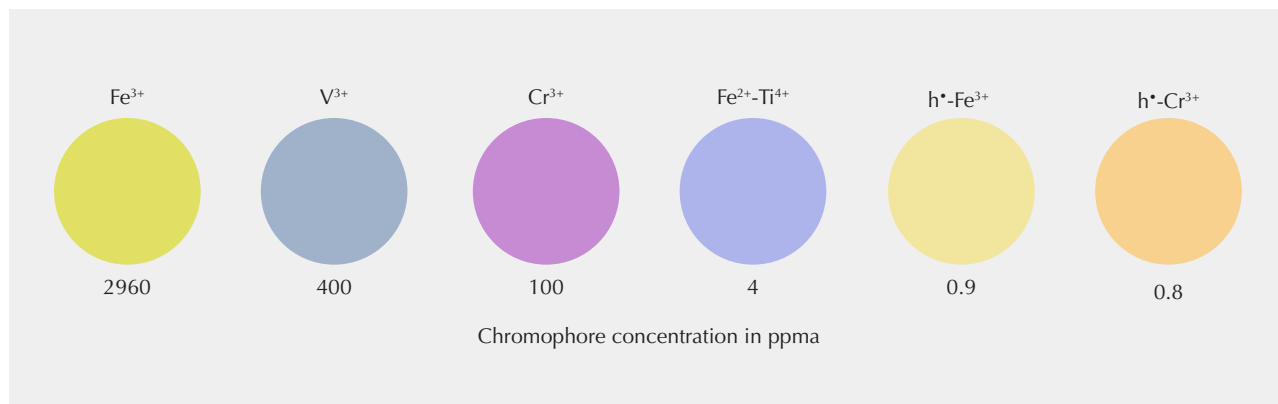
Figure 16. These color circles show the concentration of each chromophore necessary to produce similar saturation levels in corundum, thus illustrating the drastic difference in absorption strength among each of the chromophores. The circles represent the color produced by each of the chromophores in a 1-cm-thick sample viewed down the c-axis (E⊥c orientation) under CIE-D65 Illuminant. The chromophore concentration varies from nearly 3000 ppma for a weak absorber like Fe^{3+} to less than one ppma for a strong absorber like $h^\bullet$-Cr^{3+}.

matic minerals, as their magnitudes provide information on the types of absorbing species present. Applying it to other minerals might yield some new insights. Our current trace element analytical capability, at the ppma level or below, provides the critical capability to support such research.

REFERENCES

Beran A., Rossman G.R. (2006) OH in naturally occurring corundum. *European Journal of Mineralogy*, Vol. 18, No. 4, pp. 441–447, http://dx.doi.org/10.1127/0935-1221/2006/0018-0441

Berns R.S. (2000) *Billmeyer and Saltzman's Principles of Color Technology*. John Wiley & Sons, Inc., New York, 272 pp.

El-Aiat M.M., Kröger F.A. (1982) Hydrogen donors in α-Al_2O_3. *Journal of Applied Physics*, Vol. 53, No. 5, pp. 3658–3667, http://dx.doi.org/10.1063/1.331150

Emmett J.L., Scarratt K., McClure S.F., Moses T., Douthit T.R., Hughes R., Novak S., Shigley J.E., Wang W., Bordelon O., Kane R. (2003) Beryllium diffusion of ruby and sapphire. *G&G*, Vol. 39, No. 2, pp. 84–135, http://dx.doi.org/10.5741/GEMS.39.2.84

Emmett J.L., Dubinsky E.V., Hughes R.W., Scarratt K. (2017a) Color, spectra & luminescence. In R.W. Hughes, Ed., *Ruby & Sapphire: A Gemologist's Guide*. Bangkok, pp. 107–163.

Emmett J.L., Stone-Sundberg J., Guan Y., Sun Z. (2017b) The role

of silicon in the color of gem corundum. *G&G*, Vol. 53, No. 1, pp. 42–47, http://dx.doi.org/10.5741/GEMS.53.1.42

Ferguson J., Fielding P.E. (1971) The origins of the colours of yellow, green and blue sapphires. *Chemical Physics Letters*, Vol. 10, No. 3, pp. 262–265, http://dx.doi.org/10.1016/0009-2614(71)80282-8

——— (1972) The origins of the colours of natural yellow, blue, and green sapphires. *Australian Journal of Chemistry*, Vol. 25, No. 7, pp. 1371–1385, http://dx.doi.org/10.1071/CH9721371

Fritsch E., Rossman G.R. (1987) An update on color in gems. Part 1: Introduction and colors caused by dispersed metal ions. *G&G*, Vol. 23, No. 3, pp. 126–139, http://dx.doi.org/10.5741/GEMS.23.3.126

——— (1988) An update on color in gems. Part 2: Colors involving multiple atoms and color centers. *G&G*, Vol. 24, No. 1, pp. 3–15, http://dx.doi.org/10.5741/GEMS.24.1.3

Häger T. (2001) High temperature treatment of natural corundum. *International Workshop on Material Characterization by Solid State Spectroscopy: The Minerals of Vietnam*, pp. 4–10.

Harlow G.E., Bender W. (2013) A study of ruby (corundum) compositions from the Mogok Belt, Myanmar: Searching for chemical fingerprints. *American Mineralogist*, Vol. 98, No. 7, pp. 1120–1132, http://dx.doi.org/10.2138/am.2013.4388

Henderson B., Bartram R.H. (2000) *Crystal-Field Engineering of Solid-State Laser Materials*. Cambridge University Press, Cambridge, UK.

Krebs J.J., Maisch W.G. (1971) Exchange effects in the optical-absorption spectrum of Fe^{3+} in Al_2O_3. *Physical Review B*, Vol. 4, No. 3, pp. 757–769, http://dx.doi.org/10.1103/PhysRevB.4.757

Kröger F.A. (1984) Electrical properties of α-Al_2O_3. In W.D. Kingery, Ed., *Advances in Ceramics: Structure and Properties of MgO and Al_2O_3 Ceramics*. American Ceramic Society, Columbus, Ohio, pp. 1–15.

Kvapil J., Perner B., Súlovský J., Kvapil J. (1973) Colour centre formation in corundum doped with divalent ions. *Kristall und Technik*, Vol. 8, No. 1-3, pp. 247–251, http://dx.doi.org/10.1002/crat.19730080125

Li H., Robertson J. (2014) Behaviour of hydrogen in wide band gap oxides. *Journal of Applied Physics*, Vol. 115, No. 20, p. 203708, http://dx.doi.org/10.1063/1.4878415

MacFarlane R.M. (1964) Optical and magnetic properties of trivalent vanadium complexes. *Journal of Chemical Physics*, Vol. 40, No. 2, pp. 373–377, http://dx.doi.org/10.1063/1.4755936

Maiman T.H., Hoskins R.H., D'Haenens I.J., Asawa C.K., Evtuhov V. (1961) Stimulated optical emission in fluorescent solids: Spectroscopy and stimulated emission in ruby. *Physical Review*, Vol. 123, No. 4, pp. 1151–1157, http://dx.doi.org/10.1103/PhysRev.123.1151

Matsunaga K., Nakamura A., Yamamoto T., Ikuhara Y. (2004) Theoretical study of defect structures in pure and titanium-doped alumina. *Solid State Ionics*, Vol. 172, No. 1-4, pp. 155–158, http://dx.doi.org/10.1016/j.ssi.2004.01.044

Mattson S.M., Rossman G.R. (1988) Fe^{2+}-Ti^{4+} charge transfer in stoichiometric Fe^{2+},Ti^{4+}-minerals. *Physics and Chemistry of Minerals*, Vol. 16, No. 1, pp. 78–82, http://dx.doi.org/10.1007/BF00201333

McClure D.S. (1962) Optical spectra of transition-metal ions in corundum. *Journal of Chemical Physics*, Vol. 36, No. 10, pp. 2757–2779, http://dx.doi.org/10.1063/1.1732364

Moon A.R., Phillips M.R. (1994) Defect clustering and color in Fe,Ti: α-Al_2O_3. *Journal of the American Ceramic Society*, Vol. 77, No. 2, pp. 356–357, http://dx.doi.org/10.1111/j.1151-2916.1994.tb07003.x

Nassau K. (1991) The seven types of yellow sapphire and the proposed Ponahlo test. *Zeitschrift der Deutschen Gemmologischen Gesellschaft*, Vol. 40, No. 4, pp. 247–251.

Norby T. (1989) Hydrogen defects in inorganic solids. In Ø. Johannesen and A.G. Andersen, Eds., *Defect Chemistry of Solids*. Elsevier Science Publishers B.V., Amsterdam, pp. 101–142, http://dx.doi.org/10.1016/B978-0-444-88534-0.50011-4

Pajot B., Clerjaud B. (2013) *Optical Absorption of Impurities and Defects in Semiconducting Crystals: Electronic Absorption of Deep Centres and Vibrational Spectra*. Springer-Verlag Berlin Heidelberg, 512 pp.

Powell R.C. (1966) *The Interaction of Chromium Ions in Ruby Crystals*. Physical Sciences Research Papers No. 299. Air Force Cambridge Research Labs, Hanscom, Massachusetts.

——— (1998) *Physics of Solid-State Laser Materials*. Springer-Verlag, New York, 423 pp.

Pryce M.H.L., Runciman W.A. (1958) The absorption spectrum of vanadium corundum. *Discussions of the Faraday Society*, Vol. 26, pp. 34–42, http://dx.doi.org/10.1039/df9582600034

Schmetzer K., Bosshart G., Hänni H.A. (1983) Naturally-coloured and treated yellow and orange-brown sapphires. *Journal of Gemmology*, Vol. 18, No. 7, pp. 607–622.

Shtepliuk I., Lashkarev G., Khyzhun O., Kowalski B., Reszka A., Khomyak V., Lazorenko V., Timofeeva I. (2011) Enhancement of the ultraviolet luminescence intensity from Cd-doped ZnO films caused by exciton binding. *Acta Physica Polonica A*, Vol. 120, No. 5, pp. 914–917, http://dx.doi.org/10.12693/APhysPolA.120.914

Stone-Sundberg J., Thomas T., Sun Z., Guan Y., Cole Z., Equall R., Emmett J.L. (2017) Accurate reporting of key trace elements in ruby and sapphire using matrix-matched standards. *G&G*, Vol. 53, No. 4, pp. 438–451, http://dx.doi.org/10.5741/GEMS.53.4.438

Tatian B. (1984) Fitting refractive-index data with the Sellmeier dispersion formula. *Applied Optics*, Vol. 23, No. 24, pp. 4477–4485, http://dx.doi.org/10.1364/AO.23.004477

Thomas T., Rossman G.R., Sandstrom M. (2014) Device and method of optically orienting biaxial crystals for sample preparation. *Review of Scientific Instruments*, Vol. 85, No. 9, p. 093105, http://dx.doi.org/10.1063/1.4894555

Tippins H.H. (1970) Charge-transfer spectra of transition-metal ions in corundum. *Physical Review B*, Vol. 1, No. 1, pp. 126–135, http://dx.doi.org/10.1103/PhysRevB.1.126

Townsend M.G. (1968) Visible charge transfer band in blue sapphire. *Solid State Communications*, Vol. 6, No. 2, pp. 81–83, http://dx.doi.org/10.1016/0038-1098(68)90005-7

Zaw K., Sutherland L., Yui T-F., Meffre S., Thu K. (2015) Vanadium-rich ruby and sapphire within Mogok Gemfield, Myanmar: Implications for gem color and genesis. *Mineralium Deposita*, Vol. 50, No. 1, pp. 25–39, http://dx.doi.org/10.1007/s00126-014-0545-0

Zorenko Y., Zorenko T., Voznyak T. (2011) Luminescence centers in $Y_3Al_5O_{12}$:La single crystals. *Journal of Physics: Conference Series*, Vol. 289, No. 1, p. 012028, http://dx.doi.org/10.1088/1742-6596/289/1/012028

The
Dr. Edward J. Gübelin
Most Valuable Article
AWARD

First Place

Geographic Origin Determination of Blue Sapphire

WINTER 2019
Aaron Palke, Sudarat Saeseaw, Nathan Renfro, Ziyin Sun, and Shane McClure

Aaron Palke is senior manager of research at GIA in Carlsbad, California. He holds a PhD in geology from Stanford University. **Sudarat Saeseaw** is senior manager of colored stone identification at GIA in Bangkok. Ms. Saeseaw received her master's degree in analytical chemistry from Mahidol University in Thailand. **Nathan Renfro** is manager of colored stone identification at GIA in Carlsbad. He earned a bachelor's degree in geology from Appalachian State University in North Carolina. **Ziyin Sun** is a research associate in the gem identification department at GIA in Carlsbad. He holds a bachelor's degree in chemistry and a master's degree in analytical chemistry from Nanjing University in China. **Shane McClure** is global director of colored stone services at GIA in Carlsbad and co-editor of *G&G*'s Lab Notes section. He is well known for his many articles and lectures on gem identification.

Aaron Palke   Sudarat Saeseaw   Nathan Renfro

Ziyin Sun   Shane McClure

Seconad Place (tie)

A Decade of Ruby from Mozambique: A Review

SUMMER 2019
Wim Vertriest and Sudarat Saeseaw

Wim Vertriest is supervisor of field gemology at GIA in Bangkok. Mr. Vertriest has visited gemstone mining areas worldwide and oversees the field gemology department and curates GIA's colored stone research collection in Bangkok. He obtained a master's degree in geology (geodynamics and geofluids) from KU Leuven in Belgium. **Sudarat Saeseaw** was profiled in the first-place entry.

Wim Vertriest

Second Place (tie)

Gemstones in the Era of the Taj Mahal and the Mughals

FALL 2019
Dona Mary Dirlam, Chris L. Rogers, and Robert Weldon

Dona Dirlam is librarian emerita at GIA's Richard T. Liddicoat Gemological Library and Information Center in Carlsbad, California, where she established and expanded the collection known as the world's leading resource center for gems, gemology, and jewelry. Ms. Dirlam holds a master's in geology and geo-

Dona Dirlam   Chris Rogers   Robert Weldon

physics from the University of Wisconsin, Madison. **Chris Rogers** is a research librarian at GIA's Richard T. Liddicoat Gemological Library and Information Center. She holds a bachelor's degree in English from San Diego State University and a master's in library and information science from San Jose State University. **Robert Weldon** is director of GIA's Richard T. Liddicoat Gemological Library and Information Center. He is well known for his gem photography and has contributed to scores of international publications and several gem-related books.

Many thanks to the members of G&G's Editorial Review Board for voting this year.

THE EVOLUTION OF CHINESE JADE CARVING CRAFTSMANSHIP

Mingying Wang and Guanghai Shi

Craftsmanship is a key element in Chinese jade carving art. In recent decades, the rapid development of tools has led to numerous changes in carving technology. Scholars are increasingly focusing on the carving craft in addition to ancient designs. Five periods have previously been defined according to the evolution of tools and craftsmanship, and the representative innovations of each period are summarized in this article. Nearly 2,500 contemporary works are analyzed statistically, showing that piercing and *Qiaose*, a technique to take artistic advantage of jade's naturally uneven color, are the most commonly used methods. Current mainstream techniques used in China's jade carving industry include manual carving, computer numerical control engraving, and 3D replicate engraving. With a rich heritage and ongoing innovation in jade craftsmanship, as well as increased automation, the cultural value and creative designs are both expected to reach new heights.

Jade carving is one of the oldest and most important art forms in China, a craft steeped in history and tradition that reflects Chinese philosophy and culture (Thomas and Lee, 1986). Carving, called *Zhuo* and *Zhuo mo* in Chinese, represents the arduous process of shaping and decorating an intractable material with abrasives to create the desired object (Hansford, 1950; Sax et al., 2004). During its more than 5,000-year history (table 1), Chinese jade carving has experienced five peaks—the late Neolithic Age (circa 3500–2070 BCE), the late Shang Dynasty (1600–1046 BCE), the Zhanguo Period (475–221 BCE), the Han Dynasty (206 BCE–220 CE), and the Qing Dynasty (1644–1911)—and was influenced by politics, economics, culture, and war (Kong, 2007). After Emperor Qianlong abdicated in 1795, the development of jade carving craftsmanship was relatively stagnant (Thomas and Lee, 1986). With the fall of the Qing Dynasty in 1911, the royal demand for jade carving faded. During that period, the folk workshops mainly focused on the carving of common jade wares such as jewelry and vessels. After 1949, state-owned jade carving factories were established one after another, with an increasing number of employees and the gradual popularization of electrically powered

tools. In 1978, China opened its economy to the outside. With the support of the government, influenced by jade merchants and carvers from Taiwan and Hong Kong and driven by an expanded domestic consumer market, China's modern jade carving industry has seen a period of vigorous development.

In Brief

- With the prevalence of power-driven systems, China's modern jade carving technology and industry have been vigorously developing for more than 40 years.
- For thousands of years, innovations in carving tools have continuously promoted the development of Chinese jade carving craftsmanship, in a direction toward increased diversity, complexity, and delicacy.
- Modern Chinese jade carving technology includes three mainstream methods: power-driven manual carving, computer numerical control engraving, and 3D replicate engraving.
- The value of jade cultural connotation and design creativity will improve with growing industrial automation.

There is a saying in China that "workers must first sharpen their implements when they want to do their best." Indeed, the emergence of each peak in jade carving across its history in China is inseparable from the innovation of tools (Xu, 2011). Currently, jade carving tools are undergoing great changes, influenced by advances in manufacturing. However, little is known in
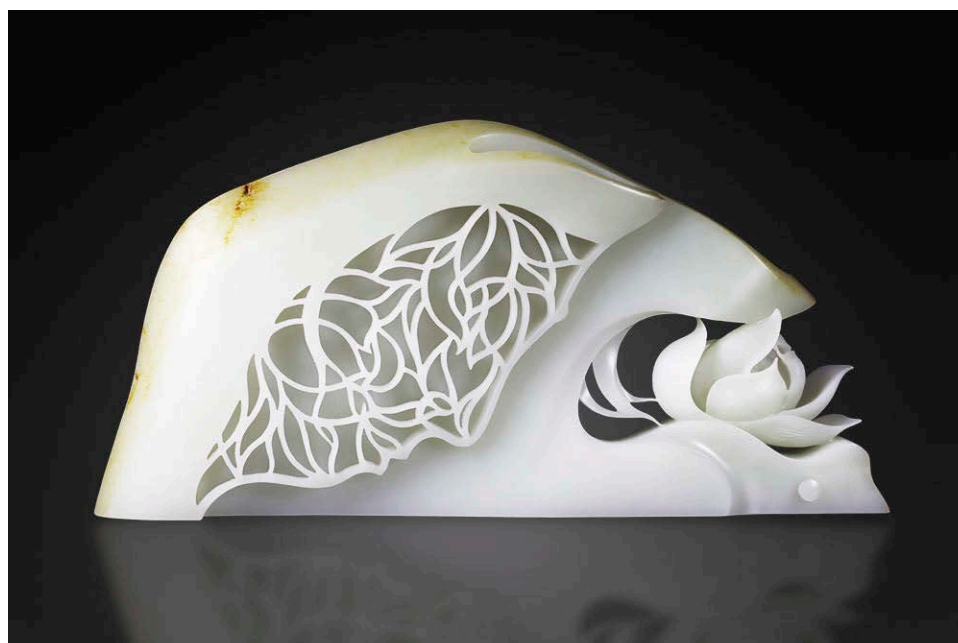
Figure 1. The white nephrite Buddhist carving by modern master Xi Yang is displayed in the British Museum. It presents an openwork papercut-style profile of Guanyin on the left and a three-dimensional carved lotus on the right, jointly manifesting the Buddhist culture with oriental characteristics (Michaelson et al., 2016). Photo © The British Museum (2017.3034.1).

the West today about the modern craft compared with ancient Chinese jade carving (Michaelson et al., 2016). Since the founding of the People's Republic of China in 1949, papers on jade carving have been published in the West, but the majority have focused on traditional carving methods and only a few on the modern methods that emerged leading up to the 1990s (Hansford, 1950; Tucker, 1982; Markbreiter, 1985; Thomas and Lee, 1986; Desautels, 1986). In 2017–2018, nephrite jade works by Xi Yang and four other contemporary masters were collected by the British Museum for permanent display (box A), indicating that modern Chinese jade wares have begun to attract interest in the West (figure 1).

The main research interests of jade wares are on their texture, shape, pattern, and craft (You, 2001). Previous studies on Chinese jade carving have focused on the exploration of shapes and patterns. In recent years, with the rapid development of jade carving tools and craft, research on craftsmanship has increasingly attracted the attention of scholars (Kong, 2007; Xu, 2011). The authors of the present article conducted field visits to carving and trading sites such as Beijing, Shanghai, Suzhou, Yangzhou, Urumqi, Sihui, and Zhenping, including requisite visits to carving workshops and technical schools, to gain a more complete understanding of the current state. This article analyzes the development of jade carving tools over five periods and the representative carving craft during these periods. Finally, the processing methods and procedures of Chinese jade carving in the modern context are introduced.

EVOLUTION OF JADE CARVING TOOLS

In the process of fashioning stone tools, human ancestors gradually mastered the method of distinguishing jade from other "non-jade" stones. The emergence of the rotary machine (circa 3500 BCE), in which jade was held against a grinding tool being rotated by the other hand or another person, indicated that jade carving had completely separated from general stone craft to become an independent category (Yang, 2004, 2006). The innovation of the rotary tool is the most important factor in the development of Chinese jade carving. As the key component of the jade carving craft, the tool displays different characteristics in different development stages. Yang (2006) divided Chinese rotary machines into five generations, and Xu (2011) divided the evolution of the jade carving craft into five periods. The present authors combined the results from these studies and offer the following five generations of jade carving rotary tools in Chinese history.

First Generation (circa 3500–circa 2070 BCE). The primitive rotary jade carving machine appeared in the Hongshan and Lingjiatan cultural sites of the Neolithic Age (Yang, 2006). These jade carving tools were made primarily from natural materials such as stone, wood, and bone. Yang (1989a,b) proposed two main features of the primitive rotary carving machine. The first is that it allowed the carver to assume a sitting position. The second is that it was manually rotated.

Period/Dynasty	Common English Name	Time Span
Neolithic Period	Neolithic Period	circa 10,000 years ago–2070 BCE
Xia Dynasty	Xia Dynasty	2070–1600 BCE
Shang Dynasty	Shang Dynasty	1600–1046 BCE
Xizhou Dynasty	Western Zhou Dynasty	1046–771 BCE
Chunqiu Period	Spring and Autumn Period	770–476 BCE
Zhanguo Period	Warring States Period	475–221 BCE
Qin Dynasty	Qin Dynasty	221–207 BCE
Xihan Dynasty	Western Han Dynasty	206 BCE–8 CE
Donghan Dynasty	Eastern Han Dynasty	25–220 CE
Sanguo Period	Three Kingdoms Period	220–265 CE
Xijin Dynasty	Western Jin Dynasty	265–316 CE
Dongjin Dynasty	Eastern Jin Dynasty	317–420 CE
Nan-bei Dynasty	Period of the Northern and Southern Dynasties	420–589 CE
Sui Dynasty	Sui Dynasty	581–618 CE
Tang Dynasty	Tang Dynasty	618–907 CE
Wu-dai-shi-guo Period	Period of the Five Dynasties and Ten Kingdoms	907–960 CE
Beisong Dynasty and Liao Dynasty	Northern Song Dynasty and Liao Dynasty	960–1127
Nansong Dynasty and Jin Dynasty	Southern Song Dynasty and Jin Dynasty	1127–1279
Yuan Dynasty	Yuan Dynasty	1271–1368
Ming Dynasty	Ming Dynasty	1368–1644
Qing Dynasty	Qing Dynasty	1644–1911
Republic of China	Republic of China	1912–1949
People's Republic of China	People's Republic of China	1949–present

From Yi (2001)

Second Generation (circa 2070 BCE–circa sixth century BCE). The bronze rotary machine emerged and thrived from the Xia and Shang Dynasties to the early to mid-Chunqiu Period (Xu, 2014) as life in this period gradually centered on bronze technology. It is speculated that operators were kneeling and manually drove the machine to faster speeds than achievable before, based on the kneeling posture depicted in unearthed human stone carvings from this period and in the tomb of Fuhao (Yang, 2006).

Third Generation (circa sixth century BCE–circa 581 CE). The iron rotary machine appeared from the late Chunqiu Period until the Nan-bei Dynasty. Carvers still knelt on the ground while operating the machine (Xu, 2014). As smelting technology improved, iron tools were increasingly used and the jade carving machine evolved accordingly. It was still manually driven but provided increased efficiency because iron tools were sharper and more wear-resistant (Xu, 2014).

Fourth Generation (circa 581–1960). The table-type iron rotary machine was used from the Sui and Tang Dynasties through the Ming and Qing Dynasties and into the 1950s (Yang, 2006; Xu, 2014). In the Sui and Tang Dynasties, interior furniture changed people's habit of sitting on the ground, and they instead sat on stools or chairs (Yang, 2006). As a result, the rotary machine in this period was of the table-type or tall-legged table-type and driven by a foot treadle that further increased its working efficiency (figure 2).

Fifth Generation (1960–present). The modern rotary machine has been used in the contemporary jade carving process since the 1960s (Yang, 2006; Xu, 2014). It was initially introduced from Europe, but with the emergence of its manufacturing industry, China began to independently research, develop, and produce these machines (Read, 1981; Markbreiter, 1985). The body of the jade rotary machine has changed from wood to iron, the grinding heads are

Figure 2. A restoration of a fourth-generation table-type iron rotary machine. The artisan sits at the table and carves the jade using the rotary tool and abrasive sands, driven by the foot treadle. Photo by Mingying Wang, from Tianjin Museum.

now carborundum-coated, and foot power has been replaced by motor power (Deng, 2011; Xu, 2014). At present, there are two main types of equipment for manual carving: grinding machines and flexible-shaft machines. The grinding machine is a large apparatus, and the seated carver holds the jade while using tools of various shapes. The flexible-shaft engraving ma-

chine is small, portable, and has a handheld electric-powered rotary tool with a flexible drive (Michaelson et al., 2016), which makes it convenient to change different grinding heads (figure 3). The emergence of motor power and the improvement of tools have not only increased carving efficiency but also benefited jade carvers. The new tools are suitable for detailed

Figure A-1. Hongwei Ma's nephrite works "Wine Cup (Jue)" (left) and "Bronze Ram Zun" (right). Photos © The British Museum (2017.3032.1 and 2018.3019.1).

In 2017–2018, eight nephrite works created by Chinese modern masters Hongwei Ma, Guang Yang, Xi Yang, Ting Yu, and Yiwei Zhai were selected by the British Museum for its permanent collection. These works are on permanent display to the public as jade carvings by living Chinese artists of the twenty-first century.

Figure A-2. Guang Yang's "Incense Pot" in nephrite. Photo © The British Museum (2017.3033.1).

Figure A-3. Xi Yang's nephrite work "Autumn in Suzhou." Photo © The British Museum (2017.3035.1). Figure 1 shows the artist's other piece on exhibit at the British Museum.

Figure A-4. Ting Yu's nephrite "Eggshell Teapot." Photo © The British Museum (2017.3036.1).

Figure A-5. Yiwei Zhai's nephrite works "Beside is a bosom friend, thou. Everywhere is paradise, enow" (left and middle) and "The Rhyme of Spring" (right). Photos © The British Museum (2017.3037.1 and 2018.3020.1).
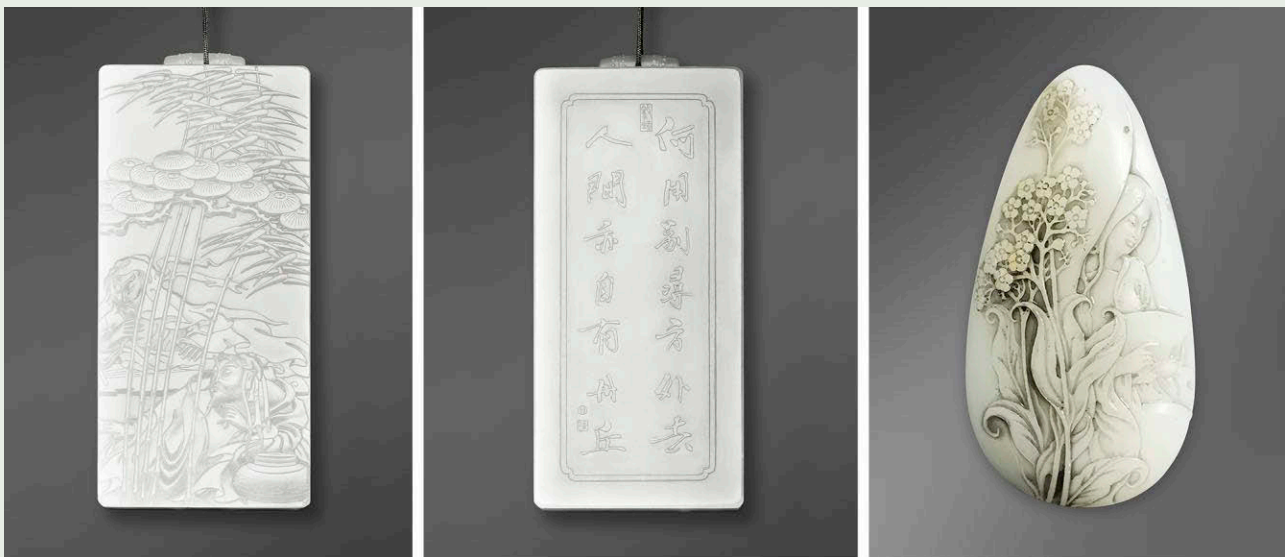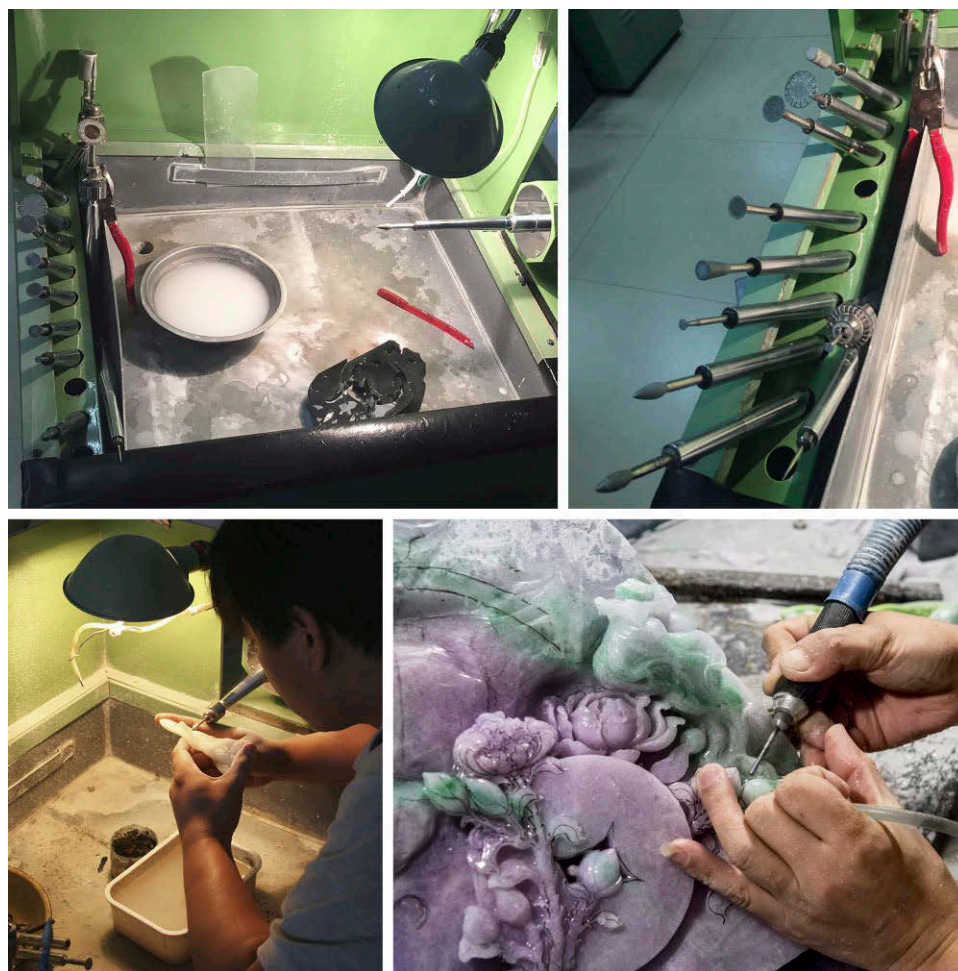
Figure 3. Top left: The driveshaft is fixed in a horizontal direction on the jade grinding machine; at the end of the shaft is the turnbuckle or bayonet where the grinding head or the long horizontal shaft can be fixed. Various grinding heads (top right) can be exchanged according to the carving needs. Photos courtesy of Yongtao Chen. Bottom left: The object is moved by hand to contact the stationary rotating tool. Photo by Mingying Wang. Bottom right: The carver works the jade piece using the hand-held burr of the flexible-shaft machine. Both the jade and the tool are movable. Photo by Eric Welch; courtesy of Mazu Jade Co.

ornaments and small jade wares as well as larger wares. Furthermore, motor-driven equipment has driven the introduction and refinement of tools for specific uses: for example, various types of cutters, ultrasonic drilling equipment, mechanized grinding beads, and vibratory polishers (Xu, 2014).

Since the 1990s, automated computer numerical control (CNC) processors have gradually been applied to jade carving. Together with design software and three-dimensional data processing, CNC engraving and milling machines can be used not only to manufacture original jade carvings but also to make 1:1 replicas of existing wares or historical relics. Three types of automated CNC engraving and milling machines are mainly used for jade carving: three-shaft, four-shaft, and five-shaft. The number of shafts represents the degree of processing freedom and in turn the quality of the resulting curved surface details. The three-shaft CNC machine is suitable for plane-relief engraving, while the four- and five-shaft CNC machines can execute three-dimensional carv-

ings. Given cost and efficiency concerns, three- and four-shaft CNC machines are more common in the Chinese market. CNC technology can be applied to a wide range of processing types and are mainly used for engraving medium- and low-end jade and stone materials of various sizes. Its emergence and popularity means that carvings can be produced in bulk, further improving efficiency while maintaining the high intricacy of jade craftsmanship (figure 4).

In addition to rotary tools, abrasive sands and powders are an important element in jade carving. Abrasive sands used in the primitive carving period were ordinary sands that contained a large amount of quartz particles, which are harder than jade. With the development of jade carving craftsmanship, abrasive sands have gradually been refined (Hansford, 1950; Sax et al., 2004; Xu, 2011). Today they include natural abrasives (such as corundum, quartz, and diamond) and synthetic abrasives (such as carborundum and synthetic diamond). In general, artificial abrasives are superior to natural ones (except for nat-

Figure 4. With a CNC engraving and milling machine, a jade carving that takes 20 days by manual carving can be made in three to four days. Photo by Mingying Wang.

ural diamond) in quality, hardness, and performance. Therefore, modern jade carving mainly utilizes artificial abrasives, which are often used for coating the grinding heads (Zhao and Zhang, 2000).

Throughout the evolution of Chinese jade carving, every tool innovation has experienced a long development cycle. The transition from the prehistoric stone tool to the bronze tool to the iron tool to the modern machine was accomplished over thousands of years. However, due to regional variations and economic constraints, new jade carving tools were not suddenly applied in a given dynasty but were gradually adopted over a longer period (Xu, 2011). For example, during the Xia and Shang Dynasties, bronze tools did not completely replace the primitive stone tools, and the two were used together for a long time (Lu et al., 2014). Nephrite, the mainstream material of Chinese jade culture, has a high toughness, which makes jade carving more difficult but promotes the innovation of tools. In early jade carving, several weeks were needed just to saw through a boulder (Hansford, 1950), making the development of tools and technology more important.

EVOLUTION OF JADE CARVING CRAFTSMANSHIP

If the tool is the fundamental force driving the evolution of jade carving, then craft is also an important factor. The two forces are inseparable. Every innovation in tools allows the carving craft to take a leap

forward (Xu, 2011). Therefore, we will now analyze and summarize representative crafts used in different tool development periods (table 2).

Table 2 shows that over 5,000 years of Chinese jade culture, the development of carving tools has featured two trends: tool speed becoming increasingly faster, and grinding powder becoming increasingly harder. The evolution of tools improved processing conditions for carvers. As a result, Chinese jade carving moved toward greater diversity, complexity, and delicacy. Consider the shapes, for example. During the Xia, Shang, and Xizhou Dynasties, jade wares were mainly two-dimensional tablet shapes. With advances in tools and craftsmanship, the forms gradually became three-dimensional. In the Ming and Qing Dynasties, most jade wares displayed rounded shapes.

Although each of the five stages in table 2 corresponds to a certain historical period, any craft or technology progresses gradually through exploration and creation. The accumulation of experience takes a long time. The refinement of a craft is first tested on a small scale and then gradually promoted and popularized. Therefore, a change in dynasty does not necessarily represent the immediate progress of a craft.

Primitive Jade Carving (circa 3500–circa 2070 BCE). In the Neolithic Age, stone tools were fashioned by cutting, sanding, and drilling. These three techniques were inherited by the primitive jade carvers and fur-

TABLE 2. Periods of Chinese jade carving tools and corresponding craftsmanship.

Period	Representative Jade Carving Tools	Representative Jade Carving Craftsmanship
Late Neolithic Age (circa 3500 BCE–circa 2070 BCE)	**Primitive jade carving period** Manually driven Grinding tools made of nonmetals, such as seashells, stones, bones, and wood	Jade collecting, cutting, grinding, carving, drilling, piercing, inlay, eggshell carving, and polishing—the basic procedure and various techniques used by later generations—initially emerge in this period
Xia, Shang Dynasties to Early to Mid-Chunqiu Period (circa 2070 BCE–circa sixth century BCE)	**Bronze rotary machine period** Manually driven Bronze grinding tools	Inlay, *Qiaose* (coloring design art), chain carving, and slope carving (oblique grinding for jade patterns) Piercing becomes sophisticated and hollowing reaches a high level
Late Chunqiu Period to Nan-bei Dynasty (circa sixth century BCE–circa 581 CE）	**Iron rotary machine period** Manually driven Iron grinding tools	Techniques related to burial jade—*Han Badao* (concise carving) Metal-related techniques—inlay and stitching "Hair-like carving," flexible connecting, and Bi carving (a disc with a central round hole) Piercing is widely applied
Sui and Tang Dynasties to the 1950s (circa 581–1960)	**Table-type iron rotary machine period** Driven by foot treadle Iron grinding tools	Inlay with gems and gold, eggshell carving, antiquing, 3D picturesque carving, large jade carvings, calligraphy engraving, and jadeite carving Qiaose is commonly applied, and importance is attached to polishing
Modern Era (1960–present)	**Modern jade machine period** Motor-driven power Iron or steel grinding tools with carborundum coating CNC machines Other automated tools include auto-cutting, auto-polishing, laser engraving, and ultrasonic drilling	The same crafts are used in the modern era, but with automation and motor-driven tools Qiaose, piercing, calligraphy engraving, chain carving, eggshell carving, miniature carving, and gem or gold inlay Plane-relief engraving, 3D engraving, and 3D replicate engraving

Modified from Xu (2011, 2012), You (2001), Yang (2006), Kong (2007), Deng (2011), and Lu et al. (2014)

ther developed (Yang, 2006). Based on evidence from unearthed relics, it can be speculated that jade carving procedures in the Neolithic period mainly comprised collecting, cutting, grinding, carving, drilling, and polishing either by hand or by rotary machine. These same basic procedures were inherited by later generations. Such representative techniques as piercing, inlay, and eggshell carving (to produce thin "skins") also made their first appearance (You, 2001; Kong, 2007; Xu, 2011). However, the quality of jade carving craftsmanship varied from place to place due to different rates of cultural development (You, 2001).

Bronze Rotary Machines (circa 2070–circa sixth century BCE). Although they emerged in the Neolithic period, inlays in the Xia, Shang, and Xizhou Dynasties outnumber those before the Xia Dynasty and dis-

play outstanding intricacy. These inlays were mainly combinations of bronze and turquoise, jade and turquoise, or bronze and jade. Jade vessels emerged in this period, with a corresponding rise in skilled hollowing (Xu, 2011).

The jade carving craft in the Shang Dynasty, which included cutting, grinding, carving, drilling, polishing, design, and shape creation, reached a high level (Technical Research Group of Beijing Jade Factory, 1976). During this dynasty, the Qiaose technique to artistically take advantage of jade's naturally uneven or different color first appeared. In the process of Qiaose craft, the shape and placement of the colors on the rough jade should be taken into account so as to utilize the colors skillfully. The jade turtle in figure 5, unearthed at Xiaotun in Henan Province, is a successful example of Qiaose (Yang et

Figure 5. This meticulously designed jade turtle unearthed in 1975 in the Yin Ruins in Xiaotun is an example of Qiaose craft from the late Shang Dynasty (1600–1046 BCE). The grayish white part of the jade is carved into the head, neck, and abdomen, and the dark part forms a vivid turtle shell, displaying the artist's skillful use of color. As a symbol of longevity in China, the turtle was often used during ancient burials. Photo from Yang et al. (2005, p. 158).

al., 2005). Chain carving, a very difficult craft carved from a single piece of stone, also emerged in the Shang Dynasty, laying the foundation for its development in later generations (Xu, 2011).

Iron Rotary Machines (circa sixth century BCE–circa 581 CE). Burial jade thrived in the Chunqiu Period and culminated in a set of special carving systems formed in the Han Dynasty. Burial jade shows no significant difference from daily jade in terms of the carving procedure but it is more concise and less exquisite (You, 2001). Take the *Han Badao* (concise carving) craft in the Han Dynasty as an example. Typical of burial jade, the lines from Han Badao are bold, vigorous, and concise, seemingly carved by swords (figure 6).

What epitomizes the craftsmanship of the Zhanguo Period is the wide application of the openwork technique (Lu and Ouyang, 2014). In this period, piercing was mainly applied to flat jade wares, but a small number of three-dimensional openwork

also appeared. The craft even exerted influence during the Han and Wei Dynasties (circa 206 BCE–265 CE). Techniques integrating jade and metal, such as inlay and stitching, also surpassed those in the Shang and Xizhou Dynasties. Here, inlay refers to embedding metals such as copper, silver, iron and gold into the jade, while stitching means using metal threads to connect jade pieces together. These two crafts reached an advanced level during the Zhanguo Period, as evidenced by the number and quality of artworks applying them (Xu, 2011). For example, the jade clothes sewn with golden or silver thread often buried in the tombs of nobility in the Han Dynasty are elaborate and complex in craftsmanship. They are typical of stitching craft at this time and exemplify burial jade culture in the Han Dynasty (figure 7).

Figure 6. This jade cicada is a typical example of the Han Badao (concise carving) craft highlighted in the Han Dynasty (206 BCE–220 CE). This technique unfolds the full vitality of the jade cicada through just a few concise lines. As the cicada implied rebirth in ancient China, cicada carvings were often found as burial items in Han tombs, placed on the tongue of the body. Photo by Mingying Wang, from Tianjin Museum.

Figure 7. Sheng Liu's jade burial suit (Xihan Dynasty, 206 BCE–8 CE) was unearthed in Mancheng, China, in 1968. Approximately 1.88 m long, the suit is composed of 2,498 jade tablets sewn together with approximately 1,100 grams of gold wire. It is the earliest and best-preserved jade burial suit in the history of Chinese archaeological excavation (Yang et al., 2005). Photos by Lin Xu (top) and Tian Wang (bottom), from Hebei Museum.

Flexible connecting, which has the same engraving principle as chain carving, was found in tombs of the Shang Dynasty but thrived and matured in the Zhanguo Period, when many quality artworks appeared (Xu, 2011). Among them, the sixteen-segmented jade ornament excavated from the tomb of Marquis Yi of State Zeng is the best-known application of the flexible connecting craft in this period (figure 8).

Table-Type Iron Rotary Machines (circa 581–1960). Gold and jade were already being combined prior to the Qin Dynasty (221–206 BCE), and the inlay of jade with gems and gold gained popularity during the Sui and Tang Dynasties. In the late Ming Dynasty, this craft was widely applied and became a striking feature. In the Qing Dynasty, influenced by Islamic jades that originated in central, western, and south-

Figure 8. This dragon-phoenix pendant with 16 grayish white components (48.0 × 8.3 × 0.5 cm), which was carved from a single piece of jade, is from the early Zhanguo Period (475–221 BCE). The movable and foldable components are carved into dragon, phoenix, or Bi-type disc openwork designs. The ornament embodies not only the flexible connecting technique but also the mature piercing technique (Gu, 2005). Top photo from Gu (2005, p. 93). Bottom photos by Yuetong Li, from Hubei Provincial Museum.
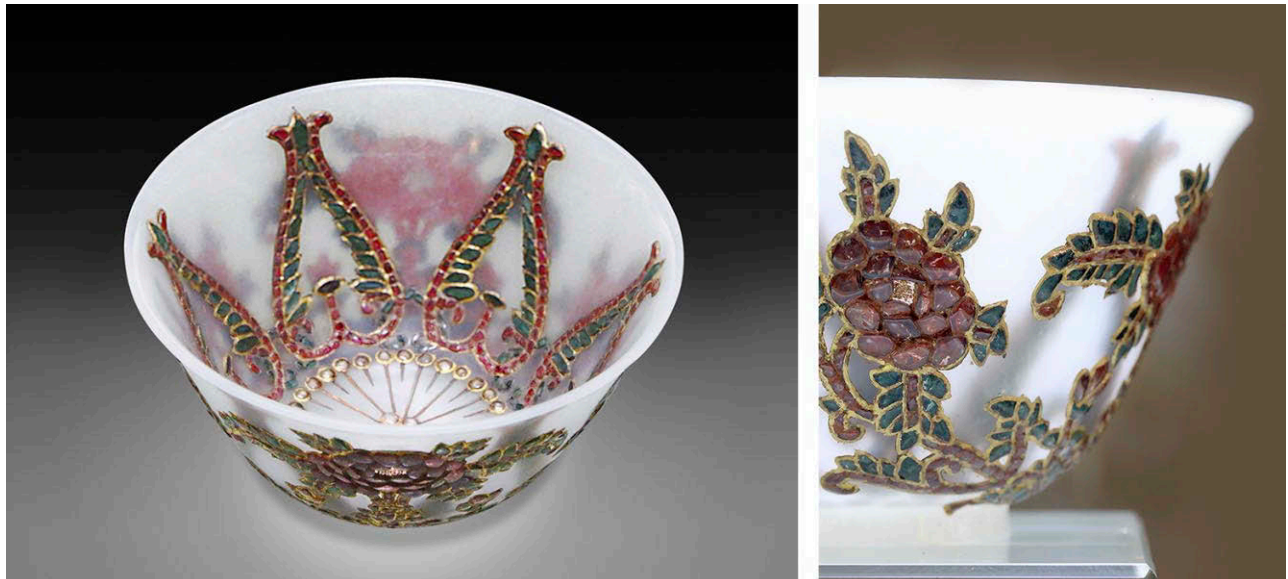
Figure 9. This white nephrite bowl with inlaid gems and gold tracery (Qing Dynasty, 1644–1911) is engraved with a lotus pattern on the outside and six sets of pomegranate patterns inside. It shows both the eggshell carving and inlay techniques and is a typical Islamic jade from China's western regions (Gu, 2010b). Photos by Rui Zhang (left) and Maiying Dong (right), from Shanxi Museum.

ern Asia in the late fourteenth century (figure 9), inlay often depicts various plant patterns, which gave off a sense of exotic charm (Deng, 2007; Xu, 2011).

During the Song, Liao, Jin, and Yuan Dynasties (circa 960–1368), influenced by the mature arts of painting and sculpture, jade carvings became three-dimensional. Themes of human figures, flowers, an-

imals, and landscapes were often accompanied by the distinctive openwork carving of the time. The piercing technique surged, and flat carvings were gradually replaced by three-dimensional picturesque jade wares (figure 10). In the Ming Dynasty, the intellectual "literati paintings" of southern Chinese culture, which are distinct from folk and royal paint-
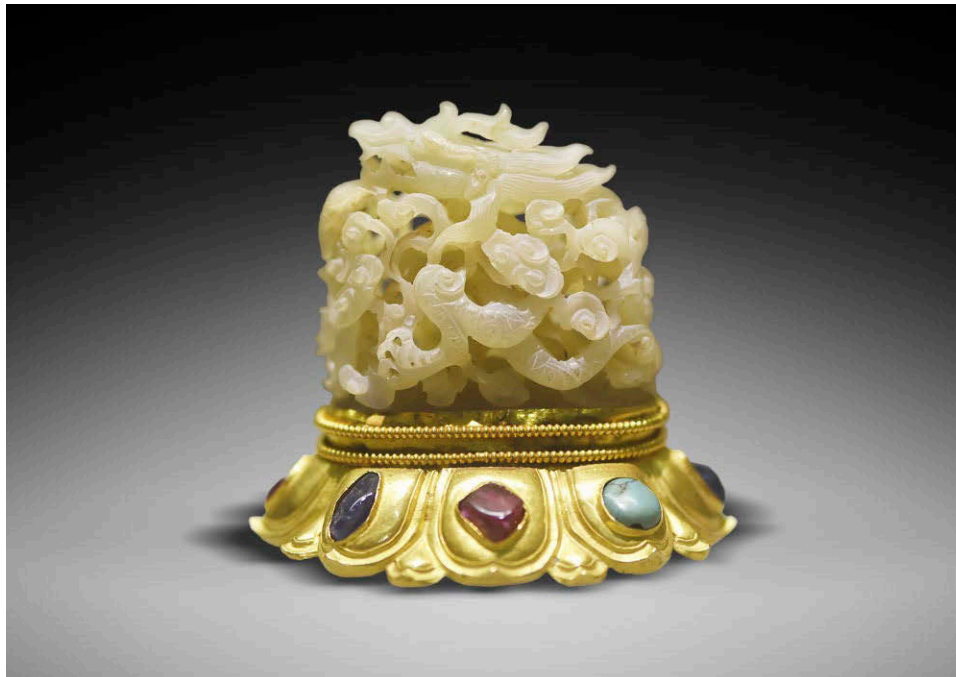
Figure 10. This gem-inlaid gold base in the shape of a lotus is topped with a carved jade dragon and cloud (Ming Dynasty, 1368–1644). The white nephrite adopts the multi-layered three-dimensional piercing technique with exquisite details. Photo by Yuetong Li, Hubei Provincial Museum.

Figure 11. The nephrite **Shan Zi** *sculpture "Emperor Yu Leading People in Subduing Floods" (224 × 96 cm, weighing at least 5,000 kg) was carved in Yangzhou from 1781 to 1787 CE. In the 53rd year of the Qianlong reign (1788 CE), the court jade craftsmen engraved the imperial poem on its back (Zhu, 2007). Photo from Zhu (2007, p. 71).*

ings, highlighted romantic charms and reflected the literati's personal feelings. This led to the incorporation of landscapes and texts in the decorative patterns of jade wares (Xu, 2011). In the Qing Dynasty, the use of royal court painters in the design of jade carvings in combination with fine craftsmanship created a peak of artistic integration (Yang, 1982; Xu, 2011).

During this period, the improvement and combination of tools and craft promoted the emergence of large jade carvings (Kong, 2007). For example, the massive bowl "Dragons Amid Waves" from the Yuan Dynasty was the first large jade carving that we know of. In the Qing Dynasty, jade carvers created several large works weighing thousands of kilograms, such as the complex three-dimensional landscape (called *Shan Zi* in Chinese) "Emperor Yu Leading People in Subduing Floods" (figure 11) and "Nine Elders Meeting During the Huichang Period" (Xu, 2013). These large carvings are mostly themed with landscapes, human figures, and animals, often accompanied by skilled calligraphy engraving on the back or sides. To create these pieces, several jade carvers had to work at the same time in an organized fashion. Under the processing conditions of the time, such a large work would take several years to complete. Thus, the production of large jade carvings marks the peak of the craft in ancient China (Xu, 2011).

Many other techniques also emerged during this period, such as the full development of Qiaose and eggshell carving, and the emergence of jadeite carving in the Qing Dynasty (You, 2001; Kong, 2007; Xu, 2011).

Modern Machines (1960–present). After the Qing Dynasty, the traditional foot treadle was used until the early days of the People's Republic (Xu, 2014). In the late 1950s, with the policy reform of the national planned economy, government-owned jade carving factories sprang up, led by the manufacturing centers of Beijing, Shanghai, Yangzhou, and Suzhou (Ma, 2014). Jade carvings were produced under industrial management using assembly lines (Ji, 1984). It was at this time that motor-driven carving machinery began to be employed.

With the popularization of power-driven systems in the 1960s and the continuous refinement of the tools (Xu, 2014), the modern carving industry ushered in a new era following the reform and opening up of trade in 1978. Modern tools and methods have

Figure 12. This modern work (9.3 × 4.2 × 2.8 cm), which retains the beautiful natural color of the jade crust, depicts ancient tree branches and a monk sitting in meditation underneath, showing a Zen sensibility. The ingenious application of traditional Chinese painting techniques to the grain carving of the branches demonstrates a natural artistic style (Ao et al., 2014). Photo courtesy of Gems and Jewelry Trade Association of China (GAC).

changed jade carving, and pieces that once took years can now be finished in months or even weeks (Tucker, 1982).

Modern jade carving inherits the characteristics of craftsmanship from past dynasties (Xu, 2014) and is further developed on the basis of various ancient techniques. With the emergence of power-driven tools, jade carving has become more elaborate, with smoother lines. The common techniques of the modern craft include Qiaose, eggshell carving, piercing, chain carving, calligraphy engraving, gem embedding, gold and silver inlay, miniature carving, and others. Artisans will often make a final decision on which techniques to use based on the color, shape, and toughness of the rough and the theme of their creation. Among these techniques, Qiaose (figure 12) and piercing (figure 13) are widely used in jade carv-

Figure 13. Because of its toughness and fine texture, nephrite is often subjected to piercing. The modern nephrite work "Holy Lingshan, Journey to the West" (38 × 26 × 8 cm) displays the scene of Xuanzang and his three disciples passing through the Lingshan holy land (Ao et al., 2009). Photo courtesy of the Gems and Jewelry Trade Association of China (GAC).

Figure 14. The gold inlay used on this dark gray nephrite vessel is elaborate and exquisite. Accompanied by traditional auspicious animal patterns, it makes the work vivid and graceful, paying homage to an antique style. Photo courtesy of Jingui Ma Jade Carving Studio.

ing and showcase the carvers' creative talents. Many of these techniques are highly specialized, and as a result jade carvers often devote their whole life to one technique. Jingui Ma, for example, devoted himself to the craft of inlay with gems and gold in the way of traditional vessels and thus formed his distinctive style (figure 14).

To illustrate modern jade carving, the authors statistically analyzed the 2,464 finalist works from 2012 to 2017 for the Tiangong Awards (Wang and Shi,

2020), China's most prestigious competition. As shown in figure 15, Qiaose and piercing are the two most common, particularly the former, followed by calligraphy and chain carving. Other crafts are more specialized and mastered by only a few. Chain carving (figure 16) and eggshell carving (figure 17) are still applied mainly to vessels; calligraphy engraving rarely appears alone and is used to provide inscriptions for the jade carvings (figure 18). By and large, two or three techniques are frequently used in combination. For instance, gem embedding is usually integrated with gold and silver inlay and eggshell carving to heighten the exotic appeal (figure 19). Techniques such as 3D and relief carving are funda-

Figure 15. Among modern jade carving techniques in China, Qiaose is by far the most common. In this chart, "Others" refers to works that contain only basic techniques, such as three-dimensional engraving or relief carving. Yearly data from Ao et al. (2012–2017).

Techniques Used in Tiangong Prize–Winning Artworks, 2012–2017

- 0.6%
- 0.9%
- 1.0%
- 1.4%
- 18.0%
- 3.0%
- 4.4%
- 24.6%
- 46.1%

- ■ Qiaose
- ■ Piercing
- ■ Calligraphy carving
- ■ Chain carving
- ■ Eggshell carving
- ■ Miniature carving
- ■ Gemstone embedding
- ■ Gold and silver inlaying
- ■ Others
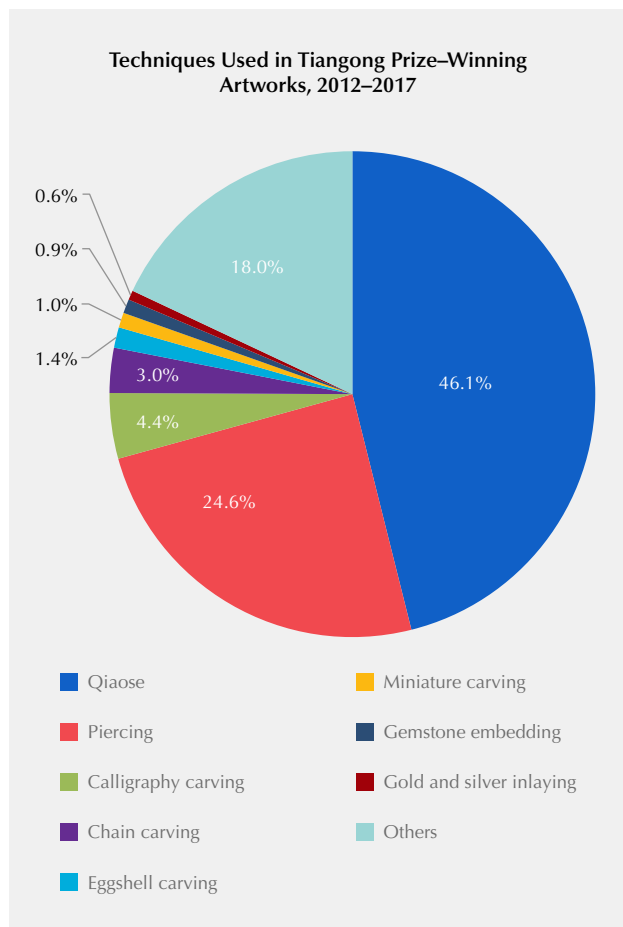
Figure 16. A modern jade bottle with chains (16 × 5 cm) showing the chain carving and piercing techniques. The shape of the work is neat, delicate, and elegant, manifesting the carver's high level of craftsmanship and ingenuity. Photo courtesy of GAC.

mental and thus used in almost all pieces, which is why they are not mentioned separately in this article (Ao et al., 2012–2017).

Although inheriting the ancient craftsmanship, modern jade carving attaches more importance to personal style and has made breakthroughs in ex-

Figure 17. This eggshell-thin nephrite vase with dark green color by Ting Yu, measuring approximately 34.6 × 11.0 cm, is uniform and exquisite. Its wall is even, thin (around 0.1 cm), and transparent, and its body is decorated with fine interlocking lotus branches that lend a dignified appearance (Ao et al., 2015). Photos courtesy of GAC.

pressing it with modern features. For instance, the traditional eggshell carving craft is mostly used in vessels. But master carver Xi Jiang broke tradition and carved nephrite with dark green color into wrinkled paper (Wang and Shi, 2020), which vividly shows the thinness and transparency of the work and

Figure 18. Wei Hu's modern nephrite work "Profiling the Red Cliff" (7.5 × 8.0 × 1.0 cm) adopts calligraphy and miniature carving to present Shi Su's prose and resorts to line-drawing carving to display the landscape of the Red Cliff, clearly demonstrating the artist's mastery (Ao et al., 2016). Photo courtesy of GAC.

Figure 19. This jade pot is light, thin, and embedded with gold wire, ruby, and sapphire in an exquisite Islamic style. It combines white nephrite with embedded gems, gold inlay, and eggshell carving techniques, fully reflecting the superb craftsmanship. Photo courtesy of Jingui Ma Jade Carving Studio.

Figure 20. "To Mountain" (19.6 × 11.0 × 5.2 cm) takes full advantage of the high toughness of nephrite and uses eggshell carving to show the thin (0.85–2.53 cm) and transparent feel of creased paper. Its theme, utilizing modern art methods, is "diligence as the path to the mountain of knowledge" (Ao et al., 2013). Photo courtesy of Xi Jiang Jade Carving Studio.

breaks new ground for the eggshell carving technique (figure 20). Master Desheng Wu, who excels at figure carving, incorporates the concept of Western sculpture. He pays great attention to the innovation and exploration of artistic style and boldly uses exaggerated ways to endow traditional jade carving craftsmanship with modern beauty (figure 21).

JADE CARVING PROCESS ILLUSTRATED BY MODERN WORKS

As mentioned above, ancient jade carving includes five steps: material selection, examination, design, carving with abrasives, and polishing (Xu, 2014). Depending on the tools and techniques, modern jade carving can be divided into three mainstream methods, each with a different procedure.

Power-Driven Manual Carving. This method inherited from ancient carving still enjoys a dominant role in modern China (figure 22). The procedure has remained essentially the same (Deng, 2011; Michaelson et al., 2016). Material selection and examination are targeted to maximize beauty. Design seeks to integrate the shape and patterns according to the features of the jade material (such as color and texture). Carving, usually the most time-consuming step in the process, is where design ideas turn into artwork through the use of tools. Polishing refers to the fine grinding of a jade's surfaces to make them smooth and bright, with an aesthetic appeal. It is interesting to note that artists sometimes use different finishes (degrees of polish or lack of polish) to create stunning designs.

Figure 21. "Snake Girl," a representative work from Master Desheng Wu's "Naked Woman" series, combines the smooth and warm luster of white nephrite jade with a modern stylized design applying openwork and Qiaose crafts. Photo courtesy of Desheng Wu Jade Carving Studio.

Figure 22. These four photos of a bodhisattva *illustrate the modern manual carving process, which includes four steps (left to right): material selection and examination, design, carving, and polishing. Photos by Xiaodong Wang.*

Computer Numerical Control (CNC) Engraving. This method is composed of two parts: model design and processing by machine. The model is designed using computer software. The designed model is first processed and programmed to determine the machining coordinate system and model size. The corresponding machining tools are then selected, and the program is written according to the machining requirements. In China, a CNC engraving and milling machine is frequently used in jade carving.

Finally, the program is imported into the CNC machine to control its operation (figure 23).

The CNC machine can achieve plane carving (figure 24) and 3D carving, but complex three-dimensional shapes and patterns can only be achieved through a combination of CNC machine and manual carving. Moreover, the CNC machine is rather limited with respect to the special techniques listed above: Only simple piercing can be achieved. The eggshell carving process has very specific require-

Figure 23. A three-shaft CNC machine engraving tabular nephrite. The machining process is monitored by the computer program. Because the cutting speed is extremely high, the machine needs fluid to keep cool. Photo by Mingying Wang.

Figure 24. Exquisite details of this dark nephrite ink slab (used to grind ink for Chinese calligraphy) were processed by a three-shaft CNC machine. Photos by Mingying Wang.

ments for jade materials, and it is difficult to use with materials with poor toughness that are prone to splitting. Qiaose, chain carving, and inlay with gold or gems rely on manual carving and cannot be achieved with the CNC machine.

3D Scanning and Auto Carving. The first step of this method is to scan the object through the 3D scanning device, which results in a 3D model profile. The 3D model profile is then reconstructed using reverse design software to generate a new model. The coordinates of the 3D model are determined with the CNC design software, and the tool parameters are compiled into a final machining program. Under the guidance of the final program, the CNC machine tool conducts the 3D carving. This method is mostly used in the replication of ancient jade relics (figure 25).

THE NATURE OF CHINESE JADE CRAFT'S EVOLUTION

You (2001) proposed that the fundamental method of studying ancient jade is to analyze it in relation to its historical and cultural background. This method applies to the study of not only ancient jade but also the modern carving craft and culture. After all, modern jade carving is integral to the history of jade. What modern power-driven implements and automated CNC engraving and milling machines are to jade carving today is no less than what iron tools are

to jade carving history. Against the background of power and tool transformation, the reform and open-

Figure 25. This piece of Manas gray-green nephrite is a 1:1 replica of the imperial jade seal with calligraphy engraving in Qianlong's reign (1736–1795). It was processed by 3D scanning and auto carving. Photo by Mingying Wang.

ing up of China, rapid economic development, and mass consumption, contemporary jade art demonstrates more diverse themes, more open art forms, more meticulous craftsmanship (figure 26), and a wider audience (Wang and Shi, 2020).

The progress of any craft or technology is a process of gradual exploration and long-term accumulation of experience (Xu, 2014). Analysis of Chinese jade carving proves a basic law—the craft learns from the past and sets a new course for the future with heritage and innovation. In general, innovation outweighs heritage. Innovation refers to multifaceted improvement and transformation based on heritage (You, 2001). Modern jade carving inherits and improves upon ancient techniques, but more importantly creates innovations in power-driven and machine engraving tools, contributing to an increase in efficiency and further development of the art. Thus, modern jade art is the best illustration of heritage and innovation working in harmony.

In Chinese jade carving, the tool plays a fundamental role and is the root of all craftsmanship trans-

formation. Influenced by the evolution of carving tools, Chinese jade carving craftsmanship has undergone long-term transformation and still continues to develop. It has distinctive characteristics—the diversity of techniques, the gradual nature of innovation, and the adoption of foreign culture and craft (You, 2001; Kong, 2007). Thus the evolution of carving craftsmanship not only helps to clarify the development of China's jade culture but also provides meaningful enlightenment for the growth of the modern jade carving industry.

THE FUTURE

A look at the evolution of Chinese jade carving tells us that every step forward in tools and production technology is immediately reflected in craftsmanship. In the contemporary era, the development of artificial intelligence and industrial automation will continue to boost mechanization and large-scale production in the Chinese jade carving industry. These trends will further contribute to the sustained im-

Figure 26. Left: A nephrite pendant (6.0 × 4.2 cm) with a poem and drawing from the Qing Dynasty. On the front is a senior, a child, and scenery. The back demonstrates calligraphy engraving, with a traditional form of expression. Photo from Gu (2010a, p. 1). Right: A modern nephrite pendant "Free Cloud and Crane" (10.0 × 5.2 cm) also features a carved landscape on the front and calligraphy on the back. Although similar to the traditional form of expression, it uses a more freehand style that retains the material's natural color, shaping it into the half red sun with a touch-of-autumn feel reminiscent of Chinese ink painting (Ao et al., 2015). Photo courtesy of GAC. A comparison of the details reveals that the modern craft is more delicate, with smoother carving lines, thanks to motor-driven tools.

provement of the creative design and cultural value of jade carvings.

In this era of advanced science and technology, automated CNC engraving has become a trend, especially for middle- and low-end carvings. In the future, however, the dominant method will continue to be manual carving, especially of high-end jade wares, which represents the inheritance of 5,000-year-plus tradition. The advancement of modern jade carving can only be achieved through enhancing creativity, deeply understanding jade culture, and balancing manual and automated machine methods.

ABOUT THE AUTHORS
Ms. Mingying Wang is a doctoral candidate at the School of Gemmology, China University of Geosciences in Beijing. Prof. Guanghai Shi (shigh@cugb.edu.cn, corresponding author) is a professor at the School of Gemmology, and director of the Journal Center, China University of Geosciences in Beijing.

REFERENCES

Ao Y., Sun F.M., Zhao Z.L., et al. (2010) *Classic Collections of 2009 China Jade Carving & Stone Carving Works Awarded with Tian Gong Prize*. Geological Publishing House, Beijing, 295 pp.

——— (2013) *Classic Collections of 2012 China Jade Carving & Stone Carving Works Awarded with Tian Gong Prize*. Geological Publishing House, Beijing, 378 pp.

——— (2014) *Classic Collections of 2013 China Jade Carving & Stone Carving Works Awarded with Tian Gong Prize*. Geological Publishing House, Beijing, 366 pp.

——— (2015) *Classic Collections of 2014 China Jade Carving & Stone Carving Works Awarded with Tian Gong Prize*. Geological Publishing House, Beijing, 402 pp.

——— (2016) *Classic Collections of 2015 China Jade Carving & Stone Carving Works Awarded with Tian Gong Prize*. Geological Publishing House, Beijing, 354 pp.

——— (2017) *Classic Collections of 2016 China Jade Carving & Stone Carving Works Awarded with Tian Gong Prize*. Geological Publishing House, Beijing, 340 pp.

——— (2018) *Classic Collections of 2017 China Jade Carving & Stone Carving Works Awarded with Tian Gong Prize*. Geological Publishing House, Beijing, 400 pp.

Bao Y.Z. (2008) Research on the Situation and Inheritance of the Chinese Miniature Sculpture Art. Master's Thesis, The Central University of Nationalities, Beijing, 44 pp.

Barnes G.L. (2018) Understanding Chinese jade in a world context. *Journal of the British Academy*, Vol. 6, pp. 1–63, http://dx.doi.org/10.5871/jba/006.001

Deng S.P. (2007) *Exquisite Beauty: Islamic Jades*. National Palace Museum, Taipei, 287 pp.

——— (2011) *Art in Quest of Heaven and Truth: Chinese Jades through the Ages*. National Palace Museum, Taipei, 172 pp.

Desautels P.E. (1986) *The Jade Kingdom*. Van Nostrand Reinhold Co., New York, 118 pp.

Gu F. (2005) *The Complete Collection of Jades Unearthed in China (10—Hubei and Hunan Volume)*. Science Press, Beijing, 240 pp.

——— (2010a) *Chinese Jades in Traditional Collections (6—Qing Dynasty)*. Science Press, Beijing, 256 pp.

——— (2010b) *Chinese Jades in Traditional Collections (7—Qing Dynasty)*. Science Press, Beijing, 256 pp.

Hansford S.H. (1950) *Chinese Jade Carving*. Lund Humphries Co., London, 145 pp.

Ji L. (1984) *Crafts and Arts in Contemporary China*. China Social Sciences Press, Beijing, 650 pp.

Kong F.A. (2007) The Study of Technology of Chinese Ancient Jade Producing. PhD Thesis, Shanxi University, Taiyuan, 332 pp.

Lu J.F., Fang X.M., Zhou X.J. (2014) *General History of Chinese Jade (the Northern Volume of the Neolithic Age)*. Haitian Press, Shenzhen, 303 pp.

Lu J.F., Yu Y.J., Fang G. (2014) *General History of Chinese Jade (the Xia & Shang Dynasties)*. Haitian Press, Shenzhen, 336 pp.

Lu J.F., Ou-yang M.Y. (2014) *General History of Chinese Jade (the Zhanguo Period)*. Haitian Press, Shenzhen, 358 pp.

Lu J.F., Li Y.D. (2014) *General History of Chinese Jade (the Qin & Han Dynasties)*. Haitian Press, Shenzhen, 392 pp.

Ma G.Q. (2014) *Xinjiang Hetian Placer Nephrite (White Jade) Grading Standards and Illustrations*. Xinjiang People's Press, Urumqi, 299 pp.

Markbreiter S. (1985) Jade carving in two cities. *Arts of Asia*, Vol. 15, No. 1, pp. 63–73.

Michaelson C., Sax M., Wu H. (2016) The renaissance of jade carving in China today. *Arts of Asia*, Vol. 46, No. 3, pp. 61–71.

Niu Q.B. (2015) Jade carving craftsmanship during the Neolithic Age and the Shang Dynasty. *Journal of Nanyang Normal Uni-*

versity (Social Sciences), Vol. 14, No. 11, pp. 46–51.

Read P. (1981) Travels in China. *Canadian Jeweller*, June, pp. 134–135, 137.

Sax M., Meeks N.D., Michaelson C., Middleton A.P. (2004) The identification of carving techniques on Chinese jade. *Journal of Archaeological Science*, Vol. 31, No. 10, pp. 1413–1428, http://dx.doi.org/10.1016/j.jas.2004.03.007

Technical Research Group of Beijing Jade Factory (1976) Some ideas on jade carving craftsmanship in Shang Dynasty. *Archaeology*, No. 4, pp. 229–233, 286–287, 290.

Thomas S.A., Lee H.W. (1986) Gemstone carving in China: Winds of change. *G&G*, Vol. 22, No. 1, pp. 24–34, http://dx.doi.org/10.5741/GEMS.22.1.24

Tucker E. (1982) Jade forms from ancient China. *G&G*, Vol. 18, No. 1, pp. 20–31, http://dx.doi.org/10.5741/GEMS.18.1.20

Wang M.Y., Shi G.H. (2020) Characteristics of modern Chinese jade carvings: The nephrite jade works that won the Tiangong Awards from 2003 to 2014. *Arts of Asia*, Vol. 50, No. 3, pp. 88–102.

Wen G., Jing Z.C. (1992) Chinese Neolithic jade: A preliminary geoarchaeological study. *Geoarchaeology*, Vol. 7, No. 3, pp. 251–275, http://dx.doi.org/10.1002/gea.3340070304

Xu L. (2011) *Chinese Ancient Jade-Making Process*. The Forbidden City Publishing House, Beijing, 269 pp.

——— (2012) An overview of jade carving technology in ancient China—A preliminary comparison with the jade culture and jade carving technology in ancient Central America. *Essence of Nature – Civilization of Ancient Jade in China and Mexico.*

The Forbidden City Publishing House, Beijing, pp. 324–338.

——— (2014) Technology of jade-making is helpful to appraisal of ancient jade. *Collectors*, No. 8, pp. 28–34.

Xu X.D. (2013) *Classics of the Forbidden City (Jade in the Collection of the Palace Museum)*. The Forbidden City Publishing House, Beijing, 300 pp.

Yang B.D. (1982) Court jades of Qing Dynasty. *Palace Museum Journal*, No. 1, pp. 49–61, 101–104.

——— (1989a) Aspects of Chinese ancient jadeware. *Palace Museum Journal*, No. 1, pp. 32–48, 99–100.

——— (1989b) Aspects of Chinese ancient jadeware. *Palace Museum Journal*, No. 2, pp. 31–40, 97–98.

——— (2004) Discussion on characteristics of the prehistoric jade carving and their differences. *Archaeology*, No. 10, pp. 62–68.

——— (2006) A review of jade carving tools. *Yang Boda's Views on Jade—Ba Zhi Selected Works*. The Forbidden City Publishing House, Beijing, 575 pp.

Yang B.D., Qi J., Zhao G.D., et al. (2005) *Chinese Jade Complete Works*. Hebei Fine Arts Publishing House, Shijiazhuang, Vol. 1, 316 pp.

Yi F. (2001) *A Brief Chinese Chronology*. The Heritage Press, Beijing, 267 pp.

You R.D. (2001) *An Introduction to Chinese Ancient Jade*. The Forbidden City Publishing House, Beijing, 367 pp.

Zhao Y.K., Zhang J.M. (2000) *Chinese Jade Carving Technology*. Beijing Industrial Art Publishing House, Beijing, 481 pp.

Zhu J.J. (2007) *Classics of the Forbidden City (The Forbidden City Treasure)*. The Forbidden City Publishing House, Beijing, 247 pp.

COLOR CHARACTERISTICS OF BLUE TO YELLOW BERYL FROM MULTIPLE ORIGINS

Yang Hu and Ren Lu

Aquamarine and heliodor are colored by Fe ions, an important coloring agent for beryl. Blue to yellow gem beryl was studied by quantitative spectroscopy and trace-element analytical techniques to explore color characteristics and chromophores. Blue color was caused by a 600 nm absorption, while yellow color was attributed to an absorption edge in the violet-blue region. Color ranged from blue to green to yellow due to different proportions of Fe ions with various valences and occupancies. Mn content was positively related to Fe, but abundant Mn ions showed no impact on color (unlike Mn in morganite and red beryl). The arrangement of alkali ions and water in channel and the charge compensation mechanism of beryl are discussed. Alkali ions (mainly Na and Cs) and water were localized in the peanut-shaped channels, and all alkali elements (Li, Na, K, Rb, and Cs) were relevant. Though alkali ions and water interacted with transition metal Fe and Mn ions, their influence on blue to yellow color was indirect and rather weak.

G em beryl is a significant gem species, including color varieties such as emerald, aquamarine, heliodor, goshenite, morganite, and red beryl. Blue to yellow beryl has been found in numerous locations, including Brazil, South Africa, Russia, Ukraine, Canada, Myanmar, the United States, Afghanistan, and China (Belakovskiy et al., 2005).

Blue color in aquamarine and yellow color in heliodor are attributed to abundant Fe ions (Wood and Nassau, 1968). Fe ions are also present in all other color varieties of beryl, though Fe content is relatively low in morganite. Although discussions on the role of Fe ions in blue to yellow beryl are not new, they have mainly focused on crystal physics and chemistry. This article explores the color characteristics and chromophore ions of blue to yellow beryl using quantitative chemical and spectral analysis.

The crystal structure of beryl is unique for having a peanut-shaped "channel" along the c-axis, and alkali ions in this channel interact with transition metal ions. Therefore, we will discuss the features of alkali elements and their roles in beryl color, based on analysis of the channel mechanism. This research was part of a series of ongoing studies on the color characteristics of beryl.

MATERIALS AND METHODS

Beryls from different origins were gathered and 14 of them with various color and alkali content were selected for this study (see table 1). They were classified in the following color varieties: goshenite (colorless to near-colorless), aquamarine (greenish blue to blue), green beryl (green to yellowish green), and heliodor (greenish yellow to yellow). With the exception of two faceted stones and one rough stone, the samples were

In Brief

- Color in beryl ranges from blue to green to yellow due to different proportions of Fe-related absorption.
- The color of green beryl can also come from Cr^{3+} and/or V^{3+} ions.
- Alkali elements and water in beryl were found to play complex roles, but their influence on blue to yellow color is indirect and likely weak.

fabricated as optical wafers perpendicular (PK-7 and PK-8) or parallel (PK-5, PK-10, PK-9, RUS-8, MOZ-2, BM-1, MOZ-1, AF-3, and AF-2) to the c-axis (figure 1).

All samples were investigated by standard gemological testing, Raman spectroscopy, Fourier-transform near-infrared (FT-NIR) and ultraviolet/visible/near-infrared (UV-Vis-NIR) spectroscopy, and laser ablation–inductively coupled plasma–mass spectrome-

Figure 1. The 14 studied beryl samples (0.63–3.50 ct) from various geographic origins. Color ranged from blue to yellow, as well as near-colorless and colorless. Photo by Yang Hu.

try (LA-ICP-MS) chemical analyses. Inclusions were captured using a Leica M205A microscopic system with oblique fiber-optic illumination. Raman spectra were collected by a Bruker Senterra R200 spectrometer coupled with a 532 nm laser for identifying various inclusions. The resolution was set at 5 cm^{-1} with a 20 second integration time, 2 accumulations, and 20 mV laser energy. To explore the characteristics of water in the beryl, FT-NIR was performed using a Bruker V80 FTIR spectrometer at 2 cm^{-1} resolution and 32 accumulations. To study the color features, UV-Vis-NIR spectra were recorded with a PerkinElmer 650s spectrophotometer equipped with a 150 nm integrating sphere accessory at 1 nm resolution.

Chemical analysis was performed by LA-ICP-MS using an Agilent 7500a and 7900 ICP-MS instrument combined with a GeoLas 193 nm laser. The carrier gas used in the laser ablation unit was He with a flow rate set at approximately 650 mL/min. Laser ablation conditions consisted of a 44 μm diameter laser spot size, a fluence of 5–6 J/cm^2, and a 6–8 Hz repetition rate. Each analysis incorporated a background acquisition time of approximately 20–30 seconds followed by 50 seconds of ablation. A multi-standard quantitative calculation method was adopted, with Al chosen as the normalizing element. Calibration standards of NIST 610, BCR-2G, BHVO-2G, and BIR-1G were used as external references (Liu et al., 2008). Three laser spots for each sample were applied in an area that was typically clean with an even color distribution. UV-Vis-NIR spectra were collected in the same area analyzed by LA-ICP-MS.

RESULTS

Gemological Properties. The beryl samples had a refractive index range of n_e=1.568–1.579 and n_o=1.573–1.586, with birefringence between 0.005 and 0.006, with the exception of samples BM-1 and BRA-3. Pale green MOZ-1 had the lowest RI (1.568–1.573) among all the samples. Burmese deep blue sample BM-1 and Brazilian dark greenish blue BRA-3 had the highest RI (1.589–1.600) and birefringence (0.009–
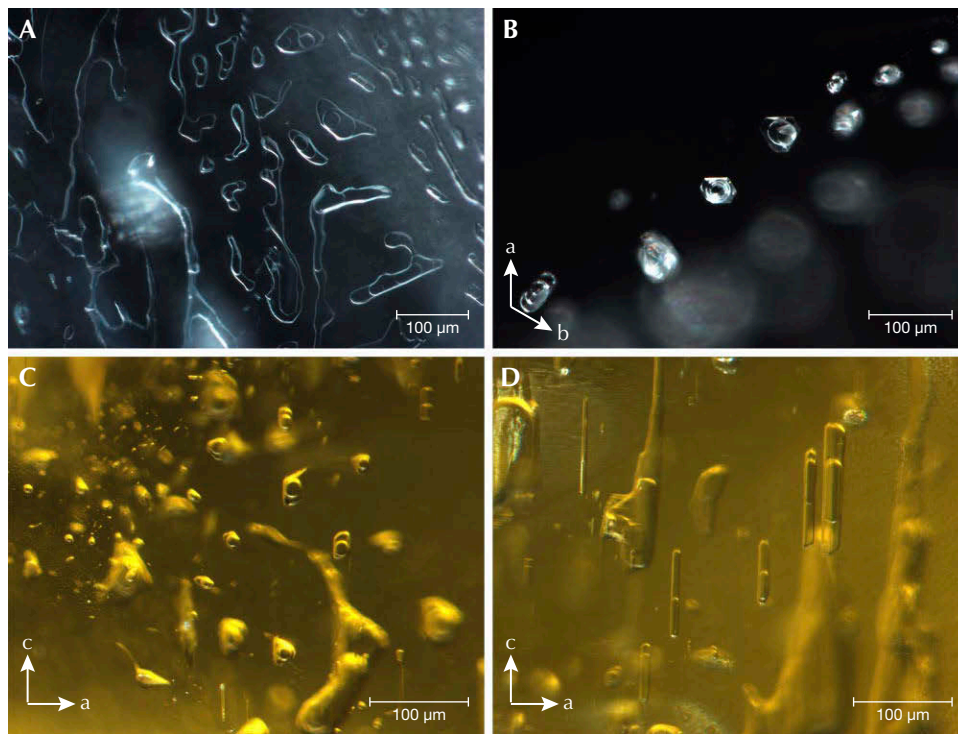
Figure 2. Two-phase inclusions in blue to yellow beryl samples. A: Fingerprint-like two-phase inclusions along a healed fissure plane in aquamarine. B: Hexagonal two-phase inclusions viewed down the c-axis in aquamarine, consistent with the crystallographic symmetry. C and D: Isolated elongated rod-like two-phase inclusions parallel to the c-axis in heliodor. Photomicrographs by Yang Hu.

0.010). All the beryl samples displayed weak to moderate dichroism. All bluish beryl samples showed more blue color along the e-ray than the o-ray. It should be noted that the dark hue of sample BRA-3 was caused by extremely tiny cloudy dark inclusions throughout nearly the whole sample. The lemon and yellow heliodor samples showed weak dichroism but a relatively saturated color.

Microscopic Observation. Two-phase inclusions were the most common type in the beryl samples, containing one gas bubble (CO_2) floating in at least one kind of fluid (figure 2). Minor CH_4, H_2S, and N_2 were found only in some of the Pakistani beryl samples. Normally the Pakistani samples had two liquid phases (CO_2 and water with minor dissolved CO_2), while samples from other deposits hosted one liquid phase (water). Some-

TABLE 1. Blue to yellow beryl samples selected for this study.

Sample no.	Variety	Geographic origin	Color
PK-7	Goshenite	Shigar Valley, Pakistan	Near-colorless
PK-5	Goshenite	Shigar Valley, Pakistan	Near-colorless
PK-10	Goshenite	Shigar Valley, Pakistan	Colorless
PK-8	Aquamarine	Shigar Valley, Pakistan	Near-colorless
PK-9	Aquamarine	Shigar Valley, Pakistan	Pale greenish blue
BRA-3	Aquamarine	Brazil	Dark greenish blue
RUS-8	Aquamarine	Russia	Greenish blue
MOZ-2	Aquamarine	Mozambique	Blue
BM-1	Aquamarine	Mogok, Myanmar	Deep blue
MOZ-1	Green beryl	Mozambique	Pale green
AF-3	Green beryl	Africa	Yellowish green
AF-2	Heliodor	Africa	Greenish yellow
UK-11	Heliodor	Unknown	Lemon yellow
UK-10	Heliodor	Unknown	Golden

RAMAN SPECTRA

223 (S)

S O

O 474 (S)

686 (B)

1388 (C1)

1243 (C2)

1284 (C1)

crystal: sulfur+orpiment

fluid I: water

gas: CO₂+CH₄

fluid II: CO₂

aquamarine (E⊥c)

B B B B B B

3606 (H1)

3200–3500 (H2)

2913 (CH₄)

INTENSITY (a.u.)

RAMAN SHIFT (cm⁻¹)

fluid II

gas

crystal

fluid I

100 μm
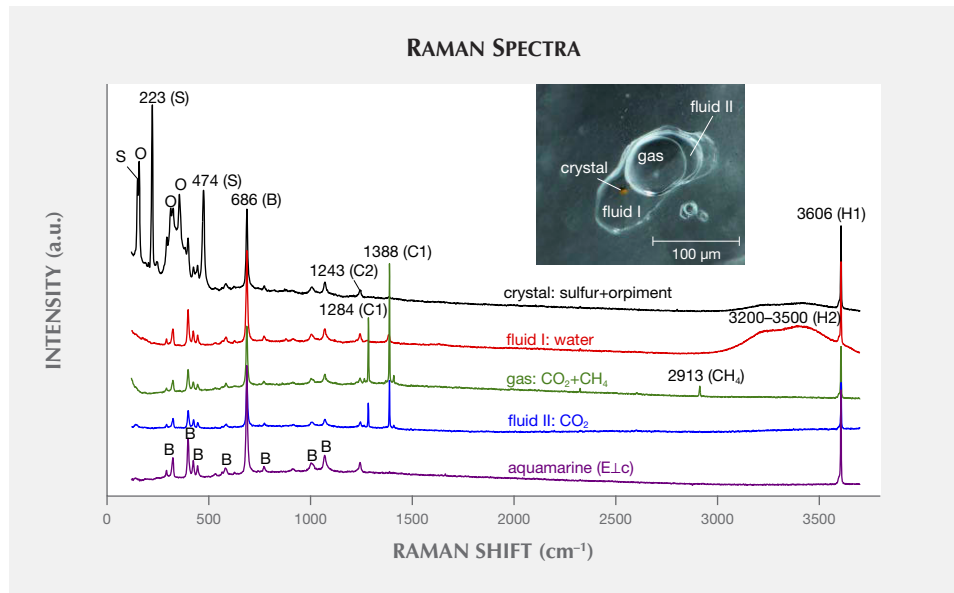
Figure 3. This multiphase inclusion had two fluid phases, one gaseous phase, and one crystal phase. Abbreviations: B—beryl, S—sulfur, O—orpiment, C1—CO_2 in the inclusion, C2—CO_2 in the beryl structure channel, H1—water in the beryl structure channel, and H2—water in the inclusion. Spectra are offset vertically for clarity. Photomicrograph by Yang Hu.

times a mineral phase was hosted in the fluid, such as native sulfur and orpiment in Pakistani samples (see figure 3). Two-phase inclusions had hexagonal, elongated, round, oval, angular, needle-like, or other irregular shapes. They were generally distributed along healed fissure planes forming "fingerprint-like" inclusions or isolated (again, see figure 2).

Our heating experiments indicated that two-phase inclusions transformed after heat treatment at 400°C or higher. Before heat treatment, a round bubble was floating on the fluid phase (figure 4, left). While cooling the sample to room temperature after heating to 300° and 400°C, we photographed the same two-phase inclusion (figure 4, middle and right). The round bubble

disappeared after heating above 400°C. Raman analysis of this two-phase inclusion detected no gas or fluid. We concluded that micro-cracks occurred after heating above 400°C, allowing the gaseous and fluid phase to escape and leaving the empty two-phase inclusion (recognizable by its original shape and distribution). Yellowish and greenish beryl are usually heated between 400° and 500°C to obtain a blue color, so this empty two-phase inclusion could potentially be used as evidence of heat treatment of aquamarine.

Various mineral inclusions could be detected by Raman spectroscopy. Tourmaline, albite, muscovite, garnet, zircon, and tantalite-columbite were typical in our samples (figure 5). Argentojarosite was identi-

Figure 4. A two-phase inclusion before and after heat treatment at 300° and 400°C. The gaseous and fluid phases disappeared after heat treatment above 400°C. Left: Unheated. Center: After heating to 300°C and cooling to room temperature. Right: After heating to 400°C and cooling to room temperature. Photomicrographs by Yang Hu.

100 μm   100 μm   100 μm
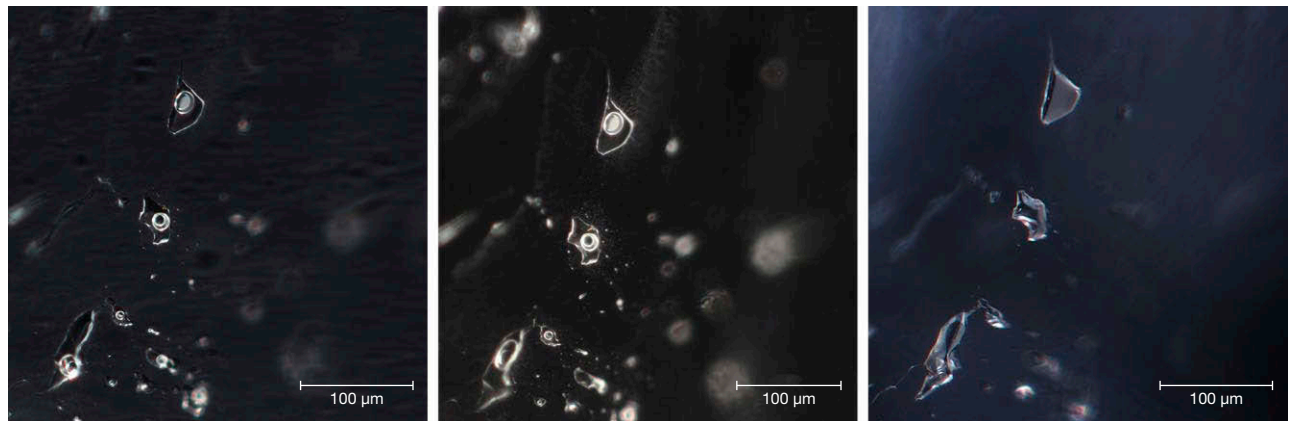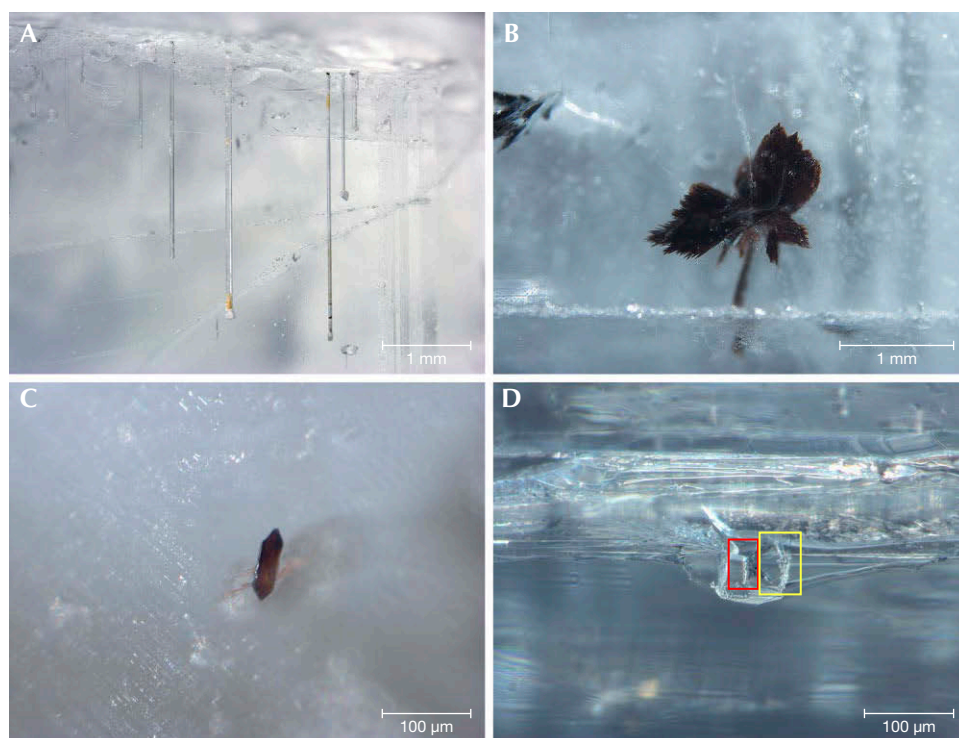
Figure 5. Various mineral inclusions in the beryl samples. A: Yellow argentojarosite inside needle-like growth tubes along the c-axis of a Pakistani aquamarine. White albite was present at the end of growth tubes. B: Brown butterfly-like tantalite-columbite in a Pakistani aquamarine. C: Hexagonal brownish tantalite-columbite in a Brazilian aquamarine. D: Bertrandite (red rectangle) and siderite (yellow rectangle) inclusions in an aquamarine from Mozambique. Photomicrographs by Yang Hu.

fied only in Pakistani aquamarine, while bertrandite and siderite were recognized only in an aquamarine sample from Mozambique.

Trace Element Analysis. The alkali element and transition element contents (in ppmw) of all beryl samples from multiple localities are reported in table 2.

Alkali Elements. Among the alkali elements, Cs and Na concentrations were relatively enriched and Rb content was lowest in nearly all samples (table 2). In Burmese aquamarine BM-1, K content (72–219 ppmw) was the lowest rather than Rb (1375–1459 ppmw). The concentration of Li was less than Na in all of the samples. Nearly all samples had total alkali content (including Li, Na, K, Rb, and Cs) below approximately 6000 ppmw. Aquamarine MOZ-2 and goshenite PK-10 had the lowest total alkali content (1250–1350 ppmw on average). The alkali content of deep blue Burmese aquamarine BM-1 and dark blue Brazilian aquamarine BRA-3 differed noticeably from those of other samples. Li, Rb, and Cs contents were more than

TABLE 2. LA-ICP-MS chemical composition analysis of beryl samples.

Trace elements (ppmw)	Goshenite PK-7	Goshenite PK-5	Goshenite PK-10	Aquamarine PK-8	Aquamarine PK-9	Aquamarine BRA-3	Aquamarine RUS-8	Aquamarine MOZ-2	Aquamarine BM-1
	Pakistan	Pakistan	Pakistan	Pakistan	Pakistan	Brazil	Russia	Mozambique	Myanmar
Li	290–357	1168–1239	68–75	292–328	73–76	5633–5745	270–272	136–145	6244–6497
Na	1103–1295	3845–3970	827–843	1099–1147	1860–2039	8988–9073	1295–1425	1031–1098	7857–8102
K	94–114	118–137	54–69	83–86	434–452	1036–1067	16–21	37–44	72–219
V	1–5	1–2	0	4–5	30–33	17–18	0	4–5	82–84
Cr	0–14	0–1	0–3	0–4	1–6	3–5	0	0–1	0
Mn	28–30	52–56	17–18	19–51	19–23	287–292	23–25	7–9	568–854
Fe	1745–1826	1459–1500	1355–1414	1802–1950	4498–5080	9306–9407	5466–5703	5542–5554	6709–7668
Rb	37–42	42–44	9–10	34–37	52–63	662–671	7–9	10–11	1375–1459
Cs	2261–2861	622–676	313–333	2229–3216	1366–1414	17789–18005	184–186	133–135	46510–47496

Data analyzed by LA-ICP-MS from three spots per sample. Data reported in minimum and maximum values. Detection limits (ppmw): Li = 0.36, Na = 7.43,
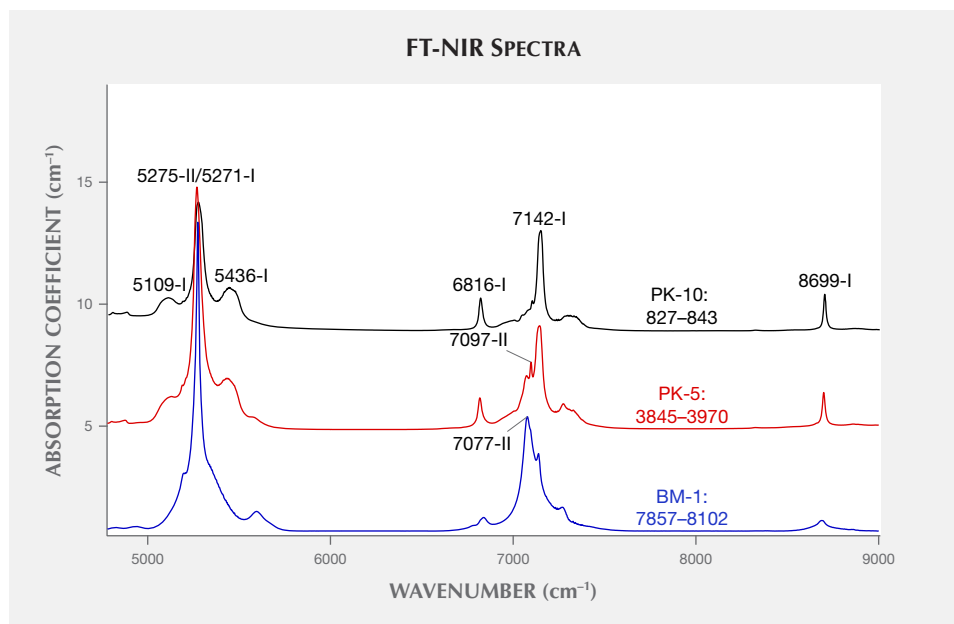
FT-NIR SPECTRA

Figure 6. FT-NIR spectra of beryl wafers parallel to the c-axis. The peak intensity of type II water at 7097, 7077, and 5275 cm⁻¹ became stronger (from top to bottom) with increasing sodium content. The spectra are displaced vertically by y+4.5 cm⁻¹ (PK-5) and y+9 cm⁻¹ (PK-10) for clarity. Note: Na content analyzed by LA-ICP-MS is listed in ppmw.

10 times higher, and Na and K were 3–10 times higher (table 2). BM-1 had the richest Cs content (46510–47496 ppmw) reported for blue aquamarine.

Transition Metals. Concentration of Fe varied from 1355 to 9407 ppmw for all colorless and blue to yellow beryl samples (table 2). Among the samples, the colorless and near-colorless beryl (PK-10, PK-7, PK-8, and PK-5) had relatively low Fe (1355–1950 ppmw). Other saturated bluish beryl contained higher Fe content, even up to 9407 ppmw. The lemon yellow and golden-colored heliodor (UK-10 and UK-11) had Fe content between 2030 and 3812 ppmw, lower than bluish beryl samples of similar saturation.

Mn content was much lower than Fe in all samples (table 2). The concentration of Mn varied between 4 and 854 ppmw, and it was below 200 ppmw in most samples. Burmese deep blue beryl BM-1 and Brazilian dark greenish blue sample BRA-3 had relatively rich Mn (187–854 ppmw). The concentration of V and Cr in bluish and yellowish beryl samples was quite low to even below detection limits (table 2). But these concentrations were relatively rich in green beryl MOZ-1 (which averaged 262 ppmw V and 279 ppmw Cr). Besides alkali and transition elements, traces of Mg, Sc, Zn, Ga, Sn, and Ta were detected in some samples.

Spectroscopy Analysis. *FT-NIR Spectroscopy.* The type of water and its relative content in the channel was revealed quantitatively by its near-infrared absorption spectrum. Peaks in the NIR region represented the overtones and combinations of "type I" and/or "type II" water absorption. Most beryl samples contain "type I" water with peaks at 8699, 7142, 6816, 5436, 5271, and 5109 cm⁻¹ (Wood and Nassau, 1967), such as PK-10 and PK-5 in figure 6. But Brazilian aquamarine BRA-3 and Burmese aquamarine BM-1 were dominated by strong "type II" water peaks at 7097, 7077, and 5275 cm⁻¹ (Wood and Nassau, 1967) (blue trace in figure 6). Also, the peak intensity of type II water became stronger with increasing sodium content.

UV-Vis-NIR Spectroscopy. Quantitative UV-Vis-NIR spectra for the e-ray and o-ray were acquired for the beryl samples. The color circles of the beryl samples in figures 7–10 were calculated from visible spectra

Green beryl MOZ-1	Green beryl AF-3	Heliodor AF-2	Heliodor UK-11	Heliodor UK-10
Mozambique	Africa	Africa	Unknown	Unknown
70–76	143–149	134–140	162–174	135–162
508–627	2507–2611	1625–1797	804–855	1204–1443
2–36	292–297	162–195	51–66	153–175
257–268	9–10	7–14	0	0
267–292	0	0–2	0–4	2–4
4–7	95–96	116–160	36–43	49–57
2698–2841	6899–7055	6292–8217	2030–2203	3225–3812
11–14	169–175	124–145	39–46	34–61
300–370	1606–1630	1791–2305	1952–2092	510–689
K = 11.22, V = 0.07, Cr = 0.88, Mn = 0.46, Fe = 12.65, Rb = 1.66, Cs = 8.22				

between 380 and 780 nm using GRAMS software, when the sample thickness was normalized to 4 mm. In order to discuss the impact of Fe on coloration, we converted ppmw to ppma in the UV-Vis-NIR region by the following formulation: ppma = [[atomic weight of beryl/number of atoms for beryl]/atomic weight of Fe] · ppmw value = [(537.49/29)/55.85] · ppmw value. That is, ppma value = 0.3318 ppmw value.

All blue to yellow beryl samples showed the typical iron absorption in their UV-Vis-NIR spectra. Peaks at 372 and 427 nm related to Fe^{3+} ions (Wood and Nassau, 1968) were observed in all samples (figures 7–9). These 372 and 427 nm peaks were more or less covered by the absorption edge in the violet-blue region in the yellowish beryl samples. They were even invisible in lemon yellow and golden heliodor (UK-10 and UK-11) (figure 7). These 372 and 427 nm peaks did not contribute to color because of their rather weak absorption.

The absorption edge in the violet-blue region leads to yellowish color in beryl. There was no obvious difference between the o-ray and the e-ray. This absorption edge was assigned to Fe^{3+} ions (Wood and Nassau, 1968). The absorption edge was present in all beryl samples, and it was in the ultraviolet region for beryl samples without yellowish color. When this absorption edge shifted to a longer wavelength from the violet-blue to the blue region, the yellow color occurred in beryl. Also, the intensity of this absorption edge was not proportional to total Fe content. For example, greenish yel-

Figure 7. Unoriented UV-Vis-NIR spectra of greenish yellow (AF-2), lemon yellow (UK-11), and golden (UK-10) heliodor samples. When the absorption edge shifted to a longer wavelength from the violet-blue to the blue region, the color turned more yellowish. The spectra are displaced vertically by y+2 cm^{-1} (UK-11) and y+4 cm^{-1} (UK-10) for clarity. Note: Fe content analyzed by LA-ICP-MS is listed in ppma.

low beryl AF-2 had the richest total Fe content (2088–2727 ppma) of the three yellowish samples, but the intensity of the absorption edge was weak compared with other yellow heliodor samples (see figure 7).

Bluish color in the beryl samples resulted from a distinct broad absorption around 600 nm in the e-ray. The 600 nm broad absorption band was present in the e-ray but quite weak in the o-ray (see figures 8
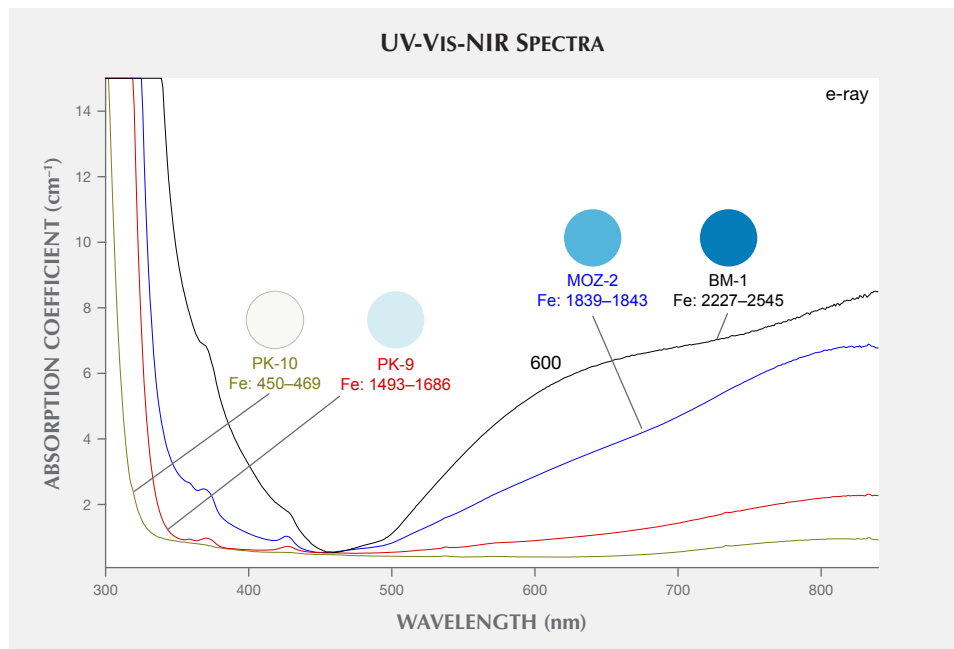
Figure 8. UV-Vis-NIR spectra of aquamarine and goshenite samples with distinguishing Fe content in e-ray. With increasing Fe content, the absorption band at 600 nm became stronger and the blue color became saturated (from bottom to top). Note: Fe content analyzed by LA-ICP-MS is listed in ppma.
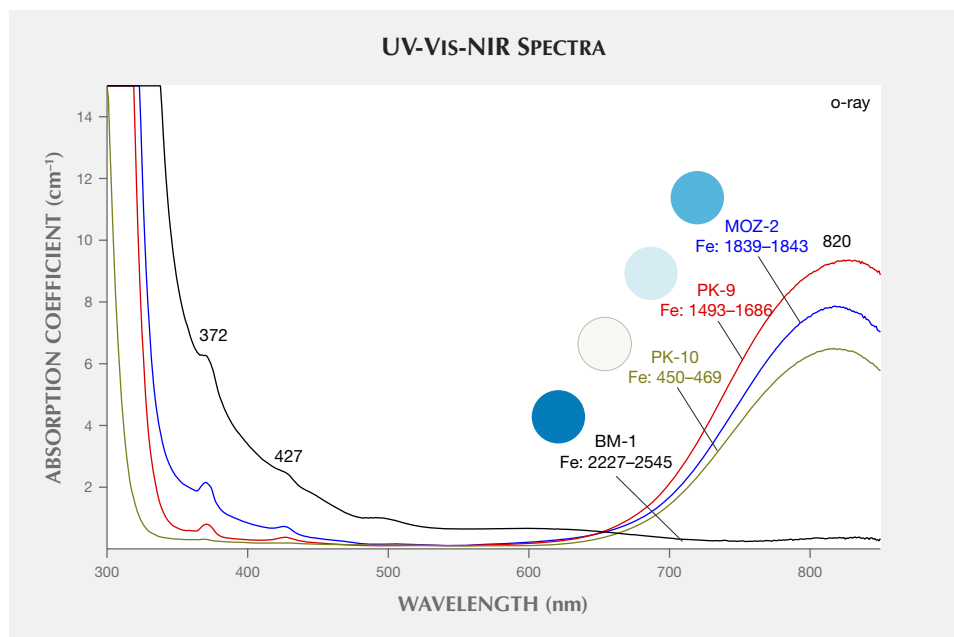
Figure 9. UV-Vis-NIR spectra of aquamarine and goshenite samples with distinguishing Fe content along the o-ray. The band intensity at 820 nm was not proportionate to the Fe content. Note: Fe content analyzed by LA-ICP-MS is listed in ppma.

and 9), which was responsible for more blue color along the e-ray than the o-ray. This absorption was associated with Fe^{2+} or Fe^{2+}-Fe^{3+} ion pairs (Wood and Nassau, 1968; Lin et al., 2013). With increasing Fe content, the 600 nm absorption band became stronger and the color became more saturated, from colorless, pale greenish blue, and medium blue to dark blue (from bottom to top in figure 8). Compared with Fe content in yellow heliodor with similar saturation, Fe ions were less efficient for coloring beryl blue than yellow: 600 ppma Fe in beryl could produce a relatively saturated yellow color. However, blue

aquamarine with similar saturation should contain at least twice the Fe content.

A broad absorption band centered at about 820 nm was stronger in the o-ray than the e-ray (see figures 8 and 9). This 820 nm broad band overlapped with the 600 nm band in the e-ray. This band in the o-ray was related to Fe^{2+} (Wood and Nassau, 1968), and its intensity had nothing to do with total Fe content. For example, the 820 nm band intensity of Burmese aquamarine BM-1 was quite weak, contrary to the abundant Fe content (see figure 9). However, the intensity of the 820 nm band in the e-ray was not in proportional to that in the o-ray. And the intensity of the 820 nm band in the e-ray was nearly positive to the total Fe content (see figure 8). So we supposed that the origin of the 820 nm band was different between the e-ray and o-ray, maybe Fe^{2+} in different occupancy.

The tail of the 820 nm band reached the visible range, but its intensity in the visible range was quite weak. So this 820 nm broad absorption could not lead to any obvious color.

Pale green beryl MOZ-1 showed typical absorption of Cr^{3+} at 426 and 600 nm for the o-ray and 630 and 660 nm for the e-ray, as well as sharp R lines at 683 nm (Wood and Nassau, 1968). A weak V^{3+} absorption shoulder was also observed at about 400 nm (see figure 10). So this green color originated from Cr^{3+} and minor V^{3+} ions in beryl, similar to emerald. This absorption was totally different from yellowish green beryl AF-3 (no absorption spectra shown for this sample), which showed the absorption features of Fe ions, though they both had greenish color.

Figure 10. The UV-Vis-NIR spectra of green beryl MOZ-1 showed typical absorption of Cr^{3+} and minor V^{3+} ions, as well as Fe ions at 372 and 820 nm.
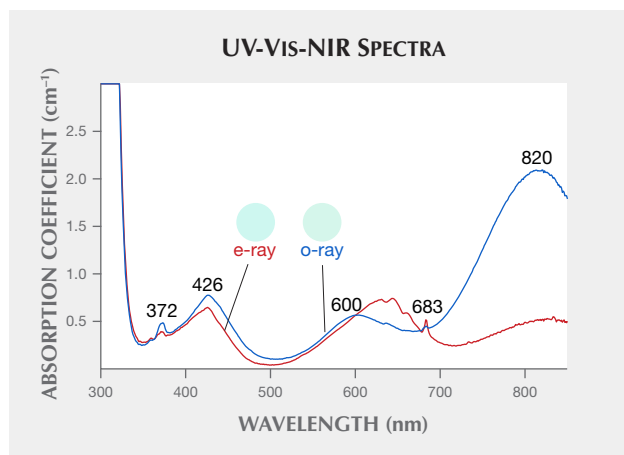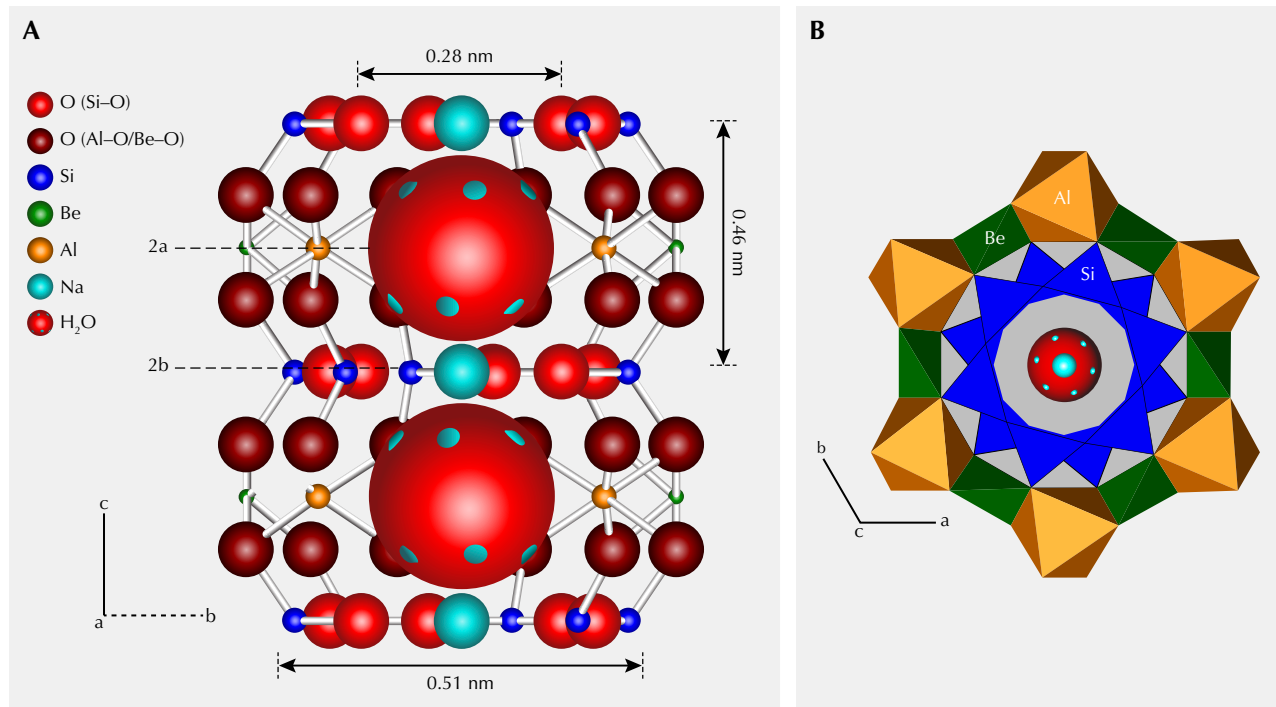
Figure 11. Diagrams of the unique peanut-shaped channel structure in beryl, and the internal arrangement of alkali ions and water, viewed as "ball-wire" down into the a-axis (with a 120° angle from the b-axis, which is projected onto the page from behind as a dashed line) (A) and as "polyhedra" down into the c-axis (B). Smaller rings of SiO_4 tetrahedra stack over larger rings of alternating BeO_4 tetrahedra and AlO_6 octahedra forming peanut-shaped enclosures. Large alkali ion Cs^+ or water would only be localized at the larger 2a site and unable to migrate along the channel. The smallest ion Na^+ fits suitably at the 2b site, interacting with "type II" water. The hydrogen-hydrogen direction is parallel to the c-axis in "type I" water and perpendicular to the c-axis in "type II" water. Selected atoms in figure A were omitted to better show internal details. Relevant parameters are from Artioli et al. (1993) and Wood and Nassau (1968).

DISCUSSION

Crystal Structural Consideration. The crystal structure of beryl, with an ideal chemical formula $Be_3Al_2(Si_6O_{18})$, consists of smaller rings of six SiO_4 tetrahedra and larger rings of alternating BeO_4 tetrahedra and AlO_6 octahedra (figure 11B). These two rings stack over each other along the c-axis, forming a peanut-shaped structural "channel" along the c-axis (figure 11A). Large ions such as Cs or water molecules would only fit within the large ring and be therefore localized at the 2a site and unable to migrate along the channel, because the ionic diameter of Cs^+ (0.376 nm) and the dimension of a water molecule ($0.28 \times 0.32 \times 0.37$ nm) are too large to fit within the 2b site. Water molecules in beryl occur in two configurations: "type I" with H-H direction parallel to the c-axis, and "type II" with H-H direction perpendicular to the c-axis (Wood and Nassau, 1967). Water molecules are only free to rotate around the c-axis according to the hexagonal system (Gorshunov et al., 2016). Due to similar ionic radii and chemical properties, minor K^+ and Rb^+ ions in the channel behave like Cs^+ ions. The smallest alkali ions coordinated in the 2b site, Na^+, are stable because of Coulomb interactions between Na^+ and adjacent type II water molecules (see again figure 11A).

Substitutions commonly occur in Be-O tetrahedra by Li^+ ions, and in Al-O octahedra by transition metal ions and other ions (such as Mg, Ca, and Ti). With Li^+ substituting for Be^{2+}, slight deformation of Be-O tetrahedra and charge deficiency arise. Substitution of divalent cations in Al octahedra or trivalent cations in Be tetrahedra could also lead to charge deficiency. Alkali ions (mainly Cs^+ and Na^+) in the channel serve to charge balance (e.g., Li^+ + transition metal ions + other substituted ions = Cs^+ + Na^+). Moreover, the substitution of transition metal ions mainly included $Fe^{2+}/Fe^{3+}/Mn^{2+}/Mn^{3+}/Cr^{3+}/V^{3+}<=>Al^{3+}$, or in some cases $Fe^{2+}/Fe^{3+}<=>Be^{2+}$.

Alkali Elements. The relative concentrations of each alkali element were nearly proportional in all beryl samples, showing similar variation (figure 12). This was in agreement with the charge balance principle, in which the charge deficiency arising from the substitu-
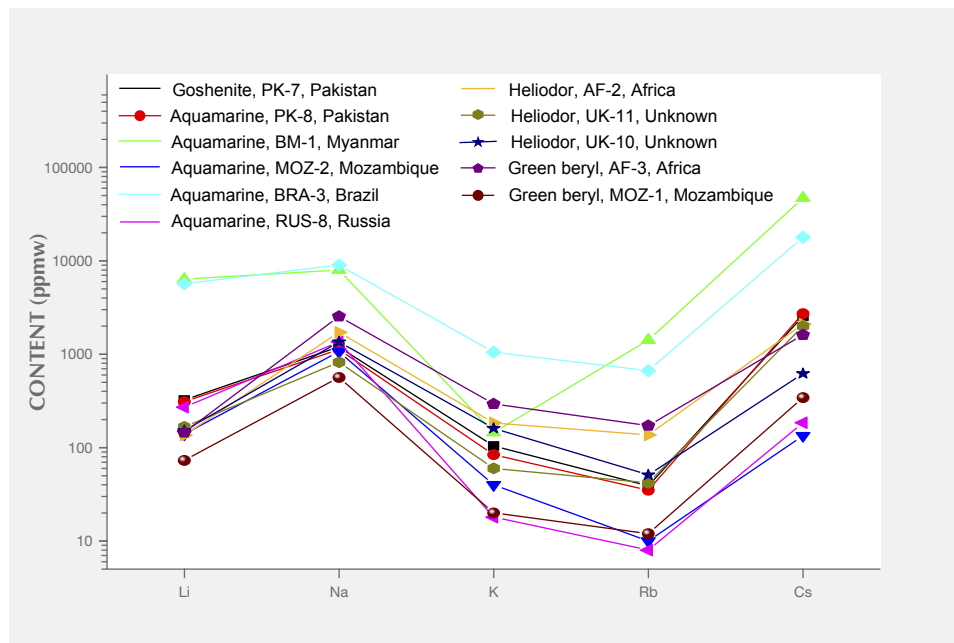
Figure 12. The concentration of five alkali elements for all beryl samples from different locations showed a similar proportional tendency. A log scale was used for the y-axis.

tion of Li are compensated by a proportional amount of Na and Cs plus minor K and Rb in the channel. But there were also some inconsistencies, especially the unexpectedly low K content in Burmese aquamarine BM-1. This proportional tendency may result from the process of crystallization in the mineralizing fluid with abundant Li, Na, K, Rb, and Cs at the same time.

The chemical fingerprint diagram of Li versus Cs content showed two concentrated areas, which could be considered the "low-alkali beryl" area (red circle in figure 13) and the "high-alkali beryl" area (blue circle in figure 13). Low-alkali beryl was dominated by type I water and high-alkali beryl by type II water analyzed by FT-NIR spectra. This was in agreement with the fact that Na^+ coordinates with type II water molecules in the channel (see figure 11A) and each alkali was nearly proportional. Beryl samples from most localities were in the low-alkali beryl area including Pakistan, Russia, Africa, Mozambique, Italy (Bocchio et al., 2009), Vietnam (Huong et al., 2011),
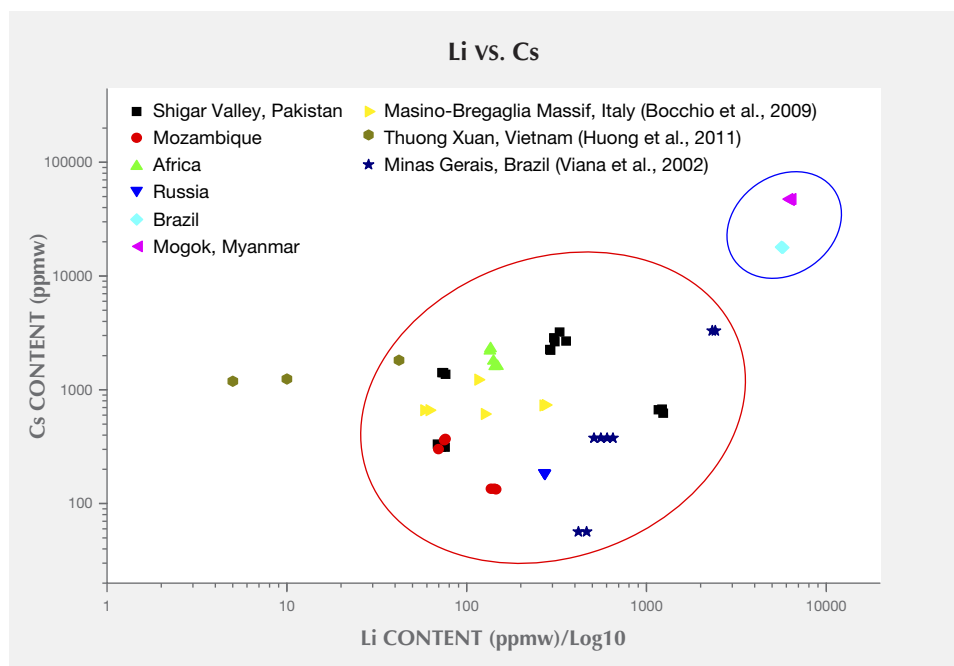
Figure 13. The chemical fingerprint diagram of the log-log plot of Li versus Cs content in beryl samples from various localities shows two concentrated areas considered the "low-alkali" (red circle) and "high-alkali" (blue circle) areas.
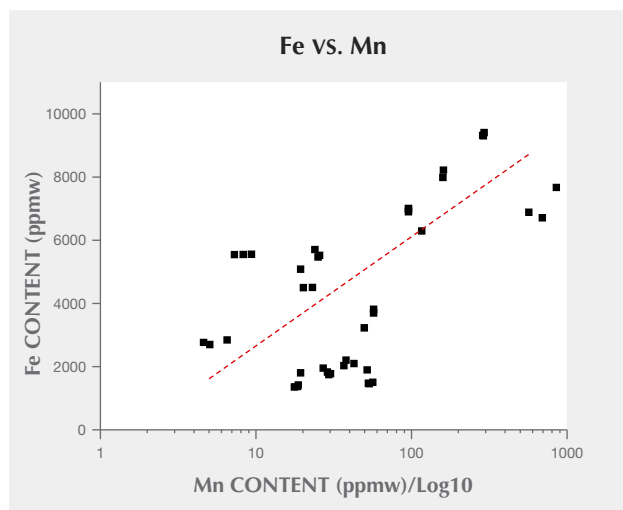
Figure 14. Fe and Mn concentrations showed an approximately positive relationship in all 14 blue to yellow samples, indicating similar substitution behavior.

and Minas Gerais, Brazil (Viana et al., 2002). Although this Li-Cs plot could not be used to distinguish the exact geographic origin, it showed the possibility of separating blue to yellow beryl from locations worldwide by various chemical fingerprint diagrams.

Chromophores Fe and Mn. Concentrations of Fe and Mn showed an approximately positive relationship in blue to yellow beryl samples, though they were not quite proportional (figure 14). This positive relationship could be explained by Fe and Mn's similar substitution behavior according to similar radii, ionic valence, and coordination. Mn and Fe ions were normally present as two possible valence states: +2 and +3 in beryl. Radii of Mn ions (approximate measurements of Mn^{2+}: 0.066–0.083 nm; Mn^{3+}: 0.058–0.064 nm) are quite similar to Fe ions (Fe^{2+}: 0.063–0.078 nm; Fe^{3+}: 0.049–0.054 nm) (Shannon, 1976). Both ions were more likely to substitute for Al^{3+} in the octahedral site due to suitable radii in beryl. Moreover, Fe and Mn ions could enrich together in mineralized fluid due to similar geochemical features. Therefore, blue to yellow beryl showed similar substitution behavior during crystallization.

The Chromophore Mn and Color. Mn ions in blue to yellow beryl did not impart an obvious red modification to the hue, and no obvious pink, purple, or orange hues were seen. Red beryl and morganite are considered to be colored by Mn^{2+} or Mn^{3+} (Nassau and Wood, 1968; Platonov et al., 1989; Fridrichová et al., 2017). Red beryl generally contains 2000 ppmw Mn (Shigley et al., 1984), and morganite has less than 200 ppmw Mn (authors' unpublished data). However, our blue to yellow beryl samples with abundant Mn con-

tent showed no obvious absorption of Mn ions in UV-Vis-NIR spectra and a corresponding pink, orange, or purple color. For example, the Mn content of deep blue aquamarine BM-1 (568–854 ppmw) was nearly half that of red beryl. And the Mn content in Brazilian dark greenish blue aquamarine BRA-3 (287–292 ppmw) and greenish yellow sample AF-2 (116–160 ppmw) was close to morganite. This indicated that Mn ions in blue to yellow beryl do not play a role in coloration, and the valence or occupancy of Mn ions should differ from that in morganite or red beryl. The valence or occupancy of Mn ions may be affected by high Fe content (the Fe/Mn ratio was at least close to an order of magnitude greater). The valence, occupation, and coloration of Mn ions in beryl will be discussed in detail in a future study.

Blue to Yellow Color Characteristics. We determined that Fe ions in beryl could lead to yellow and blue colors. Blue color has been attributed to Fe^{2+} or Fe^{2+}-Fe^{3+} pairs, and yellow color to Fe^{3+} (Wood and Nassau, 1968; Lin et al., 2013), though their accurate occupancy remains controversial. Recently, an alternative mechanism involving trapped electrons in the creation and the decay of the yellow color was proposed by Andersson (2013). But the exact configurations of the electron trap and the tetrahedral Fe^{3+} color center could not be determined. Due to different proportions of Fe ions with various valences and occupancies in beryl, color varied from yellow to greenish yellow, yellowish green, bluish green, greenish blue, and blue. The greenish color was normally modified by a yellowish or bluish component, such as yellowish green sample AF-3 and bluish green sample RUS-8. Green color could also be caused by other distinct coloration mechanisms, Cr^{3+} and/or V^{3+}, the same as emerald (e.g., green beryl MOZ-1). But the green beryl had a lower color saturation than emerald due to inadequate Cr and/or V content.

Alkali and Color. The alkali ions showed no obvious impact on blue to yellow color of beryl. The alkali ions serve for charge deficiency arising from the substitution of some transition metals, but no corresponding relationship occurred between the alkali content and Fe/Mn content for blue to yellow beryl samples. This could be because at least some Fe and Mn ions substituted without charge deficiency (i.e., $Fe^{3+}/Mn^{3+} \Leftrightarrow Al^{3+}$, or $Fe^{2+}/Mn^{2+} \Leftrightarrow Be^{2+}$), or other substituted ions (such as Zn^{2+}, Mg^{2+}) participated in charge balance. Alkali ions, therefore, had no direct impact on the chromophores and their coloration of blue to yellow beryl. Nevertheless, our high-alkali beryl appeared to show deeper

blue color. The additional dark hue of BRA-3 was caused by dark cloudy inclusions. It was worth noting that bluish samples could be "low-alkali" or "high-alkali" beryl, but all yellowish samples were "low-alkali" beryl. This manifested that the alkali may influence the valence or occupancy of Fe ions, but it required further confirmation.

Water and Color. Water type and its relative content played little role in the blue to yellow color of beryl. All blue to yellow samples contained both type I and type II water in the channel. Nor was there any relationship between the type I/type II water ratio and color hue or saturation. Water molecules were related to chromophores in beryl through Na ions, but Na ions showed no obvious impact on the coloration of blue to yellow beryl. Therefore, it was unlikely that water molecules would affect beryl's blue to yellow color.

CONCLUSIONS

Blue to yellow gem beryl was studied by quantitative chemistry and spectroscopic properties to understand the chromophores and color characteristics. Blue color was caused by a broad absorption band at 600 nm, and yellow color was attributed to an absorption edge in the violet-blue region. Both were related to Fe ions in different valences and occupancies. Green beryl was colored by a combination of yellow and blue, or by Cr^{3+} and/or minor V^{3+}. The concentration of Mn was somewhat positively related to Fe in blue to yellow beryl, but abundant Mn ions had no impact on color.

This study discussed the arrangement of alkali ions and water molecules within the structural channel, facilitating charge compensation among the channel species and aliovalent substitutions in the surrounding rings. Large Cs^+, Rb^+, K^+ ions and water molecules were localized at the 2a site and were unable to migrate along the channel. The smallest ions (Na^+) stably positioned at the 2b site, interacting with "type II" water. Non-nominal (not in chemical formula) alkali elements (Li, Na, K, Rb, and Cs) and water were relevant and played complex roles in beryl. However, we found the influence on blue to yellow color to be indirect and possibly weak.

ABOUT THE AUTHORS
Mr. Hu is a PhD student at the Gemological Institute, China University of Geosciences in Wuhan. Dr. Lu (renlu.cc@gmail.com) is a distinguished professor at the Gemological Institute, China University of Geosciences in Wuhan.

REFERENCES

Andersson L.O. (2013) The yellow color center and trapped electrons in beryl. *Canadian Mineralogist*, Vol. 51, No. 1, pp. 15–25, http://dx.doi.org/10.3749/canmin.51.1.15

Artioli G., Rinaldi R., Stahl K., Zanazzi P.F. (1993) Structure refinements of beryl by single-crystal neutron and X-ray diffraction. *American Mineralogist*, Vol. 78, pp. 762–768.

Belakovskiy D., Bradshaw J., Cairncross B., Falster A.U., et al. (2005) *Beryl and Its Color Varieties - Aquamarine, Heliodor, Morganite, Goshenite, Emerald, and Red Beryl*, English Edition. Lapis International LLC, East Hampton, Connecticut.

Bocchio R., Adamo I., Caucia F. (2009) Aquamarine from the Masino-Bregaglia Massif, Central Alps, Italy. *G&G*, Vol. 45, No. 3, pp. 204–207, http://dx.doi.org/10.5741/GEMS.45.3.204

Fridrichová J., Bacík P., Ertl A., Wildner M., Dekan J., Miglierini M. (2017) Jahn-Teller distortion of Mn^{3+}-occupied octahedra in red beryl from Utah indicated by optical spectroscopy. *Journal of Molecular Structure*, Vol. 1152, pp. 79–86, https://doi.org/10.1016/j.molstruc.2017.09.081

Gorshunov B.P., Torgashev V.I., Zhukova E.S., Thomas V.G., et al. (2016) Incipient ferroelectricity of water molecules confined to nano-channels of beryl. *Nature Communications*, Vol. 7, No. 1284, http://dx.doi.org/10.1038/ncomms12842

Huong L.T.-T., Hofmeister W., Häger T., Khoi N.N., Nhung N.T., Atichat W., Pisutha-Arnond V. (2011) Aquamarine from the Thuong Xuan District, Thanh Hoa Province, Vietnam. *G&G*, Vol. 47, No. 1, pp. 42–48, http://dx.doi.org/10.5741/GEMS.47.1.42

Lin J., Chen N., Huang D., Pan Y. (2013) Iron pairs in beryl: New insights from electron paramagnetic resonance, synchrotron X-ray absorption spectroscopy, and ab initio calculations. *American Mineralogist*, Vol. 98, No. 10, pp. 1745–1753, http://dx.doi.org/10.2138/am.2013.4472

Liu Y.S., Hu Z.C., Gao S., Günther D., Xu J., Gao C.G., Chen H.H. (2008) In situ analysis of major and trace elements of anhydrous minerals by LA-ICP-MS without applying an internal standard. *Chemical Geology*, Vol. 257, No. 1-2, pp. 34–43, http://dx.doi.org/10.1016/j.chemgeo.2008.08.004

Nassau K., Wood D.L. (1968) An examination of red beryl from Utah. *American Mineralogist*, Vol. 53, No. 5/6, pp. 801–806.

Platonov A.N., Taran M.N., Klyakhin V.A. (1989) On two colour types of Mn^{3+}-bearing beryls. *Zeitschrift der Deutschen Gemmologischen Gesellschaft*, Vol. 38, pp. 147–154.

Viana R.R., Jordt-Evangelista H., Costa G.M., Stern W.B. (2002) Characterization of beryl (aquamarine variety) from pegmatites of Minas Gerais, Brazil. *Physics and Chemistry of Minerals*, Vol. 29, No. 10, pp. 668–679, http://dx.doi.org/10.1007/s00269-002-0278-y

Wood D.L., Nassau K. (1967) Infrared spectra of foreign molecules in beryl. *Journal of Chemical Physics*, Vol. 47, No. 7, pp. 2220–2228, http://dx.doi.org/10.1063/1.1703295

——— (1968) The characterization of beryl and emerald by visible and infrared absorption spectroscopy. *American Mineralogist*, Vol. 53, No. 5, pp. 777–800.

HISTORY OF THE CHIVOR EMERALD MINE, PART I (1880–1925): FROM REDISCOVERY TO EARLY PRODUCTION

Karl Schmetzer, Gérard Martayan, and Jose Guillermo Ortiz

The history of the Chivor emerald mine in Colombia is rife with legend and adventure. The tale traces from early exploitation by indigenous people, to work by the Spanish in the sixteenth and seventeenth centuries, to 200 years of abandonment and jungle overgrowth. The story then picks up with rediscovery near the turn of the twentieth century by the Colombian mining engineer Francisco Restrepo using clues from a historical manuscript. Still the saga continued, with repeated shortages of investment funds driving multiple ownership changes and little progress toward mining the largely inaccessible deposit. The German gem merchant Fritz Klein, in cooperation with Restrepo, pursued limited mining activities with a small number of workers for a few months prior to the outbreak of World War I. After the war, the American company Colombian Emerald Syndicate, Ltd., took ownership, and mining operations resumed under the new leadership. Ownership changed yet again in the 1920s, followed by multiple cycles of expanding and shrinking mining activity, interrupted by completely unproductive periods.

The foregoing outline of the story, as presently known, has been drawn largely from three books authored by individuals who led the mining activities at Chivor during different eras: German gem merchant Fritz Klein, South African mining engineer Peter W. Rainier, and American gem hunter and buyer Russell W. Anderton. All three men wrote in a style to highlight the adventurous nature of the work. Klein's memoir covered the period from approximately 1911 to 1923 and was initially published in 1941, with a slightly updated version released in 1951. Rainier's narrative chronicled from the second half of the 1920s to the early 1930s and was printed in 1942. Anderton's work, coming to press in 1953 in the United States and 1954 in the United Kingdom, recounted activities of the late 1940s and early 1950s.

The events presented in the three books have, since their respective publications, found their way in numerous variations into historical articles or descriptions as well as gemological, mineralogical, or geological papers.[1] The rediscovery of Chivor by Francisco Restrepo (figure 1) and the clues that motivated his search have been a particularly popular topic. In general, the events described by Klein, Rainier, or Anderton have been accepted as facts in the literature, and only Klein's description and dating of the rediscovery

In Brief

- After 200 years of abandonment, the modern history of the Chivor emerald mine began with rediscovery by the Colombian mining engineer Francisco Restrepo in the 1880s.
- After several trials to sell the mine by the Colombian owners, in 1912 German gem merchant Fritz Klein then joined Restrepo in further efforts, but Klein's attempts to complete a purchase with a group of German investors were thwarted by the outbreak of World War I.
- After the war, an American company, the Colombian Emerald Syndicate, Ltd., took ownership in late 1919.
- Although operations resumed under the new leadership, lasting success was not to be found, and the Colombian Emerald Syndicate entered bankruptcy proceedings in 1923.

by Restrepo have on occasion been questioned or discussed.[2] It has been noted that Klein's time frame for the rediscovery clearly differs from that presented in

[1]See, e.g., Weldon et al., 2016, for a recent example.
[2]See, e.g., Sinkankas, 1981; Moore and Wilson, 2016.

Figure 1. Francisco Daniel Restrepo Escobar, circa 1906. Restrepo began his career at gold and silver mines in the Colombian states of Antioquia and Tolima in the 1870s and 1880s. He is credited with rediscovery of the Chivor emerald mines, an event that evidence also places in the 1880s. The early 1900s found him at gold mines in Ecuador and then leading operations at the Muzo emerald mines. In the 1910s, he returned to Chivor, where he would cooperate with German miner Fritz Klein to find investment funding for the project. Courtesy of Eduardo Restrepo Ortega.

SOURCES

The search for contemporaneous materials spanned Europe, South America, and North America, as key figures in the story hailed from or worked in Germany, the United Kingdom, Colombia, and the United States. These primary documents were compared with the known literature on the topic. Full citations for the principal existing publications consulted are summarized in the reference list. Other primary documents, such as governmental and judicial reports and decrees that may appear in broader compendiums, archived contracts, business records, newspaper articles, personal correspondence, etc., are identified to the extent feasible in the footnotes, along with brief citations to publications included in the reference list. Direct quotations from original sources in German or Spanish were translated for purposes of this publication.

Investigations began with the German Federal Archive (Bundesarchiv) and the Historical Archive of the German Ministry of Foreign Affairs (Auswärtiges Amt), both in Berlin. Stored in these repositories

Figure 2. Portrait of the gem merchant Fritz Klein by the artist Rudolf Wild, Idar-Oberstein, Germany, in the mid-1930s. At that time, Klein was engaged in writing the 1941 book describing his earlier adventures searching for new gem deposits in South America; a highlight is the saga of his engagement with the Chivor emerald mine in Colombia. Courtesy of Wolf D. Unger.

other publications. This discrepancy, in turn, provided the impetus for the present project, aiming not only to clarify this inconsistency but also, more broadly, to probe the trustworthiness of the purported historical "facts" recounted by Klein, Rainier, and Anderton.

The focus was on locating contemporaneous primary documents, such as original letters and contracts, that could elucidate events underlying the oft-repeated descriptions. Beginning with an emphasis on the period covered by Klein (figure 2), the search was subsequently augmented to consider the record from the 1880s to the 1970s. In summary, the project endeavored to present a comprehensive survey of Chivor's history from its rediscovery to the second half of the twentieth century, based principally upon primary contemporaneous materials, divided into two parts. The first installment of this work covers the period from the 1880s to 1925.

were original documents or copies thereof involving the emerald mines in Colombia, largely in materials generated during relevant periods by the German Ministry of Foreign Affairs in Berlin and the German Residency (essentially equivalent to an embassy) in Bogotá.[3] Of a similar nature and also held in Europe were correspondence and related materials in the collections of the Kew National Archives in London, derived from the United Kingdom's Foreign Office.

Principal Colombian materials were found in the form of government publications printed, typically anonymously, in the "Diario Oficial (Colombia)," in the "Gaceta Judicial (Colombia)" of the Corte Suprema de Justicia (Supreme Court), and in the reports of ministries or other government offices. These included legislative texts, decrees, governmental or judicial pronouncements, and statements on petitions and complaints. The Archivo General de la Nación (Colombia) in Bogotá further yielded notarial acts (*escrituras*) and attachments reflecting mine title transfers, sales of shares between various shareholders, and agreements shedding light on the ongoing fluctuations in Chivor ownership and related events.[4]

Europe and the Americas also proved to be sources of collections of a more personal nature, with notable materials being found both in the University Library Freiburg (Universitätsbibliothek Freiburg) archives[5] and in the private holdings of family members. For example, Francisco Restrepo's grandson Eduardo Restrepo Ortega held family documents from the late 1880s to the early 1920s describing many aspects of his grandfather's role with Chivor. Likewise, descendants of Fritz Klein and his brother August, who worked together at Chivor between 1912 and 1914, were in possession of original photos from Colombia and copies of letters written by family members between 1907 and 1920. Unfortunately, the original manuscript for Klein's 1941 book was not located by the present authors. Contributions of this nature from relatives of many key players were instrumental, and their importance cannot be overstated.[6]

Even online resources added to the available contemporaneous data. Noteworthy in this regard were digitized compilations of records detailing transit of persons, such as passenger lists maintained by the United States Immigration Office in New York and by offices in Hamburg and Bremen, Germany, and in Tilbury, London, United Kingdom.[7] Those records detailed information that could incorporate departures and arrivals through national borders, starting points, destinations, and, most importantly, specific dates to help establish or corroborate event time

frames. Similarly insightful were digital archives of newspapers across the United States, which enabled view of events as presented to the public in the early twentieth century.

LOCATION

The Chivor mining area is located northeast of Colombia's capital Bogotá, in proximity to the present-day small municipalities of Somondoco and Almeida to the north and Gachalá and Ubalá to the southwest (figure 3). In the early decades of twentieth century, the nearest community of sufficient size to host a telegraph office was Guateque, accessible via a one-day journey by horse.

The main emerald mines are situated south of the town of Chivor, founded in 1930, between the valleys of the Río Sinai and the Río Rucio, the latter of which flows into the Río Guavio. (The two valleys are alternatively referred to as Quebrada Sinai and Quebrada de las Minas, *quebrada* meaning "gorge" or "breaking reef" in Spanish.) North of the Chivor area are the Río Somondoco and the Río Garagoa. Chivor is now positioned between two large dams that were built in the second half of the twentieth century, the Embalse de Chivor (Chivor Dam) and the Embalse del Guavio (Guavio Dam). The Río Garagoa runs toward the Embalse de Chivor and south of the dam is also called the Río Bata, which in turn flows into the Río Guavio.

---

[3]In the German Federal Archive (Bundesarchiv) in Berlin, pertinent material was found in file R901, archive numbers 1303, 1304, and 1305, all covering the years 1911 to 1920. In addition, file R901, archive number 81190, contained a mining report from 1913 by a member of the German Residency in Bogotá. In the Historical Archive of the German Ministry of Foreign Affairs (Auswärtiges Amt), also in Berlin, principal relevant files were designated RAV Bogotá Volume 50 (now 136) and R Volume 91809, covering the years 1914 to 1936.

[4]Most relevant at the Archivo General de la Nación (Colombia) in Bogotá were several notarial acts (escrituras) designated herein by escritura number and date. Also useful was a file entitled "Minas de Esmeraldas" incorporating materials from 1905 to 1917, collected by the Ministerio de Relaciones Exteriores. Similarly instructive was the file "Joaquin Daza B.," Volume "Propuestas Minas 99," Ministerio de Industrias, Departamento de Minas y Petróleos, which contained documents covering 1929 to 1954 and detailing mine boundaries and history.

[5]Held at the University Library Freiburg ((Universitätsbibliothek Freiburg) was a collection of documents related to Prof. Robert Scheibe, a geologist involved in scientific investigations at and evaluation of Chivor, as detailed below.

[6]See the acknowledgments for additional indication of the scope of such contributions.

[7]MyHeritage.com, Ancestry.com, and Ancestry.de databases. The New York passenger lists record the arrival of United States or foreign citizens, the Hamburg and Bremen passenger lists record departures from Germany, and the London passenger lists record departures of British citizens from the port of Tilbury.
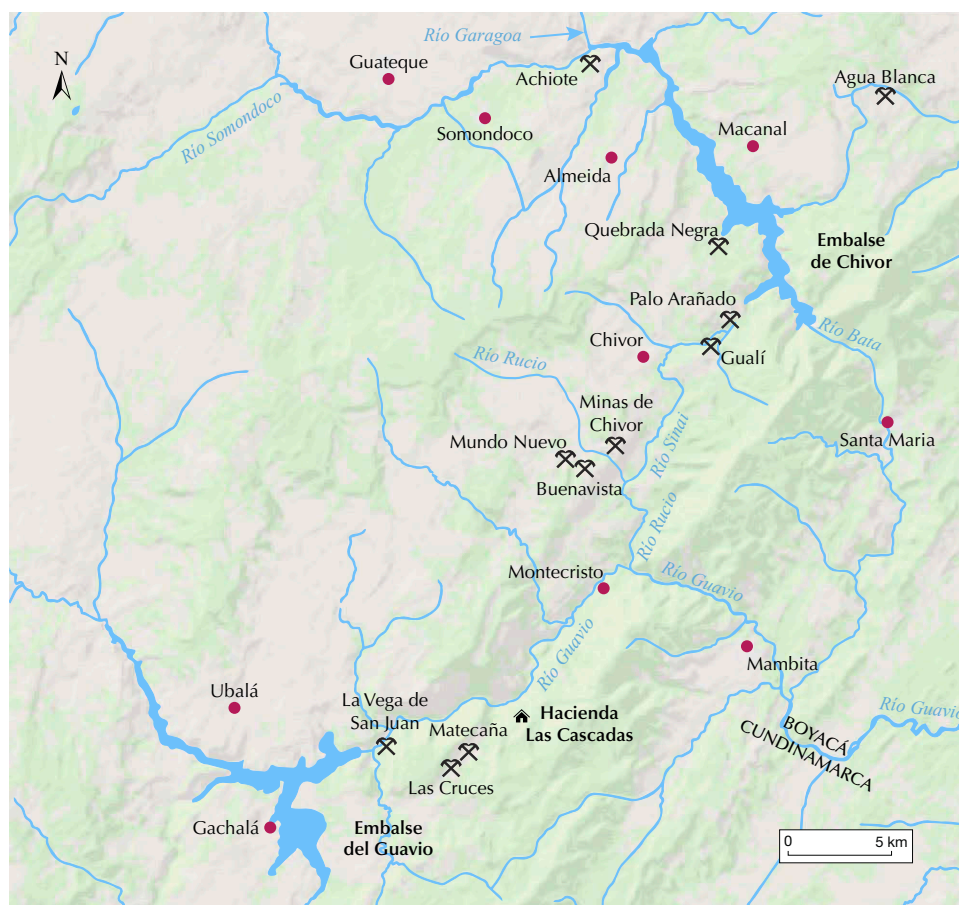
Figure 3. Map showing the location of the Chivor emerald mines, south of the towns of Somondoco and Almeida and northeast of Gachalá and Ubalá, in the Departamento de Boyacá, Colombia. The area is now located between two dams, Embalse de Chivor and Embalse del Guavio, that were built in the second half of the twentieth century. The other emerald mines in the departments of Boyacá and Cundinamarca were discovered and exploited in the twentieth century, subsequent to the rediscovery of Chivor.

The Chivor mining area currently consists of many tunnels and galleries worked employing industrial methods, with production yielding large quantities of gem-quality emeralds.[8] This scenario presents a marked contrast to the harsh working conditions and difficulties encountered in the first half of the twentieth century.

PRE-NINETEENTH CENTURY HISTORY OF THE SOMONDOCO (CHIVOR) EMERALD MINES

Beginning in early April 1536, a Spanish military expedition was conducted under the leadership of conquistador Gonzalo Jiménez de Quesada into the region that later became Nueva Granada (the New Kingdom of Granada, encompassing approximately the territory of modern Colombia).[9] The journey embarked from the Atlantic coastal city of Santa Marta, and by December 1536, the expeditionary group had begun to cross the Andes Mountains. They arrived in the territory of the indigenous Muisca in March 1537. As they traveled south, the Spanish soldiers encountered emeralds in the region, and Quesada ordered the captain Pedro Fernández Valenzuela to search for the mines. Valenzuela departed from Que-

sada's camp in late May or early June 1538 and proceeded as reported in a letter from 1539:

> Valenzuela departed with several others, and after six days they arrived at the said mines, where he and the other Spaniards with him, watched the Indians extract the emeralds from below the ground, and they witnessed such strange new things. The mines are located roughly fifteen leagues from the Valley of the trumpet, in a very high and sparse mountain range. It appears that the emeralds are extracted from an area about one league in size. The lord of the mines is a very principal Indian by the name of Somyndoco [Somondoco]. He is sovereign over many vassals and settlements, and his private residence is located three leagues' distance from the mines…. Those who went on the discovery of the emerald mines said that from the mines they could see some great planes [*llanos*], so marvelous that nothing like them ever had been seen. On hearing this news, Jiménez moved the camp closer to the mines….[10]

A similar account of the discovery of the ancient Somondoco emerald mines appeared, with minor

---

[8]Fortaleché et al., 2017.

[9]Francis, 2007.

[10]Letter from two Spanish captains, July 8, 1539, Archivo General de Indias, Seville, Spain, as translated and published by Francis, 2007. One league was equivalent to 5.57 km. See Lane, 2010.

variations, in all historical descriptions of the conquest of Nueva Granada penned by sixteenth- and seventeenth-century Spanish authors. Examples include those by Fray Pedro de Aguado, Fray Pedro Simón, and Lucas Fernández de Piedrahita.

In the following decades, the mines referred to as Somondoco in contemporaneous Spanish texts were worked with limited success, although a portion of the emerald mining activity was diverted to the Muzo deposits after their discovery to the northwest in the 1560s.[11] Exploitation at Somondoco continued under various owners and lessees[12] into the 1670s, with the last known documentary evidence of activity dated from 1672 to 1675.[13]

Beyond that time, there exists no known record of further activity at the mines, nor is there any report detailing why the mines were abandoned. While the literature refers to an order to close the mines issued by the Spanish monarch Carlos II (reigning 1665–1700),[14] such an order has never been proven and could not be located despite recent extensive research.[15] By 1772 it was noted that the mines of Somondoco were deserted and that nothing more than some vague remains of the old workings could be found.[16] Thus, over the course of more than 200 years beginning in the 1670s, any detailed knowledge about the location of the Somondoco emerald mines was essentially lost.

REDISCOVERY OF CHIVOR

The rediscovery of the historical mines of Somondoco, henceforth known primarily as the Chivor mines, has long been attributed to the Colombian mining engineer Francisco Daniel Restrepo Escobar[17] (1855–1914). Restrepo was born in Rionegro, Antioquia, Colombia, and was involved in the mines of Antioquia during his younger years.[18] By the early 1880s, he had transferred his attention to the neighboring state of Tolima, where he worked as a prospector and mine production manager. At the time, mineral deposits in Antioquia were considered nearly exhausted, while Tolima was viewed as having strong potential for alluvial gold and silver mines. Restrepo's activities in Tolima involved searching for lost mines from the colonial era as well as discovering new mines. During the first half of the 1880s, at least a portion of his work was done in association with the Compañía Minera del Tolima (not to be mistaken with the British Tolima Mining Company, Limited),[19] but from the mid-1880s Restrepo also worked in partnership with Luis Correa. From 1885 to 1887, numerous new deposits, mostly gold and silver mines, were discovered and registered with the government (to establish claims and valid mining titles) by both Restrepo and Correa, either alone or together.[20] Evidence of Restrepo's mining activities in Tolima extends to the end of the decade, with records showing mine tax payments and sales transactions for several gold and silver mines as late as 1889.[21] Conversely, records for the following two decades are silent in that regard, but those from 1910 reflect that Restrepo was still holding mining titles in the area, together with several partners.[22] Meanwhile, as of 1891 Restrepo had apparently resumed efforts back in Antioquia as well.[23]

---

[11]Lane, 2010.

[12]Canova, 1921.

[13]Slave labor at the mines was described in a document from 1672 (Kris Lane, pers. comm., 2018). Litigation in 1672 involving Somondoco mining rights has also been reported (Canova, 1921). Several additional years of activity are supported by archival material from the second half of the seventeenth century in the file "Minas-Boyacá," SC 38, 1, D10, Archivo General de la Nación (Colombia).

[14]Martin de Retana, 1990.

[15]Kris Lane, pers. comm., 2018.

[16]Moreno, 1772, published 1870.

[17]Commonly referred to as Francisco Restrepo, the names Francisco Restrepo Escobar or Francisco Restrepo E. also appear in official documents, with his signature on notarial acts taking the latter form. His year of birth is similarly ambiguous. A death certificate indicates 1853, while passenger lists reflecting his departure from Hamburg and subsequent arrival in New York in November 1913 give an age of 62, implying that he was born in 1851. File F. Restrepo, Hamburger Passagierlisten (list of passengers departing from Hamburg), November 1913, Ancestry.de; File F. Restrepo, List or Manifest of Alien Passengers for the United States Immigration Officer at Port of Arrival, New York, November 1913, Ancestry.com. However, the date 1955 was provided by his grandson. Eduardo Restrepo Ortega, pers. comms., 2018, 2019.

[18]Aguilar, 1884.

[19]Martínez Covaleda and Martínez Covaleda, 1996; Moreno Calderón, 2011.

[20]Diario Oficial (Colombia), 23, No. 7208 (1887), pp. 1194–1195; Esquivel Triana, 2001; Quintero and Centeno, 2007.

[21]Informe presentado al Congreso de la República en sus sesiones ordinarias de 1890 por el Ministro de Hacienda, Segunda Parte – Informes de los administradores departamentales de Hacienda, pp. 219–320; Skinner, 1891–1892; Escritura 556, May 25, 1899, Notaria 3, Archivo General de la Nación (Colombia).

[22]The Compañía de Minas de Los Alpes holding these mining titles was formed in 1910 and reorganized in 1916. Escritura 148, February 3, 1910, Notaria 2, Escrituras 944 and 955, May 2, 1916, Notaria 2, Archivo General de la Nación (Colombia). Restrepo was also involved in the late 1800s and early 1900s in ventures unrelated to mining. For example, through an administrator he operated two haciendas in the district of Paime, south of Muzo, named Santa Teresa and San Luis, which were abandoned during the Colombian civil war. After the war, in 1902, he was active in the coffee trade. Gaceta Judicial (Colombia), 20 (1911), pp. 49–57.

[23]Brissón, 1899.
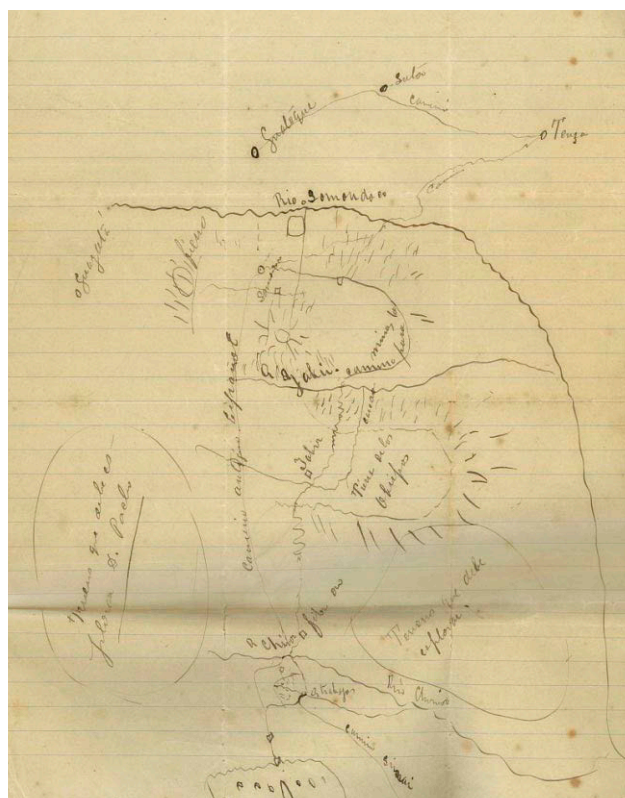
Figure 4. Undated hand-sketched map, from a collection of original documents in the possession of Francisco Restrepo's grandson, of the region south of the town of Guateque and the Río Somondoco in Colombia, incorporating notations regarding already located mines and promising areas for search. Courtesy of Eduardo Restrepo Ortega.

The foregoing regions, however, did not constitute Restrepo's sole focus. The emerald mines in Boyacá designated Chivor 1 and Chivor 2 were registered with the government in 1889, and Restrepo was clearly involved in the process, which comprised multiple steps.[24] The first step in applying for the titles (*acta de aviso*) was undertaken by Miguel Perilla in the names of Restrepo, Enrique González,[25] Bernardo Escovar,[26] and Núñez & Compañía[27] in January 1889. The application was then granted and published in March 1889. Thereafter, at a date and under circumstances not otherwise elucidated, title ownership apparently transferred from the original four applicants to Restrepo and Correa, who were recognized as the owners in documentation from 1896, seven years later.[28]

Nonetheless, two critical aspects regarding Restrepo's underlying rediscovery of the Chivor mines are fraught with discrepancy and ambiguity: the date of the rediscovery and the source of the information on which he relied.

As to the date, Klein (1941) estimates 1903 to 1904. Conversely, Spanish texts place this event in 1896 or even as early as 1888 to 1889,[29] and English-language texts mostly quote 1896.[30] The English texts primarily refer to Latham (1911), but that work offers no corroborative reference to support the 1896 date given. Domínguez[31] (1965), the most detailed Spanish textbook on the history of Colombian emeralds, cites a limited number of geological studies but does not associate historical events with any primary source. The Spanish publication by Martin de Retana (1990) chronicles historical events, but the individual facts are neither consistent nor correlated with the references cited. German authors, in most cases, follow the version and dates given by Klein (1941).

No direct written communication by Restrepo describes his search; the only known tangible evidence of his efforts consists of three rough hand-sketched maps, all undated, found in his personal papers (e.g., figure 4). These merely depict selected areas between Río Somondoco and Río Guavio and mark the locations of already discovered mines and promising sites for search. Nonetheless, a report authored by Klein in 1913 and notes by Prof. Robert Scheibe from 1914 offer verification from contemporaneous primary sources. As will be detailed below, both Klein and the geologist Scheibe spent time with Restrepo at Chivor. In the report by Klein, which was an "ex-

[24]Escritura 201, February 13, 1899, and attachments, Notaria 3, Archivo General de la Nación (Colombia); letter from a department of the Ministerio de Hacienda in Tunja, Colombia, to the Ministerio de Industrias, 1930, file "Joaquin Daza B.," Volume "Propuestas Minas 99," Ministerio de Industrias, Departamento de Minas y Petróleos, Archivo General de la Nación (Colombia).

[25]Enrique González served as director of operations at the Muzo and Coscuez emerald mines in Colombia from 1886 to 1901, first on behalf of Lorenzo Merino and later on behalf of the English Mining Syndicate, Limited. Gaceta Judicial (Colombia), 15 (1901), pp. 169–173; González, 1911.

[26]Also referred to as Bernardo Escobar in several documents, with his signature on notarial acts generally taking the form *Escovar* (used hereinafter).

[27]The background of Núñez & Compañía is vague; subsequent to the reference in the 1889 application, an entity by that name is identified as having been founded in 1895 by four brothers. Escritura 1286, November 30, 1895, Notaria 1, Archivo General de la Nación (Colombia).

[28]Escritura 201, February 13, 1899, and attachments, Notaria 3, Archivo General de la Nación (Colombia).

[29]Domínguez, 1965; Martin de Retana, 1990; Calvo Perez, 1992.

[30]Latham, 1911; Pogue, 1917; Canova, 1921.

[31]Rafael A. Domínguez was head of the financial administration (Interventor de Salinas y Esmeraldas) of the Ministerio de Minas y Petróleos in Bogotá. Memoria del Ministro de Minas y Petróleos al Congreso de 1963 (1963), p. 26.

posé"[32] likely written for potential investors, 1882 was given as the date when indications of the mine's location were found, and 1885 was noted as when the old tunnels worked centuries ago were rediscovered. Scheibe's personal notes[33] discussed the boundaries of the two mines Chivor 1 and 2 in connection with "the work that Restrepo did in the 80s of the last century." Thus, primary and secondary documentation places the search for the lost mines and their rediscovery in the 1880s.

The nature of the collaboration between Restrepo and Correa in the rediscovery remains obscure,[34] but a 1911 letter from Correa to Restrepo lends a degree of corroboration to the 1880s timing. Although the correspondence makes no direct mention of Chivor, it does discuss possible future cooperative ventures and refers back to an event in 1885 when they were "extremely lucky."[35]

Turning to the question of the source of the clues on which Restrepo relied, it is generally reported that he was guided by hints found in historical manuscripts, but further details differ widely. In nineteenth-century descriptions of Colombian history, Acosta (1848), Plaza (1850), and Groot (1869) recounted the expedition of Valenzuela in 1538 and indicated that from the Somondoco mines, or on the journey thereto, great plains (*llanos*) were visible to the east. Other nineteenth-century publications offered even somewhat misleading information such as "nine leguas [leagues] south-south-east of Guateque, close to the cascade of Nagar."[36]

With respect to Spanish authors from the colonial period, the description of Colombia's history by Lucas Fernández de Piedrahita, first published in

Antwerp in 1688, was reprinted in Bogotá in 1881 and, as a consequence, could have been readily available to Restrepo at the beginning of the 1880s.

The historical treatise by Fray Pedro Simón, one of the most prominent authors of the Spanish conquest, has frequently been mentioned as the original source for Restrepo's information. Only the first volume of this five-volume series was published in the seventeenth century, with the complete set edited and printed in Bogotá from 1882 to 1892. The second volume, which contained the description of Valenzuela's 1538 expedition to Somondoco, was published in 1891 from a handwritten manuscript preserved in the Biblioteca Nacional de Colombia (National Library of Colombia) in Bogotá. The original manuscript had been prepared by Simón in the 1620s, and that manuscript or a copy of it had been available and accessible at the national library since 1852, when it came into the collection from the private library of Joaquin Acosta.[37]

Fray Pedro de Aguado, the sixteenth-century chronicler of the Spanish conquest of Colombia and Venezuela, has also been cited as a possible source for Restrepo's information. Aguado's treatise "Recopilación Historial" was never published during the colonial period.[38] The handwritten first volume, concerning Colombia, was discovered in Madrid by Acosta in 1845 and briefly mentioned in his history of Nueva Granada published in 1848. The handwritten manuscript itself, copied in the early years of the twentieth century, was published in Bogotá in 1906. These facts indicate that Aguado's treatise on Colombia was most likely not available to Restrepo in the 1880s.

In summary, the only known information available to guide Restrepo's journey was the vague hint about the llanos being visible from the Chivor mining region (figure 5) and perhaps some approximate indication of distance from the town of Somondoco. This information would have been accessible to him from several sixteenth- and seventeenth-century authors and as repeated in nineteenth-century historical texts. The present authors are aware of neither further handwritten manuscripts from sixteenth- or seventeenth-century historians nor any other detailed accounts or maps that might have identified the location of the ancient Somondoco mines.

MINING TITLE TRANSFERS, MINING COMPANY FORMATION, AND EARLY YEARS (1896–1910)

As previously noted, titles to mines designated Chivor 1 and Chivor 2 were registered in 1889, and by 1896

---

[32]Exposé der Smaragdmine "El Chivor" by Fritz Klein, undated, 16 pp., received by the German Ministry of Foreign Affairs September 13, 1913, and preserved in the German Federal Archive. A portion of this document was translated and published in English by Canova (1921).

[33]Prof. Robert Scheibe collection, University Library Freiburg.

[34]Likewise minimal is information about Luis Correa's life after the Chivor rediscovery. He did, however, remain involved in the emerald business, serving for example as Inspector de las minas de esmeraldas de Muzo & Coscuez. Diario Oficial (Colombia), 42, No. 12693 (1906), p. 630.

[35]Letter from Luis Correa, March 15, 1911, to Restrepo.

[36]Ancizar, 1853; Schuhmacher, 1875. The cascade of Nagar was located close to Macanal but is now covered by the Chivor Dam. *Enciclopedia Universal Ilustrada Europeo-Americana*, 1931; *Geografía económica de Colombia*, 1936. This locality would be about 15 km too far northeast from the present Chivor mines; see also figure 3.

[37]Robinson López, Biblioteca Nacional de Colombia, Bogotá, pers. comm., 2017.

[38]Fals-Borda, 1955; Friede, 1964.

*Figure 5. In all the sixteenth- and seventeenth-century texts that describe the Spaniards' discovery of the Chivor emerald mines—named Somondoco at that time—it was mentioned that great plains (*llanos*) were seen from the mines or on the way to the mines in a view to the east. Courtesy of Kris Lane, Tulane University.*

Restrepo and Correa were recognized as the owners. The registration was made in accordance with the Colombian mining law then in effect, which stipulated that a gem mine could not exceed one square kilometer in size (Law No. 38 of 1887, Article 2).[39] The Chivor emerald mines thus consisted of two contiguous areas of one square kilometer each and were not otherwise split or subdivided during the relevant period. Any mining in the region employed open-pit methods, as was generally the case in Colombia prior to 1930. Although the Chibcha and Spanish in prior centuries may have attempted to build tunnels, even those extended only a few meters into the mountains.

At the Chivor claims, no mining activity took place for several years after registration. The 1891 annual taxes for the two mines were paid by Correa,[40] but no further payments are known. As a result, Chivor 1 and 2 were declared "abandoned" on August 23, 1896, on account of an absence of operations in the seven years since the registration and a failure to pay taxes on the mines since 1891.[41] Attendant legal formalities led to the titles being transferred from Correa and Restrepo to González on February 16, 1898.[42]

Later in 1898, a mining entity was formed as a joint stock company between González, Restrepo, Escovar, and Núñez & Compañía, but without Correa, and the Chivor 1 and 2 mining titles were transferred from González to that company.[43] Share distribution at formation was as follows: 40 shares for Restrepo, 20 for González, 20 for Escovar, and 20 for Núñez & Compañía. The latter two were to act as investors, while Restrepo and González, both of whom had mining experience, were to continue exploration and to start practical operations. The company later became known as the Compañía de las Minas de Esmeraldas de Chivor,[44] or, in certain materials, Sociedad Ordinaria de las Minas de Chivor. For clarity, the different companies involved in the Chivor emerald business are listed in table 1.

In 1898 and likely into the next year, Restrepo spent time at the mine, mainly supervising restoration and construction of a water supply and irrigation system. These efforts aimed to evaluate the potential of the deposit and to prepare the mine for visits by possible investors, looking for veins and samples in

---

[39]Bullman, 1892.

[40]Diario Oficial (Colombia), 28, No. 8842 (1892), p. 819.

[41]Escritura 201, February 13, 1899, and attachments, Notaria 3, Archivo General de la Nación (Colombia).

[42]Escritura 201, February 13, 1899, and attachments, Notaria 3, Archivo General de la Nación (Colombia); Report by Dr. Antonio José Cadavid, March 18, 1913, Historical Archive of the German Ministry of Foreign Affairs.

[43]Escritura 1337, August 20, 1898, Notaria 3, Archivo General de la Nación (Colombia). No name for the company was specified at that time.

[44]The name appeared in documents and reports of the Ministerio de Hacienda and the German Resident in Bogotá.

TABLE 1. Companies related to the Chivor 1 and 2 emerald mines in Colombia.

Company Name	Formation Date Registration Date	Incorporators and Agents in Colombia	References
Compañía de las Minas de Esmeraldas de Chivor; Sociedad Ordinaria de las Minas de Chivor[a]	August 20, 1898 *(Formation in Colombia)*	Francisco Restrepo, Enrique González, Bernardo Escovar, Nuñez & Cía.	Escritura 1337, August 20, 1898, Notaria 3
Syndikat El Chivor	February 14, 1914 *(Formation in Germany)*	August Stauch, Hjalmar Schacht, Rudolf Hahn & Sons, Fritz Klein	Historical Archive of the German Ministry of Foreign Affairs
Colombian Emerald Syndicate, Ltd.	June 22, 1918 *(Formation in U.S.)* May 7, 1920 *(Registration in Colombia)*	S.J. Nathan, Edgar W. Ward, J.E. Cochrane, M.F. O'Dell, F. A. Daly *Agent: Miguel S. Uribe Holguin*	State of Delaware, Department of State, Division of Corporations Escritura 1402, May 7, 1920, Notaria 1
Colombian Chivor Emerald Company Compañía Colombiana de Esmeraldas de Chivor *(Operating company of the Colombian Emerald Syndicate)*	July 6, 1920 *(Formation in Colombia)*	Wilson E. Griffiths, Carl K. MacFadden Directors: Carl K. MacFadden, Nathaniel W. Ross, William M. Schaill *Agent: Miguel S. Uribe Holguin*	Escritura 2041, July 6, 1920, Notaria 1
Chivor Emerald Corporation	March 6, 1924 *(Formation in U.S.)* February 16, 1925 *(Registration in Colombia)*	Samuel C. Wood, Harry C. Hand, Raymond J. Gorman *Agent: Miguel S. Uribe Holguin*	State of Delaware, Department of State, Division of Corporations Escritura 344, February 16, 1925, Notaria 1
Colombia Emerald Development Corporation *(Operating company in U.S. and Colombia, connected to the Chivor Emerald Corporation)*	November 7, 1924 *(Formation in U.S.)* July 11, 1925 *(Registration in Colombia)*	Edmund J. MacNamara, Ernest W. Brown, William B. Anderson *Agent: Miguel S. Uribe Holguin*	State of Delaware, Department of State, Division of Corporations Escritura 1607, July 11,1925, Notaria 1
Chivor Emerald Mines, Inc. *(Change of name from the Colombia Emerald Development Corporation)*	September 28, 1933 *(Change of name in U.S.)* November 17, 1934 *(Change of name registered in Colombia)*	*Agents (1920–1970): Miguel S. Uribe Holguin Hernando Uribe Cualla Eduardo Torres R.*	State of Delaware, Department of State, Division of Corporations Escritura 2045, November 17, 1934, Notaria 1

[a]Both names were used interchangeably in various documents between 1908 and 1921.

the process. Emerald samples were sent to Europe to attract investors (e.g., major European banks), and an estimated price of £40,000 was suggested in early negotiations.[45] However, no deal culminated before outbreak of the Colombian civil war (October 1899–November 1902) stopped all activities at the mine. Meanwhile, controversy had also developed over the water supply, as the irrigation canal ran across private land owned by the local Acosta family, and available water was also used for a nearby hacienda.[46]

In the following era, activities pertaining to Chivor tended to be more financial than operational in nature. Tax payments, share transfers, and investment pursuits featured heavily, while mining was relatively minimal. Annual taxes for Chivor 1 and 2 were paid by González in 1898, 1899, and 1900 at the

rate of 5 pesos per mine per year. Taxes for the mines were then paid for 20 years in advance, at the rate of 100 pesos per mine, by Antonio Núñez of Núñez & Compañía on behalf of the shareholders.[47]

[45]Letter from Núñez & Compañía, December 16, 1898, to Restrepo. Lorenzo Merino, who had recently completed a ten-year lease of the Muzo emerald mines (1886–1896), was involved in the discussions.

[46]Letters by Núñez & Compañía, June 18 and June 23, 1898, to Restrepo.

[47]Escritura 1242, December 3, 1901, Notaria 3, Archivo General de la Nación (Colombia). See also Reports by the German Resident in Bogotá, Dorotheus Kracker von Schwartzenfeldt, November 16, 1912, and by a member of the German Residency in Bogotá, Wilhelm Gerlach, November 15, 1912, German Federal Archive; Diario Oficial (Colombia), 48, No. 14720 (1912), pp. 812–813; Report by Dr. Antonio José Cadavid, March 18, 1913, Historical Archive of the German Ministry of Foreign Affairs; Domínguez, 1965.

TABLE 2. Transfers of shares of the Compañía de las Minas de Esmeraldas de Chivor between 1899 and 1909.

Escritura 1337, August 20, 1898, Notaria 3: 100 shares are issued and distributed among 4 shareholders as follows: Restrepo 40, González 20, Escovar 20, Núñez & Compañía 20

Vendor	Buyer	Number of shares	Total Price	Approximate price per share in pesos oro[a,c]	Escritura (notarial act), Archivo General de la Nación (Colombia), Bogotá
Francisco Restrepo	Carlos Uribe	15	1,000 £ ≙ 5,000 pesos oro	333	Escritura 189, February 13, 1899, Notaria 3
Francisco Restrepo	Carlos Uribe	2	4,000 pesos paper	600	Escritura 868, June 13, 1899, Notaria 3
Francisco Restrepo	Álvaro Uribe	2	4,000 pesos paper	600	Escritura 908, June 16, 1899, Notaria 3
Francisco Restrepo	Diódoro Sánchez	1	2,000 pesos paper	200	Escritura 100, March 27, 1900, Notaria 5
Enrique González	Christopher Dixon	1	5,000 pesos paper	500	Escritura 915, December 7, 1900, Notaria 3
Enrique González	Christopher Dixon	1	25,000 pesos paper	500	Escritura 1201, November 21, 1901, Notaria 3
Álvaro Uribe	Christopher Dixon	1	48,000 pesos paper	320	Escritura 108, March 9, 1902, Notaria 3
Francisco Restrepo	Eduardo Sayer Vega	1	25,000 pesos paper	167	Escritura 109, March 10, 1902, Notaria 3
Carlos Uribe	Fould & Compagnie	17	2,000 £ ≙ 10,000 pesos oro	588	Escritura 1848, October 10, 1905, Notaria 2
Francisco Restrepo	Emiliano Isaza	3	10,000 pesos paper	33	Escritura 758, October 28, 1905, Notaria 3
Eduardo Sayer Vega	Lisandro Moreno	1	30,000 pesos paper	300	Escritura 851, December 4, 1905, Notaria 3
Lisandro Moreno	Eduardo Sayer Vega	1	30,000 pesos paper	300	Escritura 134, March 7, 1906, Notaria 3
Núñez & Compañía	Fould & Compagnie	20	400 £ ≙ 2,000 pesos oro[b]	100	Escritura 1834, December 17, 1907, Notaria 2
Eduardo Sayer Vega	Luis Francisco Moreno	1	64,000 pesos paper	640	Escritura 749, October 15, 1908, Notaria 3
Luis Francisco Moreno	Emiliano Isaza	1/2	22,500 pesos paper	450	Escritura 174, March 20, 1909, Notaria 3
Luis Francisco Moreno	Francisco Restrepo	1/2	22,500 pesos paper	450	Escritura 174, March 20, 1909, Notaria 3

[a]Conversion factors used for pesos oro:pesos paper are 1:3.33 (1899), 1:10 (1900), 1:50 (1901), 1:150 (1902), 1:100 (1905 and later). With a total of 100 shares outstanding, 1 share represents 1% ownership of the company (see footnote 48 in text).

[b]Núñez & Compañía sold multiple assets, not only shares in Compañía de las Minas de Esmeraldas de Chivor, to Fould & Compagnie.

[c]The price for 90% of the mine offered to F. Klein in 1914 was £51,000 ≙ 255,000 pesos oro; the value for 1% of the mine (equivalent to 1 share) would be calculated at 2,833 pesos oro.

The sale price for the mine and the land to W.E. Griffiths and C.K. MacFadden in 1919 was £46,000 ≙ 230,000 pesos oro; the value for 1% of the mine (equivalent to 1 share) would be calculated at 2,300 pesos oro.

A lively trade in shares of the Compañía de las Minas de Esmeraldas de Chivor also took place during the first decade from 1899 to 1909, and examples of these transactions are summarized in table 2.[48] A notable series of transfers began in 1899 when Restrepo sold 15 shares to Carlos Uribe,[49] who in turn sold 17 shares in 1905 to Fould & Compagnie, a Parisian bank.[50] Two years later, in 1907, Fould & Compagnie became the majority shareholder upon acquiring an additional 20 shares from Núñez & Compañía.[51] Other individuals who would play a role

[48]Conversion factors reflected in certain documents indicate £1 sterling ≙ 5 pesos oro. At the time of the civil war (1899–1902), inflation caused rapid change in the exchange rate of the gold peso (peso oro) to paper currency, for example: 1:10 (1900), 1:50 (1901), 1:189 (October 1902), and 1:260 (1902/1903). After the war, the value of the paper currency stabilized, and in 1904, the exchange rate was fixed by the government at 1:100. Mitteilungen des Deutsch-südamerikanischen und Iberischen Instituts, 3 (1915), p. 198; Bürger, 1919; Eder, 2017.

[50]Escritura 1848, October 10, 1905, Notaria 2, Archivo General de la Nación (Colombia).

[51]Escritura 1834, December 17, 1907, Notaria 2, Archivo General de la Nación (Colombia).

Figure 6. Dr. Emiliano Isaza Gutiérrez—lawyer, scientist, politician, diplomat, and minister—was one of the most prominent shareholders in the Compañía de las Minas de Esmeraldas de Chivor. He cooperated with Klein in the 1910s but as president sold the company in 1919 to American interests. Courtesy of Banrepcultural, Bogotá.

then taken in March 1904, when Alvaro Uribe was authorized for a nine-month term to search for a foreign entity, especially in France and England, to lease Chivor for an estimated price of £10,000.[57] As to the apparent lack of success of such efforts, the United States Consul-General in Bogotá, Snyder, wrote in 1904: "The prohibitively high price asked by the owners of these five mines, called the 'Chivor group' is the reason, I am informed, that they are not being worked."[58]

Meanwhile, a few months before the end of the civil war, Restrepo had left Colombia. He arrived in Quito, Ecuador, in June 1902, accompanied by his older son Anibal and two other Colombians. In Ecuador, Restrepo worked on government projects such as road and railway construction, and he was involved in gold mining in the Oriente region as owner and/or supervisor of several gold mines.[59] In early 1904, Restrepo was asked to return to his home country because there was urgent need of an experi-

in Chivor's history likewise became involved as shareholders during this period, such as the English businessman and miner Christopher Ernest Dixon (1868–1961; see box A), who purchased three shares between 1900 and 1902,[52] and Dr. Emiliano Isaza Gutiérrez (figure 6),[53] who acquired three shares in 1905[54] and would later become president of the Compañía de las Minas de Esmeraldas de Chivor. Prices for one share in paper currency increased from 2,000 pesos in 1900 to 64,000 pesos in 1908, but the inflation factor impacting paper currency changed markedly during the Colombian civil war (again, see table 2).[55] The values of different Colombian and foreign currencies are compared in table 3.

Throughout the same period, the mine owners continued seeking foreign investment or participation. In November 1901, Dixon was authorized for a term of six months to attempt to form a company in Europe that would be responsible for organizing and operating the emerald mines.[56] A different tack was

[52]Escritura 915, December 7, 1900, Notaria 3, Escritura 1201, November 21, 1901, Notaria 3, and Escritura 108, March 9, 1902, Notaria 3, Archivo General de la Nación (Colombia).

[53]Dr. Emiliano Isaza Gutiérrez (1850–1930) studied law and political science, becoming a professor at the University of Antioquia in 1875. In 1876 he moved to Bogotá. Throughout his career, he authored a number of academic publications, including a classic Spanish grammar textbook *Gramática Práctica de la Lengua Castellana* (1880), and he served Colombia in various diplomatic capacities, such as plenipotentiary minister in Ecuador and as minister of public instruction in the homeland (1908–1909). See Martínez, 1950.

[54]Escritura 758, October 28, 1905, Notaria 3, Archivo General de la Nación (Colombia).

[55]For comparison, monthly salaries at the Muzo emerald mine in 1904 were 30,000 pesos paper (300 pesos oro) for the director and 3,000–4,000 pesos paper (30–40 pesos oro) for the foreman or other staff. Junta Nacional de Amortización, Informe al Congreso y al Gobierno Ejecutivo 1904, p. 62.

[56]Escritura 1172, November 12, 1901, Notaria 3, Archivo General de la Nación (Colombia).

[57]Escritura 172, March 5, 1904, Notaria 3, and Escritura 193, March 16, 1905, Notaria 3, Archivo General de la Nación (Colombia).

[58]*Bulletin of the International Bureau of the American Republics*, Vol. 18 (1904), pp. 858–859.

[59]Restrepo's activities in Ecuador between 1902 and 1904 are well documented in newspaper articles, contracts, reports, and letters remaining in the possession of his family.
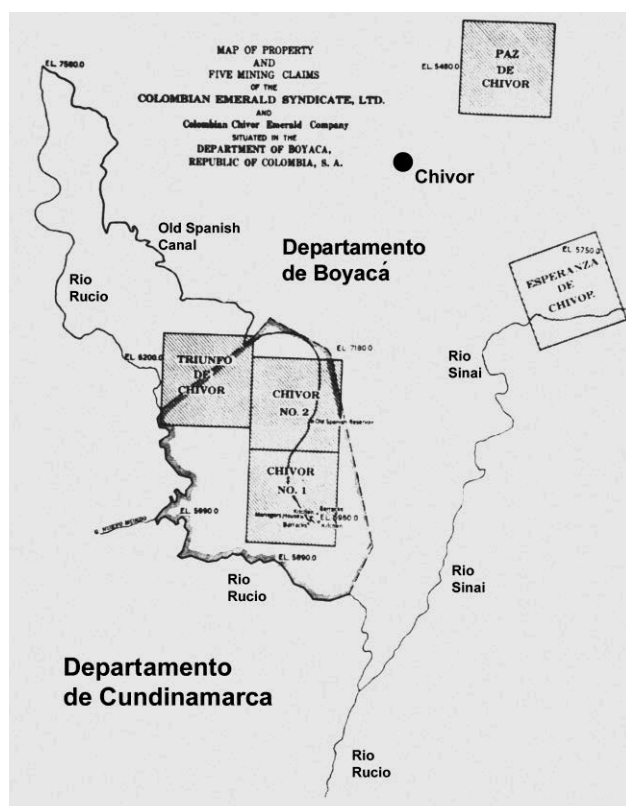
Figure 7. Map published in 1921 showing the location of the Chivor 1 and 2 emerald mines between the valleys of the Río Rucio and the Río Sinai in the Departamento de Boyacá, near the boundary with the Departamento de Cundinamarca. The mining titles for Chivor 1 and 2, measuring one square kilometer each, were registered in 1889 to Francisco Restrepo and partners; three additional mining titles were registered in 1904 for the Triunfo de Chivor, Paz de Chivor, and Esperanza de Chivor claims. After Canova (1921), representing the mine boundaries as assumed by the Colombian Emerald Syndicate, Ltd.; the town of Chivor was added. Note: In a map prepared by the Ministerio de Minas y Petróleos in 1941, Paz de Chivor and Esperanza de Chivor are located much closer to Chivor 1 and 2, at a distance of approximately 1 km.

Figure 8. Satellite photo of the region between the valleys of the Río Rucio and the Río Sinai where the areas covered by the mining titles for Chivor 1, Chivor 2, and Triunfo de Chivor are located. The area is situated in the Departamento de Boyacá, near the boundary with the Departamento de Cundinamarca (yellow line), which runs partly along the Río Rucio valley. Modified from Google Earth; the town of Chivor and the labeling were added.

enced miner to direct the Muzo emerald mines. Restrepo began in that position in March 1904.[60]

The year 1904 also saw a widening of the focus for investment activities pertaining to Chivor, beyond the existing two claims. On August 25, 1904, Restrepo, González, Escovar, Carlos Uribe, and Núñez & Compañía purchased land in the Chivor area, between Río Rucio and Río Sinai, from Aurelio Ruedo Acosta.[61] The purchase price was 100,000 pesos, and 20,000 pesos were paid by each of the five principal shareholders. Thereafter the Compañía de

las Minas de Esmeraldas de Chivor was treated as the owner of the Chivor 1 and 2 mining titles and of land in the area. Through this purchase, the mine owners resolved with the Acosta family the controversy over the water supply that had plagued the site since the late 1890s.

On December 13, 1904, three additional mining titles were registered in the vicinity of Chivor 1 and 2: "Triunfo de Chivor," "Paz de Chivor," and "Esperanza de Chivor" (figures 7 and 8), with Restrepo, Henrique Campo, and Dixon named as the co-owners.[62] From that time, the five mining titles in the

[60]El Ecuador. Guía Comercial, Agrícola, e Industrial de la República (1909), Guayaquil, Compañía "Guía del Ecuador," pp. 243–251; Ochoa Ortiz, 1921.
[61]Escritura 1479, August 25, 1904, Notaria 2, and Escritura 3084, December 27, 1919, Notaria 1, Archivo General de la Nación (Colombia).
[62]Diario Oficial (Colombia), 48, No. 14720 (1912), pp. 812–813.

BOX A: CHRISTOPHER DIXON'S LEGACY IN COLOMBIAN EMERALD MINING

Figure A-1. Christopher Dixon worked on behalf of the English Mining Syndicate, Limited, when the company operated the Muzo mine during the 1890s and early 1900s. Dixon later became one of the shareholders in the Compañía de las Minas de Esmeraldas de Chivor that owned the mining titles for Chivor 1 and 2. After the mine was sold in 1919 to the U.S.-based Colombian Emerald Syndicate, Ltd., he served as its official representative in Colombia in the early 1920s. Photo circa 1900, public domain.

Christopher Ernest Dixon was born in 1868 in Watlington, Oxfordshire, England, the eleventh of Dr. Henry and Helen Dixon's twelve children. In the mid to late 1880s, he traveled to South America along with his brother Frank (1865–1956) to join an elder brother George (1861–1911), who had been prospecting for gold and silver in the state of Tolima, in central Colombia, since 1884.[1]

Although the activities and precise whereabouts of the two younger Dixon brothers during their early years in Colombia[2] remain obscure, by 1889, at the age of 21, Christopher (figure A-1) was already operating at least 24 gold and silver mines in the Mariquita area, in northern Tolima.[3] During this period, George worked for British mining companies at the Silencio mine, in central Tolima and elsewhere.[4] Over the course of the 1880s, Tolima had become a mining bonanza for gold and silver seekers, attracting prospectors and investors from neighboring Antioquia, as well as many foreigners. During his seven-year stay in Colombia, George might also have been involved in emerald prospecting and mining at Muzo, as suggested by photos from the family album (figures A-2 and A-3).[5]

Although Christopher Dixon would become most known for his activities with emerald, he was always looking for new commercial opportunities and was active across a variety of sectors throughout his career. In 1891, he became associated with the "Magdalena Estates Company," a real estate development venture.[6] In the 1892 to 1893 period, he and his brother Frank obtained grants to parcels of public land in northern Tolima and Caldas.[7] In 1910, he was named administrator of the "H. and U. Rubber and Coffee Estates, Limited."[8] Then, in 1916, Dixon turned to cattle breeding, already an important industry in Colombia, and planned to build a new meat-packing plant on the Caribbean coast.[9]

The earliest known reference to emeralds in Dixon's career is from 1896, when he became an agent of the English Mining Syndicate, Limited, a British company operating the Muzo mines, a position he held until October 1900.[10] The early 1900s then found Dixon buying shares in the Compañía de las Minas de Esmeraldas de Chivor (see the main text) and being involved in various other activities around Chivor.

Meanwhile, in August 1898, preliminary applications for three additional mining claims in the Chivor area had been filed by Francisco Restrepo and various partners.[11] Such action was taken contemporaneously with when Restrepo was involved at Chivor in efforts to restore the water supply. The three mining claims later became known as El Triunfo de Chivor, La Paz de Chivor, and La Esperanza de Chivor.

[1]*Transactions of the Institution of Mining and Metallurgy*, Vol. 21 (1912), p. 723.

[2]The arrival of three members of the Dixon family in Colombia in 1886 is documented in the Diario Oficial (Colombia), 22, No. 6836 (1886), p. 1114, but further information as to identities is unavailable.

[3]Informe presentado al Congreso de la Republica en sus sesiones ordinarias de 1890 por el Ministro de Hacienda, Casa Editorial de J.J. Pérez, Bogotá, 1890.

[4]Skinner, 1889–1890, 1891–1892.

[5]Simon Hamilton (great-grandson of George Dixon), pers. comm., 2018.

[6]*The Mining Journal, Railway and Commercial Gazette*, Vol. 61 (1891), p. 851.

[7]Informe del Ministro de Hacienda de la Republica de Colombia al Congreso Constitucional de 1894, p. 101; LeGrand, 1988.

[8]*India-Rubber Journal*, Vol. 43 (1912), p. 21.

[9]Memoria del Ministro de Agricultura y Comercio al Congreso de 1918, pp. 173–177.

[10]Atuesta, 1899; Escritura 314, October 31, 1900, Notaria 3, Archivo General de la Nación (Colombia); Gaceta Judicial (Colombia) 15 (1901) pp. 169–173 and 16 (1903) pp. 78–79; Céspedes Cubides, 2017.

[11]Diligencia No. 2, Municipality of Macanal, August 8, 1898; Aviso No. 81, Municipality of Ubalá, August 21, 1898; Aviso No. 82, August 21, 1898, Municipality of Ubalá.

Figure A-2. View of the landscape of the Muzo area, from the family album of George Dixon, taken before 1890, with the handwritten comment reading: "A picturesque native bridge across stream. Road leading to Muzo mines." Courtesy of Simon Hamilton.

Figure A-3. A bridge in the Muzo area, from the family album of George Dixon, taken before 1890, with the handwritten comment reading: "Another rustic bridge, close to Muzo mines. Indian miners bidding adieu to their wives, no women are permitted to enter the establishment or to pass beyond a given boundary." Courtesy of Simon Hamilton.

As shown in a map by Canova (1921), El Triunfo de Chivor adjoined directly to Chivor 1 and 2, situated between the valleys of the Río Rucio and the Río Sinai (see figure 7 of the main text). La Paz de Chivor and La Esperanza de Chivor were located northeast and southeast, respectively, of the current town of Chivor. No indication exists as to why these three particular locations were chosen for claims—it is possible that emerald samples and/or former native or Spanish workings (tunnels) had been discovered by prospecting or other activities in the areas and that the claims were defined so as to cover mining rights over those regions. Regardless, and for reasons otherwise not elucidated but perhaps impacted by the outbreak of the Colombian civil war (The Thousand Days' War, 1899–1902), the registration process was not completed, and no mining claims were officially granted.

After the war and Restrepo's return to Colombia from a sojourn in Ecuador (see main text), the registration process was restarted. A February 1904 agreement between Henrique Campo (a Swiss citizen),[12] Dixon, and Restrepo set forth the conditions under which the they would join in new applications for the three claims, namely, that ownership would be divided equally among the three partners (figure A-4). The applications were then filed in September 1904,[13] and the three mining titles were granted on December 13 of that year,[14] with annual taxes being paid in advance for the period through 1910.[15] Approximately one week later, on December 19, 1904, the three owners formally granted Dixon a power of attorney covering all future matters related to the three claims.[16]

Consistent with what had generally transpired to that point with respect to Chivor 1 and 2, focus for the newly acquired claims centered on investment pursuits rather than practical mining. The 1905 to 1906 and 1915 to 1916

periods in particular saw flurries of activity in this regard, with Dixon engaged in extensive correspondence and even travel to England[17] in the search for investors. Paralleling these efforts was Dixon's long-running battle against the change in Colombian mining laws that had taken effect in 1905 (Law No. 40 of 1905), restricting applications for new emerald mines and increasing the tax burden on existing mines. A complaint was lodged against the Colombian government, and Dixon, supported by British officials in Bogotá, embarked on a multiyear quest to establish that he had been harmed by the change and was entitled to recompense from Colombia.[18]

Dixon's allegations centered on concerns that the higher taxes would prevent profitable mining and should not be applied to titles granted before 1905 and that the uncertain and detrimental situation for mine owners had

[12]Also referred to as Enrique Campo in several documents, with his signature on notarial acts generally taking the form of Henrique Campo (used hereinafter).

[13]Letter from Christopher Dixon, December 3, 1904, to Restrepo.

[14]Diario Oficial (Colombia), 48, No. 14720 (1912), pp. 812–813.

[15]Foreign Office, Political Departments, General Correspondence from 1906 to 1966, Colombia: Code 11, Files 47 - 6847 and 904, The National Archives, Kew, London.

[16]Escritura 2326, December 19, 1904, Notaria 5, Archivo General de la Nación (Colombia).

[17]File Christopher Dixon, Names and Descriptions of British Passengers Embarked at the Port of Tilbury, January 13, 1915, MyHeritage.com.

[18]Foreign Office, Political Departments, General Correspondence from 1906-1966, Colombia: Code 11, Files 47 - 6847 and 904, The National Archives, Kew, London.
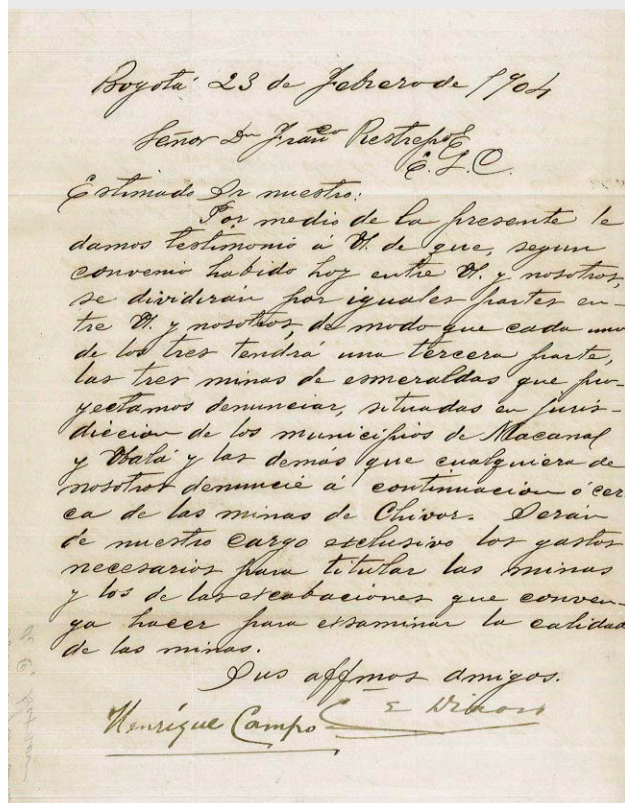
Figure A-4. A letter dated February 23, 1904, from Henrique Campo and Christopher Dixon to Restrepo memorialized an agreement under which the three would join in applying for the three additional claims in the Chivor area, sharing ownership equally and with all expenses paid by Dixon and Campo. Courtesy of Eduardo Restrepo Ortega.

caused potentially interested investors to turn away.[19] His assertions also apparently became increasingly exaggerated as the contest went on, with documents prepared by British officials even giving Dixon credit for having discovered the three mines.[20] In negotiations he offered to settle by selling the mines to the Colombian government for £200,000 but was asked to prove the value of the claims through an international expert.[21] He failed to do so and instead continued paying annual taxes for the three mines up through 1922.[22]

By 1920, Dixon had been named as the Colombian manager for the Colombian Emerald Syndicate, Ltd., the American company that had just taken over the Chivor 1 and Chivor 2 mines (see main text). From this date onwards, the historical record about the three other claims

of the so-called Chivor group is incomplete regarding specifics of any pertinent ownership transfers, and the few references are disjointed, if not contradictory, although all five mines eventually came to be considered in part or in full under the purview of the American company.[23]

Following his involvement with the Colombian Emerald Syndicate, Ltd., Dixon left the mine for a period but returned in the early 1930s to help Peter W. Rainier, then the administrator at the mine, fight attacking bandits.[24] Later, he also cooperated with Rainier during field work at the Coscuez emerald deposit.[25]

Dixon remained in Colombia with his wife and children. His last known assignment was in the mid-1940s, as one of the participants in geological investigations carried out in Colombia by the Foreign Economic Administration, in cooperation with the United States Geological Survey.[26] In the last years of his life, Dixon was celebrated in the U.S. as an authority on emerald mining.[27] He died in Bogotá in 1961, and some of his descendants still live in Colombia. He will be remembered for the legacy he left in the history of Chivor and in the modern history of Colombian mining at large.

[19]Ibid.

[20]Ibid.

[21]File "Minas de Esmeraldas," Ministerio de Relaciones Exteriores, Archivo General de la Nación (Colombia).

[22]Diario Oficial (Colombia), 50, No. 15279 (1914), p. 396; Diario Oficial (Colombia), 51, No. 15557 (1915), p. 448; Diario Oficial (Colombia), 54, No. 16306 (1918), p. 121; Diario Oficial (Colombia), 58, No. 18425–18426 (1922), p. 243.

[23]For example, a 1920 listing of Restrepo's assets at the time of his death in 1914 included a one-third share in each of the three newer mines. Escritura 188, January 27, 1920, Notaria 3, Archivo General de la Nación (Colombia). In 1921, it was represented that the titles to all five mines of the Chivor group were under the ownership or control of the Colombian Emerald Syndicate, Ltd., or its operating entity the Colombia Chivor Emerald Company. Canova, 1921. Concomitant with the bankruptcy of the Colombian Emerald Syndicate in 1923, its assets were stated to incorporate complete ownership of Chivor 1 and 2 and one-third of the three newer claims. Jewelers' Circular, Vol. 87, No. 22 (1923), p. 91. Annual payments of taxes for the three claims were made from 1929 to 1931 by Pedro Ignacio Uribe, a Colombian entrepreneur and public figure (as well as founder of the "Compañía Colombiana del Petróleo" in 1918 along with Wilson E. Griffiths and Carl K. MacFadden). Diario Oficial (Colombia), 54, No. 16364 (1918), p. 56; Diario Oficial (Colombia), 65, No. 21072 (1929), p. 191; Diario Oficial (Colombia), 65, No. 21275 (1929), p. 780; Diario Oficial (Colombia), 67, No. 21674 (1931), p. 189.

[24]See main text, Part II, and Rainier, 1942.

[25]Rainier, 1933.

[26]Singewald, 1950.

[27]Lancaster Eagle-Gazette, July 2, 1951, p. 14.

Figure 9. Handwritten register reflecting the ownership distribution of shares in the Chivor 1 and 2 emerald mines before and after a stock split between 1909 and 1912 that increased the capital from 100 to 250 shares. The participants and their holdings remained unchanged until the mines were sold in December 1919 to an American group. Courtesy of Eduardo Restrepo Ortega.

Chivor area were occasionally referred to collectively as the Chivor group (see also box B),[63] but ownership of the three mining claims registered in 1904 and that of Chivor 1 and 2 remained, at least before 1920, formally separate (see also box A).

Yet, in stark contrast to the ongoing financial and investment maneuvers, practical mining activities were nearly nonexistent. As noted above, prior to the onset of the civil war, initial steps to clean old infrastructure and restore the water supply were undertaken,[64] but endeavors were curtailed by the conflict. The decade after the war then saw Restrepo, one of the key participants with practical mining experience, either out of the country (in Ecuador) or occupied with other ventures (Muzo). With Restrepo thus unavailable and the majority of the other shareholders focused on selling the mine, there was little incentive to invest further in operations.

By 1909, the shares were distributed among Fould & Compagnie, six Colombians (mostly lawyers or engineers), and Dixon.[65] Then, between March 1909 and October 1912, a stock split increased the capital from 100 to 250 shares (figure 9).[66] By the time of the 1919 sale discussed below, ownership was distributed as follows: 92½ shares for Fould & Compagnie, 50 for descendants of Escovar, 45 for González, 41¼ for the widow and descendants of Restrepo, 8¾ for Isaza, 7½ for Dixon, 2½ for Álvaro Uribe, and 2½ for Diódoro Sánchez (figure 9).[67]

ACTIVITIES AT MUZO

As alluded to previously, the year 1904 also witnessed relevant activity connected to the Muzo mines and to the broader Colombian emerald story that included Chivor. The important mines at Muzo, as well as at Coscuez, had been owned by the Colombian government since 1886. Nonetheless, the mines were often leased to private operators against predetermined charges, and those tenants might even sublease to another individual or company. There were also repeated cycles of inactive periods.[68]

After the civil war, an entity known as the Sindicato de Muzo (Syndicate of Muzo, used hereinafter) was founded and took over exploitation of the Muzo mines from 1904 to 1909.[69] Restrepo was named as director, and his son Anibal joined the mine's payroll as well.[70] Toward the end of that period, in December 1908, it was agreed between the government of Colombia, the Syndicate of Muzo, and the London-based Colombian Emerald Company that the right to mine at Muzo from March 1909 would pass to the Colombian Emerald Company.[71] Restrepo remained in his position until resigning in December 1909, expressing in a letter to the Colombian president that he did not agree with the new company's policies.[72] The offered justification was that such policies were contrary to the interests of the Colombian nation.

The contract with the Colombian Emerald Company was to last for more than 20 years, but it was terminated by the government after just 14 months, in May 1910.[73] Mining operations were taken over by

[63]For other mines that have been erroneously associated with Chivor, see also box B.

[64]See also *Bulletin of the International Bureau of the American Republics*, Vol. 28 (1909), pp. 1027–1039.

[65]Escritura 3084, December 27, 1919, Notaria 1, Archivo General de la Nación (Colombia).

[66]Diario Oficial (Colombia), 48, No. 14720 (1912), 812–813; Escritura 3084, December 27, 1919, Notaria 1, Archivo General de la Nación (Colombia).

[67]Escritura 3084, December 27, 1919, Notaria 1, Archivo General de la Nación (Colombia).

[68]Informe del Ministro de Hacienda al Congreso de 1922, pp. 24–29.

[69]Diario Oficial (Colombia), 49, No. 15043 (1913), p. 3221.

[70]Junta nacional de Amortización, Informe al Congreso y al Gobierno Ejecutivo 1904, p. 60; Revista del Ministerio de Obras Públicas, 4 (1909), p. 49; Domínguez, 1965.

[71]*Bulletin of the International Union of the American Republics*, Vol. 29 (1909), pp. 1120–1121; Montaña, 1915.

[72]Letter from Restrepo, December 22, 1909, to the Colombian president Ramon González Valencia.

[73]Report by a member of the German Residency in Bogotá, Wilhelm Gerlach, November 15, 1912, German Federal Archive.

Box B: Mining Companies Erroneously Associated with Chivor

Two additional mining enterprises were associated with Chivor by Sinkankas (1981): Somondoco Emeralds, Limited, a successor entity to the Somondoco Company, Limited; and the Emerald Mining Company of Colombia.[1] The first company Sinkankas assumed worked at Chivor following the rediscovery by Restrepo but before Restrepo and Klein began their joint mining efforts there. The second company he realized did not fit with available references concerning the rediscovery and subsequent work. Evidence indicates, however, that each was actually involved with properties unrelated to the historical Spanish mines.

SOMONDOCO COMPANY, LIMITED, AND SOMONDOCO EMERALDS, LIMITED

Somondoco Company, Limited, was registered in London under chairman H.S. Sankey on July 1, 1895, with the stated purpose of acquiring the Somondoco emerald mines in the Republic of Colombia.[2] Somondoco Emeralds, Limited, was then registered, also in London and under chairman H.S. Sankey, on May 13, 1899, as a reconstruction of the Somondoco Company, Limited, and with property reported to comprise the Somondoco emerald mines in the Republic of Colombia.[3]

Industry publications track the company's progress through the end of the nineteenth century and the first few years of the twentieth century. As of 1899, the situation was not promising: "Up to the present it has achieved nothing of importance, and the valuable stones it has found are only to be counted by the half-dozen. It now finds itself in sore straits for money…."[4] Some improvement was reported at the annual shareholders meet-

ing in 1900. The corporate reconstruction had brought sufficient funds to pay off liabilities, but practical work had suffered due to the ongoing civil war (1899–1902). Although the superintendent Mr. Gage and the consulting engineer Mr. Russell had been working at the deposit, and some stones were ready to be sent overseas, export was impossible given the hostilities and political disruptions.[5]

The situation at the 1901 annual meeting was similar. Mr. Gage and Mr. Russell reported that they "had not been able to obtain sufficient emeralds to put a profitable consignment upon the market," but they still hoped to make the mine productive: "[W]e have passed through a period of disturbance in the veins, but that is a matter, it appears, we get full compensation for, because a disturbance of the veins is generally a precursor of good and valuable stones when the veins reunite."[6] Such expectations fell short, however, as a court order to wind up the company was issued on December 15, 1904, on the ground that the company was unable to pay its creditors.[7]

The foregoing publications tracking the company's progress never clearly indicated the location of the prop-

[1]Sinkankas, 1981, p. 411.
[2]Skinner, 1896, 1897.
[3]Skinner, 1900.
[4]*The Mining Journal*, Vol. 69 (1899), p. 936.
[5]*The Mining Journal*, Vol. 70 (1900), p. 1482.
[6]*The Mining Journal*, Vol. 71, (1901), pp. 1400–1401.
[7]Register of defunct companies, 1990. *The International Stock Exchange of the United Kingdom and the Republic of Ireland*, 2nd ed., Macmillan Publishers, London, 552 pp.

---

the Colombian government from June 1910, and the government then appointed Restrepo as director on its behalf from January to May 1911.[74] In early January 1913, production at Muzo was discontinued for several years due to lack of profitability[75] and only resumed in 1923.[76] Meanwhile, the termination of the contract in 1910 had resulted in lengthy negotiations on claims for damages involving both the Colombian Emerald Company and the Syndicate of Muzo.

FRITZ KLEIN AND HIS EARLY ACTIVITIES IN COLOMBIA (1905–1913)

Klein's family hailed from Idar, Germany, and was engaged in the gem trade. His father August Klein (1852–1927) began mining and purchasing gem-

stones, mostly red and green tourmaline and aquamarine, in Brazil in the last decade of the nineteenth century. August Senior was supported in Brazil by his sons Gustav (1876–1931), Fritz (1882–1953), and August Junior (1886–1971) from 1902, 1904, and 1906, respectively.[77] Although the Klein brothers were successful in their endeavors as gem merchants in Brazil, competition from other Idar traders in purchasing rough gemstones in Minas Gerais increased.

[74]Diario Oficial (Colombia), 47, No. 12241 (1911), p. 404; Diario Oficial (Colombia), 49, No. 15043 (1913), p. 3221.
[75]Pogue, 1917.
[76]Diario Oficial (Colombia), 59, No. 19011–19014 (1923), p. 572; Diario Oficial (Colombia), 59, No. 18849–18850 (1923), pp. 658–659.
[77]Falz, 1939.

erty involved. Nonetheless, other materials offered further insight. A 1902 report by the British Vice-Consul S.S. Dixon gave the Somondoco district as the location of the mine worked by Somondoco Emeralds, Limited, but it distinguished those workings from the historical Chivor mines. After discussing both Somondoco Emeralds, Limited, and the Muzo deposits, S.S. Dixon continued: "I am informed that an emerald-producing formation of great importance has been discovered by the aid of old Spanish parchments in the Somondoco district, but as yet has not been worked by the discoverers. At present only the old Spanish tunnels and workings indicating that in past centuries great mining operations had been carried on there…."[8] This report is the oldest known published reference related to the rediscovery of Chivor.

With similar import, a map published in 1913 showed emerald mines in the valley of the Río Somondoco near the small municipalities of Somondoco and Guazeque [Guateque][9], and Pogue (1917) expressly differentiated the historical Chivor workings from those along the river: "Some confusion of terms has arisen. These deposits [Somondoco or Chivor] are near the valley of Chivor, and have been called the Chivor deposits. Under Spanish dominion they came to be known as the Somondoco deposits… and by this name they are generally called in the literature. They do not, however, occur on Río Somondoco, but other less important deposits are known on that stream." Hence, all evidence points to one of these less important deposits in the Somondoco valley being the locality mined without great success by the British "Somondoco" company.

EMERALD MINES OF COLOMBIA, LIMITED, AND EMERALD MINING COMPANY OF COLOMBIA

Emerald Mines of Colombia, Limited, was registered in London on September 28, 1888.[10] The company purchased the Yacopi mines, located in the Western Colombian Emerald Belt, where the Muzo and Coscuez mines are also situated. The following decade, a company called the Emerald Mining Company of Colombia was mentioned in a report by George Frederick Kunz incorporated in a publication from the United States Geological Survey.[11] Kunz noted that a property had been acquired by the company that was expected to produce emeralds "quite as fine as those from the famous Muzo mine." Based on this report, the Colombia Mining Company of Colombia was later potentially associated with Chivor by Sinkankas, as previously stated. The identity of the property had not been specified by Kunz, leading to speculation connecting the company with the likewise famous Chivor mines. However, research indicates that the Emerald Mining Company of Colombia referred to by Kunz was most likely Emerald Mines of Colombia, Limited, and therefore was engaged at Yacopi, not Chivor.

---

[8]Dixon, 1902. A nearly identical text was published anonymously in *Monthly Bulletin of the International Bureau of the American Republics*, 13 (1902), pp. 1349–1350.

[9]Gamba, 1913.

[10]Skinner, 1889–1890, 1891–1892.

[11]Mineral Resources of the United States: Calendar Year 1893. United States Geological Survey, 1894, pp. 696–697.

The growing competition prompted Fritz to travel through various South American countries such as Argentina, Bolivia, and Peru, always searching for new gem materials, sources, and trade opportunities.

Fritz Klein's first trip to Colombia occurred in 1905 and nearly ended in disaster. Purchase and sale of gemstones at that time was strictly controlled through government-authorized channels, and Klein sought to buy and export rough emeralds from a private Colombian middleman in violation of applicable regulations. He was accused of this infraction by the Syndicate of Muzo and arrested in Honda, in the department of Tolima. The emeralds he had acquired were confiscated. Only through intervention of the German Resident[78] in Bogotá was he later released and permitted to leave the country.[79]

Given these incidents, returning to Bogotá would have been advisable only under protection of the German Resident.[80] Nonetheless, Klein continued to pursue his goal of establishing himself in the Colombian emerald trade. In December 1907, for instance,

---

[78]Prior to 1914, the German empire designated ambassadors to only a small number of important nations, with such individuals serving in cities such as Paris, London, Rome, Madrid, Washington, and St. Petersburg. For other countries, including Colombia, the German Empire designated officials termed residents, who held rights for purposes of international law essentially equivalent to those of ambassadors.

[79]Report by the former translator of the German Resident, September 1925, Historical Archive of the German Ministry of Foreign Affairs.

[80]Letter from Fritz Klein, January 19, 1909, to his brother-in-law August Hahn in Idar, Germany.

Figure 10. Dr. Ernst Jäckh, the brother-in-law of Fritz Klein, had access to the elite of the German Empire. In the 1910s, he served as an unofficial consultant with the Ministry of Foreign Affairs, Berlin, focusing on dealings with the Ottoman Empire (Turkey). Jäckh used his influence to further Klein's efforts both in Colombia and in finding investors for the Chivor project. Photo of Jäckh (center) in Istanbul in 1917 with German Emperor Wilhelm II (to the right of Jäckh); courtesy of the Ernst Jäckh collection, Columbia University.

Figure 11. The German Resident in Bogotá, Dorotheus Kracker von Schwartzenfeldt, was instructed by the German Ministry of Foreign Affairs to assist Fritz Klein in Colombia, especially as regarded purchasing the Chivor emerald mines. Kracker von Schwartzenfeldt later worked to clarify the legal situation in response to inquiries from the Syndicate El Chivor. Photo circa 1910, courtesy of the Historical Archive of the German Ministry of Foreign Affairs.

Klein spent a short period in Barranquilla, a port city in northern Colombia, for a meeting with a local partner.[81] By 1911, Klein's brother-in-law Dr. Ernst Jäckh[82] (1875–1959, figure 10) had asserted his influence at the Ministry of Foreign Affairs in Berlin to secure the protection needed for Klein to re-enter Colombia and stay in Bogotá.[83] An order was issued to the German Resident in Bogotá, Dorotheus Kracker von Schwartzenfeldt (1869–1935, figure 11), in support of Klein's activities.

Klein returned to Bogotá in September 1911.[84] He initially negotiated with the Colombian government

---

[81]Letter from Fritz Klein, December 23, 1907, to his father August Klein in Idar, Germany.

[82]Dr. Ernst Jäckh married Fritz Klein's oldest sister, Bertha (1874–1928), in 1899. From 1902 to 1912 he was editor-in-chief of a daily newspaper in Heilbronn, Germany. Beginning in 1908, Jäckh also made numerous trips to Turkey, where he came into contact with high-ranking representatives of the Ottoman Empire and became a friend of the German diplomat Alfred von Kiderlen-Waechter, who was appointed Minister of Foreign Affairs in 1910. Jäckh moved to Berlin in 1912 and served as a "consultant" with the Ministry of Foreign Affairs. In 1920, Jäckh founded the German Academy for Political Sciences in Berlin, and during the 1920s, he was a member of the German delegation to several international conferences. Through a conversation with Hitler in April 1933, he realized that he would not be able to keep his positions as the leader of various institutions. In May 1933 Jäckh emigrated together with his second wife Martha to Great Britain. He remained there until 1940, working for the British government in multiple functions. He moved in 1940 to the United States and taught as a professor at Columbia University in New York. See Jäckh, 1954.

[83]Letter from the German Minister of Foreign Affairs, Alfred von Kiderlen-Waechter, November 25, 1911, to Fritz Klein's brother-in-law Dr. Ernst Jäckh.

[84]Fritz Klein traveled via New York, where he arrived in June 1911. File Fritz Klein, List or Manifest of Alien Passengers for the United States Immigration Officer at Port of Arrival, New York, June 1911, MyHeritage.com.
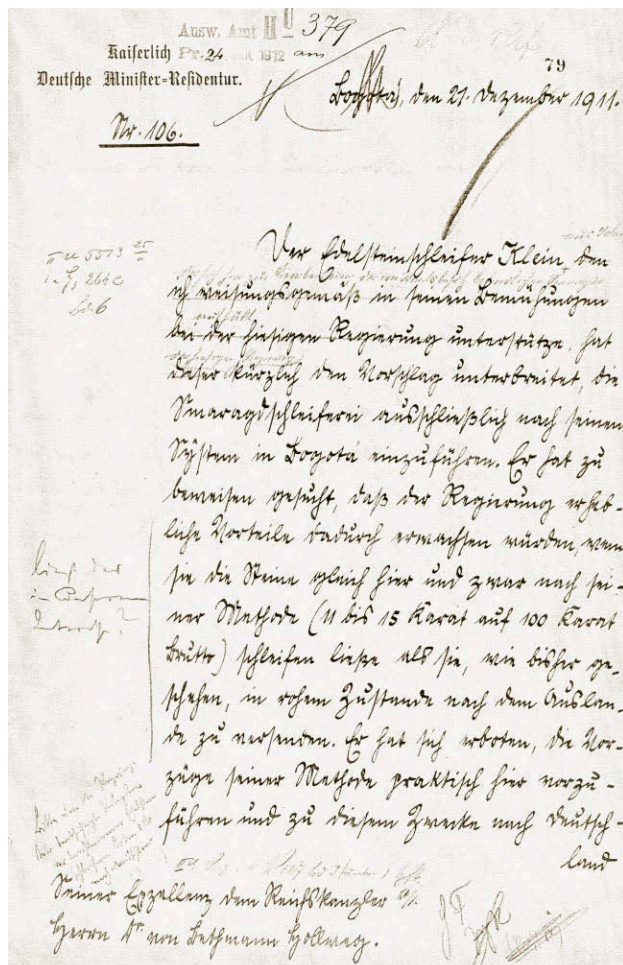
Figure 12. Opening page of a report from the German Resident in Bogotá, Dorotheus Kracker von Schwartzenfeldt, to the German Ministry of Foreign Affairs, dated December 21, 1911. The report described Fritz Klein's negotiations with the Colombian government in seeking permission to establish an emerald-cutting enterprise. Historical Archive of the German Ministry of Foreign Affairs.

in hopes of establishing an emerald-cutting enterprise (figure 12), but these efforts were unsuccessful.[85]

In November 1911, Klein became aware of the Chivor mine through another German, Hermann Span.[86] A preliminary option contract for the mine, initiated by Span, was executed on February 13, 1912, and on June 5, 1912, after Klein conducted preliminary exploration of the mining area, terms were further formalized in a notarized option contract signed between Span and Klein on one hand and the mine owners Compañía de las Minas de Esmeraldas de Chivor on the other. The latter contract provided an exclusive right to purchase the mine for £51,000 (equivalent to 255,000 pesos oro; see again table 3)

and was valid for a one-year term.[87] Span and Klein were also given the right to mine samples in Chivor during the stated pendency of the option.

Klein was not alone in his interest in Chivor during this period. Dixon (see again box A), previously active in Muzo[88] and already both a shareholder in the Compañía de las Minas de Esmeraldas de Chivor and a co-owner of the three newer Chivor mining titles, was engaged anew in exploration in the region, commencing additional mining ventures. As reported in 1911: "Mr. Christopher E. Dixon, formerly engineer in charge of Muzo mines, personally extracted over a pound of emeralds by scratching about in one place and another…. Somondoco (sometimes called 'Chivor' from the valley near it) will soon yield gems to delight the world."[89]

On June 11, 1912, Klein set out from Bogotá for Chivor to obtain samples for presentation to potential investors.[90] He was accompanied by Restrepo and remained at the mine until January 1913. During that time, from late October to early November 1912, an official from the German Residency in Bogotá visited the site and reported[91] that within a short period of four to five weeks, the work undertaken by 15 to 20 indigenous people had produced quite favor-

[85]Report by the German Resident in Bogotá, Dorotheus Kracker von Schwartzenfeldt, December 21, 1911, German Federal Archive; letter from Fritz Klein, July 24, 1912, to Kracker von Schwartzenfeldt, German Federal Archive.

[86]Exposé der Smaragdmine "El Chivor" by Fritz Klein, undated, 16 pp., received by the German Ministry of Foreign Affairs September 13, 1913, German Federal Archive. Hermann Span (1870–1943?) and his brother Emil (1869–1944), from Reutlingen, Württemberg, Germany, moved in the 1890s to Central America and were active in Guatemala, Costa Rica, and El Salvador. Hermann Span was also involved in Colombia by 1910. Hauptstaatsarchiv Stuttgart, E40-76 Bü 1370; Diario Oficial (Colombia), 48, No. 14678 (1912), pp. 411–413. Additionally, multiple notarial acts concerning Span and sundry business partners are found in the Archivo General de la Nación (Colombia).

[87]Escritura 1096, June 5, 1912, Notaria 2, Archivo General de la Nación (Colombia); Report by a member of the German Residency in Bogotá, Wilhelm Gerlach, November 15, 1912, German Federal Archive.

[88]During the 1890s and early 1900s, Christopher Dixon worked on behalf of the English Mining Syndicate, Limited, which operated the Muzo mine prior to the contract with the Syndicate of Muzo. Atuesta, 1899; Monthly Bulletin of the International Union of the American Republics, 8 (1900), pp. 581–582; Gaceta Judicial (Colombia), 15 (1901), pp. 169–173; Gaceta Judicial (Colombia), 16 (1903), pp. 78–79; Domínguez, 1965.

[89]Latham, 1911.

[90]Exposé der Smaragdmine "El Chivor" by Fritz Klein, undated, 16 pp., received by the German Ministry of Foreign Affairs September 13, 1913, German Federal Archive.

[91]Report by a member of the German Residency in Bogotá, Wilhelm Gerlach, November 15, 1912, German Federal Archive.

Figure 13. Export license issued to Fritz Klain [sic] by the Ministerio de Hacienda, March 5, 1913, for 157 "gangas" (emeralds in the host rock) and 5,450 carats of rough emerald crystals. Courtesy of Eduardo Restrepo Ortega.

Figure 14. Dr. Antonio José Cadavid, a lawyer, law professor, and politician, filed a lawsuit on behalf of three shareholders of the Compañía de las Minas de Esmeraldas de Chivor to challenge new laws and decrees affecting the independence of the "free" emerald mines in Colombia. Cadavid also worked with Fritz Klein and the German Resident Dorotheus Kracker von Schwartzenfeldt in 1913 and 1914. Courtesy of Banrepcultural, Bogotá.

able results. According to Klein,[92] they focused for the first four months on poor targets, but when he finally understood "the direction of the veins and the character of the mine, the production of emeralds began in surprising abundance. With 20 workers, I unearthed in 3½ months under the most primitive conditions conceivable about 6,000 carats of emeralds, which have a minimum value of 150,000 marks [then equivalent to US $37,500]." At the end of 1912, Klein's younger brother August arrived in Colombia for support.[93] He remained at the mine, together with Restrepo's younger son Alejandro, when Klein and Restrepo subsequently departed for Germany.

Klein left Bogotá in March 1913 to search for investors in Germany. With the approval of the local government, he carried a sample of emeralds produced during his approximately six months at the mine. The set consisted of 157 "gangas" (emeralds still embedded in the original host rock) and over 5,000 carats of crystals in varying sizes and shapes.[94] Having received a license for exportation (figure 13), Klein wanted to use these samples to interest potential European investors. In furtherance of this mission, Klein arranged before leaving to have the term of the option contract extended, this time exclusively in his own name and without Span.[95] That extension, valid for nine months, was signed in July 1913 by several of the shareholders together with Escovar, representing Restrepo, and the attorney Dr. Antonio

José Cadavid[96] (figure 14), representing Klein.[97] Word had already come to the German Residency in Bo-

[92]Exposé der Smaragdmine "El Chivor" by Fritz Klein, undated, 16 pp., received by the German Ministry of Foreign Affairs September 13, 1913, German Federal Archive.

[93]August Klein traveled from Hamburg via New York, where he arrived in October 1912. File A. Klein, List or Manifest of Alien Passengers for the United States Immigration Officer at Port of Arrival, New York, October 1912, MyHeritage.com.

[94]Report by a member of the German Residency in Bogotá, Josef Wipperfeld, March 27, 1913, German Federal Archive.

[95]Hermann Span left Colombia for Germany in August 1913 to form a banana company, apparently ending his pursuit of the Chivor emerald business. He returned to Colombia in April 1920. Diario Oficial (Colombia), 58, No. 18319–18320 (1922), p. 478.

[96]The lawyer, law professor, and politician Dr. Antonio José Cadavid (1866–1919) served in various positions as professor at the National University, Minister of the Treasury (1909–1910), and Minister of War (1915–1916). See Bermúdez (1966).

[97]Escritura 1474, July 15, 1913, Notaria 2, Archivo General de la Nación (Colombia).

Figure 15. Dr. Hjalmar Schacht served as a vice director of Dresdner Bank, one of the larger German financial institutions, from 1908 to 1915. Separate from his role at the bank, he opted in 1914 to privately invest in the Chivor mine with Fritz Klein, August Stauch, and the company Rudolph Hahn & Sons, London, in pursuing the Chivor mine. Photo circa 1900, courtesy of Cordula Schacht.

gotá that Dresdner Bank, one of the larger financial institutions in Germany, might be interested in funding the purchase of Chivor.

Klein traveled to Germany with Restrepo, who remained there until his return in November 1913.[98] Restrepo's stay in Germany included time in Idar, where he met members of Klein's family, and in Berlin, where he met Jäckh, Dr. Hjalmar Schacht (figure 15),[99] and presumably other possible investors. Restrepo's sojourn incorporated a period in May 1913 at the renowned sanatorium of Karlsbad[100] to restore his health. Restrepo also traveled to Meran, Tyrol, Austria, to see Klein's father August.[101] Klein, in turn, traveled to England in October 1913 to show the emerald samples to members of the company Rudolf Hahn & Sons, London,[102] dealers in high-end gem materials, and other potential backers.[103]

Meanwhile, initial steps were taken by unknown parties between 1913 and 1914 to start a company in London under the name Emerald Mines of Somon-

doco, Ltd. The stated aim of the entity was "to acquire and work the Emerald Mines called El Chivor No. 1 and El Chivor No. 2" (figure 16). The capital was to consist of £90,000, with 90,000 shares to be issued at £1 each.[104] Nonetheless, no further activity pertaining to this company is known, so any underlying rival or alternate plan targeting Chivor was apparently abandoned.

Soon after Restrepo's return to Bogotá, another extension to the option contract, granting Klein exclusive rights to purchase the mine until December 1914, was signed by Cadavid, representing Klein.[105]

LITIGATION BETWEEN MINE OWNERS AND THE COLOMBIAN GOVERNMENT (1912–1913)

The commercial success of a gem mine depends primarily on the value of mined stones and the cost of mining operations. Also significant are the amount of duties and taxes imposed and the ability to sell the

[98]Restrepo traveled from Hamburg via New York, where he arrived in November 1913. File F. Restrepo, Hamburger Passagierlisten, November 1913, Ancestry.de; File F. Restrepo, List or Manifest of Alien Passengers for the United States Immigration Officer at Port of Arrival, New York, November 1913, Ancestry.com.

[99]Dr. Hjalmar Schacht (1877–1970) was one of the vice directors of Dresdner Bank in Berlin from 1908 to 1915. An ascendant career thereafter led him to the presidency of the German National Bank (Reichsbank), with two terms of office from 1923 to 1930 and from 1933 to 1939. He also served concurrently as Minister of Economics from 1934 to 1937. Between 1933 and 1939 Schacht was instrumental in the financing of Hitler's rearmament, which in 1945 resulted in his indictment at the Nuremberg Trials. He was ultimately acquitted. See Kopper, 2006.

In 1909, Schacht and Klein's brother-in law Dr. Ernst Jäckh traveled together to Turkey. Following that trip and Jäckh's move to Berlin in 1912, they cooperated on many political projects. After Jäckh's emigration in 1933 and Schacht's new engagement, however, their ways parted.

[100]*Karlsbader Kurliste*, No. 135, May 23, 1913, 2 pp.

[101]Letters by Fritz Klein, November 27, 1913, and January 26, 1914, to Restrepo; Letter from August Klein Senior, December 27, 1913, to Restrepo.

[102]The company Rudolf Hahn & Sons, London, dated back to 1893 and in 1914 was managed by the brothers Eugen and Paul Hahn. The Hahn brothers had roots in Idar, Germany, and were cousins of August Hahn, brother-in-law of Fritz and August Klein. August Hahn married Klein's younger sister Luise (1884–1976).

[103]Letter from Rudolf Hahn & Sons, London, November 7, 1913, to the mine owners.

[104]Prospectus, Emerald Mines of Somondoco, Ltd., Undated. Although the prospectus and attendant documents are undated, references therein to several specific individuals (e.g., Diódoro Sánchez as president of the Sociedad Colombiana de Ingenieros and Francisco Restrepo Plata as Ministro de Hacienda, Colombia) enable preparation and publication of the material to be placed within the 1913 to 1914 timeframe.

[105]Escritura 2759, December 24, 1913, Notaria 2, Archivo General de la Nación (Colombia).
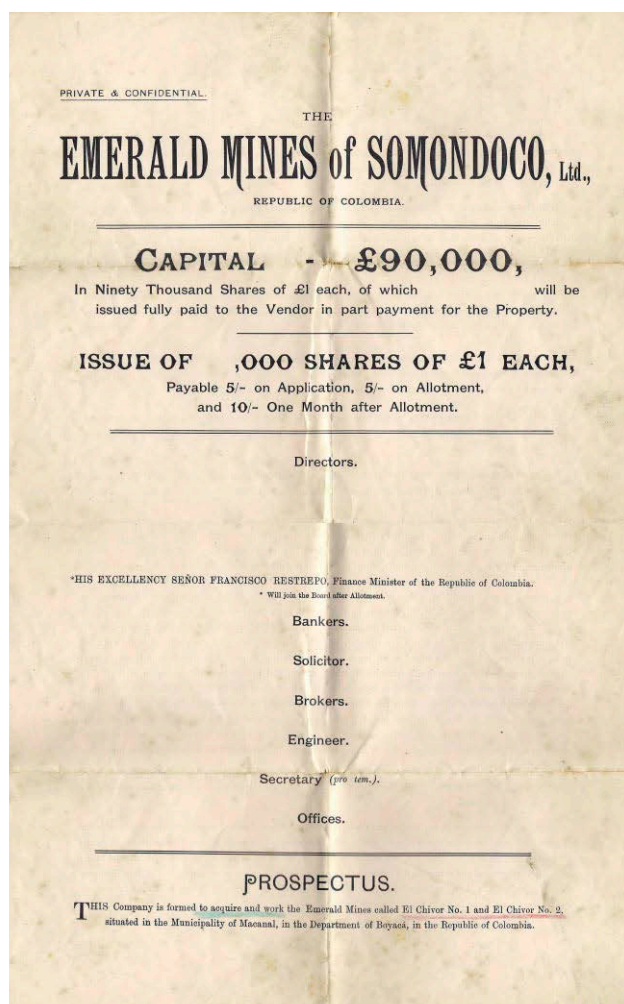
Figure 16. Prospectus drafted in 1913–1914 to form a company in London under the name Emerald Mines of Somondoco, Ltd., "to acquire and work the Emerald mines called El Chivor No. 1 and El Chivor No. 2." Courtesy of Eduardo Restrepo Ortega.

gems on the open market. During relevant periods in Colombia, the applicable framework of various laws and decrees, issued at different times and subsequently incorporating multiple addendums and amendments, was rife with complexity. The major emerald mines of Muzo and Coscuez had belonged to the government since 1886, but a number of mostly smaller mines existed under private ownership. After 1905, however, registration of new emerald mines by private owners was no longer permitted and additional taxes were imposed upon the existing mines (Law No. 40 of 1905).

Prior to the 1905 change in regulations, a provision allowed for the annual taxes on privately owned mines to be paid in advance for a period of 20 years.

Thereafter, these so-called free mines were to be forever excluded from any taxes and fees and could no longer be registered by other persons (Law No. 292 of 1875, Article 45, adapted in Law No. 38 of 1887).[106] As noted previously, the taxes for Chivor 1 and 2 had been paid in advance for 20 years.

After the law changed, the nature of the rights afforded to the free mines became a subject of repeated controversy and litigation between the mine owners and the Colombian government. The disputes centered on three issues:

1. Taxes and fees payable by the owners of free mines
2. Control of mining operations by the government
3. Control of emerald sale and export by the government

An initial legal action challenging several laws and decrees was filed by Francisco de P. Matéus in his name and on behalf of several other owners of free mines. The eventual decision of the Corte Suprema de Justicia on August 2, 1912, was a partial victory for the mine owners, ruling that governmental control of the mining operations was illegal but that state control of emerald exportation could continue.[107] A copy of the decision was mailed to Guateque to inform Restrepo and Klein, who were working at Chivor at the time.

In October 1912, the government rejected a complaint by Dixon about restrictive rules circumscribing the emerald mining business after a seven-year dispute that had begun in 1905 (again, see box A).[108]

A new decree by the Colombian government was then issued in December 1912, followed by a supplement in January 1913, which sought again to increase control by governmental institutions over free mines. Opposition to the new regulations began immediately, with a petition by Isaza, shareholder in the Compañía de las Minas de Esmeraldas de Chivor,

[106]Bullman, 1892.

[107]Corte Suprema de Justicia, Bogotá, agosto 2 de 1912, "Sobre la inexequibilidad de algunas disposiciones relacionadas con la explotación de minas de esmeraldas [About the unenforceability of some decrees related to the exploitation of emerald mines]," 21 pp.; Gaceta Judicial (Colombia), 22 (1913), pp. 2–9.

[108]Letter from Christopher Dixon, November 10, 1905, to the Ministerio de Relaciones Exteriores, Ministerio de Industrias, Archivo, Correspondencia 1905, Archivo General de la Nación (Colombia); Diario Oficial (Colombia), 48, No. 14720 (1912), pp. 812–813; Annual report on Colombia for the year 1913.
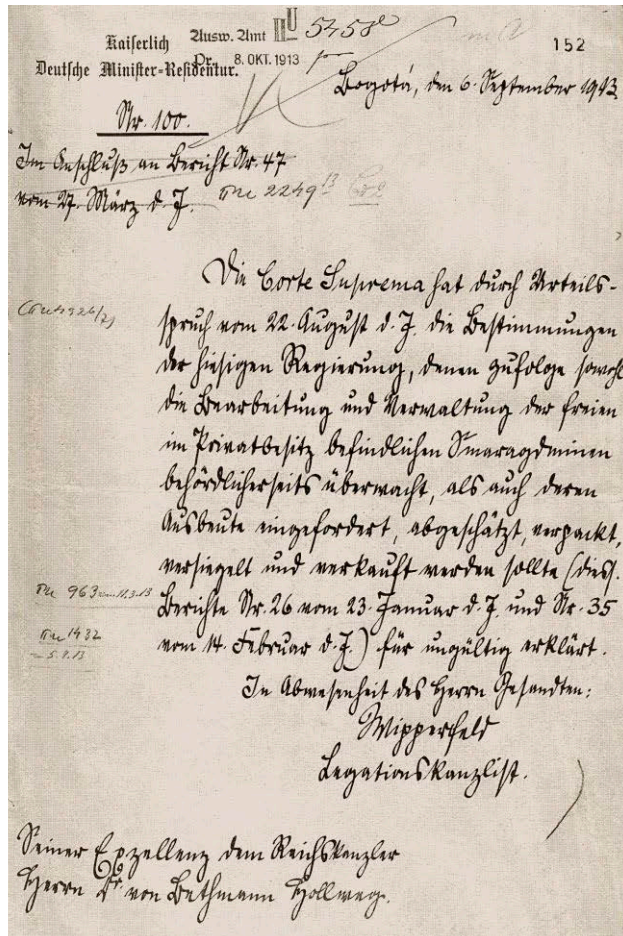
Figure 17. Report from a member of the German Residency in Bogotá, Josef Wipperfeld, to the German Ministry of Foreign Affairs, Berlin, dated September 6, 1913. The report briefly described the August 22 decision by the Colombian Corte Suprema de Justicia addressing privately owned "free" mines. Historical Archive of the German Ministry of Foreign Affairs.

to the Minister of Finance in January 1913[109] and a similar petition by Klein in February 1913.[110] An additional legal action challenging several of the older laws and decrees and the two new decrees was filed on February 22, 1913, by the attorney Cadavid in the names of three Compañía de las Minas de Esmeraldas de Chivor shareholders (the Colombian citizens Isaza, Escovar, and González).[111] The decision of the Corte Suprema de Justicia, issued August 22, 1913, nullified several of the contested laws and decrees, ruling that the free emerald mines could work without any further governmental control.[112] That result (figure 17) was telegraphed to the Ministry of Foreign

Affairs in Berlin by the German Resident in Bogotá on September 7, 1913, and Klein was promptly informed via his brother-in-law Jäckh.

ACTIVITIES IN 1914
After the favorable resolution of the legal situation in Colombia, Klein was able to continue searching for and negotiating with potential investors. In this endeavor, Jäckh and his contacts with political and business elites once again proved instrumental. Restrepo, as indicated above, had already returned to Colombia.

The search culminated on February 14, 1914, with the founding of the Syndikat El Chivor (Syndicate El Chivor, used hereinafter) between four members, with initial capital contributions as follows:[113] August Stauch (figure 18),[114] Berlin-Zehlendorf, 25,000 marks; Dr. Hjalmar Schacht, Berlin-Zehlendorf, 10,000 marks; Rudolf Hahn & Sons, London, 10,000 marks; and Fritz Klein, Idar, 5,000 marks. The founding contract further contained provisions addressing usage of the initial capital, investigation of the property by an expert, and terms of any future purchase of the mine. The services of an expert were considered necessary because the quality of Klein's samples was inadequate to convince all investors to formalize the purchase, absent independent examination of the mine (figure 19).[115] In these endeavors, the four members agreed that the company should be privately financed, without institutional funding from Dresdner Bank or any other German banking firm.

[109]Diario Oficial (Colombia), 49, No. 14823 (1913), pp. 341–342.
[110]Ibid., pp. 546–548.
[111]All four Colombians involved were well-known lawyers who had held high-level positions in Colombia as university professors, diplomats, and ministers. As previously noted, Enrique González also formerly served as director of operations at the Muzo emerald mine. Diaz, 1967.
[112]Gaceta Judicial (Colombia), 22 (1913), pp. 242–244; Cadavid, 1913.
[113]Historical Archive of the German Ministry of Foreign Affairs; Prof. Robert Scheibe collection, University Library Freiburg.
[114]August Stauch (1878–1947) has been recognized as the discoverer of the diamond deposits in Namibia, then known as German South-West Africa, in 1908. Diamond mining made him and those involved in his Colonial Mining Company extremely wealthy. Stauch bought farms in southwest Africa and a villa in Berlin-Zehlendorf, Germany. In the 1920s, he was active as an investor not only in a variety of mining companies but also in technology-focused enterprises. See Levinson, 2007. The Schacht and Stauch families lived near each other in Berlin-Zehlendorf, Germany, and might thus have interacted on a personal level as well.
[115]Letter from Rudolf Hahn & Sons, London, November 7, 1913, to the mine owners.

EMERALDS FROM THE CHIVOR MINING DISTRICT, COLOMBIA

Emeralds from the Chivor region are found as individual single crystals (A–C) or as crystal aggregates (D–F). These aggregates consist of parallel or subparallel oriented crystals or even of radiating, strongly inclined individuals. The habit of the emerald crystals is formed by six or twelve hexagonal prism faces in combination with two basal pinacoids (A–C, G–J). Occasionally, different hexagonal dipyramids are also seen (I and M). The basal pinacoid might show incomplete growth surfaces (K), and, in extreme rare cases, cavities parallel to the hexagonal crystal axis are seen (L). The mineral assemblage within the emerald-bearing veins at Chivor consists of pyrite (A–C, N–R) frequently associated with albite (var. cleavelandite), calcite, dolomite (O–R), occasionally quartz, and limonite (mainly goethite) formed by the alteration of pyrite. The host rocks of the Chivor deposit are breccia, layered limestones, albitites, and black and gray shales (C–K, M–S). Photos by G. Martayan, Paris.

A

Emerald crystal: *19 × 7.5 mm*

Habit: *hexagonal prism faces terminated by flat basal pinacoids; the large beryl crystal is intergrown at different angles with smaller crystals*

Associated minerals: *dodecahedral pyrite crystals*

B

Emerald crystal: *length 33 mm*

Habit: *hexagonal prism faces terminated by flat basal pinacoids*

Associated minerals: *albite, pyrite, calcite*

C

Specimen: *21 × 19 × 14 mm*   **Emerald crystal:** *length 7 mm*

Habit: *hexagonal prism faces terminated by flat basal pinacoids and hexagonal dipyramids*

Associated minerals: *gray dolomite, albite, pyrite*

Matrix: *gray shale*

D

Cluster of intergrown emerald crystals, specimen: *43 × 38 × 36 mm; several crystals exhibit striations (growth patterns) on basal pinacoids or on prism faces; some crystals of the aggregate contain carbonaceous inclusions*

Associated minerals: *limonite*

Specimen with emerald clusters: *45 × 33 × 23 mm, largest cluster: 18 × 16 mm*
Associated minerals: *dolomite, albite, pyrite*
Matrix: *gray shale*

Emerald cluster, specimen: *20 mm across; the crystals of the aggregate are inclined to each other*
Associated minerals: *albite*

Specimen with emerald crystal   Crystal: *length 8 mm*
Habit: *hexagonal prism faces terminated by flat basal pinacoids and hexagonal dipyramids*
Associated minerals: *pyrite, dolomite*
Matrix: *breccia*

Specimen with emerald crystal   Crystal: *11 × 4.5 mm*
Habit: *hexagonal prism faces terminated by flat basal pinacoids and hexagonal dipyramids*
Associated minerals: *white albite, pyrite, dolomite*
Matrix: *gray limestone*

Specimen with emerald crystal   Crystal: *length 8 mm*
Habit: *hexagonal prism faces terminated by flat basal pinacoids and hexagonal dipyramid*
Associated minerals: *pyrite, dolomite*
Matrix: *breccia*

Specimen with emerald crystal   Crystal: *length 5 mm*
Habit: *hexagonal prism faces terminated by flat basal pinacoids, indentations in the basal pinacoid*
Associated minerals: *gray calcite rhombs, white albite, pyrite*
Matrix: *black shale*

Specimen with emerald crystal   Crystal: *length 13 mm*
Habit: *hexagonal prism faces terminated by flat basal pinacoids*
Associated minerals: *pyrite, gray dolomite rhombs*
Matrix: *gray shale*

Emerald crystal with channels parallel to the c-axis
Specimen: *17 × 11 × 11 mm*
Associated minerals: *gray dolomite*

Specimen with emerald crystal   Crystal: *length 6 mm*
Habit: *hexagonal prism faces terminated by flat basal pinacoids and hexagonal dipyramids*
Associated minerals: *white albite*
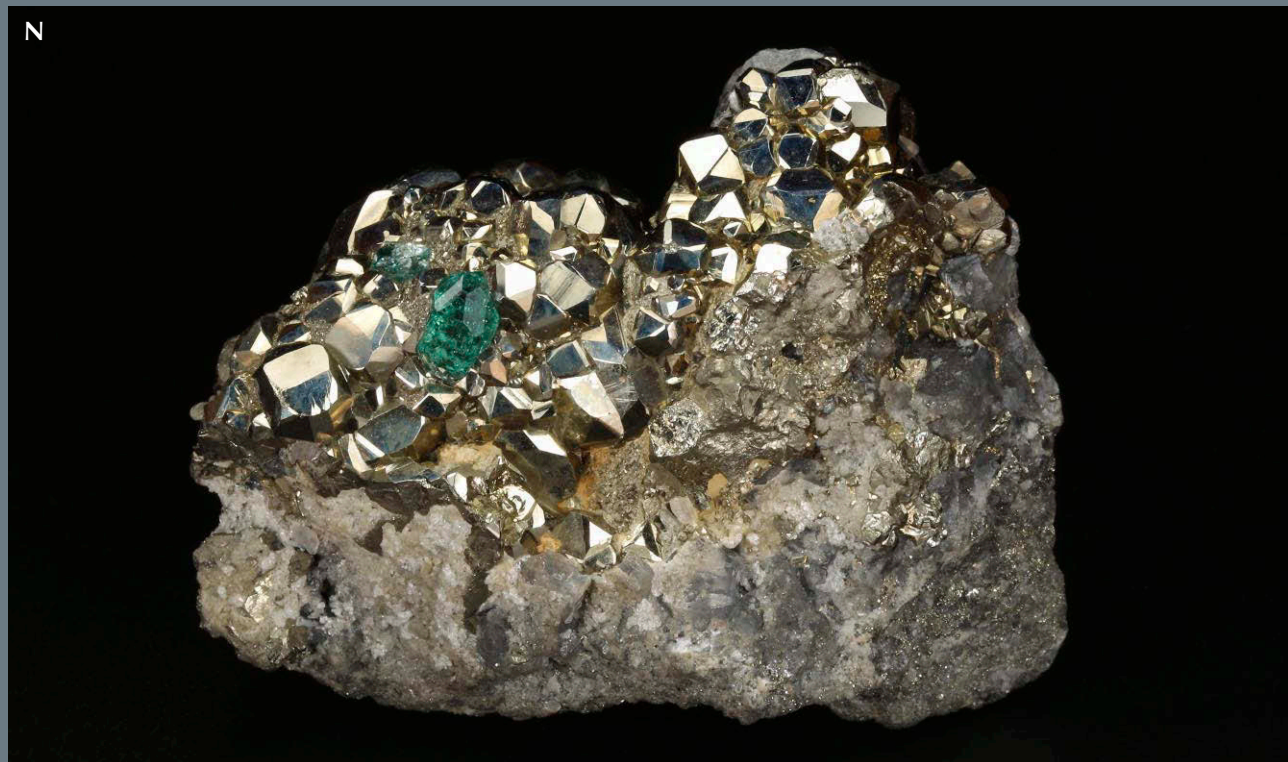
Specimen: *60 × 45 × 55 mm*   **Emerald crystal:** *length 6 mm*
Habit: *hexagonal prism faces terminated by flat basal pinacoids and hexagonal dipyramids*
Associated minerals: *pyrite, dolomite*
Matrix: *black shale*

Specimen: *42 mm across*   **Emerald crystals:** *up to 14 mm in length*

Habit: *hexagonal prism faces terminated by flat basal pinacoids, prism faces with striations parallel to the c-axis*

Associated minerals: *dolomite, pyrite, embedded in a white dolomitic matrix*

Specimen: *32 mm across*   **Emerald crystal:** *length 9 mm*

Habit: *hexagonal prism faces terminated by flat basal pinacoids*

Associated minerals: *pyrite, gray dolomite rhombs, white albite*

Matrix: *black shale*

Q

Specimen: *15 × 12 × 5 mm*
Largest emerald crystal: *length 11 mm*
Habit: *hexagonal prism faces terminated by flat basal pinacoids and hexagonal dipyramids*
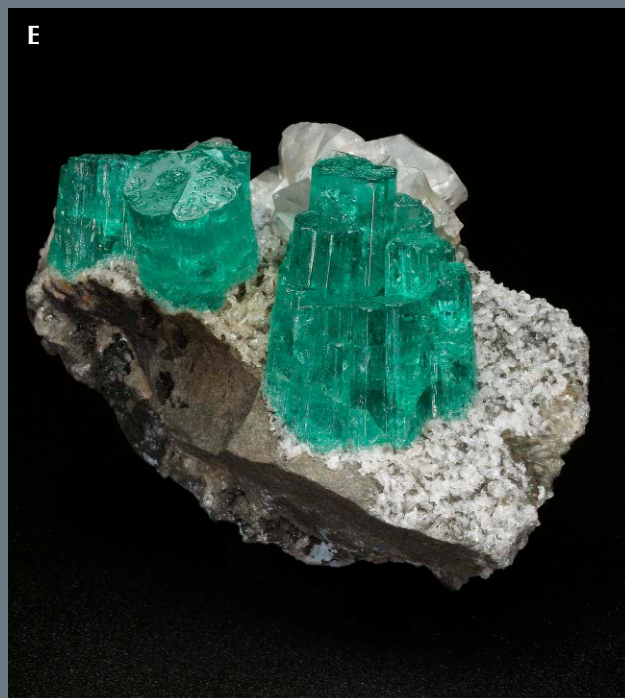**Associated minerals:** *white albite*
Matrix: *gray shale*

R

Specimen: *38 × 35 × 18 mm*   **Emerald crystal:** *length 20 mm*
Habit: *hexagonal prism faces terminated by flat basal pinacoids and hexagonal dipyramids,*
Associated minerals: *white albite, small pyrite nodules*
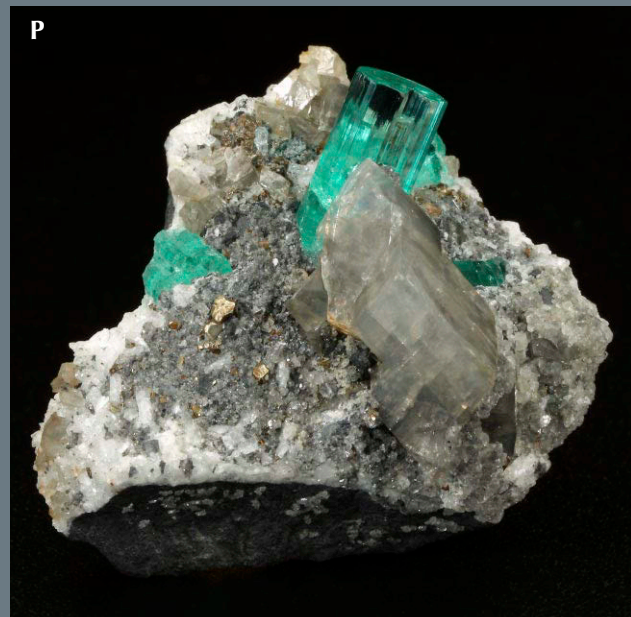**Matrix:** *black shale*

S

Specimen: *67 × 50 × 50 mm*   **Emerald crystal:** *length 18 mm*
Habit: *hexagonal prism faces terminated by flat basal pinacoids and hexagonal dipyramids*
Associated minerals: *albite, dolomite, small pyrite nodules*
Matrix: *layered gray limestone*

Figure 18. August Stauch is credited with discovering the diamond deposits in Namibia in 1908. Stauch was a key investor in the group assembled by Fritz Klein in 1914 to pursue the Chivor mine. Photo 1921, courtesy of Dr. Gabriele Schneider.

Figure 19. In a letter dated November 7, 1913, London-based Rudolf Hahn & Sons advised owners of the Chivor mines that the quality of the emerald samples shown by Fritz Klein was inadequate to justify purchase of the property. Courtesy of Eduardo Restrepo Ortega.

few days later, Klein and Scheibe embarked together in Hamburg, bound for Puerto Colombia.[118]

Following the just-described formalities, letters were sent from the Syndicate El Chivor to the German Ministry of Foreign Affairs in Berlin and to the German Resident in Bogotá.[119] Therein, Schacht and Stauch sought to obtain clarification regarding the situation in Colombia, inquiring as to the legality of the mining titles, any obligations to pay taxes or additional fees, the parameters for authorized export of the emeralds and so forth. The German Resident in Bogotá, Dorotheus Kracker von Schwartzenfeldt, in turn contacted González as a representative of the mine owners, the attorney Cadavid, and the Ministro de Hacienda for details before responding in a letter to Schacht dated June 15, 1914.[120]

The initial paid-in capital was to be used solely to finance the expert evaluation. Klein was to assist the scientific expert in his activities. Any subsequent purchase of the mine would proceed through exercise of Klein's option by paying the price of £51,000 (equivalent to 1,020,000 marks and identical to the 255,000 pesos oro specified in the option contract). Klein was to receive 1,250,000 marks cash from the investors to purchase the mine and would be entitled to 20 percent of the shares of a future mining company.

As communicated in a letter from the Syndicate El Chivor dated February 16, 1914,[116] Prof. Robert Scheibe (figure 20),[117] professor of geology at the Royal Mining Academy (Königliche Bergakademie) in Berlin and close friend of Stauch, was selected to perform the expert evaluation of the Chivor mine. A

[116]Letter from the Syndicate El Chivor, February 16, 1914, to Prof. Robert Scheibe, Historical Archive of the German Ministry of Foreign Affairs.

[117]Prof. Robert Scheibe (1859–1923) studied mathematics and natural sciences at the Martin Luther University of Halle-Wittenberg, Germany, where he received his PhD in 1882. In 1885, he became a member of the Royal Mining Academy (Königliche Bergakademie) in Berlin, where he was appointed professor in 1895. In the summer of 1908, Scheibe traveled to Namibia to study primary kimberlites. He met August Stauch, the discoverer of the secondary diamond deposits in the area of Lüderitzbucht. From late December 1908 to early January 1909, the two men made an excursion to the area south of Lüderitzbucht, where they found Pomona, potentially the richest diamond deposit ever discovered. Scheibe returned to Germany at the end of 1909, but he and Stauch remained friends for life. See Rauff, 1926; Strunz, 1970; Levinson, 2007.

[118]Files Robert Scheibe and Fritz Klein, Hamburger Passagierlisten, February 1914, Ancestry.de.

[119]Letters by the Syndicate El Chivor, March 14, 1914, and April 9, 1914, Historical Archive of the German Ministry of Foreign Affairs.

[120]Historical Archive of the German Ministry of Foreign Affairs.
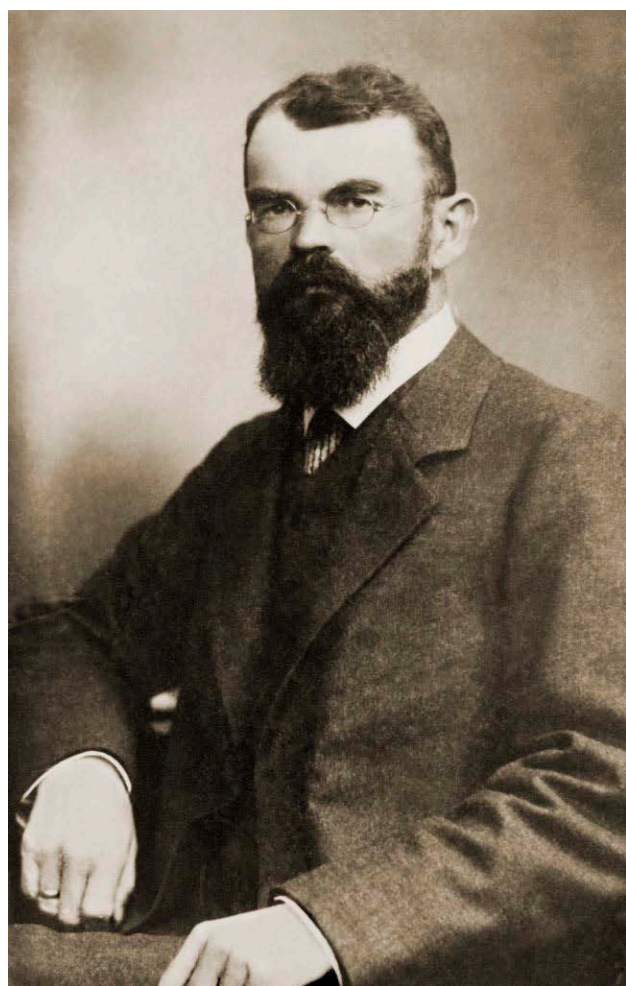
Figure 20. Prof. Robert Scheibe of the Royal Mining Academy (Königliche Bergakademie) in Berlin joined August Stauch in late 1908 to early 1909 in finding the major Pomona diamond deposit in Namibia. He was hired in 1914 by the Syndicate El Chivor to evaluate the Chivor mine. Photo circa 1910, Prof. Robert Scheibe collection, University Library Freiburg.

Figure 21. Restrepo's death certificate, dated April 24, 1914. File Inheritance F. Restrepo, Archivo General de la Nación (Colombia), Bogotá.

Scheibe arrived with Klein at Chivor on April 4, 1914. Over the course of the next several months, he prepared four interim communications[121] and a final report,[122] offering a window into circumstances at the mine during that time. At the outset of his visit, a period of heavy rain made geological fieldwork almost impossible. Progress was also impacted when, on April 20, 1914, Restrepo became seriously ill and lost consciousness. As Scheibe wrote:[123]

> We believed it a crisis in encephalitis but he did not wake up again, he lay motionless. On April 23rd we decided to transport him to Guateque despite the rain. The workers did as much as humanly as possible on the muddy and unstable mountain path. Mr. Klein and

Mr. Restrepo's son, who was working as foreman here, accompanied the transport. On arrival at Guateque late in the evening, Mr. Restrepo died and was buried the day after.

A Colombian certificate of death dated April 24, 1914, was issued documenting Restrepo's passing (figure 21).

When conditions improved, three weeks were spent repairing the mine's aqueduct, after which the first clean but small emeralds were found in

---

[121]Letters by Prof. Robert Scheibe, Historical Archive of the German Ministry of Foreign Affairs.

[122]The final report, dated September 3, 1914, was provided by the grandchildren of Prof. Robert Scheibe.

[123]Letter from Prof. Robert Scheibe, May 1, 1914, Historical Archive of the German Ministry of Foreign Affairs.

May and June and commercial material was mined in July. A representative of the German Residency in Bogotá also visited the mine from July 3 to 16, 1914, and reported on his observations.[124] Between late July and early August, Scheibe finished his investigations, planning to return to Bogotá together with August Klein on August 2.[125] The outbreak of war in early August, however, curtailed such plans and suspended Klein's pursuit of the Chivor project.

Scheibe's final report,[126] dated September 3, 1914, and written in Bogotá, offered his conclusions as to the viability of Chivor. The report began with a detailed description of the geological conditions, then covered both the expected yield and the anticipated costs. As to the yield, he reported:

> In the 4 months of my presence at the mine [April 4 to August 2, 1914] with a labor force of 25 men gem quality emeralds of a value of about 40,000 marks were mined…. I do not doubt that emeralds of a good kind are to be found elsewhere in the above mentioned area and beyond…. I consider the pit itself to be exploitable, especially since the prices of emeralds are high—also in Chivor stones were found that are estimated to 800 marks per carat. The average value of the usable stones found during my time there (1,267 ct = 39,420 marks) is about 31 marks for one carat of raw stones.

The start-up investment for mining equipment was calculated at 150,000 marks. Annual operating costs for 150 workers, six supervisors, one commercial manager, one mining engineer, and one head of operational activities was estimated at 142,000 marks. Taking into account those parameters, in combination with the material recovered during his time there and the purchase price for the mine, Scheibe saw a realistic chance for a successful venture but also an extremely high "risk" in buying the mine under the existing conditions. Hence, he was unable to offer an unqualified recommendation to buy Chivor for the contract price.

WORLD WAR I

The international conflict that became World War I began in August 1914 and had far-reaching consequences for Chivor. Germans who found themselves overseas faced an ongoing series of complications and decisions. Early on, there was hope that hostilities would end quickly and normal business pursuits could be resumed after waiting a few months. As that hope faded, the desire to return home became stronger. However, a simple trip to Germany was hindered by the fact that British warships stopped commercial or passenger ships, even vessels of neutral states, and transported any German passengers to internment camps.

Klein waited, using the time to reprise his efforts to obtain permission for an emerald-cutting enterprise in Colombia. As before, his petition dated November 12, 1914, was swiftly rejected.[127] Klein then left Colombia in December 1914 or January 1915, returning to Germany, possibly under false papers.[128] He entered a cavalry regiment stationed in Ludwigsburg, southern Germany, as a volunteer on February 20, 1915.[129] According to Klein, he felt that this service was a duty he owed to his country.[130] The equipment used at Chivor was held by a custodian in Klein's absence, presumably in hopes of resuming operations in the future.[131]

Scheibe deemed an attempt to return to Germany, combined possibly with years of internment, too risky. He therefore decided to stay in Colombia, working for the government as a geologist. Becoming head of the Comisión Científica Nacional (National Geological Commission), he devoted himself to exploring the country's important mineral resources. For instance, he prepared reports on the Muzo emerald deposit, published in 1916 and 1922, for the Ministro de Hacienda.[132] His work on behalf of the government continued until his return to Germany in the spring of 1920[133] and was recognized with appointment as an honorary professor at the University of Bogotá. Upon request of the government, Scheibe subsequently returned to Colombia in 1921 under a three-year contract, again as the head of the Comisión Científica Nacional.

---

[124]Report by a member of the German Residency in Bogotá, Josef Wipperfeld, July 20, 1914, Historical Archive of the German Ministry of Foreign Affairs.

[125]Letter from Fritz Klein, August 1, 1914, to the German Resident in Bogotá, German Federal Archive.

[126]Courtesy of Andreas Scheibe (grandson of Prof. Robert Scheibe).

[127]Diario Oficial (Colombia), 50, No. 15355 (1914), pp. 1127–1128.

[128]Klein, 1941, 1951.

[129]Military files of the 20th lancer regiment, Ludwigsburg, Germany, Hauptstaatsarchiv Stuttgart.

[130]Klein, 1941, 1951.

[131]"Inventory of the tools of the Chivor mine which are held by Anatolio Morales in El Rosal," January 5, 1916, 2 pp.

[132]The scientific studies on Muzo by Prof. Robert Scheibe were published initially in Spanish and later edited by his son, Dr. Ernst Albrecht Scheibe, in German. See Scheibe, 1916, 1922, 1926. The younger Scheibe, like his father, traveled to Colombia and worked as a geologist from 1924 to 1929.

[133]Rauff, 1926; Strunz, 1970.

Figure 22. In 1917, a group of American and Colombian businessmen and geologists associated with the Carib Syndicate, Ltd., investigated oil fields located at the border between Colombia and Venezuela. Carl K. MacFadden (left) and Wilson E. Griffiths participated in the excursion, which resulted in the 1918 transfer of property referred to as the "Barco concession" to an American oil company. Photo 1917, public domain.

PURCHASE OF CHIVOR BY AN AMERICAN COMPANY (1919)

Following World War I, both Klein and his brother August were interested in continuing with the Chivor project. Nonetheless, several developments during the interim changed their previous plans and expectations. From a personal standpoint, each of the Klein brothers had married in 1919, Fritz to Claire Cullmann and August to Liese Brill, so future work would need to take their new wives into consideration.

From a business perspective, war altered the economic landscape for the Syndicate El Chivor. The exchange rate of the mark decreased dramatically, and the financial situation for at least one investor, Rudolf Hahn & Sons, London, deteriorated substantially.[134] To accommodate this scenario, a new investor in the Syndicate El Chivor was found, the Dutch shipping firm Wm H. Müller & Co., based in The Hague and Rotterdam.[135] In addition to its primary shipping and transport business, Wm H. Müller & Co. participated in various mines and other industrial companies.

After the foregoing preparations were initiated, Klein and his wife Claire left Germany for Bogotá in late July or early August 1919.[136]

Meanwhile, a new competitor for Chivor had entered the fray after Klein's option expired during the war. The Colombian Emerald Syndicate, Ltd. had

been founded in the United States on June 22, 1918,[137] by a group of American bankers and speculators from the oil industry. Those involved were principally associated with the Carib Syndicate, Ltd. and the Colombian Petroleum Co., which pursued commercial ventures in the oil business in Colombia and Venezuela.[138] Key figures included Wilson E. Griffiths (1851–1929) and Carl K. MacFadden (1872–1952).[139] Griffiths and MacFadden (figure 22) made several trips to Colombia between 1917

---

[134]Eugen and Paul Hahn, as well as their brother Rudolf, had been interned in the United Kingdom from 1915 to 1918. Assets of the company in the United States worth $225,000 and in Britain worth £250,000 (equivalent to US $1,250,000) had been confiscated as enemy property. See *Hahn v. Public Trustee*, [1925] Ch. 715 (Eng.); [1926] 95 *Law Journal Reports* 9 (Ch.), pp. 9–22 (Eng.).

[135]Letter from August and Liese Klein, January 4, 1920, to Fritz and Claire Klein. No further relevant documentation was found in archived records of Wm H. Müller & Co., held at the Rotterdam City Archive (Stadsarchief Rotterdam).

[136]Letter from August and Liese Klein, September 26, 1919, to Fritz and Claire Klein.

[137]https://opencorporates.com/companies/us_de/74916.

[138]*The Wall Street Journal*, May 26, 1919, p. 8; *The Honolulu Advertiser*, December 7, 1919, p. 29; *The Wall Street Journal*, May 21, 1920, p. 8; *Encyclopedia of American Biography*, New Series, 9 (1938), pp. 401–402.

[139]*The Pittsburgh Press*, December 29, 1895, p. 12; Escritura 3084, December 27, 1919, Notaria 1, Archivo General de la Nación (Colombia); Rausch, 2014; Torres del Río, 2015. MacFadden's name is also written as Mac Fadden or McFadden.

Carib Syndicate Limited

———

Colombian Emerald Syndicate Ltd.

———

Carib Trading Co.
(Compañia Comercial del Caribe)

———

Oficinas en
Bogotá—Cartagena
Colombia, S. A.

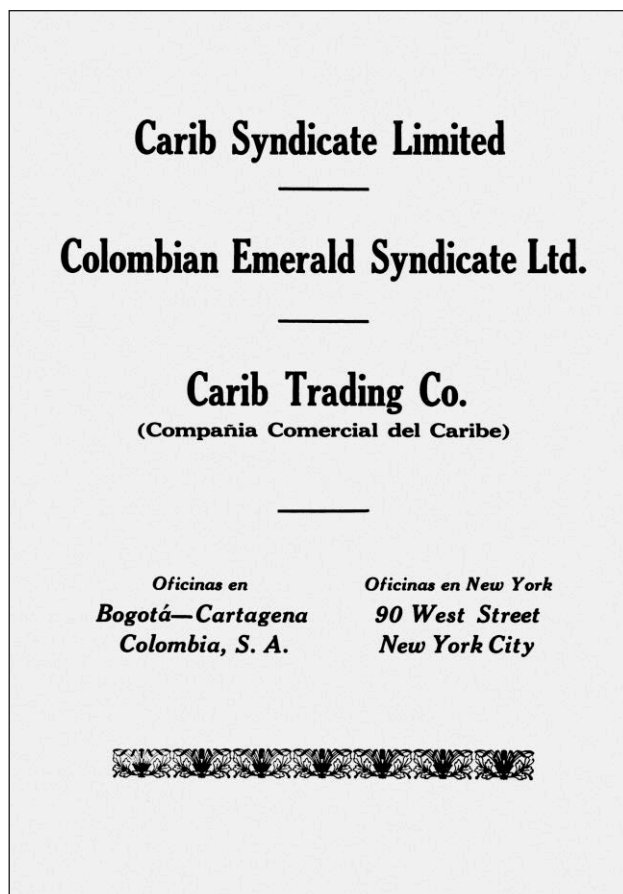Oficinas en New York
90 West Street
New York City

Figure 23. Although the American companies involved in Colombian oil and emerald were formally separate, they were led by the same individuals and were even marketed in joint advertisements. Image from "The Colombian Review," published by the Government Information Bureau of the Republic of Colombia, New York, 1920.

and 1920, focused generally on establishing American interests in the oil business there and particularly on obtaining control of an oil field at the border between Colombia and Venezuela, referred to as the "Barco concession." The emerald business was merely an adjunct to their activities in the oil industry. The companies operating in the two sectors were formally separate but were led by the same officials and were even marketed jointly in advertisements (figure 23).

An option contract to purchase Chivor had already been obtained on April 3, 1918,[140] prior to establishing the Colombian Emerald Syndicate in June 1918.[141] A second option contract was executed on August 13, 1919,[142] with a term running to December 8, 1919.[143] MacFadden's attention had been

drawn to the Chivor emerald mine and its history by Dixon.[144]

Upon his arrival at the Colombian port of Barranquilla, Klein was informed of a legally valid option contract held by the U.S.-based corporation.[145] Hence, Klein could only wait to see if the Americans exercised the option, as expressed by his brother: "Now, December 8 is getting close, and thus the final decision. We are of course all very excited about the result and would be very happy if it turns out in your favor."[146]

In a last-ditch effort to thwart the signing of a deal by the Americans, Klein on December 22, 1919, filed a complaint with the Colombian government alleging that the legal status of Chivor 1 and 2 was unclear.[147] Such a move, which would likely have rendered the property unavailable for sale pending any attendant investigation, resulted only in directives that Klein support his assertions with documentary evidence.[148] When he failed to do so, the complaint was dismissed in April 1921, having had no effect.[149]

On December 27, 1919, Chivor 1 and 2 were purchased from the Sociedad Ordinaria de las Minas de

[140]This first option was mentioned in the sales contract for Chivor, Escritura 3084, December 27, 1919, Notaria 1, Archivo General de la Nación (Colombia).

[141]These two events coincided with the travels of Griffiths and MacFadden, who were together in Colombia in early 1918 before leaving the country on April 20 and arriving in New York on May 3, 1918. Files Wilson E. Griffiths and Carl K. MacFadden, List of United States Citizens, Arriving at Port of New York, May 3, 1918, Ancestry.com. The option was thus signed while they were in Colombia, and the company was incorporated shortly after their return to the United States. Although the actual April 3, 1918, option contract for Chivor has not been found, an option contract with that date and signed by Griffiths was located for the transfer of an oil field concession from Virgilio Barco to the Compañía Colombiana de Petróleo. Escritura 331, April 3, 1918, Notaria 4, Archivo General de la Nación (Colombia).

[142]This second option was also mentioned in the sales contract for Chivor, Escritura 3084, December 27, 1919, Notaria 1, Archivo General de la Nación (Colombia).

[143]Letter from August and Liese Klein, December 5, 1919, to Fritz and Claire Klein; Canova, 1921.

[144]Rainier, 1931, p. 223 (comment by Carl K. MacFadden).

[145]Letter from August and Liese Klein, September 26, 1919, to Fritz and Claire Klein.

[146]Letter by August and Liese Klein, December 5, 1919, to Fritz and Claire Klein. The more dramatic situation suggested by Klein (1941, 1951) and by Canova (1921) appears to have been exaggerated. The Historical Archive of the German Ministry of Foreign Affairs contains only a brief note, dated December 29, 1919, concerning the sale of Chivor to an American company.

[147]Diario Oficial (Colombia), 56, No. 17080–17081 (1920), p. 273.

[148]Diario Oficial (Colombia), 56, No. 17102–17103 (1920), pp. 361–362.

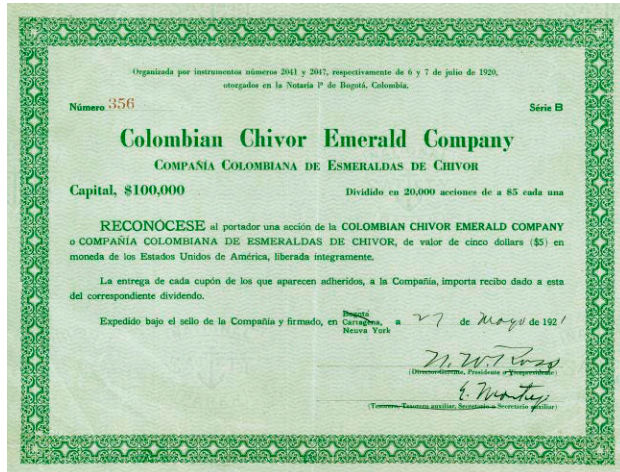[149]Diario Oficial (Colombia), 57, No. 17687–17688 (1921), p. 258.

Figure 24. Share certificate for the Colombian Chivor Emerald Company (Compañía Colombiana de Esmeraldas de Chivor), formed in 1920 in Colombia as the operating company for the U.S.-based Colombian Emerald Syndicate, Ltd., which had purchased the Chivor mines in December 1919. Courtesy of Eduardo Restrepo Ortega.

Chivor by the American group.[150] Pursuant to the sale contract, the mine titles for Chivor 1 and 2 and the land holdings of the Colombian company were transferred for a purchase price of £46,000 (equivalent to US $230,000) to Griffiths and MacFadden. Griffiths and MacFadden were represented in the transaction by Leon J. Canova, acting under a power of attorney dated October 31, 1919.[151]

In retrospect, circumstances rendered it almost a foregone conclusion that the Colombian Emerald Syndicate would not turn away from the opportunity to purchase Chivor. Between the corporation's founding and the time the option was exercised, the price of the 4,000 issued shares had increased from $25 to approximately $1,100,[152] with continued appreciation to $4,000 or $5,000 expected.[153] Moreover, the company had already started mining operations, and president Nathaniel W. Ross (1874–1938) was by October 1919 referring to Chivor as "the company's mine."[154] Civil mining engineer Harold Case Willcox had been hired in December 1919 to map the area for a deeper understanding of the geological setting, and he continued in that position until March 1920.[155] Later, Willcox worked for the Carib Syndicate, Ltd., in Colombia, underscoring the interconnectedness of the companies involved with the American investors.[156]

In July 1920, a local mining company was formed in Colombia by Griffiths and MacFadden to serve as the operating entity for the Colombian Emerald Syndicate.[157] Known as Colombian Chivor Emerald Company (Compañía Colombiana de Esmeraldas de Chivor), stated capital was to consist of 20,000 shares at $5 each (figure 24; again, see table 2).

In September 1920, Ross retired from business and was thereafter succeeded by MacFadden as president of the Colombian Emerald Syndicate.[158] Griffiths served as one of the company's directors, and Dixon acted as the Colombian manager.[159]

By 1921, interests in the titles to the other three Chivor mines, Triunfo de Chivor, Paz de Chivor, and Esperanza de Chivor were represented to be under the ownership or control of the Colombian Emerald Syndicate or the Colombian Chivor Emerald Company,[160] but the nature of any relevant transactions is not otherwise elucidated (again, see box A).

KLEIN'S ACTIVITIES FOR THE COLOMBIAN EMERALD SYNDICATE, LTD. (1920–1921 AND 1922–1923)

After the sale of Chivor to the American corporation at the end of 1919, Klein and his wife remained in Colombia. Although the idea of opening a jewelry shop in Bogotá was apparently broached by the Klein

[150]Escritura 3084, December 27, 1919, Notaria 1, Archivo General de la Nación (Colombia).

[151]Ibid.

[152]A share split was performed in late October to early November 1919, with the value of 50 new shares being equivalent to that of one old share. *The Washington Post*, December 11, 1919, p. 11.

[153]*The Buffalo Enquirer*, May 27, 1919, p. 8; *New York Tribune*, October 26, 1919, p. 26; *Quad-City Times*, October 27, 1919, p. 12; *Springfield Missouri Republican*, November 7, 1919, p. 6; *The Salt Lake Tribune*, December 3, 1919, p. 18; *The Washington Post*, December 11, 1919, p.11.

[154]*The Wall Street Journal*, October 29, 1919, p. 15.

[155]Schwarz, 1953.

[156]*American Society of Civil Engineers, Year Book 1920*, p. 312; *Oildom*, 12 (1921), pp. 28–30.

[157]Escritura 2041, July 6, 1920, Notaria 1, and Escritura 2047, July 7, 1920, Notaria 1, Archivo General de la Nación (Colombia). Diario Oficial (Colombia) 56, No. 17238-17239 (1920), pp. 99–100.

[158]MacFadden, 1920; *National Petroleum News*, 12, December 1, 1920, pp. 75–76; *Pittsburgh Daily Post,* April 27, 1921, p. 11; Canova, 1921; Moore and Wilson, 2016. MacFadden had also become president of the Carib Syndicate, Ltd., in September 1920. *The New York Times*, September 10, 1920, p. 24.

[159]*Moody's Manual of Investments: American and Foreign*, 11, Part 2 (1920), p. 1189; *Moody's Manual of Investments: American and Foreign*, 12, Part 2 (1921), p. 697; Canova, 1921.

[160]Canova, 1921.

Figure 25. Fritz Klein was unable to purchase the Chivor mining titles in 1919 on account of intervening developments during World War I. The U.S.-based Colombian Emerald Syndicate, Ltd., obtained option contracts in the interim and subsequently completed the acquisition. Klein remained in Colombia and was hired in the fall of 1920 by the new mine owners to lead operations at Chivor. Photo circa 1920 to 1921, courtesy of Carola Kroll.

brothers, such a plan was never implemented. Instead, Klein (figure 25) was hired by the Colombian Emerald Syndicate for two terms as head of mining operations at Chivor, from 1920 to 1921 and 1922 to 1923.[161]

At the time of Klein's hiring, Dixon had been overseeing Chivor's administration.[162] According to Klein (1941, 1951), he was hired because Dixon had failed

to obtain a profitable supply of gem-quality emeralds. However, during Klein's first engagement, Dixon continued to be involved in the background, still working for the Colombian Emerald Syndicate.

At that time, the mine was worked exclusively by the traditional open-cut method of preparing terraces or steps in the extremely steep environment (figure 26). During the initial contract period of approximately six months from the fall of 1920 to the spring of 1921, Klein was assisted by several American mining engineers, including Eugene Brossard.[163] A notable discovery occurred in December 1920 when a 632 ct emerald crystal (figure 27) was found at Chivor by miner Justo Daza.[164] Klein (1941, 1951) recounted that Daza located the cavity and that Klein himself carefully removed the crystal. The emerald was personally transported to New York by Brossard in January 1921.[165] The extraordinary stone generated great interest in the United States, and its arrival in New York was widely reported in the nation's press.[166]

The crystal was subsequently named the "Patrizius" or "Patricia" emerald after the patron saint of Ireland, the green island, according to Klein.[167] Speculation that it might have been named after Klein's

[161]Klein, 1941, 1951. No known contracts have been preserved to offer specific details, but general parameters and time frames can also be drawn from other contemporaneous materials such as newspaper reports and travel documents.

[162]An example of Christopher Dixon's leadership can be found in the form of a certificate he signed on September 27, 1920, at the time of Anibal Restrepo's departure from employment at Chivor and recognizing nine months of exemplary service for the Colombian Emerald Syndicate, Ltd.

[163]Eugene Brossard's work in Colombia was recognized in an alumni publication of his alma mater: "Eugene Brossard Madison, is in the employ of the Colombian Emerald Syndicate… as assistant to the superintendent of the Chivor emerald mines." *The Wisconsin Alumni Magazine*, 21, No. 6 (1920), p. 171. Another assistant at Chivor was F. Stewart Turneaure. *Wisconsin State Journal*, September 4, 1921, p. 7; *Proceedings of the Geological Society of America for 1945*, published 1946, p. 106. Yet another American involved at Chivor was the mining engineer William Burns, who was first employed by the Colombian Emerald Syndicate, Ltd., returning to New York in May 1922, and who later worked for the Colombia Emerald Development Corporation at Chivor in 1925. File William Burns, List of United States Citizens, Arriving at Port of New York, May 14, 1922, MyHeritage.com; Brock (1929).

[164]Canova, 1921; Klein 1941, 1951; Johnson, 1959, 1961; Weldon et al., 2016.

[165]File Eugene Brossard, List of United States Citizens, Arriving at Port of New York, January 14, 1921, MyHeritage.com.

[166]*The Brooklyn Daily Eagle*, February 2, 1921, p. 1; *The Montana Standard*, February 7, 1921, p. 3; *Sikeston Standard*, February 8, 1921, p. 3; *The Tennessean*, February 15, 1921, p. 9. Inconsistently, multiple articles or reports in American newspapers from February or March 1921 provided a weight of 630 ct.
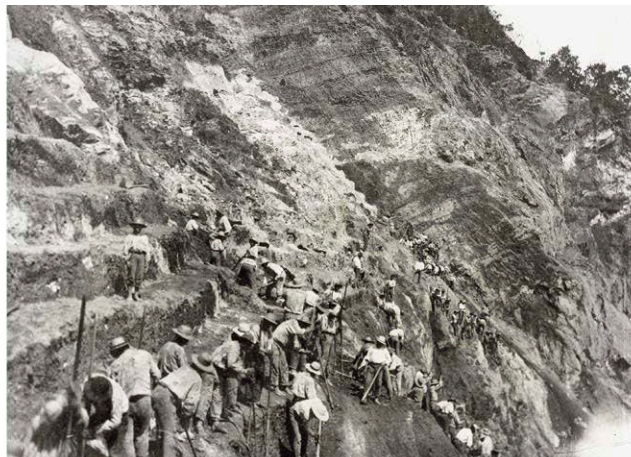
[167]Klein, 1941.

Figure 26. Mining at Chivor in the 1920s was performed exclusively by the open-cut method, preparing terraces or narrow steps in the extremely steep environment. Indigenous miners worked with long iron bars and hoes to remove the overburden and locate emerald-bearing veins or cavities. Photos of open-cast mining at Banco Klein, circa 1920 to 1921, courtesy of Carola Kroll.

daughter[168] (whose name was Susanne)[169] is unfounded. Whether to cut the stone was initially debated, but the crystal was preserved as such.[170] The

Figure 27. Left: In 1920, while Fritz Klein was leading mining operations at Chivor, an extraordinarily large emerald crystal weighing 632 ct was discovered in the open-cast mine. The crystal was transported to New York by mining engineer Eugene Brossard and widely reported in the American press. The emerald was donated to the American Museum of Natural History, New York, in 1953. Courtesy of the American Museum of Natural History. Right: Klein (1941) also depicted the crystal, named the "Patricia" emerald.

632 ct emerald crystal is now in the collection of the American Museum of Natural History, New York, inventory number 42027, and was donated to the museum in 1953 by Mr. and Mrs. J. Robert Rubin.[171] Rubin (1882–1958), a New York lawyer, served as one of the trustees and/or directors of the Colombian Emerald Syndicate in the 1920s.[172] Prior to its donation, the emerald was transferred internally among company officials after financial pressures in March 1923 led the company to borrow $3,000 from two of the directors, pledging the emerald as security.[173]

After Klein's first contractual commitment with the Colombian Emerald Syndicate ended, he and his wife returned to Germany via New York. They arrived at the New York port in August 1921 and may have spent a period of several months before continuing their journey.[174]

[168]https://www.internetstones.com/patricia-emerald-632-carat-uncut-colombian-origin-chivor-mine.html.

[169]Carola Kroll (granddaughter of Fritz Klein), pers. comm., 2017.

[170]Jewelers' Circular, 82, No. 6 (1921), p. 79.

[171]Press release, November 9, 1953, American Museum of Natural History, New York; Jamie Newman, American Museum of Natural History, New York, pers. comm., 2016.

[172]Encyclopedia of American Biography, New Series, 9 (1938), pp. 401–402.

[173]Jewelers' Circular, 86, No. 10 (1923), p. 83.

[174]The documentation cites the Colombian Emerald Syndicate, Ltd., as Fritz Klein's employer and gives four months as the intended length of stay in the United States. File Fritz Klein, List or Manifest of Alien Passengers for the United States Immigration Officer at Port of Arrival, New York, August 1921, MyHeritage.com.
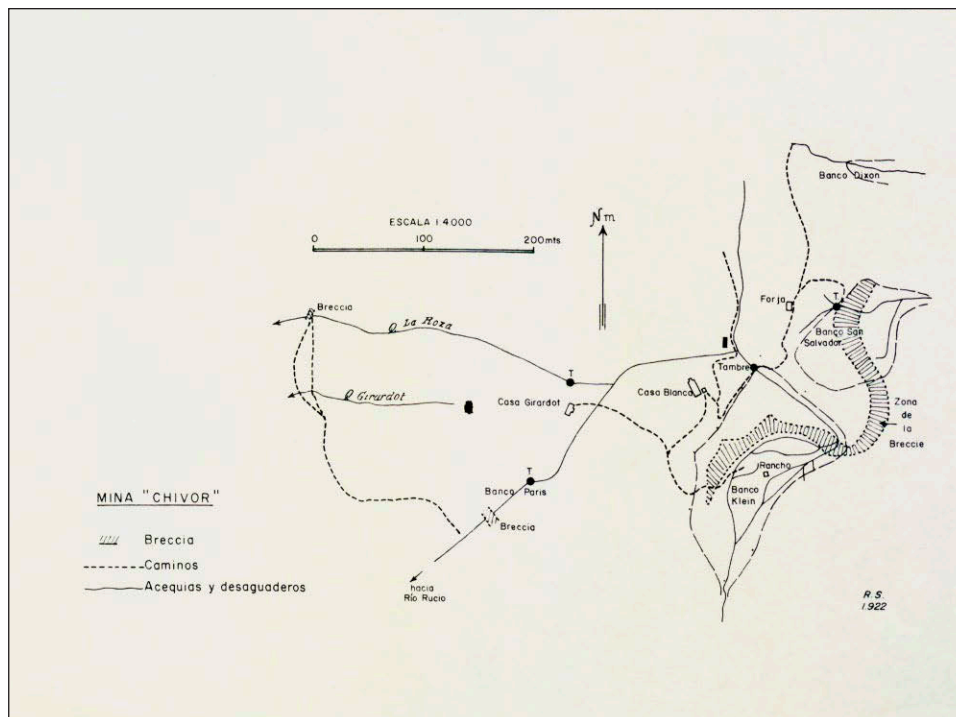
Figure 28. Hand-drawn map showing the topography of the Chivor mine and related geological details, signed R.S. [Robert Scheibe] 1922. The drawing also identified the locations principally worked by Fritz Klein and Christopher Dixon, labeled "Banco Klein" and "Banco Dixon," respectively. Prof. Robert Scheibe collection, University Library Freiburg.

Following Klein's initial engagement at the helm in Chivor, Dixon resumed leadership of mining operations.[175] Dixon reportedly claimed that during the six months from June to December 1921, emeralds worth $176,000 were recovered under his management.[176] Meanwhile, the corporate leadership in New York had undergone a transition. MacFadden resigned in September 1921 from his role at the head of the Colombian Emerald Syndicate and was succeeded by Julian A. Arroyo.[177] In summer of 1922, the company's vice president, Joseph J. Paris, visited Colombia, returning to New York on June 15.[178] About one week later, Dixon arrived in New York,[179] and he spent time in the city during June and July,[180] presumably meeting with Colombian Emerald Syndicate officials to discuss further activities at Chivor. Because no documentation after 1922 mentions Dixon in a management role at Chivor, the implication is that no agreement for his continued employment was reached.[181] That, in turn, might have led to the rehiring of Klein.

The precise dates of Klein's second contractual commitment with the Colombian Emerald Syndicate are unknown. He first traveled alone to Colombia, and his wife followed in August 1922.[182] Good production was reported during this time,[183] and Scheibe returned to conduct further scientific study at Chivor (figure 28).[184] Nevertheless, the financial support for work at the mine was reduced, and, ultimately, mining activities were terminated. Even now, the reasons that precipitated the decline remain shrouded in history. On the corporate side, Paris replaced Arroyo as president in October 1922.[185] Min-

[175]*Moody's Manual of Investments: American and Foreign*, 11, Part 2 (1920), p. 1189; *Moody's Manual of Investments: American and Foreign*, 12, Part 2 (1921), p. 697; Canova, 1921.

[176]Gilles, 1930.

[177]*New York Tribune*, September 13, 1921, p. 6; *Engineering and Mining Journal* 112 (1921), p. 466; *The New York Herald*, September 13, 1921; *The New York Times*, September 13, 1921. Some months later Carl K. MacFadden was also dismissed from his role at the Carib Syndicate, Ltd., oil company. *New York Times*, April 18, 1922, p. 32.

[178]File Joseph Paris, List or Manifest of Alien Passengers for the United States Immigration Officer at Port of Arrival, New York, June 1922, MyHeritage.com; *Investor & Trader*, July 1, 1922, p. 6.

[179]File Christopher Dixon, List or Manifest of Alien Passengers for the United States Immigration Officer at Port of Arrival, New York, June 1922, MyHeritage.com.

[180]*The Washington Times*, July 2, 1922, p. 3.

[181]*Moody's Manual of Investments: American and Foreign*, 13, Part 2 (1922), p. 874; *Investor & Trader*, June 24, 1922, p. 6.

[182]Claire Klein traveled alone from Hamburg to Puerto Colombia. File Claire Klein, Hamburger Passagierlisten, August 1922, Ancestry.de.

[183]*Investor & Trader*, August 19, 1922, p. 2, September 9, 1922, p. 2, and September 30, 1922, p. 12; Klein, 1941, 1951.

[184]Prof. Robert Scheibe fell ill in Colombia in February 1923 and died on March 3, following appendicitis and peritonitis. As a result, the Chivor study was never completed. A decree by the Colombian President dated March 8, 1923, was issued in honor of the deceased, and numerous Colombian newspapers carried his obituary. The congress in Bogotá honored his work and his selfless service to Colombia in June 1923 with an official state ceremony. Historical Archive of the German Ministry of Foreign Affairs. Diario Oficial (Colombia) 59, No. 18841-18842 (1923), p. 629.

[185]*Investor & Trader*, October 14, 1922, p. 8.

ing engineer Brossard, with whom Klein had worked at Chivor, returned to the United States in July 1923.[186]

BANKRUPTCY OF THE COLOMBIAN EMERALD SYNDICATE, LTD. (1923)

As noted above, financial pressures at the company had become severe by March 1923 on account of expenses that exceeded the income generated from emerald sales. By April 4, 1923, an involuntary petition in bankruptcy had been filed against the Colombian Emerald Syndicate in the United States District Court in New York.[187] At that time, Paris was still serving as the president, and Wolcott H. Pitkin was appointed receiver for purposes of the bankruptcy proceeding.[188] Liabilities were initially estimated at between $45,000 and $48,000.[189] Schedules detailing the assets of $314,039 and liabilities of $37,816 were then filed with the court on December 17, 1923.[190]

At that time, the Colombian Emerald Syndicate owned the Chivor 1 and 2 mine titles and a one-third interest in the titles to the three other mines of the Chivor group.[191] Outstanding debts were owed to, among others, present or former presidents, vice presidents, and/or directors of the corporation, such as MacFadden, Griffiths, Arroyo, and Rubin. Other listed creditors included Klein, mining engineer Brossard, the corporation's attorney in Colombia Miguel S. Uribe Holguin, the Carib Syndicate, and the German firm Hahn & Klein.[192]

Meanwhile, a stockholders' committee was established to devise a method of raising funds to pay off the liabilities, and it was proposed that a new company would be formed to bid for the assets in an anticipated bankruptcy auction.[193] A special meeting of creditors was held in January 1924 to consider and act upon offers to purchase the property.[194]

The mining titles for Chivor 1 and 2 and the related land ownership were sold on or about August 23, 1924, to the recently formed U.S. company Chivor Emerald Corporation.[195] Another new entity, the Colombia Emerald Development Corporation, was then established on November 7, and the Chivor claims and land were transferred to that company in late 1924.[196] Throughout these machinations, the value of stock in the Colombian Emerald Syndicate fell precipitously, dropping from 65 cents per share in June 1922 and 40 cents in December 1922 to 5 cents in April 1923 and 1 cent in December 1923.[197] The downward spiral continued thereafter, and the value was reported in 1925 at $1 for 600 shares.[198]

With his employer's demise, Klein returned to Germany and over the following months established his own company in Idar in 1924, focused on the emerald trade.[199] He decided to travel to Colombia once again in March 1925.[200] At that time, the sale of Colombian emeralds was still strictly controlled by the government, with the only authorized channel being through the firm Rosenthal in Paris. Klein's aim was to obtain a similar authorization under which emeralds could also be sold to him directly or to a partner company. After intensive negotiations with Colombian officials, Klein was hired by the government as an evaluator for rough emeralds in Paris, in cooperation with the Colombian government's representative in the city, J.M. Arango.[201] Klein was never again active as a miner in Colombia, but remained at the center of the emerald trade. Several trips to Colombia in the second half of the 1920s and the early 1930s reflect his ongoing involvement.

[186]File Eugene Brossard, List of United States Citizens, Arriving at Port of New York, July 1923, MyHeritage.com.

[187]*Jewelers' Circular*, Vol. 86, No. 10 (1923), p. 83; *The Wall Street Journal*, April 5, 1923, p. 14; *The Cumulative Daily Digest of Corporation News*, No. 2 (1923), pp. 142–143.

[188]*The Wall Street Journal*, April 5, 1923, p. 14; *The Cumulative Daily Digest of Corporation News*, No. 2 (1923), p. 142; *Jewelers' Circular*, Vol. 86, No. 10 (1923), p. 83.

[189]*The Wall Street Journal*, April 5, 1923, p. 14; *The Cumulative Daily Digest of Corporation News*, No. 2 (1923), pp. 142–143; *Jewelers' Circular*, Vol. 87, No. 22 (1923) p. 91.

[190]*Jewelers' Circular*, Vol. 87, No. 22 (1923), p. 91; *The Cumulative Daily Digest of Corporation News*, No. 4 (1923), p. 118.

[191]*Jewelers' Circular*, Vol. 86, No. 10 (1923), p. 83; *Jewelers' Circular*, Vol. 87, No. 22 (1923), p. 91.

[192]A company based in Idar, Germany, owned by August Klein and his brother-in-law August Hahn.

[193]*The Cumulative Daily Digest of Corporation News*, No. 2 (1923), p. 143; No. 3 (1923), p. 125.

[194]*The Cumulative Daily Digest of Corporation News*, No. 1 (1924), p. 164.

[195]*The Cumulative Daily Digest of Corporation News*, No. 3 (1924), p. 150, 161.

[196]*The Cumulative Daily Digest of Corporation News*, No. 4 (1924), pp. 209, 222; Winkler, 1928; Rainier, 1929, 1931.

[197]*The Buffalo Enquirer*, June 30, 1922, p. 5; *The Baltimore Sun*, December 30, 1922, p. 11; *Democrat and Chronicle*, April 27, 1923; *The Tampa Tribune*, December 14, 1923, p. 15. Additional details charting stock values can be traced through issues of *Investor & Trader* published in 1922 and 1923.

[198]*Engineering and Mining Journal-Press*, 21 (1925), p. 999.

[199]Carola Kroll (granddaughter of Fritz Klein), pers. comm., 2017.

[200]Klein traveled via the port of Hull in Great Britain to Santa Marta in Colombia. https://www.findmypast.co.uk/Colombia. Findmypast.co.uk

[201]J.M. Arango was nominated General Consul of Colombia in Paris in March 1925 and was responsible for the selling of emeralds to Rosenthal. Diario Oficial (Colombia), 61, No. 19862 (1925), p. 519.

TABLE 4. History of Chivor, 1880–1925.

Date	Events in Colombia, Germany, or the United States
1880s	Search for and rediscovery of old native and Spanish tunnels by F. Restrepo
March 1889	Mining titles for Chivor 1 and 2 are granted to F. Restrepo, E. González, B. Escobar, and Núñez & Compañía
August 1896	F. Restrepo and L. Correa are referred to as the mine owners; E. González declares the Chivor mines "abandoned"
February 1898	Transfer of the mining titles to E. González
August 1898	Formation of a company by F. Restrepo and three companions; transfer of the mining titles to the company
1898–1899	Cleaning of former tunnels and repair of water channels at the mine by F. Restrepo
1899–1909	Numerous sales of shares involving different shareholders take place
1902	First publications by the British Vice-Consul S. Dixon mentioning the rediscovery of Chivor
August 1904	The five principal shareholders buy land from A. Acosta
December 1904	Three additional claims near Chivor 1 and 2 are registered for the Triunfo de Chivor, Paz de Chivor, and Esperanza de Chivor mines, with F. Restrepo, C. Dixon, and H. Campo named as co-owners of the three titles
1905–1906	C. Dixon attempts but fails to sell the three additional mines
February 1912	Preliminary option contract between F. Klein, H. Span, and the mine owners
June 1912	Formalized option contract with the mine owners; F. Klein and F. Restrepo start mining at Chivor
End of 1912	A. Klein joins the miners at Chivor
March 1913	F. Klein and F. Restrepo travel to Germany; A. Klein remains at Chivor
July 1913	Option contract with F. Klein is extended by Klein's lawyer
November 1913	F. Restrepo leaves Germany for Colombia
December 1913	F. Klein's option contract is extended again
February 1914	Formation of the "Syndikat El Chivor"; F. Klein and R. Scheibe leave Germany for Colombia
April 1914	R. Scheibe begins evaluation of Chivor; Restrepo becomes ill and dies at Guateque
August 1914	R. Scheibe finishes the evaluation of Chivor; outbreak of World War I
End of 1914 or early 1915	F. Klein leaves Colombia for Germany
1915–1916	C. Dixon again fails to sell the three additional mines
April 1918	Option contract between W.E. Griffiths, C.K. MacFadden, and the mine owners
June 1918	Formation of the "Colombian Emerald Syndicate, Ltd."; N.W. Ross becomes president
July or August 1919	F. Klein and his wife leave Germany for Colombia
August 1919	Second option contract between W.E. Griffiths, C.K. MacFadden, and the mine owners
December 1919	Purchase of Chivor 1 and 2 by W.E. Griffiths and C.K. MacFadden
By early 1920	C. Dixon serves as Colombian manager for the "Colombian Emerald Syndicate, Ltd."
By September 1920	C.K. MacFadden becomes president of the Colombian Emerald Syndicate, Ltd., succeeding N.W. Ross
Fall 1920–Spring 1921	F. Klein serves as head of mining operations at Chivor
December 1920	632 ct "Patricia" emerald is found and sent to New York
June–December 1921	C. Dixon serves as head of mining operations at Chivor
September 1921	C.K. MacFadden resigns as president and is succeeded by J.A. Arroyo
June–July 1922	C. Dixon travels to New York and presumably meets with company officials to discuss further activities at Chivor
Summer 1922–1923	F. Klein again serves as head of the mining operations at Chivor
October 1922	J.A. Arroyo is succeeded by J.J. Paris
By April 1923	An involuntary bankruptcy petition is filed in New York against the "Colombian Emerald Syndicate, Ltd."
August 1924	Properties are sold to the "Chivor Emerald Corporation" in a bankruptcy sale
End of 1924	Properties are transferred to the "Colombia Emerald Development Corporation"

LEGENDS AND REALITY: KLEIN AND RESTREPO

The present authors have endeavored to describe the events between 1880 and 1925 to the extent corroborated by contemporaneous primary documents, without filling gaps with dramatizations and apparent fabrications, some of which have been repeated so often as to become accepted "facts." Also, no effort has been made to explain the origin of these discredited or unverified views. Consequently, the story given here leaves various points open, waiting for future closure through discovery of further records, whether in Colombian archives or elsewhere. A few of these lingering ambiguities and the milieu in which they arise may be highlighted as follows.

Klein's 1941 memoir describes in a lively way his travels in South America, always connected with the pursuit of new gem deposits. It went to press in the middle of World War II and was geared toward a circle of readers interested in gemstones and the "adventures" associated with their discovery, mining, and trading. The book was not intended to be a historical document, consistent in all aspects with the rather complex and vacillating legal situation in Colombia, but was written for the entertainment of the interested reader.

Notably, the book was penned after an interval of almost 30 years, in terms of events before 1915, and nearly 20 years, based on the events after 1918. It is not known what contemporaneous documents and records were available to Klein when drafting the original manuscript or to what extent such manuscript was edited by the publisher or elsewhere, much less the expertise or awareness of those involved in the editorial process. A degree of liberality with facts is evidenced by the statement on the back cover of the 1941 edition referring to "drill holes that produced surprising results," although no underground mining activities or their results were mentioned in the pages.

Looking at the chronology of events (see table 4), it can be seen that actual developments in Germany and Colombia, especially regarding the acquisition of Chivor, formed a rough framework for the story told by Klein. This background was supplemented and embellished in some places and even substantially dramatized in others. For instance, the purported one-and-a-half-year search for the first emeralds in Chivor, Restrepo's death in 1914, and the "fight" for the mine with the American competitors in 1919 are all illustrative of the tendency to sensationalize.

Nonetheless, Klein did recount a large number of details that have been verified by contemporaneous materials, particularly concerning travel arrangements and individuals involved. The names offered for ships by which he journeyed between Germany, Colombia, and the United States have been corroborated by manifests, contracts, or letters, and many persons are accurately named and characterized, aside from minor spelling errors (e.g., the Colombian Emerald Syndicate's attorney Uribe-Holguin and Klein's lawyer Cadavid in Bogotá). On the other hand, some key figures are inexplicably absent or given a much diminished role. Stauch, a principal investor in the German group, is missing, and Klein's brother-in-law Jäckh is given little credit for his crucial influence in obtaining protection for Klein to return to Colombia in 1911 and in facilitating contact with potential investors such as Schacht. The name of his own brother August, who spent nearly two years at Chivor, is never mentioned.

Further complicating the situation created by the dramatized version of events is the problem of gaps in the historical record. Regarding Restrepo, for example, certain aspects of his activities are clear, while others are unexplained. Materials found to date are silent as to his partner Correa's involvement in the search for the forgotten Chivor mines in the 1880s; the reasons why the mining titles were twice transferred, first from Restrepo and three partners to Restrepo and Correa between 1889 and 1896, and later from Restrepo and Correa to González between 1896 and 1898; and the rationale for González shortly thereafter in 1898 to form a new entity in partnership with Restrepo and the other two original title applicants. Restrepo's activities during several largely silent periods and his involvement in a range of other ventures, such as farming and the coffee trade,[202] are equally obscure.

The record is likewise deficient as to the dealings of the Colombian Emerald Syndicate, including Dixon's mining activities for the company, the circumstances that led to Klein's employment simultaneously with Dixon during one interval, and the reasons precipitating the 1923 bankruptcy. Thus the story, and the search, continues.

---

[202]Gaceta Judicial (Colombia), 20 (1911), pp. 49–57.

REFERENCES

Acosta J. (1848) *Compendio histórico del descubrimiento y colo-nización de la Nueva Granada en el siglo décimo sexto.* Im-prenta de Beau, Paris.

Aguado P. de, Fr. (1906) *Recopilación Historial.* Imprenta Na-cional, Bogotá.

Aguilar F.C. (1884) *Ligero estudio sobre las minas de Méjico y Colombia.* Anales de la Instrucción Pública en los Estados Unidos de Colombia, Vol.7, pp. 493–528.

Ancízar M. (1853) *Peregrinación de Alpha: por las provincias del norte de la Nueva Granada en 1850 y 51.* Imprenta de Echev-erría Hermanos, Bogotá.

Anderton R. (1953) *Tic-Polonga.* Doubleday, New York.

——— (1954) *Tic-Polonga.* Museum Press Limited, London.

Annual report on Colombia for the year 1913. In: Philip G., Ed., British documents on foreign affairs – reports and papers from the Foreign Office Confidential print. Part I, from the mid-nine-teenth century to the First World War. Series D, Latin America, 1845–1914, published 1992, pp. 182–193.

Atuesta D. (1899) *Informe relativo al levantamiento de los planos y mensura de los terrenos de las minas de esmeraldas de propiedad de la nación.* Imprenta Nacional, Bogotá.

Bermúdez J.A. (1966) Antonio José Cadavid. *Revistas Universidad Pontificia Bolivariana*, Vol. 28, No.100, pp. 347–354.

Brisson J. (1899) *Viajes por Colombia en los años de 1891 á 1897.* Imprenta Nacional, Bogotá.

Brock F.W. (1929) Investment pitfalls. *Oral Hygiene*, Vol. 19, pp. 789–795.

Bullman C. (1892) *The Mining Laws of the Republic of Colombia.* The Scientific Publishing Company, New York.

Bürger O. (1919) *Reisen eines Naturforschers im tropischen Süd-amerika.* Dieterich'sche Verlagsbuchhandlung, Leipzig.

Cadavid A.J. (1913) *En defensa del derecho de propiedad.* Imprenta de La Luz, Bogotá.

Calvo Perez B. (1992) *Minas y minerales de Iberoamérica.* IGME, Madrid.

Canova L.J. (1921) *Legend of the Discovery of Emeralds in the Colombian Andes.* Colombian Emerald Syndicate, Ltd., New York.

Céspedes Cubides J.E. (2017) *Reminiscencias de la Guerra de los Mil Días. Descripción y análisis del régimen de responsabili-dad extracontractual del Estado, con posterioridad a la Guerra Civil de 1899 a 1902.* Universidad del Rosario, Facultad de Ju-risprudencia, Maestria en derecho administrative, Bogotá.

Díaz C.A. (1967) *Páginas de Historia Colombiana. Recuerdo de Antonio José Cadavid.* Imprenta del Departamento, Bucara-manga.

Dixon S.S. (1902) Mining in Colombia in 1901. *The Mining Jour-nal*, Vol. 72, p. 429.

Domínguez R.A. (1965) *Historia de las esmeraldas de Colombia.* Gráficas Ducal, Bogotá.

Eder P.J. (2017) A banker invites other bankers to make money in Colombia. In Farnsworth-Alvear A., Palacios M., and Gómez López A.M., Eds., *The Colombia Reader: History, Culture, Pol-itics.* Duke University Press, Durham and London, pp. 457–463.

Enciclopedia universal ilustrada europeo-americana: Apéndice 2 (BED-CEQ). (1931) Espasa-Calpe, Madrid.

Esquivel Triana R. (2001) Fuentes para la historia agraria e indus-trial de la provincia de Neiva 1778-1938. *Memoria y Sociedad: Revista del Departamento de Historia y Geografía*, Vol. 5, No. 9, pp. 61–88.

Fals-Borda O. (1955) Odyssey of a sixteenth-century document – Fray Pedro de Aguado's "Recopilacion Historial." *The Hispanic American Historical Review*, Vol. 35, No.2, pp. 203–220.

Falz E. (1939) *Von Menschen und Edlen Steinen.* Selbstverlag, Idar.

Fernández Piedrahita L. (1881) *Historia general de las conquistas del nuevo reino de Granada.* A la S.C.R.M. de D. Carlos Se-gundo Rey de las Españas y de las Indias. Imprenta de Medardo Rivas, Bogotá.

Fortaleché D., Lucas A., Muyal J., Hsu T., Padua P. (2017) The Colombian emerald industry: Winds of change. *G&G*, Vol. 53, No. 3, pp. 332–358, http://dx.doi.org/10.5741/GEMS.53.3.332

Francis J.M. (2007) *Invading Colombia.* The Pennsylvania State University Press, University Park, PA.

Friede J. (1964) Fray Pedro Aguado, con Ocasión del 450° Aniver-sario de su Nacimiento. *The Hispanic American Historical Re-view*, Vol. 44, No. 3, pp. 382–389.

Gamba F.P. (1913) Emerald fields of Colombia. *Mining and Scien-tific Press*, Vol. 107, p. 345.

Geografía económica de Colombia, Tomo III: Boyacá, 1936. Bo-

gotá, Contraloría General de la República.

Gilles V.A. (1930) Geology of the Chivor emerald mine. In Buis, O. and Bronkie W.F., Eds., *Guide Book to the Geology of the Chivor Emerald Mine*. Colombian Society of Petroleum Geologists and Geophysicists, published 1966, pp. 5–18.

González E. (1911) *Esmeraldas de las minas de Muzo y Coscuez*. Imprenta Moderna, Bogotá.

Groot J.M. (1869) *Nueva Granada, escrita sobre documentos auténticos*. Imprenta a cargo de Foción Mantilla, Bogotá.

Jäckh E. (1954) *Der Goldene Pflug*. Deutsche Verlags-Anstalt, Stuttgart.

Johnson P.W. (1959) The emeralds of Chivor today. *Lapidary Journal*, Vol. 13, No. 4, pp. 516–524.

——— (1961) The Chivor emerald mine. *Journal of Gemmology*, Vol. 8, No. 4, pp. 126–152.

Klein F. (1941) S*maragde unter dem Urwald*. Oswald Arnold Verlag, Berlin.

——— (1951) *Smaragde unter dem Urwald*. Selbstverlag, Idar-Oberstein.

Kopper C. (2006) *Hjalmar Schacht: Aufstieg und Fall von Hitlers mächtigstem Bankier*. Deutscher Taschenbuch Verlag, Munich.

Lane K. (2010) *Colour of Paradise: The Emerald in the Age of Gunpowder Empires*. Yale University Press, New Haven and London.

Latham E.B. (1911) The newly discovered emerald mines of "Somondoco." *The School of Mines Quarterly*, Vol. 32, No. 3, pp. 210–214.

Legrand C. (1988) *Colonización y protesta campesina en Colombia (1850-1950)*. Universidad Nacional de Colombia, Bogotá.

Levinson O. (2007) *Diamanten im Sand: Das wechselvolle Leben von August Stauch*. Kuiseb Verlag, Windhoek.

MacFadden C.K. (1920) Petroleum in Colombia. *The Colombian Review*, Vol. 1, pp. 36–38.

Martin de Retana J.M., Ed. (1990) *El gran libro de la esmeralda*. Editorial la Gran Enciclopedia. Vasca, Bilbao.

Martínez F.A. (1950) Don Emiliano Isaza. *Thesaurus: Boletín del Instituto Caro y Cuervo*, Vol. 6, No. 2, pp. 271–278.

Martínez Covaleda H.J., Martínez Covaleda R. (1996) Economía y región: aproximación a la historia del siglo XIX en el Huila. In Tovar Zambrano, B., Ed., *Historia general de Huila, Vol. 3,* Academia Huilense de Historia, pp. 15–76.

Montaña F. (1915) *Renta de esmeraldas: Apuntes fiscales*. The Salesian Press, London.

Moore T.P., Wilson W.E. (2016) The emerald mines of Colombia. *The Mineralogical Record*, Vol. 47, No. 1, pp. 5–68.

Moreno F.A. (1772) Estado del Virreinato de Santafé, Nuevo Reino de Granada. *Anales de la Universidad Nacional de los Estados Unidos de Colombia*, Vol. 4, No. 19, 1870, pp. 34–96.

Moreno Calderón D. (2011) Cronología de la historia del Estado Soberano del Tolima. *HUILA*, Vol. 14, No. 62, pp. 29–67.

Ochoa Ortiz F. (1921) Immigration into Ecuador. *The Republic of Ecuador*, Vol. 1, No. 1, pp. 24–25.

Plaza J.A. (1850) *Memorias para la historia de la Nueva Granada desde su descubrimiento hasta el 20 de julio de 1810*. Imprenta del Neo-Granadino, Bogotá.

Pogue J.E. de (1917) The emerald deposits of Muzo, Colombia. *Transactions of the American Institute of Mining Engineers*, Vol. 55, pp. 910–934.

Quintero A., Centeno R. (2007) *Hacendados, comerciantes y negociantes de Neiva a finales del siglo XIX: actores, capitales, sociedades y negocios*. Universidad Surcolombiana, Neiva.

Rainier P.W. (1929) The Chivor-Somondoco emerald mines of Colombia. The American Institute of Mining and Metallurgical Engineers, Technical Publication No. 258.

——— (1931) The Chivor-Somondoco emerald mines of Colombia. *Transactions of the American Institute of Mining and Metallurgical Engineers AIME*, Vol. 96, pp. 204–223.

——— (1933) Las minas de esmeraldas de Muzo y Coscuez. Internal Report printed 1958 in *Boletín de Minas* Vol. 5, Nos. 56–57, pp. 10–19.

——— (1942) *Green Fire.* Random House, New York.

Rauff H. (1926) Robert Scheibe †. Gedächtnisreede. *Jahrbuch der Preußischen Geologischen Landesanstalt zu Berlin*, Vol. 47, No. 2, pp. 63–71.

Rausch J.M. (2014) *Colombia and World War I: The Experience of a Neutral Latin American Nation during the Great War and its Aftermath, 1914-1921*. Lexington Books, Lanham, Maryland.

Scheibe R. (1916) Minas de Muzo. Informe del Ministro de Hacienda (Colombia) 1916, pp.181–198.

——— (1922) Informe del doctor Robert Scheibe sobre la mina de Muzo. *Informe del Ministro de Hacienda al Congreso de 1922*, pp. 99–112.

——— (1926) Die Smaragdlagerstätte von Muzo (Kolumbien) und ihre nähere Umgebung. *Neues Jahrbuch für Mineralogie*, Beilagenband 54, Abt. B, pp. 417–447.

Schuhmacher H.A. (1875) Ueber die Columbischen Smaragden. *Zeitschrift der Gesellschaft für Erdkunde zu Berlin*, Vol. 10, pp. 38–62.

Schwarz H.F. (1953) In memory. *The Explorers Journal*, Vol. 31, No. 4, pp. 54–55, 64.

Simón P., Fr. (1891) *Noticias historiales de las conquistas de Tierra Firme en las Indias Occidentales, Segunda Parte*. Casa Editorial de Medardo Rivas, Bogotá.

Singewald Q.D. (1950) Mineral resources of Colombia (other than petroleum). *Geologic Investigations in the American Republics, 1949*. Geological Survey Bulletin 964-B, pp. 53–61.

Sinkankas J. (1981) *Emerald and Other Beryls*. Chilton Book Company, Radnor, Pennsylvania.

Skinner W.R. (1889-1890) *The Mining Manual*, Vol. 3, pp. 116–117, 333.

——— (1891–1892) *The Mining Manual*, Vol. 4, pp. 75, 121, 341.

——— (1896) *The Mining Manual*, Vol. 8, p. 1151.

——— (1897) *The Mining Manual*, Vol. 9, pp. 1279–1280.

——— (1900) *The Mining Manual*, Vol. 12, p. 1190.

Strunz H. (1970) *Von der Bergakademie zur Technischen Universität Berlin 1770-1970*. Förderer der Berliner Fakultät für Bergbau und Hüttenwesen e.V., Berlin.

Torres del Río C.M. (2015) *Colombia siglo XX: desde la Guerra de los Mil Días hasta la elección de Álvaro Uribe*. Editorial Pontificia Universidad Javeriana, Bogotá.

Weldon R., Ortiz J.G., Ottaway T. (2016) In Rainier's footsteps: Journey to the Chivor emerald mine. *G&G*, Vol. 52, No. 2, pp. 168–187, http://dx.doi.org/10.5741/GEMS.52.2.168

Winkler M. (1928) *Investments of United States Capital in Latin America*. World Peace Foundation, Boston.

RHODONITE-PYROXMANGITE FROM TANATZ ALP, SWITZERLAND

Franca Caucia, Luigi Marinoni, Maria Pia Riccardi, Omar Bartoli, and Maurizio Scacchetti

The chemical, physical, and gemological properties of attractive rhodonite-rich rocks from Tanatz Alp (Switzerland) were investigated using classical gemological methods, petrographic observation, and analytical techniques such as X-ray powder diffraction, Raman spectroscopy, and scanning electron microscopy. The color of the samples varied from pale pink to purplish pink; they were opaque and contained braunite, rhodochrosite, and spessartine. The gem-quality samples have an attractive color and are compact with no fractures. Tanatz Alp rhodonites are characterized by the presence of other minerals such as kutnohorite, spessartine, ankerite, rhodochrosite, khristovite-(Ce), pyroxmangite, and chlorite. The presence of the polymorph pyroxmangite was also confirmed by micro-Raman analyses. The samples had a chemical composition of MnO (45.97–48.64 wt.%) and SiO_2 (46.70–47.92 wt.%), with very low amounts of MgO (0.64–1.65 wt.%) and CaO (<5 wt.%). Rhodonites from Tanatz Alp have some economic importance because of their use in jewelry and ornamental objects.

R hodonite is the Mn-rich member of the pyroxenoid group; it is triclinic with a structure made up of silicate chains parallel to the c-axis, in turn composed of a repeating sequence of five tetrahedral units. The chains alternate with M octahedral sites, designated M1 though M5, where divalent cations reside (Deer et al., 1997, and references therein). The ideal chemical formula is $MnSiO_3$. Rhodonite of this composition has been synthesized but has never been found in nature, where Ca, Mg, and Fe^{2+} replace Mn (Ito, 1972).

Rhodonite was first discovered in 1790 in the Ural Mountains near Sidelnikovo. The mineral was named in 1819 by the German naturalist Christoph Friedrich Jasche. The name is derived from the Greek *rhodo*, which means "rose," because of its characteristic pink color (figure 1). The Hermitage Museum in Saint Petersburg preserves many precious and decorative objects made with rhodonite that belonged to the Russian aristocracy, especially the czars. Even today, Russian children exchange rhodonite eggs for Easter as a gesture of friendship. In the United States there are important rhodonite mines in New Jersey and in Massachusetts, which declared it the official

state gem in 1979. Rhodonite is collected as a lapidary material and ornamental stone and is used to make cabochons, beads, small sculptures, tumbled stones, and other objects. High-quality crystals of

In Brief

- Rhodonite from Tanatz Alp in Switzerland is associated with kutnohorite, spessartine, ankerite, and rhodochrosite.
- Classical gemological methods, petrographic observation, and analytical techniques demonstrated the presence of the two polymorphs of $MnSiO_3$: rhodonite and pyroxmangite.
- Fashioned rhodonites from Tanatz Alp display an attractive pale pink purplish pink color.

this mineral can be very expensive. Rhodonite is generally found in massive translucent to opaque aggregates, and the best-quality gems are transparent. The crystals have perfect cleavage in two directions and low hardness (5.5–6 Mohs), making it one of the most difficult gemstones to cut. For this reason, faceted rhodonites are typically sold as collectible gems rather than for jewelry use.

Rhodonite is very similar to its polymorph, pyroxmangite, and to rhodochrosite ($MnCO_3$). Pyroxman-

Figure 1. Rhodonite bead necklace and earrings. Photo by Emily Lane; courtesy of Dona Dirlam.

gite has a structure very similar to that of rhodonite, with a repeating sequence of seven tetrahedral units; the distinction from rhodonite therefore requires more accurate investigations with techniques such as X-ray powder diffraction (XRPD) and electron microprobe. Rhodochrosite differs in that it frequently shows white streaks of calcite and is reactive to hot acids, whereas rhodonite is resistant to acids and usually associated with manganese oxides.

Rhodonite and pyroxmangite contain small amounts of Ca, Mg, and Fe^{2+} substituting for Mn^{2+}; the *P-T* compositional stability limits have been investigated by many authors, but there are still uncertainties (Ito, 1972; Peters et al., 1973; Ohashi et al.,

1975; Maresch and Mottana, 1976; Brown et al., 1980; Akaogy and Navrotsky, 1985; Abrecht, 1988; Takahashi and Hariya, 1995; Zanazzi et al., 2008; Diella et al., 2014, and references therein). The two minerals can generally be distinguished on the basis of their chemical composition, as rhodonite contains a higher amount of Ca (more than 0.05 wt.%) than pyroxmangite. Rhodonite and pyroxmangite often occur together as a bladed intergrowth, in various types of ore deposits and Mn-rich lithologies (Ohashi et al., 1975; Jefferson et al., 1980; Pinckney and Burnham, 1988; Millsteed et al., 2005; Michailidis and Sofianska, 2010).

Deposits of rhodonite are found all over the world. The most important are those at Broken Hill in New South Wales, Australia, where the best single-crystal gems are found (Millsteed et al., 2005; Millsteed, 2006); Franklin, New Jersey, in the United States (Nelson and Griffen, 2005); many areas of the Ural Mountains (Bukanov, 2006; Brusnitsyn, 2010); British Columbia, Canada (Simandl et al., 2001); Huánuco, Peru (Wilson,1989); Minas Gerais, Brazil (Quinn, 2004; Leverett et al., 2008); Pajnsberg, Sweden (Lee, 1958); and several localities in Japan (Ohashi et al., 1975). A variety of rhodonite containing high levels of zinc (up to 10 wt.% ZnO), called fowlerite, was found at Franklin, New Jersey (Nelson and Griffen, 2005).

In the Italian Alps, rhodonite has been found in the Praborna mine near San Marcel in Valle d'Aosta (Mottana, 1986), Feglierec near Alagna Valsesia in Piedmont (Peters et al., 1978), Monte Forno in Malenco Valley, Scerscen in Lombardy (Diella et al., 2014), and Monte Civillina in Veneto (Schiavinato, 1953). Rhodonite is also found in the Apennines chain, in the mines of Gambatesa and Molinello in Graveglia Valley in Liguria (Marchesini and Pagano, 2001), Alpe Ravinella in Strona Valley (Bertolani, 1967), Scortico in the Apuan Alps (Di Sabatino, 1967; Mancini, 1997), and Campiglia Marittima in Tuscany (Capitani et al., 2003). Italian rhodonites are translucent or opaque and microcrystalline with a pale to deep pink color; only those from Monte Forno in Val Malenco (Diella et al., 2014) and Scortico (Apuan Alps) can be truly considered gem-quality since they are transparent enough to be faceted.

The manganese deposits in the Rhetic Alps of Switzerland that contain rhodonite, such as Falotta and Alpe Parsettens in the Oberhalbstein or Fianel and Starlera in Val Ferrera, have been widely investigated (Trommsdorff et al., 1970; Peters et al., 1973, 1978; Wenk and Maurizio, 1978; Brugger and Giere,

1999), but those in the Tanatz Alp (figure 2) are less well known. This work investigates the chemical, physical, and gemological properties of rhodonite from Tanatz Alp.

DESCRIPTION OF THE DEPOSIT

Tanatz Alp is located about 2.5 kilometers south of the village of Splügen in the Swiss canton of Grisons. The geological setting is similar to that of the more famous Val Ferrera. Tanatz Alp lies between the crystalline basement and the sedimentary cover of the Tambo nappe in the so-called Spluga zone; a short distance to the east is the nappe of Suretta. Both nappes belong to the Pennidic domain and are formed by rocks of the crystalline basement, metamorphosed during the Alpine orogeny, and by overlying shallow-basin sedimentary sequences, which were subsequently metamorphosed into Mn- and Fe-rich schists and quartzites (Biggioggero and Montrasio, 1990; figure 2). The first description of the minerals from Tanatz Alps was by Kenngott (1866), who reported the discovery of rhodonite in Mount Splügen.

At the beginning of the twentieth century, interest in manganese minerals increased considerably, and this Swiss resort became an economically important source (Grenouillet, 1920). Rhodonite in Tanatz Alp occurs in large isolated boulders between half a meter and a meter long (figure 3), distributed along an extension of about 100 meters on the slope to the west of the switchbacks ascending the pass at an elevation of 1,720 m. Between 1918 and 1920, excavations were carried out to identify the original outcrop of this mineral, but without success. Since 1970, stonecutters and artisans have rediscovered an appreciation for the manganese minerals of Tanatz Alp, which are multi-colored, hard, and free of cavities and cracks. Many collectors around the world also became interested in this area, where several very rare and attractive minerals can be found (gasparite, khristovite, franklinfilite, tiragalloite, and manganberzeliite; Roth and Meisser, 2011).

The source region of these rhodonite-bearing boulders has never been identified, and its mineralogical composition is still the subject of investigation. It is believed that the manganese-rich deposits formed during the Tertiary, under zeolite and greenschists facies metamorphic conditions (Roth and Meisser, 2011). It was assumed that the mineralization took place in the Triassic carbonate sediments, similar to the famous deposits of Fianel and Starlera in nearby Val Ferrera (Brugger and Giere, 1999), but
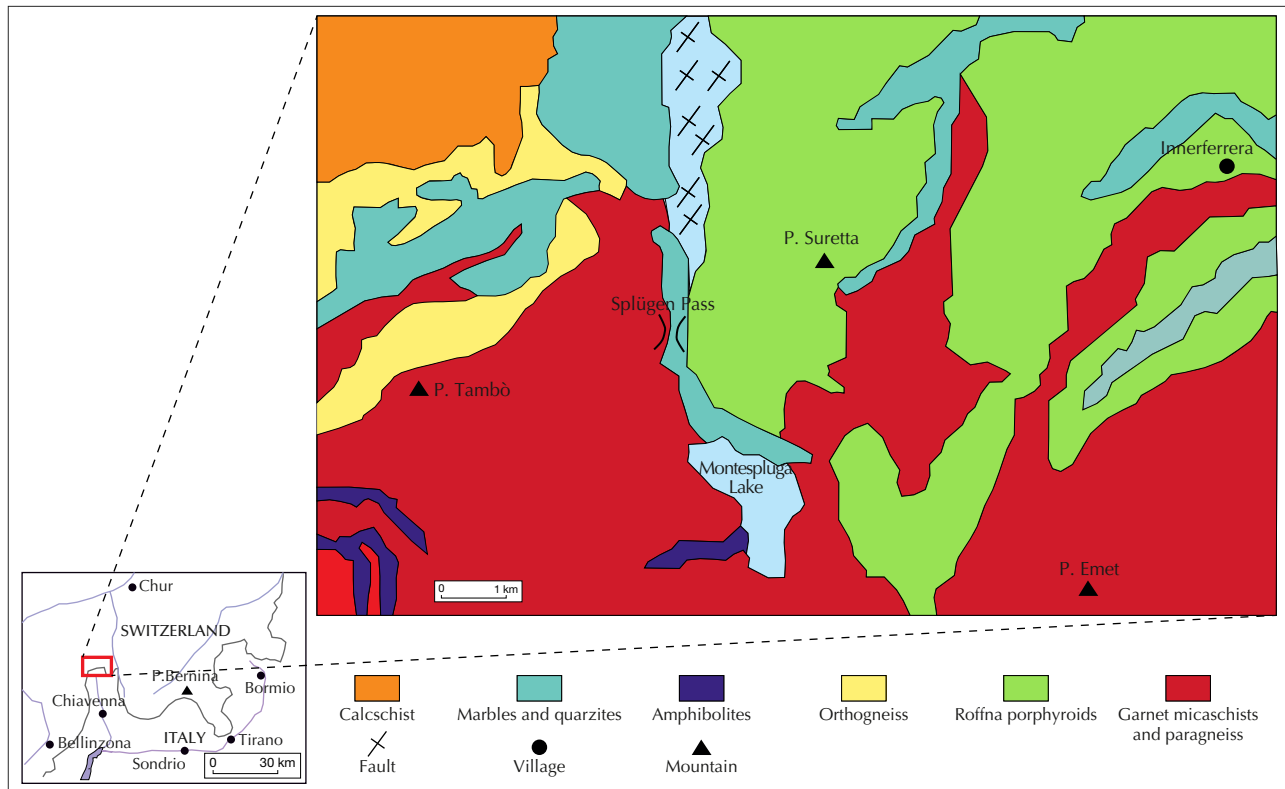
Figure 2. Geological map of the Tanatz Alp area in Switzerland. Modified from Bedogné et al. (1995).

the original outcrop is likely located in the crystalline intercalation of the Splügen area, which is tectonically very complex (figure 2).

The mineralogy of the rhodonite-bearing rocks from Tanatz Alp shows similarities with that of deposits from Scerscen in Val Malenco, located about

Figure 3. A loose assortment of blocks containing the rhodonite mineralizations investigated in this work. The largest is about 1 m long, while the overlying blocks are about 20–25 cm long. Photo by F. Vanini.
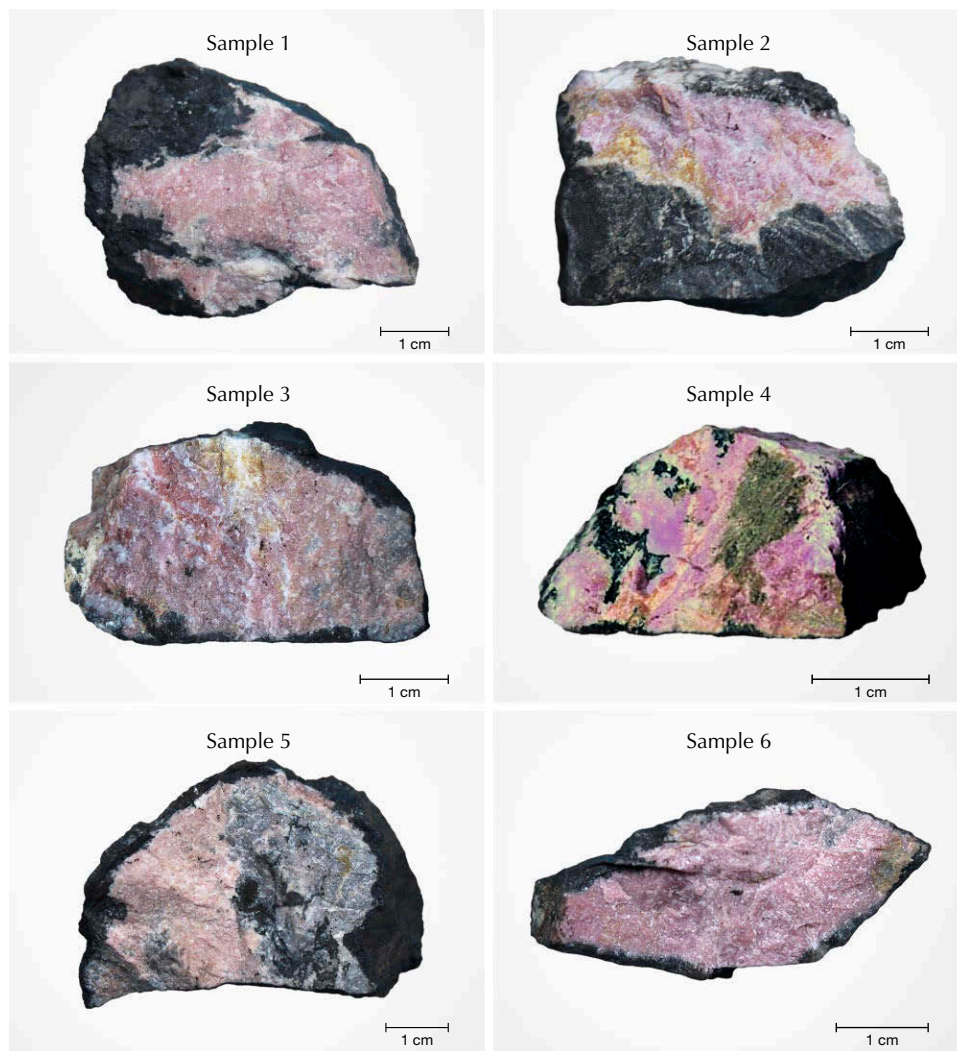
Figure 4. Rough samples of rhodonite from Tanatz Alp investigated in this work (samples 1–6). Photos by Maurizio Scacchetti.

40 km away (Bedogné et al., 1993, 1995; Diella et al., 2014). On the surface, the manganese boulders are black. The alteration layer varies from a few millimeters to one centimeter and is composed of rancieite. Rhodonite is present in small, needle-like crystals with a characteristic and very pleasing pink color, often in contact with spessartine.

MATERIALS AND METHODS

Analyses were carried out on six samples of rock containing rhodonite (figure 4), collected from Maurizio Scacchetti in the summer of 2017 along the main road leading to the Splügen Pass. The samples were in centimeter sizes, with very uneven color due to the presence of different minerals. The rhodonite was present in these samples as fine needle-like crystals. There were also millimeter-sized and rounded orange crystals of spessartine and light pink rhodochrosite

and brown or blackish portions made up of braunite and manganese oxides such as rancieite. All the samples were compact.

Standard gemological analyses were carried out on seven fashioned stones (figure 5), cut from the rough samples in figure 4, to describe the optical properties, specific gravity, and ultraviolet fluorescence. Density was measured using a Presidium PCS100 Sensible hydrostatic balance, and the color was evaluated with an RGB (red, green, blue) color table. Refractive index was measured by the distant vision method using a Kruss refractometer (1.45–1.80 range) and a contact liquid with an RI of 1.80. Ultraviolet fluorescence was investigated with a short-wave (254 nm) and long-wave (365 nm) UV lamp.

X-ray powder analyses to determine the mineralogical composition were carried out using a Philips PW1800 powder diffractometer, with CuKα radiation
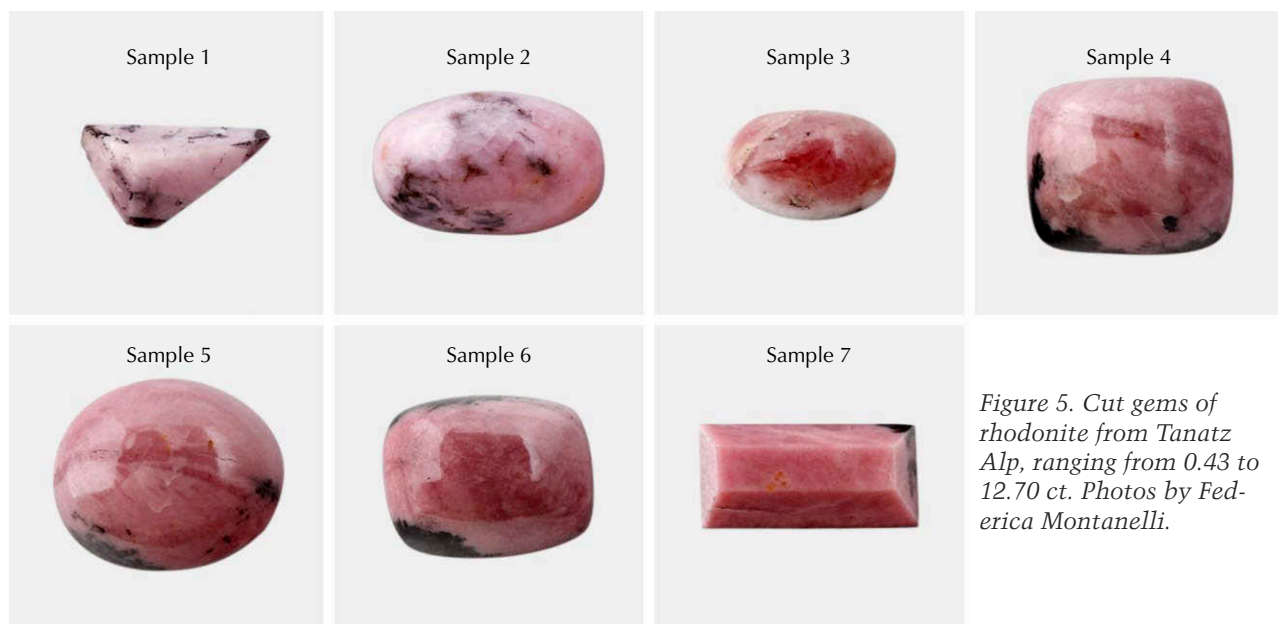
Figure 5. Cut gems of rhodonite from Tanatz Alp, ranging from 0.43 to 12.70 ct. Photos by Federica Montanelli.

(λ = 1.5418 Å) and a scan speed of 1°/min, in the 2–65° 2θ range. The samples for the analyses (about 3 g) were previously ground in an agate mortar and reduced to a very fine powder (about 5 microns). We ground the rough samples shown in figure 4. The material was selected based on the pink color before the grinding. Unfortunately, many phases of rhodonite-bearing rock show a similar color (spessartine orange-pink, rhodochrosite reddish pink, and kutnohorite pale pink). Therefore, in the Results section rhodonite represents less than 50% of all samples except sample 2. Qualitative and semi-quantitative evaluation was performed with X'Pert HighScore software, which is designed to obtain all phase information from loose and pressed powders and other polycrystalline samples (Markvardsen et al., 2008; Degen et al., 2014).

Major element analysis (Si, Mn, Ca, Mg, Fe, Zn, Ti, and Al) was carried out on select crystals from all the rhodonite samples with an electron microscope, model TESCAN series Mira XMU, coupled with an EDAX system with energy dispersion and no internal standard (analytical error of about 3%). The accelerating voltage was 20 KV, while the analysis area was $100 \times 100 \ \mu^2$. The accuracy of the analyses is related to the calibration of the detector and the maintaining of standard conditions during the work.

Micro-Raman scattering measurements were conducted with a Horiba Jobin Yvon Explora Plus single monochromator spectrometer (grating of 2400 groove/mm) equipped with an Olympus BX41 microscope. Raman spectra were recorded with 532 nm excitation. The spectrometer was calibrated to the silicon Raman peak at 520.5 cm^{-1}. The spectral resolution was ~2 cm^{-1}, and the instrumental accuracy in determining the peak positions was approximately 0.56 cm^{-1}. Raman spectra were collected in the spectral range 100–1300 cm^{-1} for 5 seconds averaging over 40 scans accumulated.

RESULTS

Microscopic Observations. Figure 6A shows a macroscopic section of a rhodonite sample (no. 2) that contains a pink and a dark part. Thin-section investigation revealed that the pink portion (figure 6B) consists of an intimate association of rhodonite (or pyroxmangite) and kutnohorite (see chemical analyses in table 5). Here, the size of rhodonite/pyroxmangite crystals ranges from tens of micrometers to a few millimeters. Conversely, the dark part is composed mainly of spessartine and Mn oxides (figure 6C).

Gemological and Physical Properties. Seven cabochons and faceted stones were cut with various shapes (figure 5) from the six rough samples; table 1 presents the gemological data.

The cabochons and faceted stones had a massive and opaque aspect with an intense and variable pink color (pink, pale violet red, and Indian red according to the RGB color table). The rhodonites were strongly inhomogeneous due to the presence of various associated minerals in spots that were dark to black and yellow-orange. The measured specific gravity ranged from 3.40 to 3.63, in agreement with data for other alpine rhodonites (Deer et al., 1997; Diella et al.,
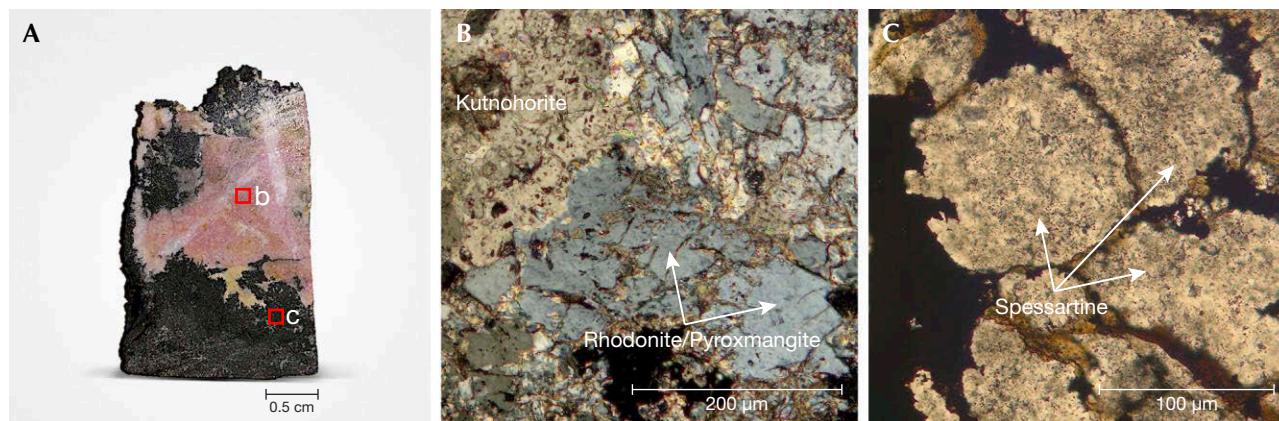
Figure 6. A: In this slice obtained from rough sample 2, red squares indicate the points of microscopic observation shown in figures 4B and 4C. B: A crossed polarizer image reveals the coexistence of kutnohorite and rhodonite/pyroxmangite. C: A plane-polarized light image shows the presence of Mn-rich garnet. Photos by Omar Bartoli.

2014). The refractive indices measured with the distant vision method ranged from approximately 1.72 to 1.74 (in agreement with Deer et al., 1997; Diella et al., 2014). The absorption spectra were characterized by a broad band at 550 nm, a strong narrow line at 500 nm, and a diffuse weak band at 450 nm. All the samples were inert to short-wave (254 nm) and long-wave (365 nm) UV.

XRPD. Figure 7 shows the X-ray patterns of some investigated samples, while the mineralogical composition is reported in table 2. The samples showed a variable occurrence of rhodonite-pyroxmangite, but distinguishing the two phases is quite difficult be-

cause of the two polymorphs' overlapping peaks at 26.6, 29.1, 30.2, 34.4, and 36.5° 2θ. The rhodonite was identified by the characteristic peaks at 21.5, 25.0, 27.4, 28.5, 30.5, 32.2, and 35.4° 2θ, while the sole pyroxmangite presented diffraction effects at 25.5, 28.1, 29.8, 31.3, 40.8, and 44.3° 2θ.

The samples showed variable amounts of rhodonite-pyroxmangite (22–66%) and kutnohorite (8–62%); samples 1, 4, and 6 also contained ankerite. Other detected minerals were spessartine, rhodochrosite, calcite, braunite, chlorite, and traces of quartz. In samples 1, 2, 4, and 6, the X'Pert software also suggested traces of the rare mineral khristovite, identified by the peaks at 25.3, 30.6, 32.8, and 34° 2θ.

TABLE 1. Gemological data of the rhodonite cabochons and faceted stones investigated.

Sample	Color (RGB color table)	Dimensions (mm)	Cut	Weight (ct)	Specific gravity	RI[a]
1	Pink; black spots	7 × 4 × 3	Triangular cabochon	0.43	3.40	1.72
2	Pink/pink1; black spots	12 × 7 × 6	Oval cabochon	5.30	3.41	1.73
3	Pale violet/"Indian red 2"; pink veins	7 × 5 × 5	Oval cabochon	1.08	3.42	1.73
4	Pale violet/"Indian red 2" veins	10 × 12 × 6	Rectangular cabochon	12.01	3.60	1.74
5	Pale violet/"Indian red 2" veins; black spots	12 × 13 × 5	Oval cabochon	12.51	3.56	1.74
6	Pale violet/"Indian red 2"; black spots	13 × 10 × 7	Rectangular cabochon	12.70	3.58	1.74
7	"Indian red"; black spots	12 × 6 × 4	Rectangular emerald-cut	3.70	3.63	1.74

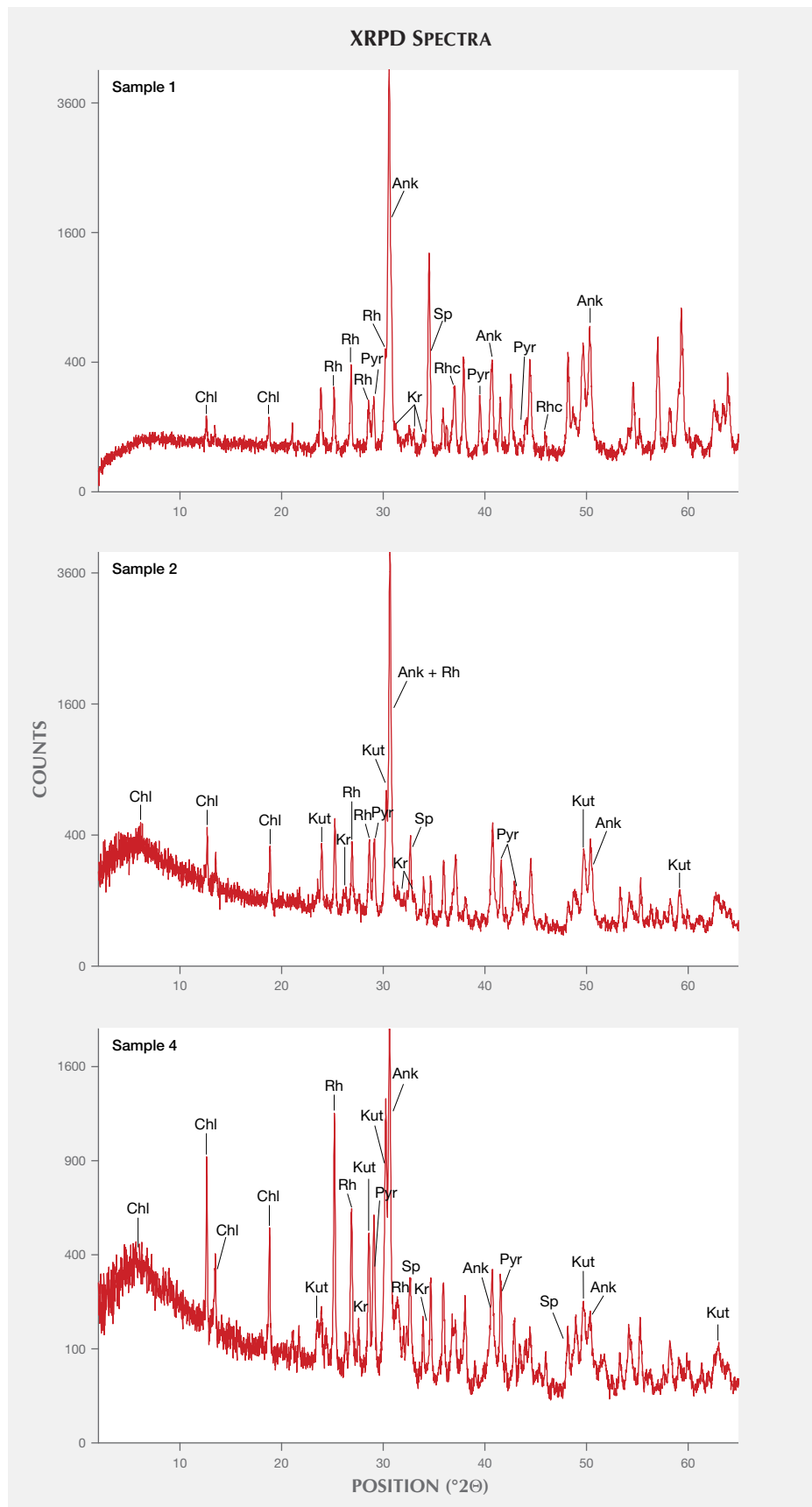*[a]Determined using the distant vision method*

Figure 7. XRPD patterns of the rhodonite samples 1, 2, and 4 from figure 4. The most important minerals are reported, close to their diagnostic peaks. Ank = ankerite; Pyr = pyroxmangite; Rh = rhodonite; Kut = kutnohorite; Sp= spessartine; Rhc = rhodochrosite; Chl = chlorite.

TABLE 2. Mineralogical composition of the analyzed samples (from figure 4) obtained through XRPD analysis.

Sample no.	Mineral assemblages (wt.%)
1	Ankerite (60%), rhodonite-pyroxmangite (20%), rhodochrosite (20%), khristovite (traces), chlorite (traces)
2	Rhodonite-pyroxmangite (65%), kutnohorite (25%), spessartine (5%), chlorite (5%), quartz (traces), khristovite (traces)
3	Kutnohorite (60%), rhodonite-pyroxmangite (30%), calcite (10%)
4	Rhodonite-pyroxmangite (35%), spessartine (30%), ankerite (15%), kutnohorite (10%), chlorite (10%), khristovite (traces)
5	Rhodonite-pyroxmangite (45%), braunite (20%), ankerite (10%), kutnohorite (10%), spessartine (10%), quartz (5%)
6	Rhodonite-pyroxmangite (40%), spessartine (30%), kutnohorite (20%), ankerite (10%), khristovite (traces)

Mineral Chemistry. SEM analyses performed on selected crystals of rhodonite-pyroxmangite are shown in table 3 (error of analyses about 3%). Table 4 reports the chemical composition of rhodonites from the Alps and other worldwide occurrences reported in the literature, for comparison. In our samples the most abundant oxides were MnO (46–48.64 wt.%) and SiO_2 (46.70–47.92 wt.%), with very low amounts of MgO (0.64–1.65 wt.%) and CaO (<5 wt.%).

Figure 8 and table 5 provide the backscattered electron images and corresponding analyses of the association of rhodonite (points 3, 4, and 5) with Ca-Mn-carbonate kutnohorite ($CaMn^{2+}(CO_3)_2$; points 1 and 2). We also observed the presence of Mn oxides and spessartine as accessory phases. The rhodonite in the samples appeared to be composed of microcrystals, and the chemical composition was not homogeneous. Similar to what was reported for rhodonites from Val Malenco (Diella et al., 2014), we observed that the Si content was almost stoichiometric (Si = 1.00–1.01 apfu) while that of Mn deviated (0.82–0.88 apfu) from the idealized formula (1.00 apfu), due to the occurrence of other cations such as Ca and Mg in the M-sites.

The Ca and Mn contents in our samples were similar to those reported for other samples from Val Scerscen, Val Sesia Val d'Ayas, and Val Malenco (Peters et al., 1978; Mottana, 1986; Diella et al., 2014; see table 4).

CaO contents also showed large variability in the same areas investigated by energy-dispersive spectroscopy (EDS) analyses. It varied from 0.97% to 3.90% in samples 1 and 2, from 0.99% to 3.97% in sample 4, and from 1.02% to 4.64% in sample 5; see table 3. The values of Ca vs. Mn are plotted in figure 9 with the different fields for rhodonite and pyroxmangite (see also Diella et al., 2014).

Fe was absent in our samples, as in rhodonite from other localities in the Alps such as Praborna and Val Sesia and from Japan; see table 4. In the

TABLE 3. Chemical composition (wt.%) of the rhodonite/pyroxmangite samples investigated, obtained through SEM analyses.

Oxides	1/1[a]	1/2	2/1	2/2	3/1	3/2	4/1	4/2	5/1	5/2	6/1	6/2
SiO_2	46.91	46.62	47.02	46.63	46.70	47.03	47.43	46.92	47.66	46.53	47.62	47.54
MgO	0.67	1.44	0.70	1.45	0.64	0.68	0.57	1.65	0.75	1.46	0.84	0.85
MnO	48.52	50.75	48.42	50.95	48.64	48.49	48.33	50.44	46.95	50.98	46.85	47.41
CaO	3.90	0.98	3.86	0.97	4.01	3.80	3.67	0.99	4.64	1.02	4.70	4.20
Total	100	99.99	100	100	99.99	100	100	100	100	99.99	100.01	100
						apfu (3 oxygens)						
Si	1.00	1.00	1.01	1.00	1.00	1.01	1.01	1.01	1.01	1.00	1.01	1.01
Mg	0.02	0.05	0.02	0.05	0.02	0.02	0.02	0.06	0.02	0.05	0.03	0.03
Mn	0.88	0.93	0.88	0.93	0.88	0.88	0.87	0.90	0.85	0.93	0.84	0.85
Ca	0.09	0.02	0.09	0.02	0.09	0.09	0.08	0.02	0.11	0.02	0.11	0.10

[a]Sample/crystal
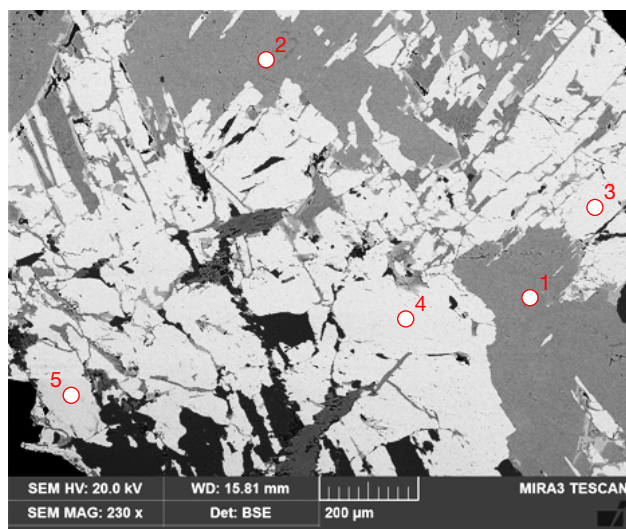Fe_2O_3 was below detection limits (0.1 wt.%).

Figure 8. Backscattered electron image of rhodonite/pyroxmangite (points 3, 4, and 5) and associated kutnohorite (points 1 and 2) in rough sample 2.

Figure 9. Compositional variation of Ca vs. Mn of co-existing rhodonite-pyroxmangite from Tanatz Alp in Switzerland.

rhodonites from the famous deposits of Broken Hill (Australia) and Franklin (New Jersey), Fe is an important chromophore element; again, see table 4.
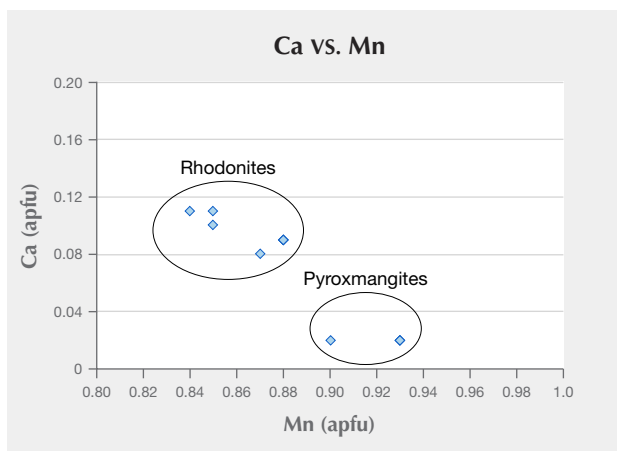
Micro-Raman Spectroscopy. Mineral polymorphs are distinguishable by Raman spectroscopy (Mazzoleni et al., 2015), and this analysis was carried out to confirm the presence of the polymorph pyroxmangite with rhodonite.

TABLE 4. Chemical composition (wt.%) of rhodonite samples reported in the literature: Italy (Peters et al., 1978; Mottana, 1986; Diella et al., 2014); United States and Australia (Nelson and Griffin, 2005); and Japan (Aikawa, 1984).

Oxides	Italy (Praborna[a])	Italy (Val Malenco 1)	Italy (Val Malenco 2)	Italy (Val Sesia[a])	Italy (Monte Alpe[a])	United States (Franklin Mine 1, New Jersey)	United States (Franklin Mine 2, New Jersey)	United States (New York)	United States (Plainfield, Maine)	Australia (Broken Hill)	Australia (Broken Hill)	Australia (Broken Hill)	Japan (Sankei)	Japan (Sankei)
SiO₂	46.82	46.76	46.40	46.91	46.70	46.35	46.46	45.71	45.69	46.15	45.94	45.83	46.88	47.34
TiO₂	n.d.	n.d.	0.07	n.d.	n.d.	0.04	n.d.	0.01	0.01	n.d.	0.04	0.02	n.d.	n.d.
Al₂O₃	n.d.	0.02	n.d.	n.d.	n.d.	0.01	0.02	0.01	0.01	0.93	0.03	0.04	0.07	0.59
MgO	n.d.	0.66	0.65	0.95	1.71	1.54	0.88	0.13	0.08	1.41	0.3	0.25	1.50	0.87
FeO	n.d.	3.27	3.20	n.d.	5.21	2.79	1.91	12.34	1.93	10.51	11.76	11.92	0.45	0.31
MnO	47.07	41.80	41.68	46.74	40.0	35.71	38.04	40.21	48.13	38.62	37.35	37.91	50.69	44.18
ZnO	n.d.	n.d.	n.d.	n.d.	n.d.	6.96	5.09	0.16	0.03	n.d.	0.33	0.35	n.d.	n.d.
CaO	6.11	6.41	6.79	5.40	6.38	6.59	7.61	1.73	3.65	2.01	4.32	3.94	1.37	7.11
Total	100.00	100.02	99.99	100.00	100.00	99.99	100.01	100.30	99.53	99.63	100.07	100.26	100.06	100.41
Cations based on 3 oxygens apfu														
Si	1.00	1.006	1.000	1.00	0.99	0.994	0.996	0.994	0.994	0.992	0.993	0.991	0.998	0.998
Ti	n.d.	n.d.	0.001	n.d.	n.d.	0.001	n.d.	n.d.	n.d.	n.d.	n.d.	n.d.	n.d.	n.d.
Al	n.d.	n.d.	n.d.	n.d.	n.d.	n.d.	0.001	n.d.	n.d.	0.024	0.001	0.001	0.002	0.015
Mg	n.d.	0.021	0.020	0.03	0.05	0.049	0.028	0.004	0.003	0.04	0.010	0.008	0.048	0.027
Fe	n.d.	0.057	0.058	n.d.	0.09	0.050	0.034	0.224	0.035	0.188	0.213	0.216	0.008	0.031
Mn	0.85	0.761	0.761	0.85	0.72	0.649	0.690	0.740	0.887	0.702	0.684	0.694	0.914	0.806
Zn	n.d.	n.d.	n.d.	n.d.	n.d.	n.d.	0.081	0.003	n.d.	n.d.	0.005	0.006	n.d.	n.d.
Ca	0.12	0.148	0.157	0.12	0.15	0.151	0.175	0.034	0.072	0.040	0.099	0.090	0.032	0.164

[a]EDS analyses
n.d. = not detected

TABLE 5. EDS analyses of the five backscattered electron image spots from figure 8.

Oxides (wt.%)	1 (kutnohorite)	2 (kutnohorite)	3 (rhodonite/ pyroxmangite)	4 (rhodonite/ pyroxmangite)	5 (rhodonite/ pyroxmangite)
MgO	1.79	1.81	1.37	1.28	1.53
SiO_2	—	—	47.87	47.83	47.92
CaO	26.03	25.31	3.79	3.89	4.58
MnO	30.73	31.50	46.97	47.01	45.97
CO_{2calc}	41.45	41.38	—	—	—
Total	100	100	99.99	100.01	100
	apfu (6 oxygens)		apfu (3 oxygens)		
Mg	0.09	0.10	0.04	0.04	0.05
Si	—	—	1.01	1.01	1.01
Ca	0.99	0.96	0.09	0.09	0.10
Mn	0.92	0.94	0.85	0.86	0.82
C	2	2	—	—	—

The Raman spectrum of the sample shown in figure 6A (area b) is presented in figure 10. The spectrum is characterized by an intense band at 1000 cm^{-1} assigned to the 1 symmetric stretching mode and two bands at 972 and 944 cm^{-1} assigned to the v_3 asymmetric stretching modes. The band at 670 cm^{-1} has been assigned to the v_4 Si-O-Si bending mode (Mills et al., 2005). The low wavenumber region of rhodonite is complex (Mills et al., 2005). There are two small bands at 399 and 424 cm^{-1} assigned to the v_2 bending mode. The spectra reported in literature are very similar to ours; the small differences observed can be attributed to cationic substitution of Mn by Ca, Fe, and Mg (Mills et al., 2005; Diella et al., 2014).

The Raman spectra of pyroxmangite (from the RRUFF database, ID R070212 at rruff.info) present many bands that overlap with those of rhodonite (figure 10). However, the small bands at 185, 252, and 299 cm^{-1} are characteristic of pyroxmangite and confirm the presence of this polymorph in our samples.

DISCUSSION AND CONCLUDING REMARKS

The present study, performed on both cut and rough samples of rhodonite-rich rocks from Tanatz Alp, provided new data to better understand the characteristics of this attractive gemstone.

The color of the investigated rhodonite rocks varied from pale pink to purplish pink. The mineralogi-
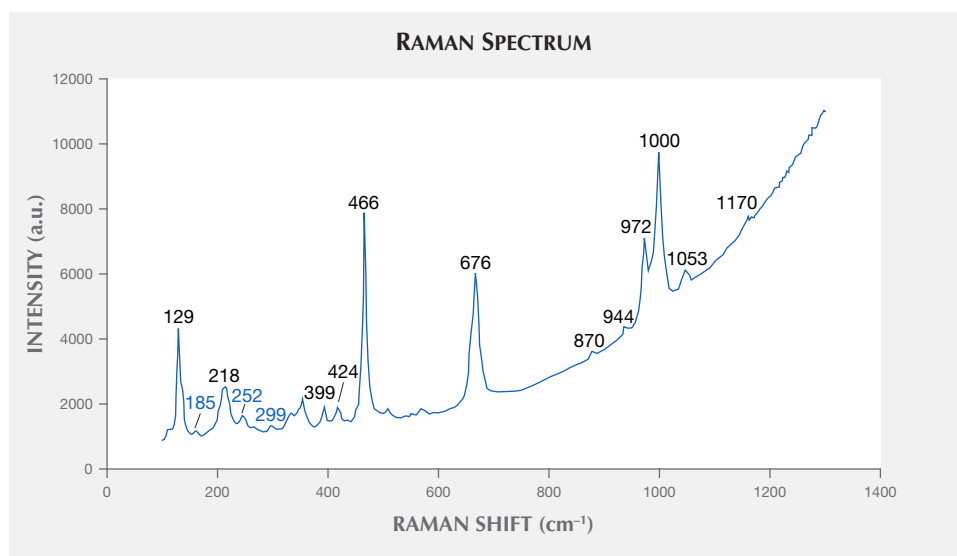

Figure 10. Raman spectrum of the rhodonite from figure 6A (area b).

cal composition is an assemblage of rhodonite and pyroxmangite and other Mn-rich minerals such as kutnohorite, spessartine, ankerite, and rhodochrosite. Low amounts of chlorite, calcite, and quartz were also detected. We also identified the presence, as an accessory phase, of khristovite, a Ce-Fe-Mn^{2+}-rich epidote group mineral. This finding is very interesting owing to the rarity of this mineral; the presence of khristovite in this locality was also reported by Roth and Meisser (2011).

The chemical composition of our rhodonite samples highlights a negative correlation between Ca and Mn, which was previously observed in rhodonites from Tanatz Alp and the Rhetic Alps (Peters et al., 1978; Diella et al., 2014). The amount of Mg ions substituting for Mn in the samples we analyzed showed large variations that reflect the type of carbonate mineral present, the bulk composition of the mother rock and the availability of the element (Diella et al., 2014). It is interesting to observe that our samples did not show the presence of FeO, which has been reported in rhodonites from other occurrences such as Broken

Hill (up to about 12%; Millsteed et al., 2005; Millsteed, 2006), Franklin (up to about 2.8%; Nelson and Griffen, 2005), and Val Malenco (up to 3.27%; Diella et al., 2014). Together with Mn and Ca, Fe substitutes for Mg in the octahedral sites of the mineral's structure. The presence of Fe modifies the color from pink to deep pinkish red, as reported for rhodonites from Broken Hill and the Franklin mine, which are Fe-rich and have a deep pinkish red color (Millsteed, 2005; Nelson and Griffen, 2005). Since Fe is absent in our samples, the color is softer; the Praborna material, which also lacks Fe, is similar in color to our samples from Tanatz Alp.

The Ca content in our rhodonites ranged between 0.97% and 4.70 wt.%, lower than that of other rhodonites from the Alps (table 4). The variability of Ca content in deposits worldwide can be related to the coexistence of pyroxmangite and rhodonite.

XRPD patterns, micro-Raman analyses, and low Ca contents indicate that the pyroxmangite should coexist with rhodonite in the Mn-rich rocks from

Figure 11. Handmade jewels produced with rhodonite from Tanatz Alp by Lutezia Gioielli (Stradella, Italy). Left: necklace of freeform rhodonite beads. The knot in the center of the necklace contains a pink rhodonite cabochon. Right: Vintage pendant with a drop-shaped rhodonite. Photos by Federica Montanelli.

Tanatz Alp. The pyroxmangite crystals probably intergrow with rhodonite crystals, but the two phases are visually undetectable. The intergrowth of the two phases is also confirmed by the large variability of Ca in the same areas of EDS analyses, ranging from 0.02 to 0.10 apfu. Both polymorphs usually form through processes of regional or contact metamorphism, as well as metasomatic processes from carbonate rocks that underwent low-grade regional or very high-grade contact-metamorphic conditions (Abrecht, 1988). Several studies on the coexistence of pyroxmangite and rhodonite have been performed on synthetic crystals of $MnSiO_3$; synthetic pyroxmangite is usually stable at temperatures below about 400°C and pressures < 2 kbar, while rhodonite is stable at higher temperatures (Abrecht and Peters, 1975; Maresch and Mottana, 1976; Pinckney and Burnham,1988).Yet the application of these studies to natural rocks is quite difficult because of the great variety and the extent of cation substitutions observed in natural pyroxenoids (Ca, Mg, $Fe^{2+} \rightarrow$ Mn).

Furthermore, the inability to identify the original outcropping represents a significant challenge in understanding the genesis of the manganese mineralization of Tanatz Alp.

Regarding gemological properties, the rhodonite-bearing rocks investigated in this study were compact with no fractures. They also showed a pink color, though it was not homogeneous and contained orange and purple tints due to spessartine and rhodochrosite, respectively. Since these rhodonites are translucent and microcrystalline, their commercial value is far lower than that of the transparent gems from Broken Hill (Millsteed, 2005) or Franklin (Nelson and Griffen, 2005). Although some Tanatz Alp rhodonites were carved and traded in the past, their marketing did not begin until the end of the twentieth century. This charming pink stone with a fine-grained structure is now available for pendants, necklaces, brooches, and ornamental objects (figure 11).

At present the deposit is only mined occasionally with hand tools and not for commercial purposes. Despite the difficulty of access, the geological characteristics of the locality suggest the possibility of substantial future production if a small commercial mine were to be established.

ABOUT THE AUTHORS
Dr. Caucia is associate professor, Dr. Marinoni is a geologist, and Dr. Riccardi is associate professor with the Department of Earth Sciences and Environment, University of Pavia, Italy. Dr. Bartoli is associate professor with the Department of Geosciences, University of Padova, Italy. Dr. Scacchetti is a geologist with Reggiana Society of Natural Sciences, Reggio Emilia, Italy.

REFERENCES

Abrecht J. (1988) Experimental evaluation of the $MnCO_3$ +SiO_2=$MnSiO_3$+CO_2 equilibrium at 1 kbar. *American Mineralogist*, Vol. 73, No. 11-12, pp. 1285–1291.

Abrecht J., Peters T. (1975) Hydrothermal synthesis of pyroxenoid in the system $MnSiO_3$–$CaSiO_3$ at Pf = 2kb. *Contributions to Mineralogy and Petrology*, Vol. 50, No. 4, pp. 241–246, http://dx.doi.org/10.1007/BF00394851

Aikawa N. (1984) Lamellar structure of rhodonite and pyroxmangite intergrowths. *American Mineralogist*, Vol. 69, No. 3-4, pp. 270–276.

Akaogy M., Navrotsky A. (1985) Calorimetric study of high-pressure polymorph of $MnSiO_3$. *Physics and Chemistry of Minerals*, Vol. 12, No. 6, pp. 317–323, http://dx.doi.org/10.1007/BF00654341

Armbruster T., Bonazzi P., Akasaka M., Bermanec V., Chopin C., Gieré R., Heuss-Assbichler S., Liebscher A., Menchetti S., Pan Y., Pasero M. (2006) Recommended nomenclature of epidote-group minerals. *European Journal of Mineralogy*, Vol. 18, No. 5, pp. 551–567, http://dx.doi.org/10.1127/0935-1221/2006/0018-0551

Bedogné F., Montrasio A., Sciesa E. (1993) *I minerali della Provincia di Sondrio*. Bettini Editore, Sondrio.

Bedogné F., Maurizio R., Montrasio A., Sciesa E. (1995) *I minerali della Provincia di Sondrio e della Bregaglia Grigionese*. Val Bregaglia, Val Masino, Val Codera, Bettini Editore, Sondrio.

Bertolani M. (1967) Rocce manganesifere tra le granuliti della Valle Strona (Novara). *Periodico di Mineralogia*, Vol. 36, pp. 1011–1032.

Biggioggero B., Montrasio A. (1990) Val Chiavenna e Valle Spluga. Itinerario n. 9. In *Guide Geologiche Regionali. 1. Alpi e Prealpi Lombarde*. Società Geologica Italiana, BE-MA Editore Milano.

Brown P.E., Essene E.J., Peacor D.R. (1980) Phase relations inferred from field data for Mn pyroxenes and pyroxenoids. *Contributions to Mineralogy and Petrology*, Vol. 74, No. 4, pp. 417–425, http://dx.doi.org/10.1007/BF00518121

Brugger J., Giere R. (1999) As, Sb and Ce enrichment in minerals from a metamorphic Fe-Mn deposit, Val Ferrera, Eastern Swiss Alps. *Canadian Mineralogist*, Vol. 37, pp. 37–52.

Brusnitsyn A.I. (2010) Mineralogy of metamorphosed manganese deposits of the South Urals. *Geology of Ore Deposits*, Vol. 52, No. 7, pp. 551–565, http://dx.doi.org/10.1134/S1075701510070044

Bukanov V.V. (2006) *Russian Gemstones Encyclopedia*. Granit Editor, Saint Petersburg.

Capitani G.C., Grobéty H.B., Mellini M. (2003) Reaction sequences, polysomatic faults and chemical compositions of manganese pyroxenoids from Campiglia Marittima skarn. *European Journal of Mineralogy*, Vol. 15, No. 2, pp. 381–391, http://dx.doi.org/10.1127/0935-1221/2003/0015-0381

Deer W.A., Howie R.A., Zussman J. (1997) *Rock Forming Minerals*, Vol. 2A, 2nd ed. Single Chain Silicates. The Geological Society, London.

Degen T., Sadki M., Bron E., König U., Nénert G. (2014) The High-Score suite. *Powder Diffraction*, Vol. 29, No. S2, pp. S13–S18, http://dx.doi.org/10.1017/S0885715614000840

Di Sabatino B. (1967) Su una paragenesi del giacimento manganesifero di Scortico (Alpi Apuane). *Periodico di Mineralogia*, Vol. 36, pp. 965–992.

Diella V., Adamo I., Bocchio R. (2014) Gem-quality rhodonite from Val Malenco (Central Alps, Italy). *Periodico di Mineralogia*, Vol. 83, pp. 207–221.

Grenouillet W. (1920) Geologische Untersuchungen am Splügenpass und Mte di San Bernardino. *Jahresbericht der Naturforschenden Gesellschaft Graubundens*, N.F. 60, pp. 31–60.

Ito J. (1972) Rhodonite-pyroxmangite peritectic along the join $MnSiO_3$-$MgSiO_3$ in air. *American Mineralogist*, Vol. 5, pp. 865–876.

Jefferson D.A., Pugh N.J., Alario-Franco M., Mallison L.G., Millward G.R., Thomas J.M. (1980) The ultrastructure of pyroxenoid chain silicates. I. Variation of the chain configuration in rhodonite. *Acta Crystallographica Section A*, Vol. 36, No. 6, pp. 1058–1065, http://dx.doi.org/10.1107/S0567739480002136

Kenngott A. (1866) *Die Minerale der Schweiz*. Engelmann Editor, Leipzig.

Lee D.E. (1958) An andradite-spessartine garnet from Pajsberg, Sweden. *American Mineralogist*, Vol. 43, pp. 208–215.

Leverett P., Williams P.A., Hibbs D.E. (2008) Ca-Mg-Fe-rich rhodonite from the Morro da Mina mine, Comselheiro Lafaiete, Minas Gerais, Brazil. *Mineralogical Record*, Vol. 39, No. 2, pp. 125–130.

Mancini S. (1997) Le miniere di manganese di Scortico (Fivizzano, Massa-Carrara). *Rivista Mineralogica Italiana*, Vol. 3, pp. 295–296.

Marchesini M., Pagano R. (2001) The Val Graveglia manganese district, Liguria, Italy. *Mineralogical Record*, Vol. 32, No. 5, pp. 349–379.

Maresch W.V., Mottana A. (1976) The pyroxmangite-rhodonite transformation for the $MnSiO_3$ composition. *Contributions to Mineralogy and Petrology*, Vol. 55, No. 1, pp. 69–79, http://dx.doi.org/10.1007/BF00372755

Markvardsen A.J., Shankland K., David W.I.F., Johnston J.C., Ibberson R.M., Tucker M., Nowell H., Griffin T. (2008) ExtSym: a program to aid space-group determination from powder diffraction data. *Journal of Applied Crystallography*, Vol. 41, No. 6, pp. 1177–1181, http://dx.doi.org/10.1107/S0021889808031087

Mazzoleni P., Barone G., Aquilia E., Bersani D., Cirrincione R., Raneri S. (2015) Application of micro-Raman spectroscopy for the identification of unclassified minerals preserved in old museum collections. *Plinius*, Vol. 42, pp. 112–120, http://dx.doi.org/10.19276/plinius.2016.02015

Michailidis K., Sofianska E. (2010) Spheroidal and radiating aggregates of Mn-pyroxenoids in the Olympias carbonate-hosted polymetallic sulphide ore deposit, E. Chalkidiki peninsula, N. Greece. *Review of the Bulgarian Geological Society*, Vol. 71, pp. 59–68.

Mills S.J., Frost R.L., Kloprogge J.T., Weier M.L. (2005) Raman spectroscopy of the mineral rhodonite. *Spectrochimica Acta*, Vol. 62, No. 1-3, pp. 171–175, http://dx.doi.org/10.1016/j.saa.2004.12.022

Millsteed P.W. (2006) Faceting transparent rhodonite from Broken Hill, New South Wales, Australia. *G&G*, Vol. 42, No. 2, pp. 151–158, http://dx.doi.org/10.5741/GEMS.42.2.151

Millsteed P.W., Mernagh T.P., Otieno-Alego V., Creagh D.C. (2005) Inclusions in transparent gem rhodonite from Broken Hill, New South Wales, Australia. *G&G*, Vol. 41, No. 3, pp. 246–254, http://dx.doi.org/10.5741/GEMS.41.3.246

Mottana A. (1986) Blueschist-facies metamorphism of manganiferous cherts: A review of the alpine occurrences. In B.W. Evans and E.H. Brown, Eds., *GSA Memoirs: Blueschists and Eclogites*, Vol. 164, pp. 267–300, http://dx.doi.org/10.1130/MEM164-p267

Nelson W.R., Griffen D.T. (2005) Crystal chemistry of Zn-rich rhodonite ("fowlerite"). *American Mineralogist*, Vol. 90, No. 5-6, pp. 969–983, http://dx.doi.org/10.2138/am.2005.1694

Ohashi Y., Kato A., Matsubara S. (1975) Pyroxenoids: A variation in chemistry of natural rhodonite and pyroxmangite. In *Carnegie Institution of Washington Year Book 75*.

Peters T., Schwander H., Trommsdorff V. (1973) Assemblages among tephroite, pyroxmangite, rhodochrosite, quartz: Experimental data and occurrences in the Rhetic Alps. *Contributions to Mineralogy and Petrology*, Vol. 42, No. 4, pp. 325–332, http://dx.doi.org/10.1007/BF00372610

Peters T., Trommsdorff V., Sommerauer J. (1978) Manganese pyroxenoids and carbonates: Critical phase relations in metamorphic assemblages from the Alps. *Contributions to Mineralogy and Petrology*, Vol. 66, No. 4, pp. 383–388, http://dx.doi.org/10.1007/BF00403423

Pinckney L.R., Burnham C.W. (1988) Effects of compositional variation on the crystal structures of pyroxmangite and rhodonite. *American Mineralogist*, Vol. 73, No. 7-8, pp. 798–808.

Quinn E.P. (2004) Gem News International: Rhodonite of facet and cabochon quality from Brazil. *G&G*, Vol. 40, No. 3, pp. 260–261.

Roth P., Meisser N. (2011) I minerali dell'Alpe Tanatz. Passo dello Spluga (Grigioni, Svizzera). *Rivista Mineralogica Italiana*, Vol. 17, pp. 90–99.

Schiavinato G. (1953) Sulla johannsenite dei giacimenti a silicati manganesiferi del Monte Civillina presso Recoaro (Vicenza). *Rendiconti Società Mineralogica Italiana*, Vol. 9, pp. 210–218.

Simandl G.J., Paradis S., Nelson J. (2001) Jade and rhodonite deposits, British Columbia, Canada. In L. Bon, Ed., *Proceedings of the 35th Forum on the Geology of Industrial Minerals: The Intermountain West Forum, 1999*. Utah Geological Survey, Salt Lake City.

Takahashi K., Hariya Y. (1995) Phase relations of pyroxenoid in the system $MnSiO_3 - MgSiO_3 - CaSiO_3$. In J. Pašava et al., Eds., *Mineral Deposits: From Their Origin to Their Environmental Impacts*. CRC Press, Prague, pp. 1011–1014.

Trommsdorff V., Schwander H., Peters T. (1970) Mangasilikate der alpinen metamorphose in Radiolariten des Julier-Bernina-Gabietes. *Schweizerische Mineralische und Petrographische Mitteilungen*, Vol. 50 pp. 539–545.

Wenk H.R., Maurizio R. (1978) Kutnahorite, a rare Mn mineral from Piz Cam (Bergell Alps). *Schweizerische Mineralische und Petrographische Mitteilungen*, Vol. 58, pp. 97–100.

Wilson W.E. (1989) What's new in minerals: Springfield Show 1989. *Mineralogical Record*, Vol. 20, No. 1, p. 481.

Zanazzi P.F., Nestola F., Nazzareni S., Comodi P. (2008) Pyroxmangite: A high-pressure single crystal study. *American Mineralogist*, Vol. 93, No. 11-12, pp. 1921–1928, http://dx.doi.org/10.2138/am.2008.2963

TAKE THE 2020 GEMS & GEMOLOGY

CHALLENGE

The following 25 questions are from the four 2019 issues of *G&G*. Please refer to the articles in those issues to find the single best answer for each question.

Mark your choice on the response card provided in this issue or visit gia.edu/gems-gemology to take the Challenge online. Entries must be received no later than **Friday, October 9, 2020**. All entries will be acknowledged with an e-mail, so please remember to include your name and e-mail address (and write clearly).

Score 75% or better, and you will receive a certificate of completion (PDF file). Earn a perfect score, and your name also will be listed in the Fall 2020 issue of *Gems & Gemology*.

1. Platelet inclusions are generally diagnostic of rubies from
   A. Cambodia.
   B. Madagascar.
   C. Afghanistan.
   D. Mozambique.

2. The perceived color of faceted alexandrite
   A. shows less noticeable difference with orientation for step-cut stones.
   B. is essentially the same in all orientations with brilliant-cut stones.
   C. is strongly dependent upon orientation regardless of cut.
   D. is more greenish in incandescent light.

3. Fancy white diamonds
   A. always have a "D" color grade.
   B. always show blue fluorescence with long-wave UV light.

C. owe their "hazy" appearance to strong blue fluorescence.
   D. exhibit unusual light scattering from inclusions or dislocations.

4. Coarse silk, both long and short, is seen in sapphires from
   A. Thailand.
   B. Ethiopia.
   C. Australia.
   D. All of the above

5. Which material is *not* found in Ethiopia?
   A. "Zebra sapphire"
   B. Star sapphire
   C. Garnet
   D. Gold

6. Mugloto-type and Maninge Nice-type rubies from Mozambique differ in that
   A. Maninge Nice–type rubies tend to be associated with pri-

mary deposits.
   B. Mugloto-type rubies have stronger fluorescence.
   C. Maninge Nice–type rubies have a slight orangy tint.
   D. Mugloto-type rubies tend to be flatter and hexagonally shaped.

7. With increasing iron content in nephrite,
   A. the refractive index increases.
   B. the specific gravity increases.
   C. the color deepens.
   D. All of the above

8. Which of these statements regarding Malipo emeralds is true?
   A. They have extremely high Cr^{3+} levels.
   B. They display distinct dichroism.
   C. They display high UV fluorescence.

D. They display no color zoning.

9. The center gemstone of the Talisman of Charlemagne was once described as
    A. surrounded only by pearls.
    B. originating from Egypt.
    C. being set in silver.
    D. emerald.

10. Which process starts with an artist drawing out a pattern with henna dye on a marble surface?
    A. *Parchin kari*
    B. *Pietra dura*
    C. Intarsia
    D. Inlay

11. In general, a freshwater non-bead cultured (NBC) pearl would exhibit
    A. lower manganese (Mn) levels than saltwater pearls.
    B. lower strontium (Sr) levels than saltwater pearls.
    C. no reaction to optical X-ray fluorescence.
    D. pronounced voids.

12. Which location produces emeralds with few inclusions?
    A. Afghanistan
    B. Ethiopia
    C. Russia
    D. Brazil

13. Dating zircon inclusions in sapphire
    A. always gives an accurate age of the sapphire host.
    B. is straightforward, as there is no zoning in zircon.
    C. is done using Raman spectroscopy.
    D. None of the above

14. Laser ablation–inductively coupled plasma–mass spectrometry (LA-ICP-MS) analysis of tourmaline
    A. is more accurate and precise than electron microprobe analysis (EMPA).
    B. can separate hydroxy- from oxy-tourmaline species.
    C. can separate liddicoatite from dravite.
    D. reliably measures lithium (Li).

15. What variety of amber is most prized in the Chinese market?
    A. Chicken-fat yellow beeswax
    B. Roasted old beeswax
    C. Golden amber
    D. Transparent

16. What do natural rhodochrosite and imitation rhodochrosite made from pressed gibbsite and calcite have in common?
    A. Within each, the composition and properties of their red and white areas are very similar
    B. Both contain calcium
    C. Refractive index
    D. Luster

17. Pearls originating from bivalves of the Tridacnidae family
    A. likely rotate during growth.
    B. always display a visible flame structure.
    C. rarely have a white bodycolor.
    D. are always nacreous.

18. Which mineral inclusion is most often found in ruby and purple sapphire from the Bo Welu mine in Chanthaburi, Thailand?
    A. High-alumina diopside
    B. Monazite
    C. Sapphirine
    D. Pyrope garnet

19. What is one reason emerald occurrences are rare?
    A. They can only form in one type of geological environment.
    B. All emerald crystals are more than nine million years old.
    C. Aluminum is not very prevalent in the continental crust.
    D. Beryllium is very rare in the upper continental crust.

20. Which of the following methods is most accurate in positively identifying an inclusion species in a gem?
    A. Energy dispersive X-ray fluorescence spectroscopy
    B. UV-Vis-NIR spectroscopy
    C. Raman spectroscopy
    D. Optical microscopy

21. Freshwater cultured pearls from the United States
    A. contain higher levels of calcium (Ca) on average than Chinese freshwater cultured pearls.
    B. contain higher levels of manganese (Mn) on average than natural freshwater pearls from the United States.
    C. are indistinguishable from Chinese freshwater cultured pearls.
    D. contain unusually high levels of lead (Pb).

22. Chalky blue fluorescence was observed in Madagascar sapphires
    A. prior to any heat treatment.
    B. only if they contained yellow colored regions.
    C. with short-wave UV light after heating to 1300°C.
    D. with long-wave UV light after heating to 1000°C.

23. What difference is seen between pearls produced by small and large *Pteria penguin* mollusks?
    A. Pink hue for pearls from small mollusks
    B. Rate of nacre deposition
    C. Pearl quality
    D. Pearl shape

24. Alexandrite from Brazil
    A. demonstrates a more distinct color change than material from Russia.
    B. may show chatoyancy, unlike alexandrite from all other countries.
    C. can have strong color change with good clarity and size.
    D. is a byproduct of emerald mining.

25. Graphitization in diamond
    A. is rarely observed in cut diamonds with no treatment.
    B. can indicate HPHT treatment.
    C. can happen naturally.
    D. All of the above

To take the Challenge online please scan the QR code to the right.

Lab Notes

Editors
Thomas M. Moses | Shane F. McClure
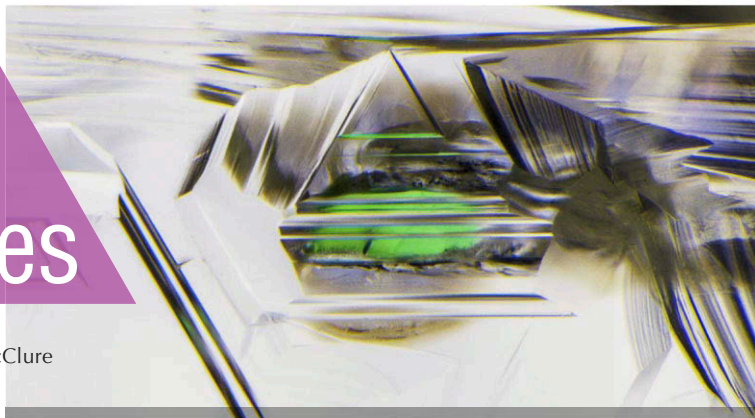
DIAMOND

Diamond with Cavities Showing Radiation Evidence

The Carlsbad laboratory recently examined a 0.70 ct, E-color round brilliant. Infrared spectroscopy showed this to be a type IIa diamond, so we performed a variety of additional spectroscopy and imaging to verify its natural origin. This diamond also had I_1 clarity due to a large inclusion under the table (figure 1). Raman analysis of the inclusions verified that this crystal was a metastable composite of the minerals wollastonite ($CaSiO_3$) and $CaSiO_3$-breyite (E.M. Smith et al., "The very deep origin of the world's biggest diamonds," Winter 2017 *G&G*, pp. 388–403), which indicates a sublithospheric origin. These minerals are believed to be the lower-pressure phases of $CaSiO_3$-perovskite. Around these minerals were large disk-like graphitic fractures indicating inclusion expansion as pressures on the diamond reduced during exhumation from the mantle. The other inclusion present was unidentifiable due to its graphitic casing. Recent research of inclusions in other type II diamonds shows that many, if not most, have a superdeep origin (again, see Smith et al., 2017). This stone is one more example of diamonds forming at incredible depths of

Figure 1. This 0.70 ct natural diamond contained an inclusion of wollastonite and $CaSiO_3$-breyite with a large disk-like graphitic fracture due to exhumation from the mantle. Field of view 1.15 mm.

360–750 km before being transported to near the surface.

But even after such a tumultuous journey, the earth was not finished writing the story of this diamond. While in the earth's crust, the diamond was exposed to radioactive fluids, particularly in etch channels now in the form of cavities on the table and crown facets. DiamondView imaging revealed fluorescing green halos around these cavities (figure 2). Although these isolated areas of fluorescence around the cavities indicated they had likely been filled with a radioactive fluid, there was none of the greenish color or radiation staining that would likely accompany higher radiation doses.

Photoluminescence (PL) mapping with 532 nm (figure 3) and 455 nm (figure 4) excitation shows a pronounced increase in radiation-related defects such as GR1, 3H, and TR12 and other vacancy-related peaks such as NV^-, NV^0, and H4 (a B aggregate with an additional vacancy) within these cavities (figures 3 and 4). Although this diamond was type IIa, there was sufficient nitrogen to form related defects that could be observed at the lower level of detection of PL spectra.

A number of other peaks often seen in natural diamonds but not yet identified, such as those at 490.7, 498,

Figure 2. This DiamondView fluorescence image of the table and crown facets shows green fluorescence halos around two cavity features (as indicated by the red arrows). The green fluorescence, caused by the H4 defect, was caused by localized radiation within those cavities while the diamond resided within the earth's crust and was exposed to radioactive fluids.
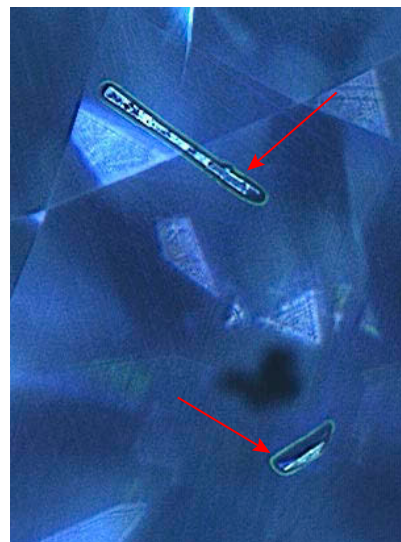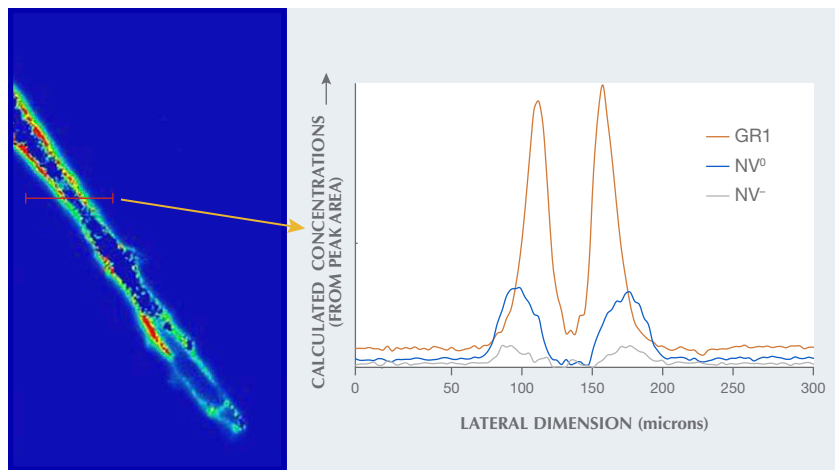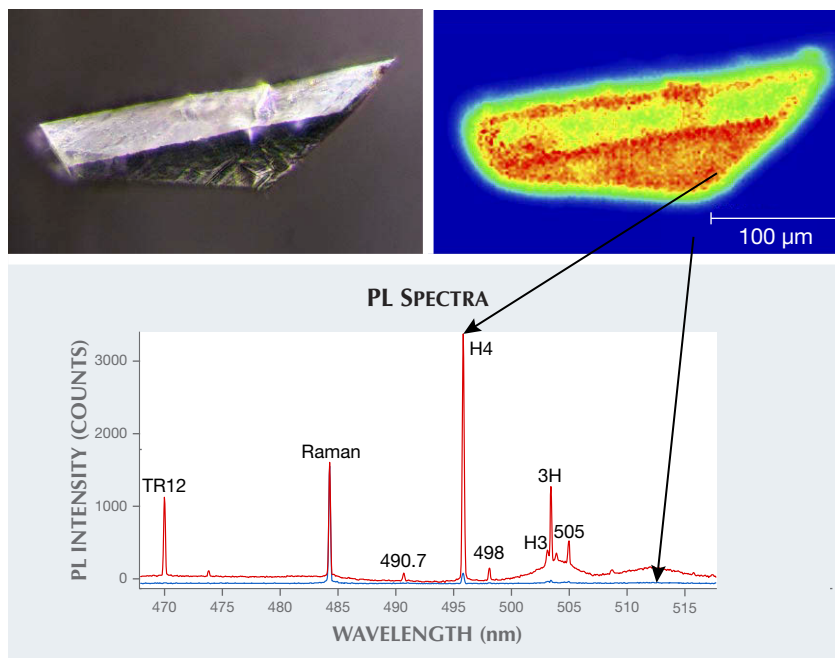
Figure 3. Left: A 532 nm PL map of the top cavity pictured in figure 2 shows a false-color image of GR1 intensity, revealing much higher concentrations along the perimeter of the cavity. Right: A plot of calculated concentrations for several vacancy-related centers from the PL map at left and collected at 3 µm intervals along the red line in the left image. The plot shows the elevated concentrations along the cavity edges of GR1 (neutral vacancy; zero-phonon line [ZPL] at 741.2 nm), NV⁰ (ZPL at 575 nm), and NV⁻ (ZPL at 637 nm).

and 505 nm, also showed elevated concentrations in these cavities; their enhanced presence due to natural radiation was consistent with prior ob-

servations (I.A. Dobrinets et al., *HPHT-Treated Diamonds: Diamonds Forever*, 2013, Springer). The width of the fluorescence halos in figure 2 and the elevated GR1 shown in figure 3 is approximately 30 µm, consistent with the penetration depth of alpha radiation (S. Eaton-Magaña and K.S. Moe, "Temperature effects on radiation stains in natural diamonds," *Diamond and Related Materials*, Vol. 64, 2016, pp. 130–142). We know this radioactive fluid exposure must have occurred in the crustal region because many of the features, such as 3H, would not survive if this exposure occurred at greater depths and, therefore, higher temperatures.

These localized effects of radiation are particularly interesting because the dose was low enough to not impart green coloration or green to brown radiation stains. Nevertheless, the radioactive fluids left their mark on this diamond with the green fluorescence halos around the cavities, providing an excellent example of how many peaks are enhanced by radiation compared with the unaffected portions within the remainder of the diamond. It is also interesting that two distinctly different geological conditions and depths within the earth both contributed to the gemological characteristics of this diamond. The sublithospheric depths imparted some notable minerals as evidence of its superdeep formation, and radioactive fluids within the shallow, crustal region of the earth created the green-fluorescing halos and other radiation features.

Sally Eaton-Magaña and Garrett McElhenny

Formation of the "Matryoshka" Diamond from Siberia

A freely moving diamond trapped inside another diamond was discovered in Siberia by Alrosa in 2019. The unusual diamond, nicknamed the "Matryoshka" after the traditional Russian nesting dolls, attracted widespread interest in how this feature formed.

Figure 4. A photomicrograph (top left) of the lower cavity pictured in figure 2 is also shown in a 455 nm PL map (top right) displaying a false-color image of the H4 intensity. The corresponding spectra (bottom) for two points from the red and blue color regions are shown. Although the spectra were collected at only ~50 µm distance, there are pronounced differences in peak intensities. The diamond Raman peaks within the two spectra are scaled as equal.

Figure 5. The 0.62 ct green "Matryoshka" diamond (4.8 × 4.9 × 2.8 mm) from Siberia has an internal open cavity connected by two small channels to the outside. The surface is covered by etched trigons and striations. A small diamond crystal can move freely inside the cavity.

Figure 6. The small, flat diamond crystal enclosed in the cavity showed a hexagonal outline. The surface of the small diamond was covered with groups of parallel straight striations following the diamond crystal symmetry.

The 0.62 ct flat octahedral diamond, a twinned macle, was recently examined by the New York laboratory. Flat-bottom trigon etch pits were well developed on the face {111} (figure 5). The crystal showed a clear green bodycolor, with small dark green radiation stains in shallow fractures along the edges when viewed from the top of the crystal. Two etch channels on opposite sides of the

edges had rectangular openings about 0.2 mm in width. The channels extended into the internal enclosed cavity. These features made this diamond unique. Trapped in the cavity was a small, flat diamond crystal with a hexagonal outline. The small diamond, covered with some green radiation stains on the surface, is entirely detached from its host crystal and can move freely inside (see video 1 at

https://www.gia.edu/gems-gemology/spring-2020-labnotes-matryoshka). The surface of the small diamond was covered with groups of straight parallel striations following the diamond crystal symmetry. No etched trigons were observed on the surfaces of the small diamond (figure 6). Except for tiny foreign-material contaminations at the two entrances of the open channels, no other inclusions were observed in this crystal (figure 7).

Absorption spectroscopy in the infrared region indicated a type Ia diamond, with high concentration of aggregated nitrogen. A moderately strong absorption at 3107 cm^{-1} from the N3VH defect was also observed. More detailed analysis of selected areas with and without the small internal crystal showed almost identical spectral features, confirming that the small crystal is a diamond with nearly identical trace element chemistry as the host. The UV-Vis absorption spectrum collected at liquid nitrogen temperature (–196°C) showed clear absorptions from the N3 defect (ZPL at 415 nm) and GR1 (ZPL at 741 nm). These spectral features are typical for a natural type Ia diamond, except for the strong GR1 absorption, which is attributed to irradiation. Occurrence of the small dark green radiation stains revealed that this diamond was naturally irradiated. Under various laser excitations at liquid nitrogen temperature, photoluminescence spectroscopy showed emissions at 911, 787, 741 (GR1), 700, 535, 503.5 (3H), 489, and 468 nm. Absence of emission from the H3 defect (N2V, ZPL 503.2 nm) indicated that the diamond crystal was not annealed to any elevated temperature after being naturally irradiated.

X-ray computed microtomography (μ-CT) scanning and analysis revealed some very interesting observations (video 2 at https://www.gia.edu/gems-gemology/spring-2020-labnotes-matryoshka). First, the small internal crystal showed the same intensity of X-ray absorption as the host diamond supporting the conclusion that the small crystal is a diamond. Second, CT technology can accurately compile the
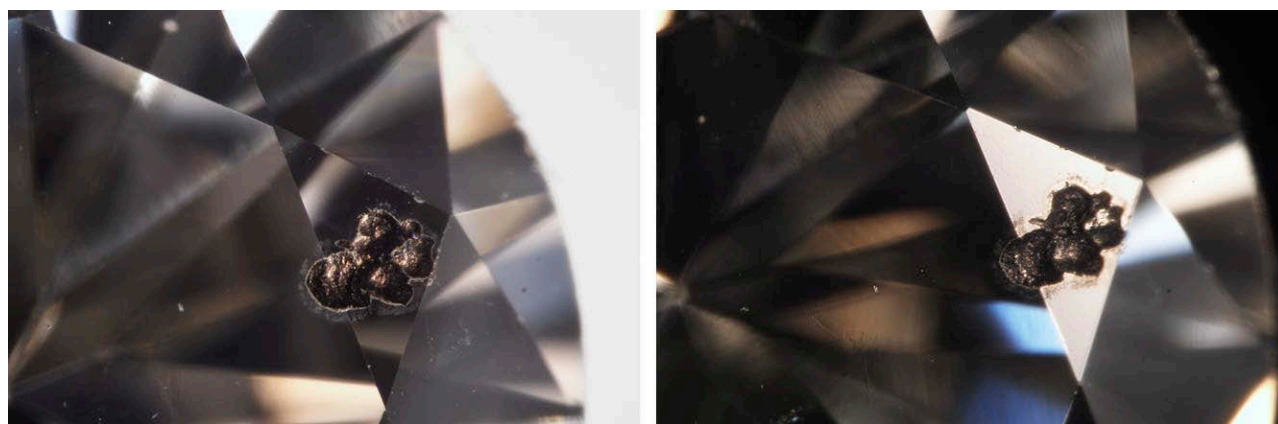
Figure 7. An open channel about 200 μm in width connected the internal cavity with the outside.

GEMS & GEMOLOGY

Figure 8. The laser cavities on the star facet (left) and in reflected light (right). Field of view 1.5 mm.

morphology of the internal cavity through stacked imaging. The cavity showed a flattened octahedral shape, composed of two octahedron crystals of parallel growth. The crystal habit of the void, an extremely important observation of this study, strongly indicated that the open cavity was originally occupied by another diamond crystal instead of other mantle minerals. Once crystallized in the earth's mantle under very high pressure, it is not possible for a diamond crystal to have any internal open space. Other mantle minerals such as garnet, olivine, or pyroxenes will show entirely different crystal habits. Finally, volumes of different parts of this crystal were calculated. The external crystal was 33.16 mm³ in volume (0.58 ct), while the internal small crystal had a volume of 1.51 mm³ (0.03 ct). The total calculated weight of 0.61 ct is very close to the actual weight of 0.62 ct (excluding the contaminations at entrances of the etching channels). The volume of the open cavity was 5.99 mm³, equal to 0.11 ct of diamond originally occupying that space. Based on these calculations, the total initial weight of this crystal would have been about 0.72 ct.

In summary, this diamond crystal was initially a solid diamond without the cavity when it formed in the earth's mantle. Due to chemical heterogeneity in trace element chemistry or sub-micro inclusions/structure (such as those fibrous diamonds), the middle part of the diamond crystal (now represented by the void) was se-

lectively dissolved during interactions with special type(s) of melt/fluid after its crystallization. About 0.11 carats of diamond dissolved through the two small open channels that created the pathway for the internal cavity. The host diamond and the small internal diamond crystals were inactive or less active to the melt/fluid and consequently survived. Fluid with radioactive elements responsible for the green bodycolor and formation of radiation stains would have been the last step in decorating this crystal. Special chemistries and interactions with multiple types of melt/fluid subsequent to its initial crystallization led to the formation of this unique diamond in Siberia.

Wuyi Wang, Emiko Yazawa, Stephanie Persaud, Elina Myagkaya, Ulrika D'Haenens-Johansson, and Thomas M. Moses

Graphitic Cavities on Diamond

An atypical series of graphitized cavities was recently observed on a star facet (figure 8, left) of a 0.45 ct near-colorless round brilliant diamond. The presence of graphite was confirmed with Raman spectroscopy. The observed residue surrounding the craters could have been the result of a lasering process.

Laser sawing is now the standard way to shape rough into blocked shapes for brillianteering and polishing, and laser drilling is used to treat internal inclusions. The laser marks

were not the typical oscillating lines of manufacturing remnants. These remnants on extra facets or natural surfaces are usually left behind for a variety of reasons such as saving weight. Neither was there an associated internal inclusion, which one would expect if this were a treatment, though a shallow inclusion could have been completely removed by this lasering. The only other internal inclusion was a dark brown crystal on the opposite side of the table, which had not been treated by lasering.

Reflected light (figure 8, right) revealed a small "island" of the original facet left behind, evidence that many craters in close proximity joined together to form one larger cavity. This is also the reason it is suspected that this cavity system was caused by a laser as opposed to another thermal process, such as a jeweler's torch. Something like a torch is unlikely to have left an intact section of the facet in the center of a burnt-out cavity. The fact that there were many connected craters does make these cavities seem intentional, though the purpose is not obvious.

Troy Ardon

Corundum Inclusions in Gem Diamond

Inclusions can tell us a great deal about a diamond's formation history. Inclusions such as olivine, garnet, and chromite are more common, while others such as kyanite, zircon, and
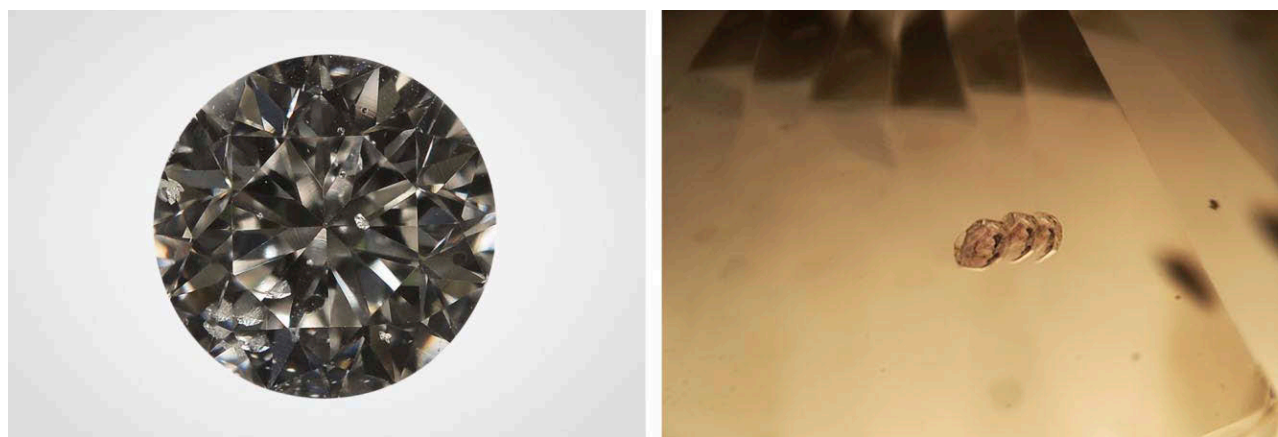
Figure 9. Left: Face-up image of the 0.13 ct round brilliant diamond. Right: Photomicrograph of the largest corundum inclusion exhibiting a slight pinkish color when viewed through a microscope with a diffuser plate. The triple image of the inclusion is due to the diamond's faceting. Field of view 1.76 mm.

corundum (Al_2O_3) can be quite rare. Regardless of their rarity, diamond inclusions are often quite fascinating as they trap a small bit of the deep earth that cannot otherwise be sampled.

To our knowledge, the only previously recorded occurrence of chromium-bearing corundum (i.e., ruby or pink sapphire) as an inclusion in a gem diamond was nearly 40 years ago (H.O.A. Meyer and E. Gübelin, "Ruby in diamond," Fall 1981 *G&G*, pp. 153–156). In that study, the 0.06 ct round brilliant diamond contained a

surface-reaching ruby crystal. The exposed inclusion was analyzed using single-crystal X-ray diffraction, and chemical analysis was conducted using a reference ruby to calculate oxide percentages. At least two occurrences of blue corundum (i.e., sapphire) have also been reported (Summer 2006 Lab Notes, pp. 165–166; M.T. Hutchison et al., "Corundum inclusions in diamonds—discriminatory criteria and a corundum compositional dataset," *Lithos*, Vol. 77, No. 1-4, 2004, pp. 273–286).

Here we report the second identification of chromium-rich corundum in a natural gem diamond. This diamond was discovered by Michael Turner at Stuller during routine screening for undisclosed laboratory-grown diamonds. Mr. Turner determined that it was type IIa using FTIR spectroscopy and then noted a peculiar chromium doublet emission in PL. The diamond was sent to the Carlsbad laboratory for further testing. Upon examination, the 0.13 ct round brilliant (figure 9, left) contained at least five internal inclusions that were positively identified as chromium-rich corundum (ruby or pink sapphire). The largest inclusion (figure 9, right) measured 0.18 mm long; the additional inclusions were 0.07 mm or smaller.

When viewed through the microscope with a diffuser plate, the largest of the inclusions displayed a very light pinkish color, while the rest exhibited no visible coloration. A DXR2xi Raman imaging microscope was used to create a map of the individual inclusions. These maps, consisting of thousands of individual Raman spectra, were analyzed and compared to Raman spectra from known corundum samples to determine that at least five of the inclusions in the diamond were in fact corundum (figure 10). A chromium doublet centered around 1369 and 1399 cm^{-1} (~693 and 694 nm) was also

Figure 10. Raman spectra identifying the corundum inclusions. The red trace shows the figure 9 (right) inclusion, while the blue trace is a known corundum reference. Spectra vertically offset for clarity.
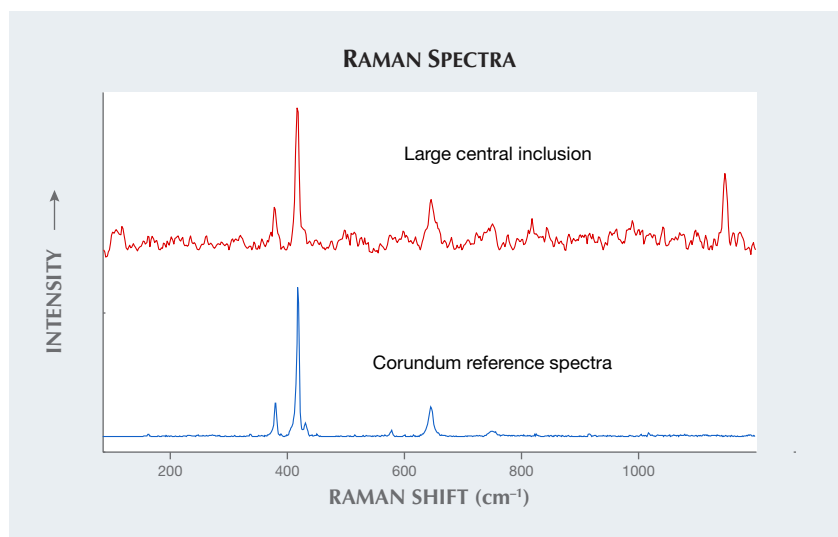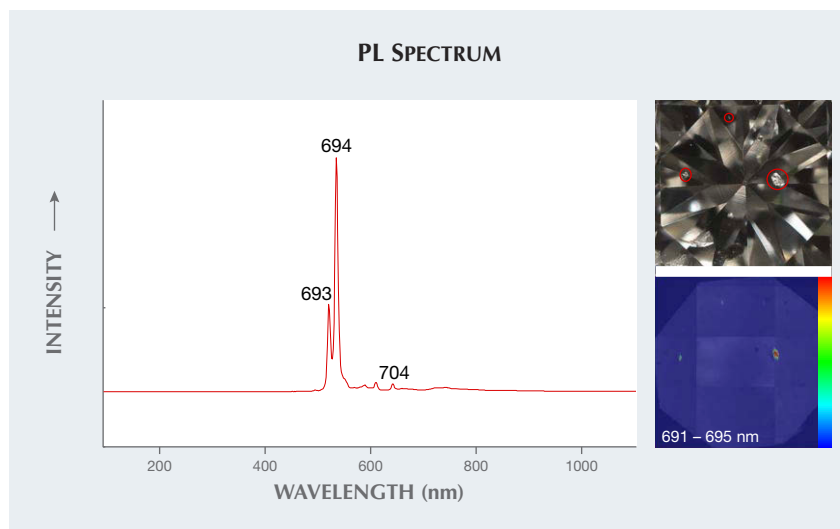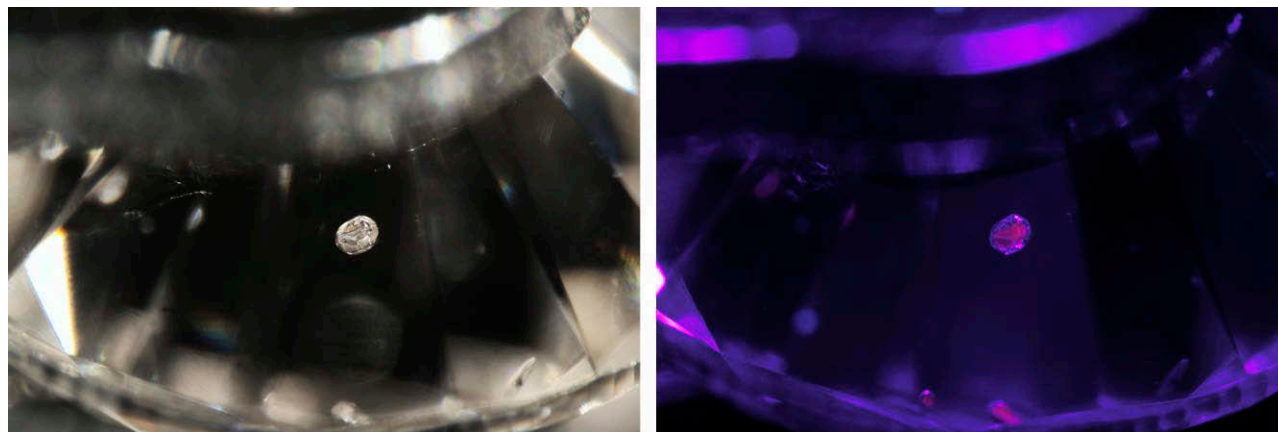
PL Spectrum

Figure 11. Left: Photoluminescence spectrum showing the detection of chromium with 532 nm laser excitation. Top right: Photo of the table with the corundum inclusions circled in red. Bottom right: False-color PL map generated by the Raman imaging microscope collected from the table in the same orientation showing the 693–694 nm chromium peaks and peak intensities.

detected in the Raman spectra, further confirming that the corundum contained significant chromium. Also observed in the inclusions were additional luminescence peaks that are not typical of diamond (figure 11). In particular, a 704 nm peak was localized around the corundum inclusions.

After identifying the inclusions, we tested their reaction to UV light. Under illumination from a long-wave ultraviolet light source (365 nm), the largest one displayed a beautiful deep red color (figure 12). Ruby and pink sapphire typically exhibit a weak to strong red color when exposed to long- and short-wave UV due to fluorescence from abundant chromium impurities; the same was observed for some of the corundum inclusions within this diamond. Other corundum inclusions were either too weak to photograph or did not display any visible reaction to UV light.

Previous research by G.R. Watt et al. ("A high-chromium corundum (ruby) inclusion in diamond from the São Luiz alluvial mine, Brazil," *Mineralogical Magazine*, Vol. 58, No. 392, 1994, pp. 490–493) and Hutchison et al. (2004) found that inclusions of corundum (colorless, ruby, and sapphire) in their non-gem type II diamonds contained large amounts of chromium and nickel. Both studies declared the diamonds to be sublithospheric in origin with an eclogitic paragenesis due to the association of the corundum inclusions with other deep-mantle inclusions. We did not perform chemical analysis on the inclusions described here because they were entirely encased within the diamond. While we cannot determine the depth of formation for this diamond, it can be reasonably inferred, based on previous studies, to have a sublithospheric origin and eclogitic paragenesis, as Al_2O_3 is rare in peridotitic mantle. Opportunities to examine diamonds containing rare inclusions provide an intriguing glimpse into the deep earth.

It is with great sadness that we note the passing of Michael Turner. Michael was a well-respected contributor to GIA, and he will be dearly missed.

Garrett McElhenny, Michael Turner, and Christopher M. Breeding

Figure 12. The largest of the corundum inclusions shown with ordinary fiber-optic lighting (left) and long-wave UV illumination (right). The right image displays the corundum's deep red fluorescence color. Field of view 2.34 mm.

Figure 13. This carved Fancy Dark gray diamond ring weighs 13.15 ct. The whitish areas are clear viewing windows.

Figure 14. Needle clusters in the carved Fancy Dark gray diamond ring.

Solid Carved Dark Gray Diamond Ring

A ring made entirely of natural diamond (figure 13) was recently submitted to GIA's New York laboratory. A large rough weighing approximately 20 ct was used to create this unusual 13.15 ct carved piece. It is common to find solid carved rings of jade and wood, which were traditionally worn as symbols of status or wedding rings signifying eternity. This is the first example of a solid diamond ring submitted to GIA for identification.

This solid type IaB diamond ring owes its Fancy Dark gray color to the graphite needles (figure 14) trapped during formation deep below the earth's surface. Like famous gem-quality black diamonds such as the Black Orlov, the Korloff Noir, the Black Star of Africa, and the Spirit of de Grisogono, this diamond has clear spaces creating viewing windows that capture a snapshot of the ring's formation history. The ring was fashioned from the Beaufort diamond from Canada's Northwest territories and named the "Beaufort Ring."

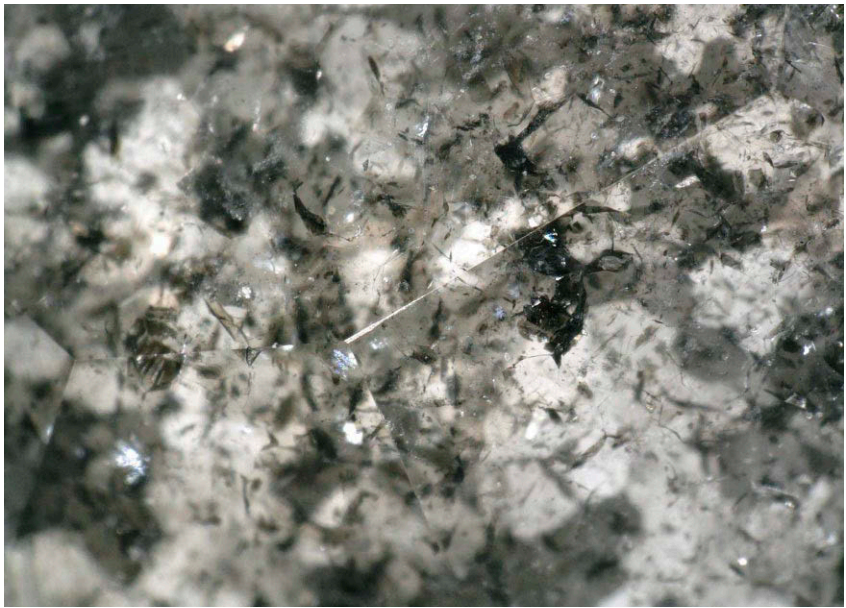This diamond rough from which the ring was carved likely formed billions of years ago under high pressure. During regional metamorphism, H3 and NiN complexes were formed within the crystal lattice (K. Smit et al., "Black diamonds from Marange (Zimbabwe): A result of natural irradiation and graphite inclusions," Summer 2018 *G&G*, pp. 132–148). These impurities were detected by photoluminescence spectroscopy. Infrared spectroscopy was used to detect the B aggregates and hydrogen complexes within the diamond lattice, categorizing this diamond as type IaB. Fluorescence imaging of the ring using the DiamondView showed bundled dislo-

Figure 15. Fluorescence imaging using the DiamondView shows bundled dislocation networks.
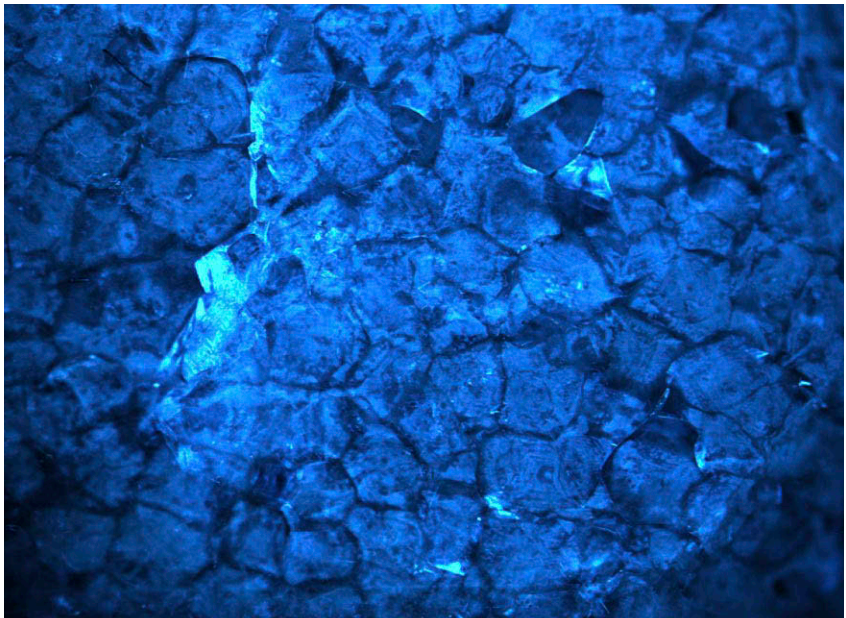
cation networks indicative of natural diamond growth (figure 15). While this diamond ring may not be a traditional piece, it carries many unique aspects capturing a snapshot of Earth's history within a true infinity band.

Stephanie Persaud, Paul Johnson, and John King

Clarity-Enhanced GLASS Imitating Emerald

The Carlsbad lab received a transparent green octagonal step cut for identification. This stone visually resembled emerald due to its rich green color and large fractures. However, its single refractive index of 1.510 was not consistent with emerald's double refractive index of 1.577 to 1.583.

Examination with a standard gemological microscope revealed no natural inclusions. Instead, it showed rounded gas bubbles in the body as well as flattened gas bubbles in surface-reaching fractures (figure 16). This stone has also been examined with FTIR and long-wave UV. When observed with long-wave UV, the fractures emitted a weak white fluorescence while the body of the stone showed a very weak blue fluorescence. The presence of these features was enough to conclude it had been clarity enhanced.

Additionally, rounded gas bubbles separate from fractures, an RI of 1.51, and the sample's FTIR spectrum (figure 17) were consistent with manufactured glass.

These gemological properties and observations identified the material as clarity-enhanced manufactured glass. Due to emerald's high value, it is common for imitations to show up in the market. Items such as this demonstrate the need to always be cautious when purchasing gemstones.

Michaela Stephan

Unusually Large GRANDIDIERITE

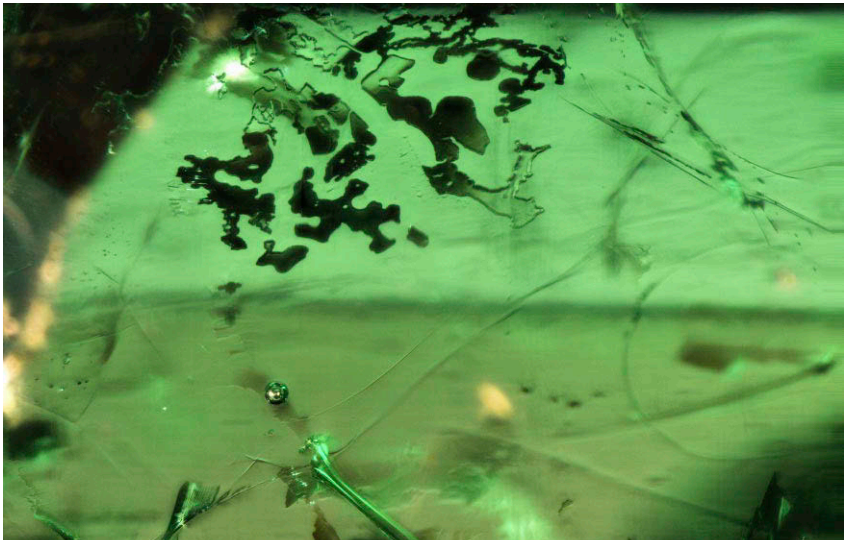The Carlsbad laboratory received a green-blue translucent to semi-

Figure 16. Round gas bubbles in host material and flat gas bubbles within the break of fractures. Field of view 1.99 mm.

translucent stone weighing approximately 763.5 ct and measuring 50.32 × 48.15 × 36.17 mm (figure 18). Standard gemological examination revealed a refractive index of 1.621–1.581, weak green-blue to green pleochroism, and absorption lines at 480 and 490 nm seen in the handheld spectroscope. Examination with a standard gemological microscope revealed the stone to be heavily included with fractures, fine particulate clouds, and miscellaneous whitish minerals. The results from Raman

Figure 17. Shown are the infrared spectrum for the octagonal step cut (red line) and the typical reference spectrum for manufactured glass (dotted black line). The spectra have been offset for clarity.
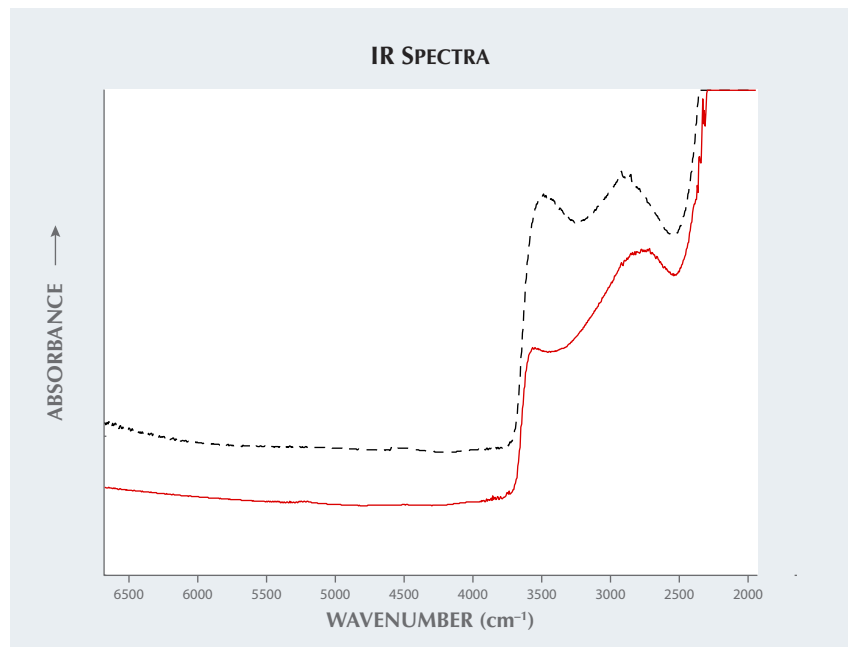

IR SPECTRA

ABSORBANCE →

WAVENUMBER (cm⁻¹)

Figure 18. A green-blue translucent to semi-translucent grandidierite weighing 763.5 ct.

spectroscopy, microscopic observations, and standard gemological examination were consistent with the rare mineral grandidierite.

Named after French naturalist Alfred Grandidier (1836–1912), grandidierite is a very rare mineral first discovered in 1902 at the cliffs of Andrahomana on the southern coast of Madagascar (D. Bruyere et al., "A new deposit of gem-quality grandidierite in Madagascar," Fall 2016 *G&G*, pp. 266–275). Gem-quality material of facetable size was not found in the market until after the summer of 2015 (Winter 2015 Gem News International, pp. 449–450). Grandidierite is found in various localities as an accessory mineral in aluminous boron-rich pegmatites and in rocks subjected to local high-temperature, low-pressure metamorphism such as contact aureoles and xenoliths (again, see D. Bruyere et al., 2016). It very seldom reaches large sizes, and this is the largest grandidierite GIA has seen to date.

Michaela Stephan

PEARL

"Electronic Device" in an Atypical Bead Cultured Pearl

GIA's Hong Kong laboratory recently received a white metal ring adorned with a round partially drilled dark gray nacreous pearl measuring 16.30 mm in diameter (figure 19). Externally, the pearl appeared to be a typical bead cultured pearl, routinely referred to in the trade as "Tahitian," that had formed in

a *Pinctada margaritifera* mollusk. Advanced testing supported this initial observation; a 700 nm feature in the UV-Vis spectrum (Summer 2016 Gem News International, pp. 207–208), a "bumpy" Raman spectrum, and a series of peaks at around 620, 650, and 680 nm in the photoluminescence (PL) spectrum confirmed the mollusk's identification (S. Elen, "Identification of yellow cultured pearls from the black-lipped oyster *Pinctada margaritifera*," Spring 2002 *G&G*, pp. 66–72).

Preliminary examination with the unaided eye and subsequent microscopic observation revealed characteristic features of an untreated nacreous pearl: soft luster; slightly smoothened platy structure with a few negligible blemishes, pits, and scratches; and no indications of color concentration or coatings. Although the mounting prevented clear observation of the drill hole, some greenish blue material was observed and did not conform to the features expected for a traditional shell bead nucleus. This therefore appeared to be an atypical bead cultured pearl. While not routinely encountered in the trade, this is not the first example GIA's laboratories have examined. Indeed, some branded products even exist in the market, such as Galatea's carved atypical bead cultured pearls ("Atypical 'beading' in the production of cul-


Figure 19. The dark gray round nacreous Tahitian cultured pearl mounted in a ring that was submitted for identification.

tured pearls from Australian *Pinctada maxima*," *GIA Research News*, February 13, 2017) with a variety of untraditional nuclei. Further testing might have assisted in identifying the greenish blue material in the submitted pearl, but that would have required the pearl's removal.

Despite the typical Tahitian bead cultured pearl appearance, real-time microradiography (RTX) quickly revealed a rather uncharacteristic internal structure. Instead of a traditional shell bead nucleus (figure 20, left), a "nucleus" containing a probable electronic "capsule-like" device was exposed (figure 20, right). Greater detail

Figure 20. Real-time X-ray (RTX) microradiographs showing a traditional freshwater shell bead nucleus in a typical bead cultured pearl (left) and the unusual internal scene within the client's pearl (right). The majority of the "bead" material within the client's pearl looks more radio-translucent than the shell bead, and the various thicknesses of the metal components are visible as more radio-opaque areas.
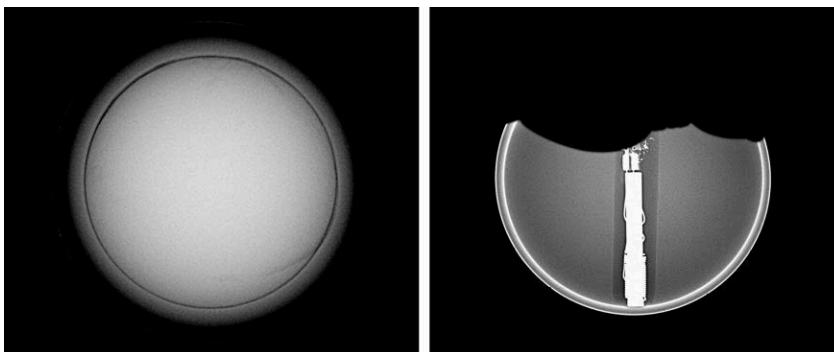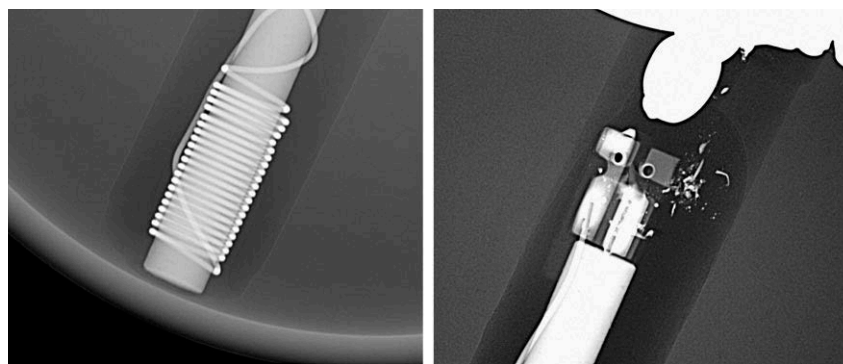
Figure 21. Greater detail of the coiled wire around one end of the metal capsule component (left) and the two contact points at the opposite end (right).

of the device's structure showed an elongated metal component with coiled wire around one end and two contact points at the opposite end (figure 21). The other notable feature observed was that the radio-opacity of the remaining constituent of the nucleus was not in keeping with that expected of typical freshwater shell. The white outer layer represents the nacreous layers that overgrew the inserted materials, and the nacre thickness also seemed rather thin in comparison to that typically observed in Tahitian bead cultured pearls routinely examined.

The RTX results reminded the author of a recently patented pearl identification technology that introduced radio-frequency identification (RFID) to pearl culturing. As a result, GIA's Hong Kong team obtained some pearl samples containing the RFID chips directly from the local supplier (Fukui Shell Nucleus Factory) for comparison.

The pearls were found to contain RFID chips in each nucleus (figure 22, A and B), consistent with previous reports (H.A. Hänni and L.E. Cartier, "Tracing cultured pearls from farm to consumer: A review of potential methods and solutions," *Journal of Gemmology*, Vol. 33, No. 7-8, 2013, pp. 239–246). The RTX images clearly revealed an RFID chip positioned within a small recess inside the shell bead nucleus (figure 22C). The sup-
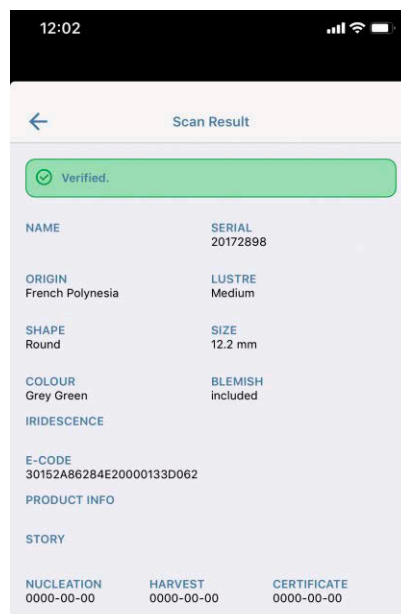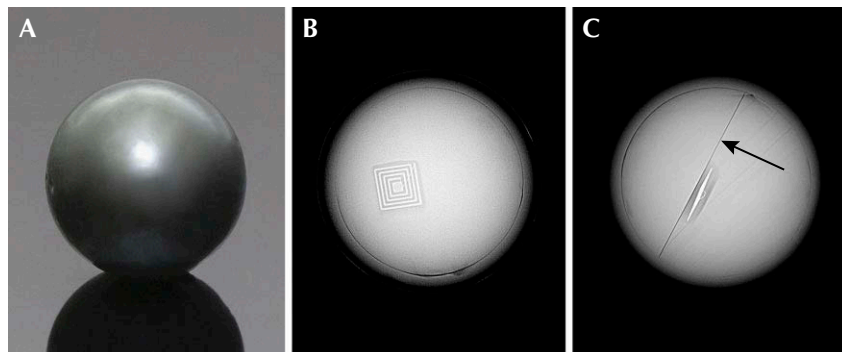

Figure 23. A registered smart phone app (connected to an RFID reader) will display the scan result after an RFID chip is detected. The result shows the information uploaded to a particular chip. The optional information (e.g., product info, nucleation date, harvest date) has not been entered for this sample.

plier stated that the chips are placed slightly off-center to prevent damage from drilling and that the beads are fashioned from freshwater shell, like the vast majority of nuclei used in the cultured pearl industry. The freshwater environment of an intact bead nucleus (before RFID chip insertion) provided by the same company was confirmed by energy-dispersive X-ray fluorescence (EDXRF) analysis. Another characteristic feature of these RFID bead cultured pearls revealed by the RTX work was that the beads were sawn in half prior to the chip's insertion (indicated by the black line seen in figure 22C when aligned correctly) and then bonded back together.

By connecting a registered smart phone app to an RFID reader, the information saved in the chips may be retrieved (figure 23). The purpose of introducing such technology is to enable consumers to identify, track, and trace the sources of the pearls encountered ("Fukui unveils South Sea

Figure 22. Externally, this specimen with an RFID chip embedded (A) looks no different from bead cultured pearls routinely seen in the market. However, RTX examination revealed a square chip positioned inside a recess within a sawn and reconstructed shell bead nucleus (B and C). The arrow in image C indicates the sawn plane.

pearls with Metakaku nuclei," *Jewellery News Asia*, No. 392, 2017, pp. 66–67).

Obviously the RFID beads revealed in the pearls we sourced in no way match the internal structure observed in the client-submitted pearl described in this note. The RFID reader also failed to read the information (if any) stored in the capsule-like electronic device. Thus, we still cannot be certain of the identity of the materials incorporated in the unusual cultured pearl, but we will continue to investigate.

Pearl culturing technologies are forever adapting in order to meet the perpetually high demand. Besides RFID, near-field communication (NFC) technology has also been adopted by some pearl brands (e.g., Galatea and Gyso) to gain market share. One of their selling points is that by simply scanning the pearl with an NFC-enabled smart phone with the registered app installed, digital information such as audio, videos, and photos can be retrieved. It is too soon to tell whether these tracking and marketing technologies for pearls will be widely accepted by the buying public. Nonetheless, GIA will remain alert to these developments.

Cheryl Ying Wai Au

Fluorescence Spectroscopy for Colored Pearl Treatment Screening

Color is one of the most important value factors for pearls. Commonly applied treatment methods used to alter their color to increase commercial value include dyeing, irradiation, and bleaching. Unfortunately, the identification of some color treatments is challenging and time consuming. In this study, we tested the use of a fluorescence spectroscopy system to nondestructively inspect pearls by measuring their near ultraviolet (UV) response to visible fluorescence under mid-UV excitation.

When excited by deep to mid-UV (200 to 300 nm) light, naturally colored pearls emit a fluorescence band between 320 and 400 nm centered at
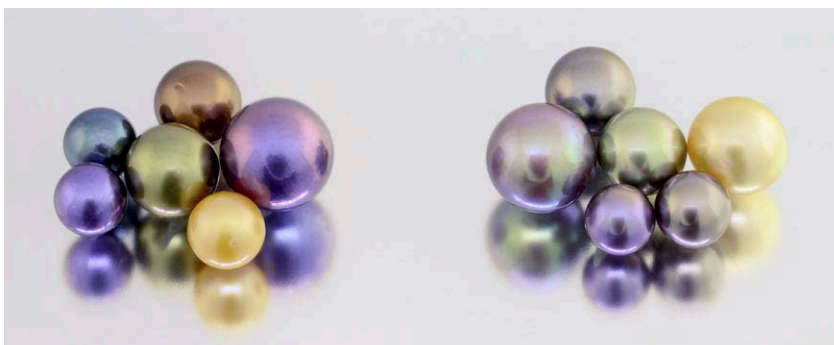

Figure 24. Treated pearls (left) with a similar range of colors as naturally colored pearls (right).

340 nm. This fluorescence feature may be attributable to the organic compounds contained within the nacreous layers (J. Hiramatsu et al., "Non-destructive assessment of the effects of heat and sunlight on akoya pearl quality," *Seibutsu Kogaku*, Vol. 88, No. 8, 2010, pp. 378–383; F.W.J. Teale, "The ultraviolet fluorescence of proteins in neutral solution," *Journal of Biochemistry*, Vol. 76, No. 2, 1960, pp. 381–388). It can be identified in all untreated pearls, corresponding to the UV absorption band around 280 nm (J. Yan et al., "Origin of the common UV absorption feature in cultured pearls and shells," *Journal of Materials Science*, Vol. 52, No. 14, 2017, pp. 8362–8369).

Commonly applied color treatments such as dyeing and irradiation tend to damage or mask the conchiolin in the nacre, significantly reducing the fluorescence intensity. By evaluating the intensity of a pearl's fluorescence in the UV region, it is possible to rapidly detect potential color treatments on pearls in a nondestructive manner.

A prototype fluorescence spectroscopy system was designed to measure the fluorescence signal in order to detect potential color treatments. A 275 nm UV light-emitting diode (LED) was used as the excitation source. The excitation light was guided by a bi-fabricated fiber probe to generate the fluorescence signal from the pearl sample, and the fluorescence signal was relayed by the same fiber probe to the detector. Finally, a spectrometer was used to disperse the fluorescence light emitted and monitor

the response in the 300 to 700 nm range.

A set of 12 pearl samples was selected for evaluation. Figure 24 shows six treated-color pearls (left) and six naturally colored pearls (right). The samples included both freshwater and saltwater cultured pearls of colors frequently encountered in the market.

Figure 25 shows the experimental results of this fluorescence measurement prototype. The horizontal axis indicates the fluorescence wavelengths from 300 to 550 nm while the vertical axis shows the normalized detector counts, which is the relative intensity of the signal normalized to the spectrometer's integration time per millisecond. Based on the results, the six naturally colored pearls showed fluorescence signals in the UV region at least 2.5 times stronger than the six treated pearls. This characteristic feature may be a useful and rapid screening technique for gemological laboratories to detect color treatments in pearls.

Tsung-Han Tsai and Chunhui Zhou

A Fossilized Shell Blister and Blister Pearl

Fossils are the remains or impressions of prehistoric organisms preserved from past geological ages. Some of the most common fossils are shells of various marine mollusks and, occasionally, their associated pearls (Winter 2015 Lab Notes, pp. 432–434). Recently two interesting fossilized specimens were studied by staff of GIA's New York laboratory. One resembled

FLUORESCENCE SPECTRA

Legend:
- Natural color golden
- Natural color strong purplish pink
- Natural color strong pinkish purple
- Natural color brown
- Natural color dark gray
- Natural color pistachio
- Treated color golden
- Treated color strong pinkish purple
- Treated color strong pinkish purple
- Treated color dark bluish gray
- Treated color chocolate
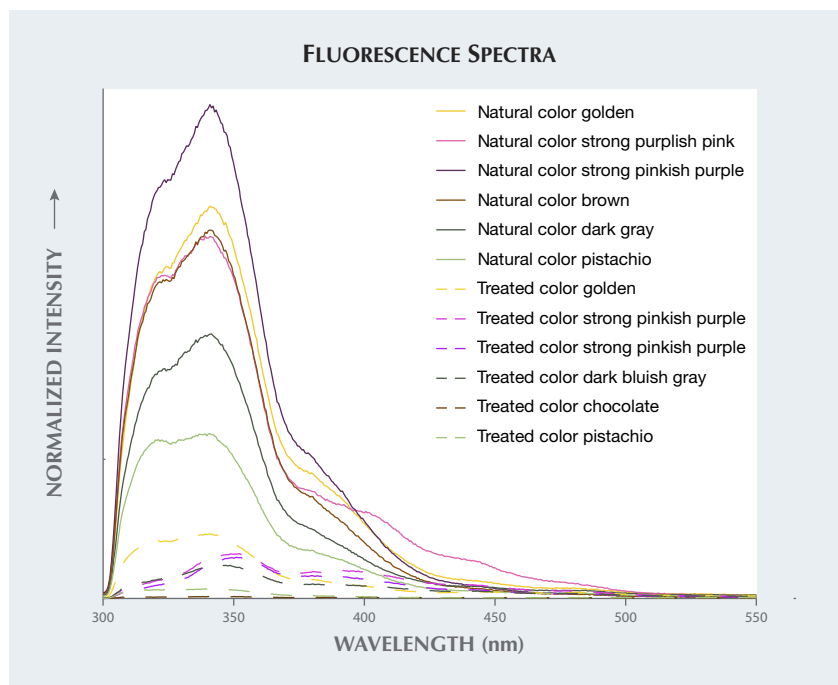- Treated color pistachio

Figure 25. Fluorescence spectra of naturally colored and treated-color pearls. The horizontal axis represents the wavelength of the signal, and the vertical axis displays the signal level in normalized intensity.

Figure 26. Two fossilized specimens, a shell blister (left) and a blister pearl (right), both with their associated shell. Courtesy of Gina Latendresse, American Pearl Company, Inc.

a shell blister and the other a blister pearl, both with associated shell (figure 26).

The smaller sample appeared to be a shell fragment measuring approximately 24.4 × 18.6 × 6.5 mm and weighing 12.62 ct. The back of the shell showed even striations and a cellular crystal growth pattern, while the cross section showed a columnar structure (figure 27). A shallow "bump" noted on the face side could be best described as a shell blister, according to a recent study ("Natural shell blisters and blister pearls: What's the difference?" *GIA Research News*, https://www.gia.edu/gia-news-research/natural-shell-blisters-and-blister-pearls). No additional information was provided about this specimen.

The second sample measured approximately 37 × 25 mm and weighed 32.63 ct. Its form resembled a concave shell fragment, and a near-round blister pearl was clearly attached to its inner surface (figure 28). According to our source, this specimen was found in Ellis County, Kansas, and formed within an *Inoceramus* mollusk genus (an extinct marine bivalve resembling

the related winged pearly oysters of the extant genus *Pteria*). Fossils of the *Inoceramus* are commonly found in the Pierre Shale of the Western Interior Seaway in North America, where the state of Kansas lies today (figure 29). The specimen is reportedly estimated to be as much as 86 million years old.

EDXRF analysis detected low concentrations of manganese and high concentrations of strontium, typical of marine mollusks. Iron was also detected in both specimens, probably introduced through infiltration from the surrounding environment over millions of years. Microradiography did not reveal any clear internal growth

Figure 28. A near-round blister pearl seen lightly attached to its host shell.

Figure 27. Left: Clear striations are visible on the back of the shell blister (measuring approximately 24.4 × 18.6 × 6.5 mm). Center: Cellular crystal growth patterns are evident on the back of the shell blister. Right: Columnar growth structures are prominent with the cross section of the shell fragment.

Figure 29. Map of North America highlighting the shallow inland seaways present during the mid-Cretaceous period. The arrow indicates the present-day state of Kansas. © Colorado Plateau Geosystems Inc.

structures. These two intriguing specimens created by Mother Nature and preserved by her until their discovery provide unique insights into ancient mollusks and their associated pearl or pearl-like companions.

Chunhui Zhou and Tao Z. Hsu

Saltwater Bead Cultured Pearl with Laminated Nucleus

The nuclei used for bead cultured pearl production are usually spheres fashioned from nacreous shell (J. Taylor and E. Strack, "Pearl production," in P.C. Southgate and J.S. Lucas, *The Pearl Oyster*, 2008, Elsevier, Oxford, UK, pp. 273–302). The majority of this shell is sourced from freshwater mussels found in the Mississippi and Tennessee River systems in the United States (L.E. Cartier and M.S. Krzemnicki, "New developments in cultured pearl production: Use of organic and baroque shell nuclei," *Australian Gemmologist*, Vol. 25, No. 1, 2013, pp. 6–13), and the resulting nuclei typically range between 6.0 and 8.0 mm. When a white round nacreous pearl weighing 28.89 ct and measuring

16.00 mm (figure 30) was submitted to GIA's Bangkok laboratory for identification, the gemologists were intrigued by what the X-rays revealed.

Externally, the pearl showed characteristics typical of bead cultured pearls originating from the silver-lipped variety of *Pinctada maxima*: large size, symmetrical shape, satiny luster, and white color. Preliminary observation with a loupe and microscope revealed faint and smooth overlapping nacre platelets with some surface blemishes and polishing lines. Energy-dispersive X-ray fluorescence (EDXRF) analysis failed to detect any manganese (Mn) but did reveal high levels of strontium (Sr), while X-ray luminescence revealed a moderate greenish yellow reaction. These results are consistent with those expected for saltwater cultured pearls containing a freshwater shell bead nucleus (H.A. Hänni et al., "X-ray luminescence, a valuable test in pearl identification," *Journal of Gemmology*, Vol. 29, No. 5/6, 2005, pp. 325–329).

However, several interesting features were revealed by examination with real-time microradiography (RTX) (figure 31). The bead nucleus was clearly visible in the RTX images and measured approximately 10.21 mm in diameter. This uncommon size was the first indication that this was not a standard bead. Moreover, two sharp planes were clearly visible, another interesting observation since most shell bead nuclei examined

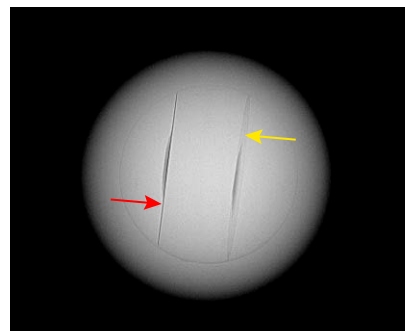Figure 30. A white round nacreous pearl weighing 28.89 ct and measuring 16.00 mm.

Figure 31. Real-time microradiography revealed two planes and two recesses (one in the center of each plane) within a large shell bead nucleus. In the optimal direction, one plane (red arrow) shows as a distinct dark line owing to the perfect alignment with the X-ray source relative to the detector, while the other plane (yellow arrow) is less well aligned and hence appears more like a discoid feature.

with RTX do not show such defined bands. (These are not to be confused with the mostly weak and more diffused bands sometimes seen that relate to the shell's layered growth structure.) The parallel lines matched structures observed in GIA's previous research on known samples of bead cultured pearls in which laminated shell bead nuclei were used. In keeping with samples from that research, the most defined line appears when the nucleus is in the optimal direction (figure 31, red arrow) relative to the X-ray source and detector, while the less defined line (figure 31, yellow arrow) appears more like a discoid feature when the alignment is not so perfect. Additionally, a shallow and circular-looking recessed feature in the center of each plane aroused further curiosity. Such structures are not typical of other laminated beads previously examined by GIA.

Laminated shell bead nuclei originated a few decades ago when some Australian pearl farms attempted to produce large pearls to meet demand. However, the high price of the larger shell bead nuclei needed for this forced them to experiment with other

Figure 32. A 5.35 ct purplish red cabochon displaying asterism.

Figure 33. Left: Blue flashes and trapped gas bubbles of various sizes and shapes along surface-reaching fractures and cavities. Field of view 7.64 mm. Right: The bismuth glass-filled fractures and cavities were easily visible in the X-ray image.

materials such as dolomite (Summer 1998 Lab Notes, pp. 130–131; Winter 2001 Gem News International, pp. 332) to produce the large nuclei. Unfortunately, none of the materials were suitable from a commercial perspective. Some farms started bonding strips of shell together to fashion larger bead nuclei of around 10–10.9 mm. The majority of such pearls were produced from second operations. Since this experiment proved more successful, a number of saltwater bead cultured pearls possessing a laminated shell bead nucleus are still encountered in the market today.

GIA labs globally have encountered numerous laminated shell bead nuclei. However, this is the first example with the unusual recessed features, and the reason for their existence is unclear. They are unlikely to be related to damage caused during the manufacturing of the bead. The almost identical positions and appearances suggest that they were created for some purpose. Since the pearl is undrilled, damage resulting from any drilling process (Summer 1995 Lab Notes, pp. 125) may also be eliminated. Another possibility is that they may be related to placement areas for radio-frequency identification (RFID) chips (see Spring 2020 Lab Notes, pp. 134–136 of this issue). But since it is customary to only use one chip per pearl and the recesses are relatively thin with rounded outlines, which differ from the usual deeper square recesses encountered for RFID pearls, this seems unlikely.

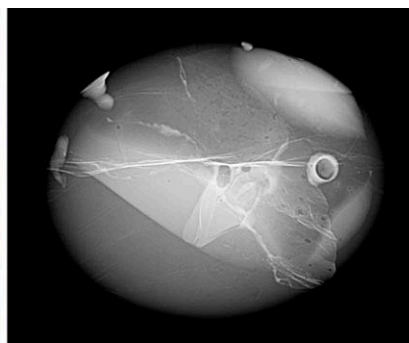The presence of faint banding within the nucleus and the pearl's X-ray luminescence reaction prove that the bead was fashioned from freshwater shell. Therefore, even though the nucleus is laminated, the pearl is still classified as a "bead cultured pearl." The only mystery left is the reason for the two shallow circular recesses in the surfaces of two of the shell pieces used to form the laminated bead nucleus.

Areeya Manustrong and Kwanreun Lawanwong

Bismuth Glass-Filled Burmese Star RUBY

The Hong Kong laboratory recently examined a 5.35 ct purplish red oval cabochon displaying asterism (figure 32). Standard gemological tests yielded a spot refractive index (RI) of 1.76, medium red fluorescence under long-wave ultraviolet (UV) light, weak red fluorescence under short-wave UV, and a diagnostic spectrum in the handheld spectroscope, all of which were consistent with ruby.

Magnification revealed iridescent silk and arrowhead-like inclusions similar to those frequently found in Burmese rubies. Apart from the natural inclusions, easily observable foreign substances for clarity enhancement were found along surface-reaching fractures and cavities. Numerous rounded to flattened gas bubbles and blue flashes were visible within filled fractures (figure 33, left). The filler also exhibited a different luster from that of the ruby under reflected light. X-ray radiography indicated heavy element depositions along these fractures and cavities (figure 33, right). The Fourier-transform infrared (FTIR) spectrum showed two broad absorptions centered at 3500 and 2670 cm^{-1} associated with manufactured glass. Qualitative analysis using energy-dispersive X-ray fluorescence (EDXRF) spectroscopy revealed the presence of bismuth, whereas no lead was detected. This confirmed that the foreign material was actually a bismuth-based glass.

Based on internal features and advanced testing results, the stone was positively identified as a manufactured product consisting of bismuth glass and ruby. Although bismuth-based glass has occasionally been applied to corundum as a filling material (Spring 2017 Lab Notes, p. 94), it is rare to detect it in star ruby.

Xiaodan Jia and Mei Mei Sit

G&G Micro-World

Editor
Nathan Renfro

Contributing Editors
Elise A. Skalwold and John I. Koivula

Actinolite in Spinel

Lotus Gemology received a vivid cobalt blue spinel from Vietnam for laboratory testing. Despite its small size of well under a carat, its stunning color stood out immediately. The stone proved to be exceptionally clean. Most cobalt spinels we test contain fissures, small crystals, or other inclusions. After careful examination, we found just one tiny inclusion, a transparent teardrop-shaped crystal (figure 1).

Raman microscopy revealed the crystal to be actinolite, a mineral in the amphibole group. As far as we are aware, this is the first reported inclusion of actinolite in spinel.

E. Billie Hughes
Lotus Gemology, Bangkok

Bavenite in Quartz

The author recently had the opportunity to examine a 233.60 ct faceted quartz containing numerous white radial inclusions, courtesy of Mike Bowers (figure 2). The unusual inclusions were identified as the mineral bavenite by Raman and laser ablation–inductively coupled plasma–mass spectrometry (LA-ICP-MS) analysis.

South America claims a long history of gemstone production and arguably produces some of the finest gem specimens in the world. Of the South American gem-producing areas, Brazil is by far the most prolific source of important gemstones. Due to the array of different geologic environments, a number of uncommon minerals can be
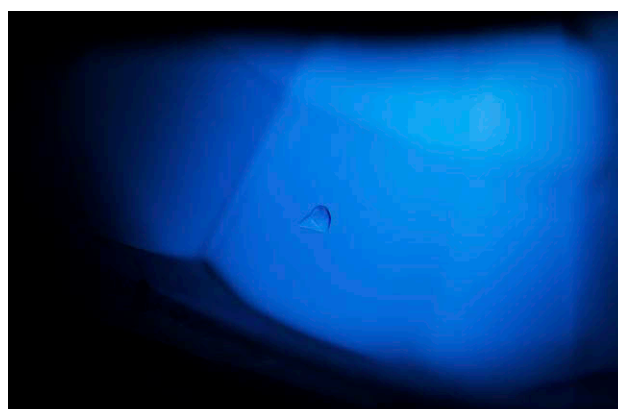

Figure 1. This small transparent colorless crystal in spinel was identified by Raman analysis as actinolite. Photomicrograph by E. Billie Hughes; field of view 1.7 mm.

found. The mineral bavenite, $Ca_4Be_2Al_2Si_9O_{26}(OH)_2$, is an uncommon orthorhombic mineral that occurs as drusy in

Figure 2. Clusters of white radial needles of the mineral bavenite were seen in this 233.60 ct quartz. Photomicrograph by Nathan Renfro; field of view 13.43 mm. Courtesy of Mike Bowers.

miarolitic cavities in granite and associated pegmatite, formed by a low-temperature alteration of beryl and other beryllium-bearing minerals, and also in hydrothermal veins and skarns. It generally forms in more alkali environments and is often associated with bertrandite, titanite, danalite, and zeolites (J.W. Anthony et al., Eds., *Handbook of Mineralogy*, Mineralogical Society of America, http://www.handbookofmineralogy.org). This is believed to the first time GIA has encountered bavenite inclusions in quartz.

Maxwell Hain
GIA, Carlsbad

Diamond with Mobile Green Diamond Inclusion

Diamond inclusions are relatively common guests in diamond crystals. They generally go unnoticed as the refractive index of the host and guest are the same. So it is often the case that the only visual clues to such an inclusion lie in the interface between the host and guest, where the slight mismatch traps fluids from the growth environment and leaves a delicate optical irregularity with the appearance of a ghost-like framework of diamond. Inclusions like this can be further explored by examining stones in polarized light, which often reveals significant strain around the guest diamond.

One of the most interesting examples of a diamond inclusion in diamond the authors have encountered is a 0.87 ct sawn crystal section containing a negative crystal cavity (figure 3) that is open at the surface. Inside is a tiny green octahedral diamond crystal that is free to rattle around but too large to exit through the opening at the surface (figure 4). For a video of the green diamond inclusion moving inside the negative crystal contained in the host diamond, go to https://www.gia.edu/gems-gemology/spring-2020-microworld-diamond-mobile-diamond-inclusion.
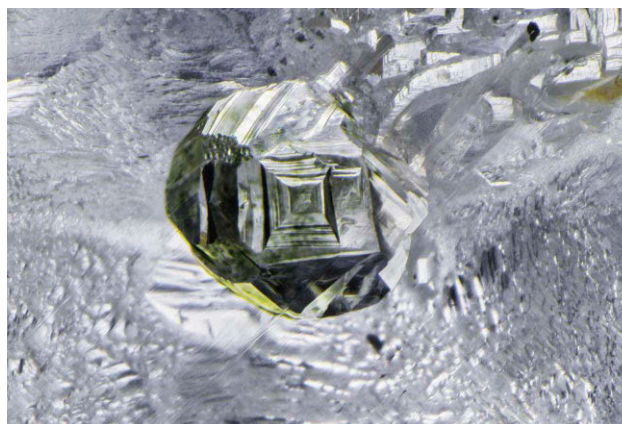

Figure 3. This negative crystal in a diamond is colored green by radiation staining and contains a loose green diamond crystal. Photomicrograph by Nathan Renfro; field of view 4.23 mm.

Presumably this diamond inclusion was completely encased in its diamond host, but dissolution occurred as the host made its way to the earth's surface, causing the interface between the two crystals to widen until the small entrapped crystal was liberated enough to become mobile (J.I. Koivula, *The MicroWorld of Diamonds*, Gemworld International, Northbrook, Illinois, 2000, 157 pp.). Subsequently, the diamond must have been exposed to fluids carrying radioactive materials that entered through the small opening, causing green radiation staining of the negative crystal and guest diamond inclusion. While mobile diamond inclusions in diamond are always remarkable (see Lab Notes, pp. 127–129 of this issue), this example is the only one the authors have observed of a mobile green diamond inclusion trapped in a colorless diamond.

Nathan Renfro and John I. Koivula
GIA, Carlsbad

Figure 4. This registered pair of images shows how the green diamond contained inside the negative crystal can change position inside the host diamond and how the green diamond is too large to fit through the opening to the surface. Photomicrographs by Nathan Renfro; field of view 3.20 mm.
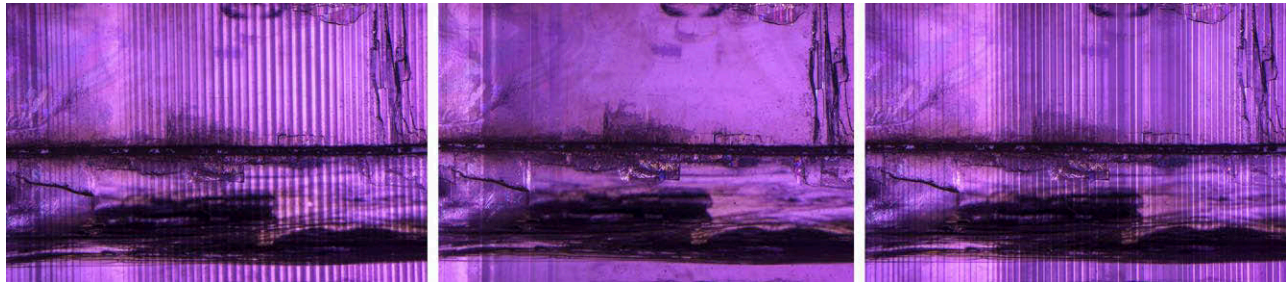
Figure 5. Neodymium pentaphosphate is a rare experimental synthetic material that shows reversible lamellar twinning under polarized light when gentle pressure is applied perpendicular to the twinning planes. This series of images shows vertical striations that have changed with slight pressure. Photomicrographs by Nathan Renfro; field of view 14.10 mm.

Reversible Twinning in Neodymium Pentaphosphate

Unusual synthetic gem materials are often the result of experimental crystal growth for industrial applications, including use in the laser industry. One such experimental synthetic that was produced in a very limited quantity is neodymium pentaphosphate, with the chemical formula of NdP_5O_{14} (Winter 1997 Gem News, pp. 307–308). Examined using polarized light, it displays very prominent lamellar twinning. Lamellar twinning is a regular parallel repeated reversal in growth that causes the twinning planes to appear as alternating dark and light bands when observed in polarized light (figure 5). The material's most unusual property is that when slight pressure is applied perpendicular to the twinning planes, the twinning reverses so that the dark areas can become light, and the light areas become dark. See video of this at https://www.gia.edu/gems-gemology/spring-2020-microworld-reversible-twinning-ndp. Interestingly, the reversal is also accompanied by a weak clicking sound. The unusual elastic twinning of this material makes it exceedingly difficult to cut into a gem, though a 5.33 ct stone was faceted by Art Grant of Coast-to-Coast Rare Gems in the 1990s. To the authors' knowledge, no other material displays this interesting property.

Nathan Renfro and John I. Koivula

Pallasitic Peridot with Iridescent Needle-Like Inclusions

Pallasite is a rare type of stony iron meteorite that contains crystalline olivine. The author recently had the opportunity to examine a suite of pallasitic peridot that were reported to have originated from the Jepara meteorite found on the Indonesian island of Java in 2008 (figure 6). The stones were selected by Bradley Payne for the abundance of needle-like inclusions that showed vibrant interference colors. To observe the inclusions, oblique fiber-optic illumination was used to explore the gems until the light re-
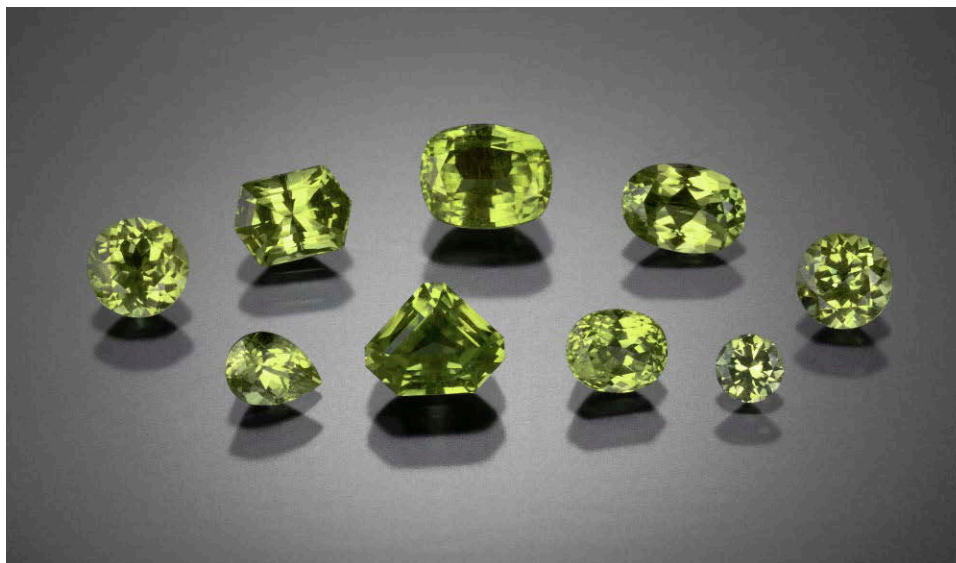

Figure 6. This suite of pallasitic peridot (0.17–1.40 ct) from the Jepara meteorite contains colorful needle-like inclusions. Photo by Robison McMurtry; courtesy of Bradley Payne.
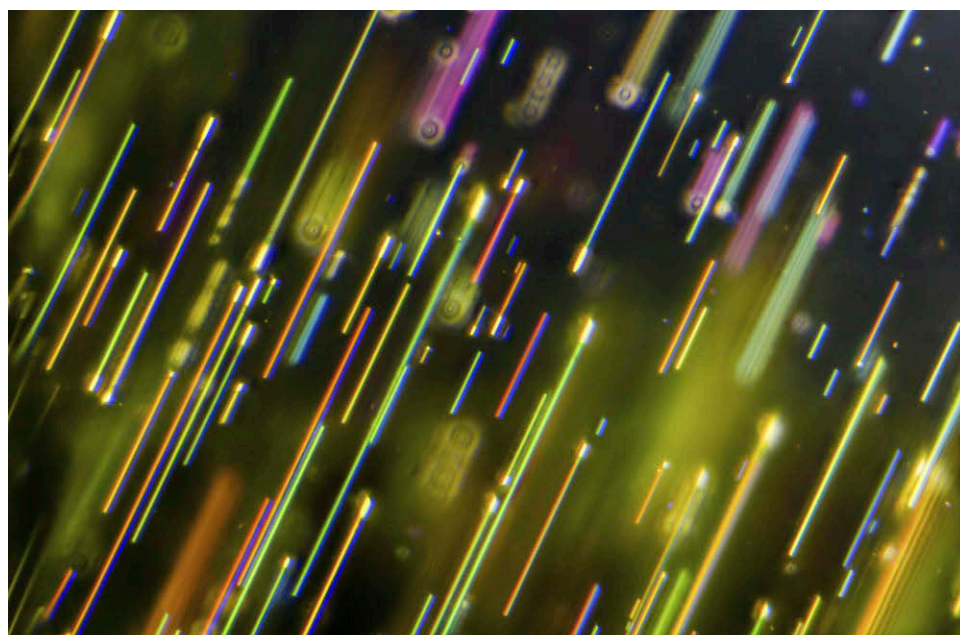
Figure 7. Oblique fiber-optic illumination revealed colorful iridescent needle-like inclusions in the pallasitic peridot from Java. Photomicrograph by Nathan Renfro; field of view 1.83 mm.

flected off the inclusions at the same time, revealing their hidden colorful beauty (figure 7) and confirming the crystallographic alignment of the inclusions. According to Payne, less than 5% of the gems from the Jepara meteorite show these types of inclusions. These are the most beautiful inclusions the author has examined in a suite of pallasitic peridot from the Jepara meteorite.

Nathan Renfro

Phenomenon Resembling Play-of-Color in Sapphire

A phenomenon resembling play-of-color was seen in a 4.13 ct unheated sapphire recently examined by the author. When tilted in darkfield lighting (watch the video at https://www.gia.edu/gems-gemology/spring-2020-microworld-play-of-color-sapphire), the sapphire displayed this noteworthy effect, which is most commonly seen in precious opal. It occurred within a small section of a single fine, milky cloud with an unusual shape (figure 8, left). The cloud also possessed extensive transparent graining confined within its borders, best seen in brightfield illumination (figure 8, right).

Some regions of the cloud displayed an appearance of rainbow graining with spectral colors confined to the linear grain lines and looked one-dimensional. Other regions, however, expressed a soft billowy broad flash of altering colors with diffuse edges resembling play-of-color and did not follow linear grain lines (figure 9). Play-of-color in opal is defined

Figure 8. Left: A fine, angular milky cloud as seen in darkfield illumination. Right: Brightfield illumination of the same cloud reveals fine transparent graining causing diffraction of light into spectral colors. Photomicrographs by Britni LeCroy; field of view 3.57 mm.
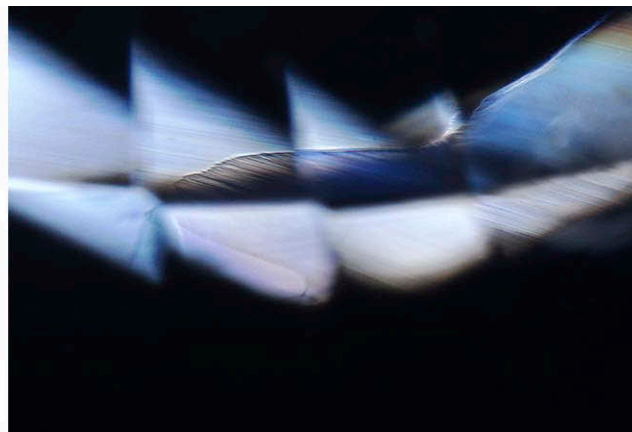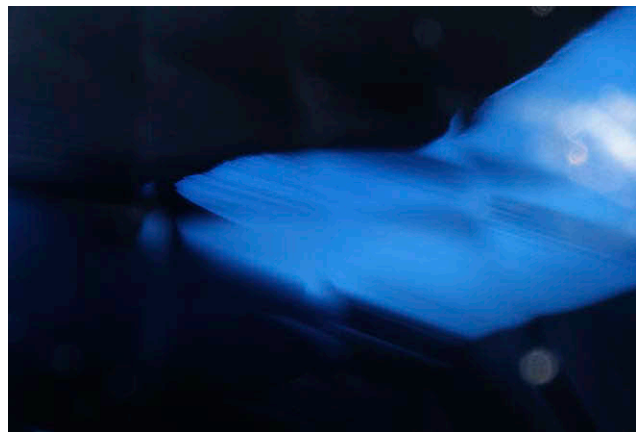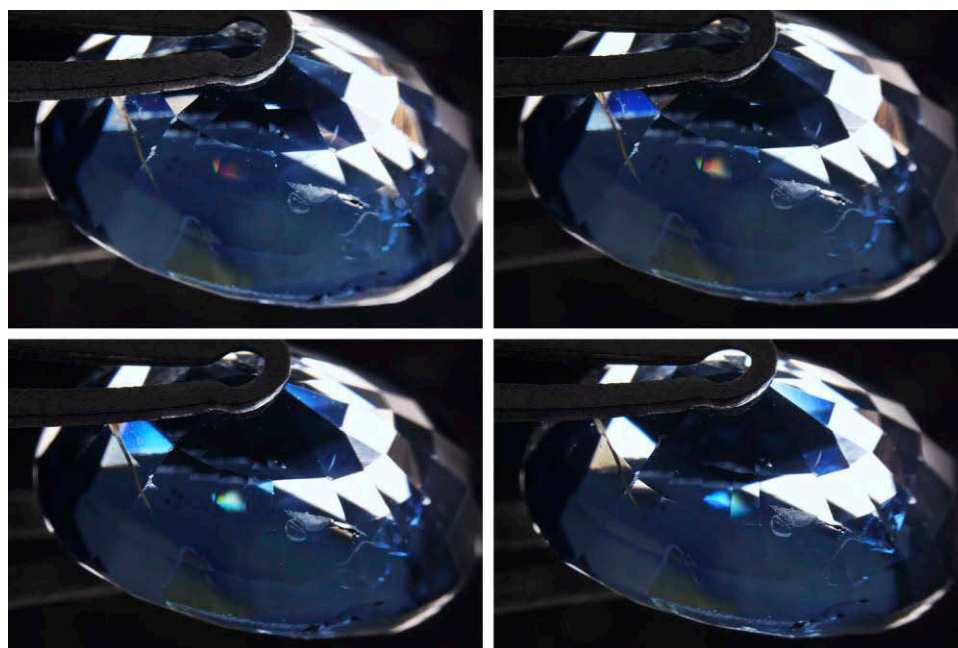
Figure 9. Subtle tilting of the sapphire, as shown in this image sequence viewed with darkfield illumination, revealed a play-of-color phenomenon within the milky cloud. Photomicrographs by Britni LeCroy; field of view 14.52 mm.

as a display of spectral colors due to the diffraction of light as it passes through organized, submicroscopic spherical particles. It is possible that the combination of fine milky particles and abundant transparent graining within the cloud were able to diffract light in a way that resembles play-of-color.

Britni LeCroy
GIA, Carlsbad

Staurolite in Ruby

We have examined thousands of rubies in Lotus Gemology's laboratory, yet the hours spent peering into the microscope are never mundane because each stone captures its own piece of history through its inclusions. Recently a client submitted one such gem for testing, a 3.04 ct specimen measuring 11.98 × 7.13 × 4.21 mm that was identified as an untreated ruby from Madagascar based on inclusions.

In the microscope, a few bright brownish red crystal inclusions immediately stood out. They were transparent, with a saturated red hue that, in darkfield illumination, was conspicuous even against their ruby-red background (figure 10). Some were also cut through on the surface, allowing us to view them with reflected light. Observation of the surface showed that the crystals had a luster just

Figure 10. Viewed with darkfield illumination, a transparent brownish red crystal inclusion clearly stands out, even in a ruby matrix. This is believed to be the first staurolite inclusion found in corundum. Photomicrograph by E. Billie Hughes; field of view 2 mm.
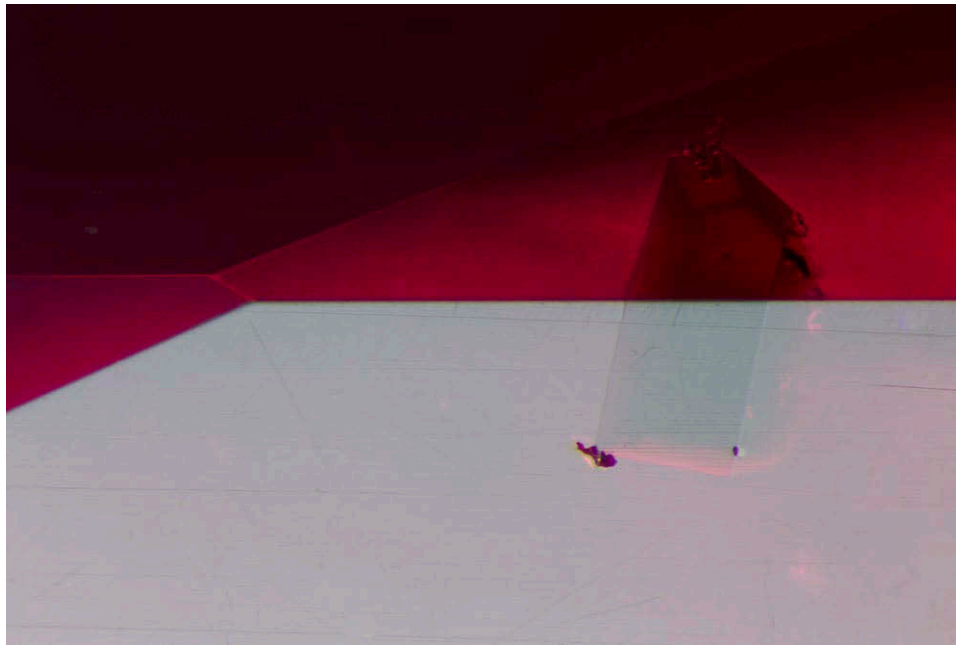
slightly lower than that of the surrounding corundum, suggesting a slightly lower RI (figure 11).

To get a better idea of the crystals' identity, we examined them using micro-Raman spectroscopy with a WITec Alpha 300R Raman imaging system with a 532 nm laser, which identified them as staurolite. Staurolite, $Fe_2Al_9Si_4O_{22}(OH)_2$, is a red to brown mineral known to occur in Madagascar. Its RI values are $n_\alpha = 1.736–1.747$, $n_\beta = 1.740–1.754$, and $n_\gamma = 1.745–1.762$. Corundum has a slightly higher RI range, with $n_\omega = 1.767–1.722$ and $n_\varepsilon = 1.759–1.763$. The combination of microscopic observation and Raman spectroscopy gave us confidence that these were indeed staurolite crystals.

It is no wonder these crystals initially stood out. To the best of our knowledge, this is the first recorded observation of staurolite as an inclusion in corundum. This Madagascar ruby has encapsulated a fascinating kernel of history within its depths.

E. Billie Hughes

Triplite in Beryl

Among our Lotus Gemology lab clients and the gem trade as a whole, inclusions have often been seen as negative features. However, people are starting to become more interested in inclusions and see them as unique characteristics rather than mere imperfections.

One such client brought us a colorless beryl with a large brownish orange crystal near the culet (figure 12), hoping to learn the inclusion's identity. Raman microscopy revealed it to be triplite. Triplite, $(Mn,Fe)_2PO_4(F,OH)$, is a mineral named for the Greek *triplos*, or triple, which refers to its three directions of cleavage. While some triplites have been faceted, they are quite rare both as a mineral and as a gem material. The specimen's owner stated that the

beryl came from Pakistan. As triplite is known to be found in Pakistan, this is certainly a possibility. The owner was happy to learn that his gem contained a relatively rare mineral.

We are excited to see these examples of inclusions being viewed as points of interest within a gem.

E. Billie Hughes

Quarterly Crystal: Unknown Inclusion in Triphane Spodumene

When exploring in the micro-world, we occasionally run into problems we cannot solve and inclusions that cannot

Figure 12. A dark orange triplite inclusion stands out against its colorless beryl host. Photomicrograph by E. Billie Hughes; field of view 8 mm. Courtesy of Ayub Muhammad.

Figure 13. The interior of this 91.02 ct Afghani spodumene plays host to a 4 mm translucent orange crystal. Photo by Diego Sanchez.

be identified. Such was the case with the dominant orange inclusion in this 91.02 ct, 39.29 × 19.34 × 12.93 mm, terminated light yellow triphane spodumene crystal. This spo-

dumene crystal clearly hosts a prominent 4 mm translucent orange crystal surrounded by a stress-related iridescent cleavage halo (figure 13). The spodumene crystal, from Dara-
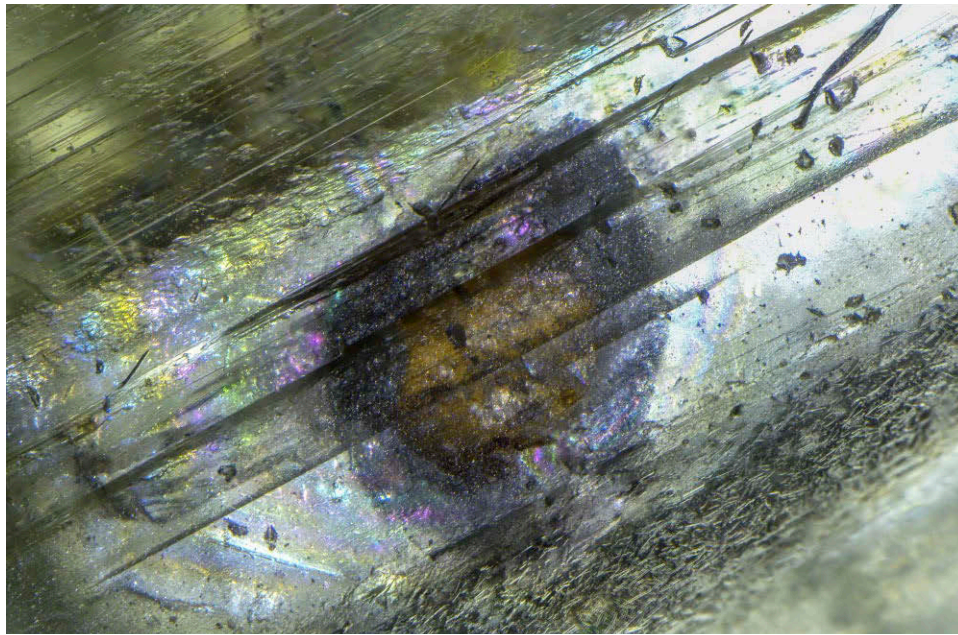
Figure 14. None of the analytical techniques at our disposal were able to conclusively pin down the identity of the orange inclusion. Photomicrograph by Nathan Renfro; field of view 9.31 mm.

i-Pech pegmatite field, Chapa Dara District, Konar Province, Afghanistan, was acquired from gem and mineral dealer Russell E. Behnke of Meriden, Connecticut. The bodycolor and rounded habit of the orange inclusion (figure 14), together with its origin in spodumene from a pegmatite field, suggested that it might be spessartine. However, laser Raman microspectrometry was not able to pin down the identification of that inclusion. This was because the crystal faces of the spodumene were etched, which interfered with the passage of the laser in the hosting spodumene. As a next step, energy-dispersive X-ray fluorescence (EDXRF) was tried to see if we could pick up any hints of the chemistry in the inclusion. In particular, we were looking for manganese which did show up in the EDXRF scan. Through the microscope, in polarized light, no pleochroism was detected in the inclusion which pointed to the inclusion being isometric. This was as far as we could take the analysis. In order to determine for certain what the unknown inclusion was we realized that destructive analysis would be needed to get a clear identification of the orange inclusion. Since this inclusion specimen was relatively valuable we decided that destructive analysis would not be used, and we would keep the spodumene crystal as it is for future exploration.

John I. Koivula and Nathan Renfro

Diamonds Are Not Forever! Diamond Dissolution

Before cutting and polishing, diamonds have highly variable surface features rarely, if ever, seen by the jewelry wearer. These features can tell an interesting story of diamond's geological history deep within Earth—both in the mantle rocks where diamonds grew and during their subsequent volcanic transport. Our previous column showed that volcanic eruptions of kimberlite are how diamonds make their way from depth in the mantle to Earth's surface. But this violent process does not leave the rough diamond unscathed.

These early histories are rarely considered once the diamond has been faceted and set into jewelry, but they raise interesting and geologically important questions:

- Why do rough diamonds look so different from each other, and what might this tell us about their geological history?
- What effect does the kimberlite magma have on the diamond cargo?
- How can we see through this later stage of the diamond's history to its millions and billions of years of mantle storage?

Features on Natural Rough Diamonds

There is so much variety in natural diamond surfaces that, like snowflakes, no two diamonds are exactly alike. These differences can give us useful information about how diamonds react with fluids in the mantle after crystallization and also reveal the dissolving properties of the kimberlite magma that brought them to Earth's surface.

External surface and internal features are related to the internal crystallographic structure of the diamond. Deformation lamellae (also known as "graining" to gemologists) can be subtle and evenly distributed. Other features relating to diamond structure, such as trigons, are only skin deep, microscopic, and can seem randomly distributed. The external form of a diamond crystal can be dissolved to form secondary shapes by the partial removal of crystalline diamond in a geological process known as dissolution or resorption. Left alone without dissolution, diamond will form a perfect octahedron or a cube. But with dissolution,

diamond can change from an octahedron to other forms such as dodecahedron or tetrahexahedron, and even form "irregular" diamonds with no discernible shape.

These transformations to the rough diamond's exterior surface can be distinguished from one another. Complex shapes can form in the mantle prior to being picked up by the kimberlite. Resorption to secondary shapes and trigon formation can occur during kimberlite eruption. Surface features like hillocks and frosting are also regarded as features imposed by the kimberlite. Finally, if released from easily weathered kimberlite, diamond lying in streambed deposits known as "placers" and in crudely sorted sedimentary rocks known as "conglomerates" can take on new surface features. Crystal rounding and percussion marks form when a diamond is transported in high-energy fluvial environments. Green and brown radiation stains are surface features that are due to a diamond's proximity to radioactive fluids or minerals.

Dissolution During Kimberlite Transport and Mantle Storage

Unless a diamond is weathered out of kimberlite, kimberlite eruption will produce the last visible resorption effects, as it is the last event affecting the diamond before it reaches Earth's surface. Features produced by the kimberlite will overprint or even remove those features produced in the mantle. Once kimberlite effects are studied and understood, we can peer beyond them to a diamond's earlier history in the mantle. But why does kimberlite magma attack diamonds in the first place?

Successful diamond transport and delivery occurs because kimberlites erupt very fast (transiting 150–200 km in <10 hours to ~2 days; Russell et al., 2019). This rapid eruption means that any entrained mantle components—such as xenoliths and diamonds—lose pressure very quickly, are violently tumbled with upward movement, and can break apart.

Because kimberlites are more oxidizing than diamonds, they typically are in the process of dissolving diamonds—it's just that this process has often not gone to completion. The chemical composition of the kimberlite and its volatile components (such as carbon dioxide and water) are important factors. For example, as pressure drops during ascent, the kimberlite magma is not able to dissolve as much carbon dioxide, and a fluid rich in carbon dioxide and water exsolves from the magma (figure 1; Brey and
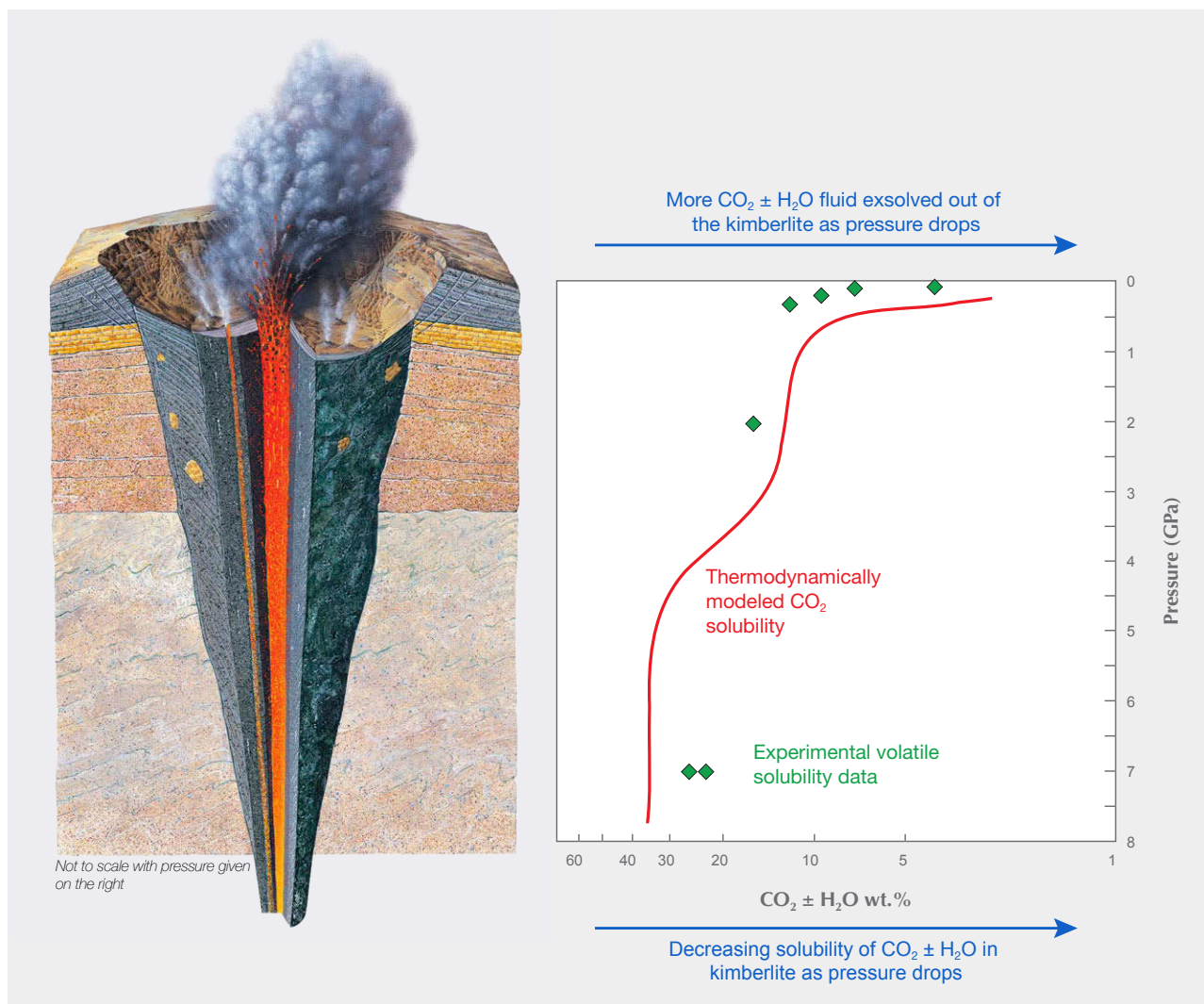
Figure 1. Volatile solubility in kimberlite versus pressure as determined by high-pressure experiments and thermodynamic modeling. At lower pressures, volatiles start to exsolve from the kimberlite magma, and these volatiles often start to etch and dissolve diamonds. Modified from Foley et al. (2019), with data from Edgar et al. (1988), Brey and Ryabchikov (1994), Brooker et al. (2011), Sharygin et al. (2017), Stamm and Schmidt (2017), and Moussallam et al. (2016).

Ryabchikov, 1994). This fluid, which often dissolves diamond, normally starts to exsolve at around 3–4 GPa (a gigapascal is a unit of pressure equal to 10,000 times atmospheric pressure), with maximum exsolution once the kimberlite is at pressures below 1 GPa.

The starting composition of the kimberlite melt at depth in the mantle affects the amount of carbon dioxide that can be dissolved in it, and hence the amount of carbon dioxide that will exsolve as it reaches the near-surface. Carbon dioxide solubility is significantly lower in water- and silica-rich kimberlites, meaning they will exsolve more carbon dioxide than water- and silica-poor kimberlites (Brooker et al., 2011; Russell et al., 2012; Moussallam et al., 2016). The amount of carbon dioxide that exsolves

from the kimberlite melt at the near-surface will have a direct effect on the amount and style of resorption that the diamond cargo experiences.

Storage in the mantle is static for the most part and does not involve such drastic pressure changes. But we know that dissolution in the mantle occurs regularly since the internal structures of most diamonds show evidence for multiple growth episodes often intersected by periods of resorption (figure 2). We know from diamond ages, and the much younger kimberlite eruption ages, that diamonds reside in the mantle for millions to billions of years. Geochemical analysis shows that during this time, fluids pass through the mantle during a process known as mantle metasomatism. Mantle metasomatism seems to be similar
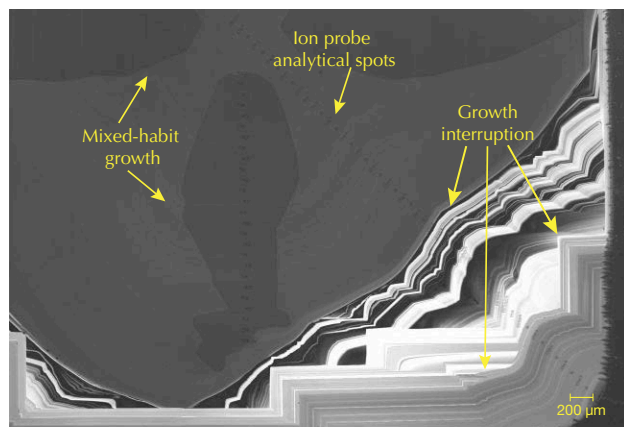
Figure 2. Cathodoluminescence image of a plate cut through the center of a diamond. The image reveals growth zones (similar to tree rings) that are ubiquitous in the majority of natural diamonds. Diamond grows in stages, and these growth periods are often interrupted by periods of dissolution or stasis. Courtesy of Richard Stern (University of Alberta).

to the process by which infiltrating fluids lead to diamond crystallization in the first place. Thus these fluids have the potential to react with the diamonds that are already there. Over this long duration in the mantle, there is the potential for many different carbon-bearing fluids/melts to contribute to diamond growth.

Timescales for Mantle Resorption/Dissolution from Radiometric Dating. In rare instances, diamonds with multiple inclusions concurrently crystallizing with different growth zones have revealed the timescales over which some diamonds grow in the mantle. A diamond from the Mir mine in Russia contains multiple sulfide inclusions in core and rim growth zones. The inclusions in each zone are hosted by diamond with vastly different carbon isotope compositions and have a core that differs by about 1 billion years from the rim, which is much greater than the age uncertainty (Wiggers de Vries et al., 2013; Bulanova et al., 2014). An even larger age difference of around 2 billion years was recorded by garnet and clinopyroxene inclusions in a diamond from the Letlhakane mine in Botswana (Timmerman et al., 2017). These growth events are intersected by periods of diamond dissolution/resorption, or otherwise by periods of stasis where neither growth nor resorption is occurring.

It is unclear whether such long periods between growth and resorption are normal or just rare examples. For example, the oldest diamonds ever, dated from the Ekati mine in Canada (Westerlund et al., 2006) with ages of 3.5 billion years, show older cores and younger rims that are likely separated by less than 100 million years of age. These zones may even have grown with a very slight age separation, perhaps almost contemporaneously.

Even the best age dating techniques we can apply simply do not have the precision to distinguish the small differences (e.g., <100 million years) in age when diamonds are often billions of years old. However, microscopic imaging techniques such as cathodoluminescence and Diamond-View can reveal the growth layering that occurs internally in most gem diamonds. Based just on cross-cutting relationships and the superposition of younger diamond layers on top of older, preexisting diamond, we are sure that different generations of diamond-forming fluids exist. We can see what layer must have come first and what layer second, and that dissolution of preexisting diamond is part of the story.

Experiments Reveal Which Features Originate During Storage Versus Transport. The only way to find out whether features originate during mantle storage or kimberlite transport is to classify the type of dissolution features seen, and then to reproduce them experimentally to match the conditions in each setting. Dissolution experiments on diamonds have been conducted for decades, but many recent advances in our understanding of how different fluid compositions affect the resorption and features on diamond surfaces have been made by Yana Fedortchouk and Zhihai Zhang, working at Dalhousie University in Canada. For a detailed overview of the experimental literature on diamond dissolution, the reader is referred to Fedortchouk (2019) and Fedortchouk et al. (2019).

Their work has produced a roadmap of the dissolution features (figure 3), allowing gemologists and research scientists to peer into the complicated history of diamond revealed by its surface features. The scientific goal of such work is to understand the fluids that exist in the mantle and during kimberlite transport: If these fluids can dissolve diamond, they are also the kind of fluids from which diamond can grow.

Diamond Resorption into Rounded Shapes

Sometimes octahedral shapes are near perfect (figures 4 and 5) and show very little attack by fluids either during mantle storage or during kimberlite transport. In other instances, diamonds are resorbed from their primary octahedral shapes into secondary shapes that are often grouped together and called "dodecahedra," or "dodecs" for short.

Dodecahedra are actually (at least) two different secondary shapes, and they should have names ending in -oid to reflect the fact that they have curved resorption surfaces that approximate similar crystallographic directions to true crystal faces.

Dodecahedroids have 12 curved resorption surfaces that approximate true dodecahedra. Tetrahexahedroids (THHs) have 24 curved resorption surfaces that approximate the shape of tetrahexahedra.

Dissolution experiments show that three main factors may impact the shape of a resorbed diamond (Fedortchouk, 2019; Fedortchouk et al., 2019). Different features can be
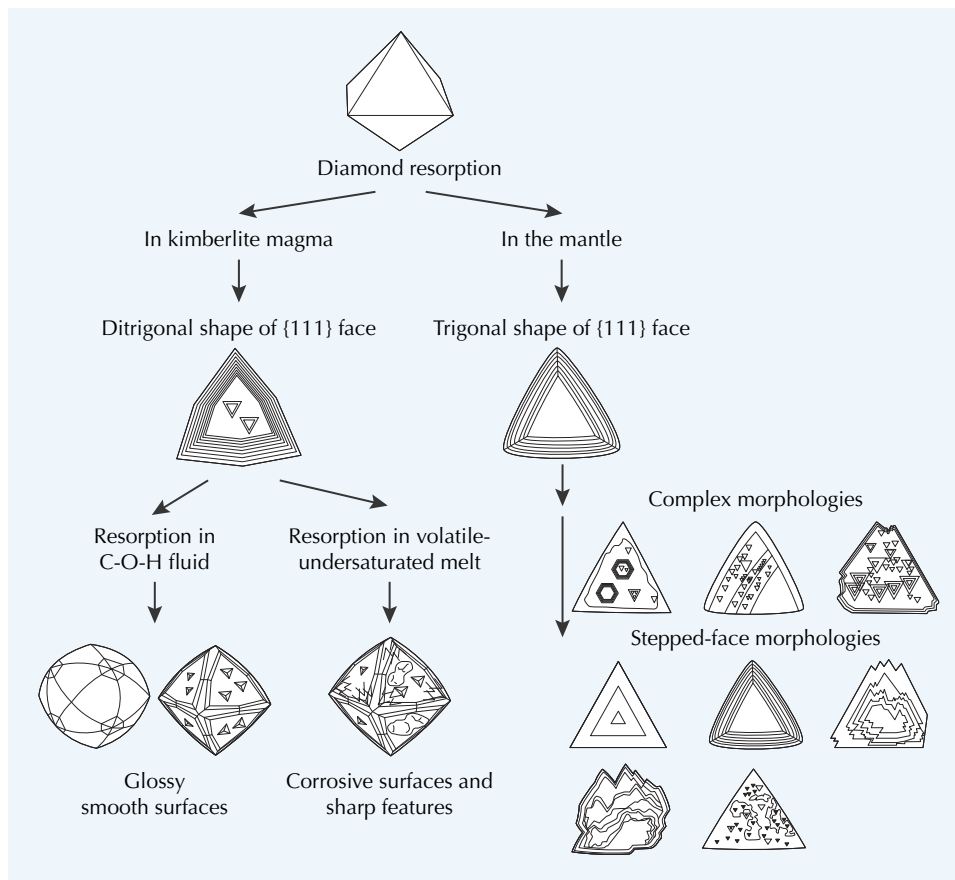
Figure 3. Surface features on diamond that indicate resorption in the kimberlite magma versus those features resulting from resorption by mantle fluids/melts prior to diamond entrainment in the kimberlite (original figure from Fedortchouk et al., 2019; used with permission). Features originating in the mantle can be preserved during kimberlite eruption if the diamonds are shielded by mantle xenoliths, or they can be overprinted by features resulting from the kimberlite magma.

produced by varying the depth of the fluid exsolution from the kimberlite, or through varying the Si content and temperature of melts in the mantle:

1. **Whether a fluid phase is present or not.** A fluid-free kimberlite melt will not lead to rounded resorbed THH. Instead, there is some resorption along the oc-
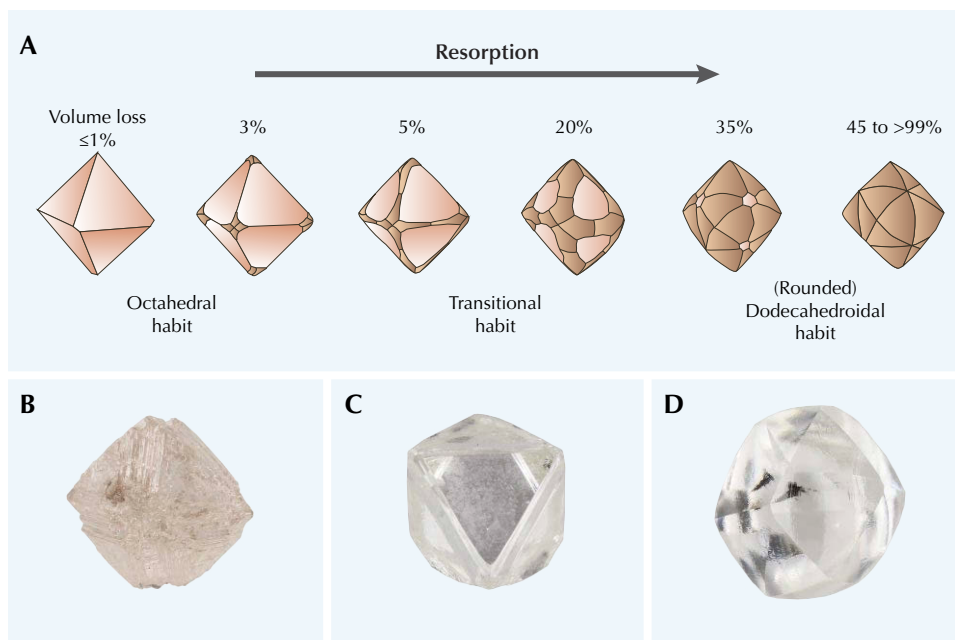
Figure 4. A: General sequence of resorption from primary octahedron to a secondary rounded shape often called a dodecahedroid (modified from Tappert and Tappert, 2011; McCallum et al., 1994). B, C, and D: Rough diamonds from the Diavik mine (Canada) that show various features of growth and resorption. B: Terraces or growth faces in an octahedral diamond that has undergone very little resorption. C: Partially resorbed octahedral diamond with rounded corners and edges. D: Rounded, resorbed, tetrahexahedroidal (THH) diamond. Photos by Jian Xin (Jae) Liao.

Octahedron
8 crystal faces

Primary growth shape

Resorption starting along crystal edges

Tetrahexahedroid (THH)
24 curved resorption surfaces

Secondary shape from resorption
mostly during kimberlite eruption

Exposed growth terraces are often
shield-shaped (ditrigonal)

Dodecahedroid
12 curved resorption surfaces

Secondary shape from resorption
mostly during mantle storage
before kimberlite eruption

Figure 5. Examples of the primary octahedral growth shape of diamond and the two shapes that form after resorption. Photos by Thomas Hunn (top left), Robert Weldon (top right), and Karen Smit (middle and bottom).

tahedral crystal edges and the development of "sharp" corrosive surface features (Fedortchouk and Zhang, 2011).

2. **Depth of fluid exsolution from the kimberlite.** A water-rich fluid at 3 GPa will favor rapid formation of THH, whereas the same fluid at 1 GPa will favor octahedra preservation (Zhang et al., 2015).

3. **Amount of CO_2 and H_2O in the fluid.** Experimental work by Fedortchouk et al. (2007) shows that at 1 GPa, there is higher preservation of the octahedral faces in a CO_2-rich fluid. A water-rich fluid would favor formation of THH and elimination of octahedral faces. Since kimberlite magmas change composition during ascent, so does the magma's effect on diamond resorption. Different resorption styles can be expected, even during the same eruption!
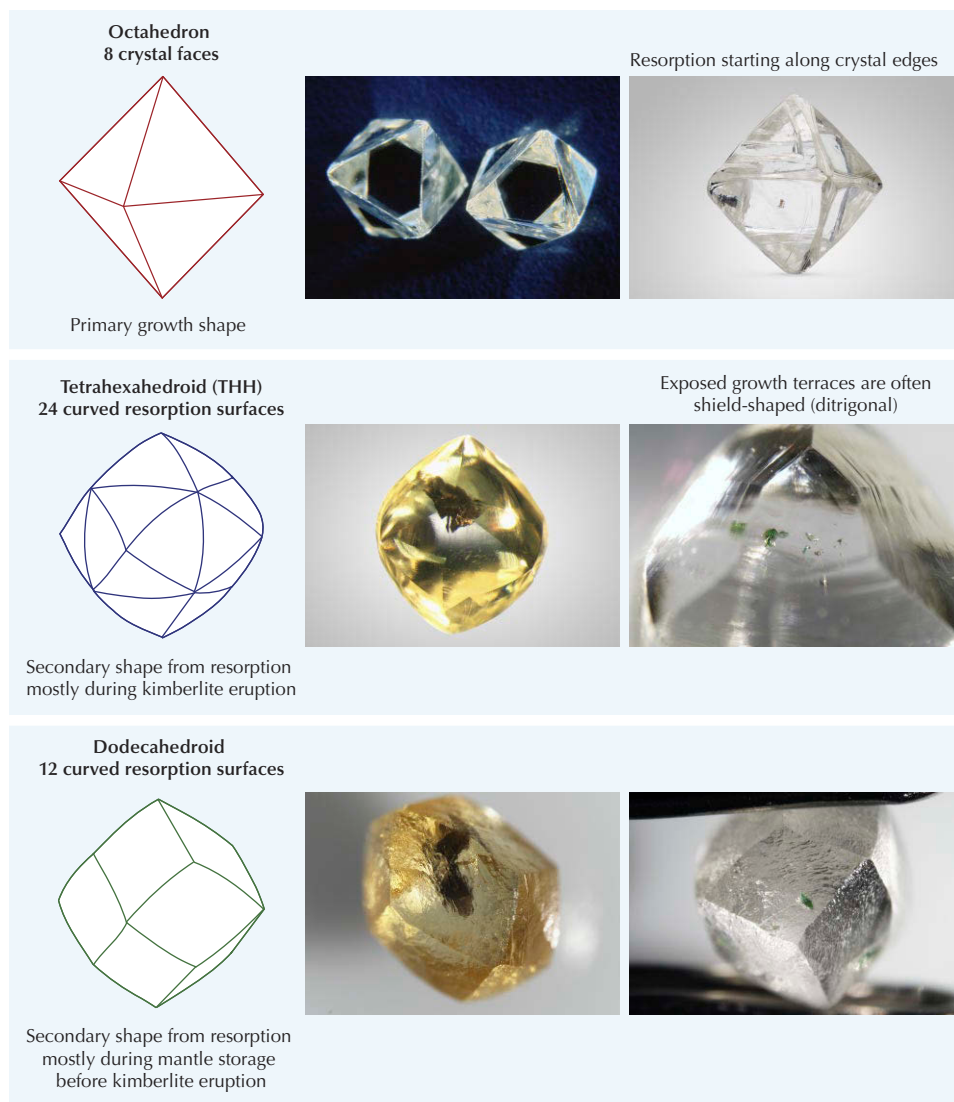
Tetrahexahedroid (THH). Experiments indicate that tetrahexahedroids (THH) form in water-rich carbonate melts

(Chepurov et al., 1985; Khokhyrakov and Pal'yanov, 2007). Tetrahexahedroid crystals have been experimentally produced at 1.0–1.5 GPa by dissolution in natural kimberlite with 6.2 wt.% H_2O and 4.8 wt.% CO_2 (Kozai and Arima, 2005) and in experiments with H_2O and CO_2 fluids (Fedortchouk et al., 2007). Because they form during kimberlite eruption, THH diamond crystals are much more common than dodecahedroids, and their formation may overprint any mantle resorption features or shapes.

Dodecahedroid. Dodecahedroids form in CO_2-rich carbonate melts that are poor in water (Khokhyrakov and Pal'yanov, 2007, 2010 and many references therein). They are thought to form mostly during dissolution processes in the mantle (Fedortchouk and Zhang, 2011). Dodecahedroidal shapes are more rare, as they can be overprinted to THH during kimberlite eruption. These shapes have a higher likelihood of survival if the kimberlite magma and its exsolving fluids are water poor, and also if diamonds are
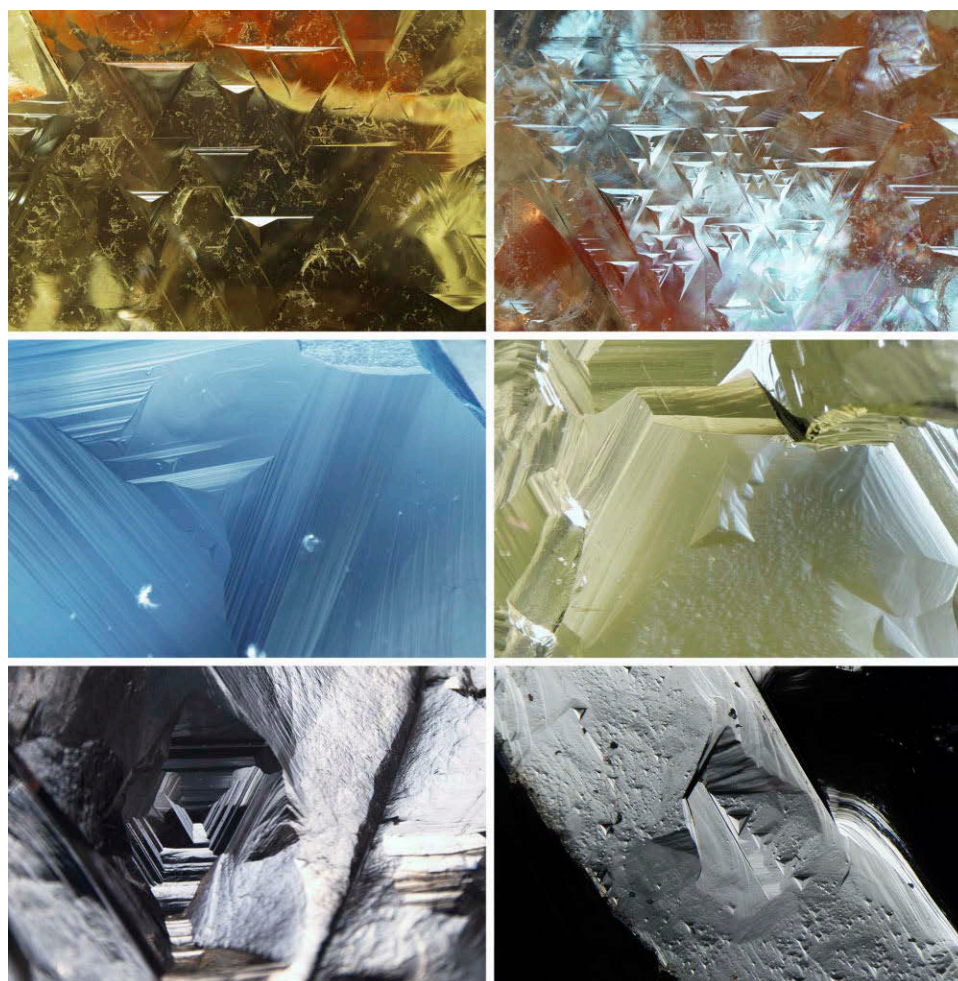
Figure 6. Trigons and hexagons are dissolution features related to the effect of more oxidizing fluids/melts on the diamond's surface. Dissolution typically starts at a lattice dislocation or imperfection. Photos by Evan Smith and Ulrika D'Haenens-Johansson.

shielded from the kimberlite magma by enclosure in their mantle host rocks such as peridotite and eclogite.

Trigons

Examples of one of the most common surface details of rough natural diamonds—trigons—are shown in figure 6. Additional excellent examples can be found in the book *Diamonds in Nature: A Guide to Rough Diamonds* (Tappert and Tappert, 2011).

Trigons can be either "negative" or "positive," where a "negative trigon" has an opposite orientation to the octahedral face of the diamond (figure 7). In the past, there was significant debate about whether trigons were growth features (e.g., Tolansky, 1955, 1960) or etch pits (e.g., Frank and Puttick, 1958; Patel et al., 1964; Lang, 1964). These days it is accepted that a trigon is an etch feature, produced when oxidizing fluids/melts start to dissolve the diamond. Dissolution typically starts at an imperfection, such as a lattice dislocation (Wilks and Wilks, 1991).

When Do Rare Positive Trigons Form? Positive trigons are extremely rarely seen. Snap Lake in Canada is one locality that has a high proportion of diamonds with positive trigons, and their development was attributed to near-surface reaction of the diamonds with late-stage, low-temperature C-O-H fluids (Li et al., 2018). This is consistent with early experimental work that showed that positive trigons are the

Figure 7. Trigons can be either "negative" or "positive," where a "negative trigon" is more common and has an opposite orientation to the octahedral face of the diamond.
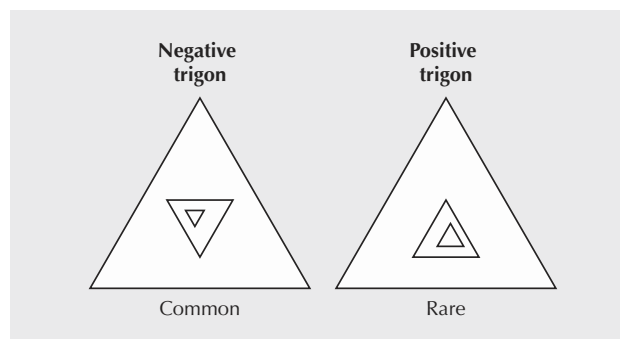
most common etch feature at atmospheric pressure (Evans and Sauter, 1961). These early experiments also showed that the orientation of a trigon (positive versus negative) could be changed by using different etchants at different temperatures (Frank and Puttick, 1958; Evans and Sauter, 1961).

More recent experiments have shown that positive trigons can be produced by dry carbonate melts, and that increasing water content changes trigon orientation to negative (Khokhyrakov and Pal'yanov, 2000, 2010). Fedortchouk (2019) attributes positive trigons to resorption by a rare type of mantle fluid (rare since positive trigons are associated with other rare features such as hexagons and transverse hillocks). It is possible that the development of positive trigons is common in the mantle, and that they have just been "erased" by later resorption of the diamond into THH during kimberlite transport.

Influences on the Shape of a Trigon. Experimental work has shown that the shape of trigons is influenced by the amount of H_2O and CO_2 in the fluid, as well as temperature. Trigons produced by water-rich fluids have a limited size range but a large depth variation; in contrast, trigons produced by CO_2-rich fluids can have varying sizes but always with a positive correlation between depth and diameter (Fedortchouk, 2015). Large trigons are produced at higher temperatures (Kanda et al., 1977; Fedortchouk, 2015). Additionally, experiments at 1 to 3 GPa showed that CO_2-rich fluids mostly produced trigons with pointed and curved bottoms, whereas CO_2-poor fluids produced mostly flat-bottomed trigons (Zhang, 2016).

The Importance of Understanding Resorption, and Remaining Questions

Since the surface features of diamonds are heavily influenced by the composition and temperature of the dissolving fluid/melt, these features are another tool that mantle geochemists can use to study carbon-bearing fluids/melts in the deep Earth. Actual fluids are preserved in fibrous diamonds, but these may be a specific subtype of mantle fluids and their universal applicability to all monocrystalline gem diamonds needs to be better established. Since very few diamonds actually contain fluids, the study of fluids resulting in surface features on a wide variety of different diamonds may provide a broader understanding of carbon fluids in the deep Earth. Furthermore, there is a need to understand diamond resorption styles during the economic evaluation of kimberlite since complete resorption can destroy diamond grade by eliminating diamonds altogether. Identification of diamond quality in each kimberlite unit leads to better decisions about which kimberlite units to prioritize during mining.

When does a fluid result in diamond growth, and when does it dissolve diamonds? We need a better understanding of how diamonds are resorbed and destroyed in the mantle. Carbon-bearing fluids in the mantle seem to be largely responsible for diamond growth (e.g., Stachel et al., 2017) and *do not* contribute to diamond dissolution at high pressures during mantle storage (Fedortchouk et al., 2019). Conversely, carbon-bearing fluids exsolved at low pressures (figure 1; less than 3 GPa) during kimberlite eruption *do* dissolve diamonds to form rounded THH (figure 5; Fedortchouk et al., 2019). In the mantle, the main diamond dissolution agents seem to be carbonate melts that can produce several features through variation of silica contents and temperature (Fedortchouk and Zhang, 2012; Fedortchouk et al., 2019).

We have shown that diamond can be dissolved during two periods of residence within the earth: where it grew in the mantle and during its volcanic transport to the surface. Given that diamond dissolution is common, it is fortuitous that the mantle's temperature, high pressure, and low oxygen state makes it friendly for diamond growth. Similarly, given that diamond dissolution can occur in fluid-rich kimberlites, it is a good thing that transport is fast enough to overcome the speed of dissolution. In the end, given that diamond dissolution is common in two settings in Earth, it is rather miraculous that diamonds do actually survive. Here we have yet another way in which natural diamonds are remarkable.

REFERENCES

Brey G.P., Ryabchikov I.D. (1994) Carbon-dioxide in strongly silica undersaturated melts and origin of kimberlite magmas. *Neues Jahrbuch fur Mineralogie, Monatshefte*, Vol. 10, pp. 449–463.

Brooker R.A., Sparks R.S.J., Kavanagh J.L., Field M. (2011) The volatile content of hypabyssal kimberlite magmas: Some constraints from experiments on natural rock compositions. *Bulletin of Volcanology*, Vol. 73, No. 8, pp. 959–981, http://dx.doi.org/10.1007/s00445-011-0523-7

Bulanova G.P., de Vries D.F.W., Pearson D.G., Beard A., Mikhail S., Smelov A.P., Davies G.R. (2014) An eclogitic diamond from Mir pipe (Yakutia), recording two growth events from different isotopic sources. *Chemical Geology*, Vol. 381, pp. 40–54, http://dx.doi.org/10.1016/j.chemgeo.2014.05.011

Chepurov A.I., Khokhryakov A.F., Sonin V.M., Pal'yanov Y.N. (1985) Forms of dissolution of diamond crystals in silicate melts at high pressure. *Doklady Akademii Nauk SSSR*, Vol. 1, pp. 212–216.

Edgar A.D., Arima M., Baldwin D.K., Bell D.R., Shee S.R., Skinner E.M.W., Walker E.C. (1988) High-pressure-high-temperature melting experiments on a SiO_2-poor aphanitic kimberlite from the Wesselton mine, Kimberley, South Africa. *American Mineralogist*, Vol. 73, No. 5, pp. 524–533.

Evans T., Sauter D.H. (1961) Etching of diamond surfaces with gases. *Philosophical Magazine*, Vol. 6, No. 63, pp. 429–440, http://dx.doi.org/10.1080/14786436108235896

Fedortchouk Y. (2015) Diamond resorption features as a new method for examining conditions of kimberlite emplacement. *Contributions to Mineralogy and Petrology*, Vol. 170, No. 4, p. 36, http://dx.doi.org/10.1007/s00410-015-1190-z

——— (2019) A new approach to understanding diamond surface

features based on a review of experimental and natural diamond studies. *Earth-Science Reviews*, Vol. 193, pp. 45–65, http://dx.doi.org/10.1016/j.earscirev.2019.02.013

Fedortchouk Y., Zhang Z. (2011) Diamond resorption: Link to metasomatic events in the mantle or record of magmatic fluid in kimberlitic magma? *Canadian Mineralogist*, Vol. 49, No. 3, pp. 707–719, http://dx.doi.org/10.3749/canmin.49.3.707

Fedortchouk Y., Canil D., Semenets E. (2007) Mechanisms of diamond oxidation and their bearing on the fluid composition in kimberlite magmas. *American Mineralogist*, Vol. 92, No. 7, pp. 1200–1212, http://dx.doi.org/10.2138/am.2007.2416

Fedortchouk Y., Liebske C., McCammon C. (2019) Diamond destruction and growth during mantle metasomatism: An experimental study of diamond resorption features. *Earth and Planetary Science Letters*, Vol. 506, pp. 493–506, http://dx.doi.org/10.1016/j.epsl.2018.11.025

Foley S.F., Yaxley G.M., Kjarsgaard B.A. (2019) Kimberlites from source to surface: Insights from experiments. *Elements*, Vol. 15, No. 6, pp. 393–398, http://dx.doi.org/10.2138/gselements.15.6.393

Frank F.C., Puttick K.E. (1958) Etch pits and trigons on diamond: II. *Philosophical Magazine*, Vol. 3, No. 35, pp. 1273–1279, http://dx.doi.org/10.1080/14786435808233309

Kanda H., Yamaoko S., Setaka N. (1977) Etching of diamond octahedrons by high pressure water. *Journal of Crystal Growth*, Vol. 38, No. 1, pp. 1–7, http://dx.doi.org/10.1016/0022-0248(77)90365-7

Khokhryakov A.F., Pal'yanov Y.N. (2000) Dissolution forms of diamond crystals in $CaCO_3$ melt at 7 GPa. *Russian Geology and Geophysics*, Vol. 41, No. 5, pp. 682–687.

——— (2007) The evolution of diamond morphology in the process of dissolution: Experimental data. *American Mineralogist*, Vol. 92, No. 5-6, pp. 909–917, http://dx.doi.org/10.2138/am.2007.2342

——— (2010) Influence of the fluid composition on diamond dissolution forms in carbonate melts. *American Mineralogist*, Vol. 95, No. 10, pp. 1508–1514, http://dx.doi.org/10.2138/am.2010.3451

Kozai Y., Arima M. (2005) Experimental study on diamond dissolution in kimberlitic and lamproitic melts at 1300–1420°C and 1 GPa with controlled oxygen partial pressure. *American Mineralogist*, Vol. 90, No. 11-12, pp. 1759–1766, http://dx.doi.org/10.2138/am.2005.1862

Lang A.R. (1964) Dislocations in diamond and the origin of trigons. *Proceedings of the Royal Society of London, Series A: Mathematical and Physical Sciences*, Vol. 278, pp. 234–242.

Li Z., Fedortchouk Y., Fulop A., Chinn I.L., Forbes N. (2018) Positively oriented trigons on diamonds from the Snap Lake kimberlite dike, Canada: Implications for fluids and kimberlite cooling rates. *American Mineralogist*, Vol. 103, No. 10, pp. 1634–1648, http://dx.doi.org/10.2138/am-2018-6496

McCallum M.E., Huntley P.M., Falk R.W., Otter M.L. (1994) Morphological, resorption and etch feature trends of diamonds from kimberlite populations within the Colorado-Wyoming state line district. In H.O.A. Meyer and O.H. Leonardos, Eds., *Diamonds: Characterization, genesis and exploration. Proceedings of the 5th International Kimberlite Conference*, Volume 2, pp. 32–50.

Moussallam Y., Morizet Y., Gaillard F. (2016) H_2O–CO_2 solubility in low SiO_2-melts and the unique mode of kimberlite degassing and emplacement. *Earth and Planetary Science Letters*, Vol. 447, pp. 151–160, http://dx.doi.org/10.1016/j.epsl.2016.04.037

Patel A.R., Goswami K.N., Desai C.C. (1964) Trigon patterns on etched calcium fluoride cleavages. *Philosophical Magazine*, Vol. 10, No. 108, pp. 931–935, http://dx.doi.org/10.1080/14786436408225401

Russell J.K., Porritt L.A., Lavallée Y. (2012) Kimberlite ascent by assimilation-fuelled buoyancy. *Nature*, Vol. 481, No. 7381, pp. 352–356, http://dx.doi.org/10.1038/nature10740

Russell J.K., Sparks R.S.J., Kavanagh J.L. (2019) Kimberlite volcanology: Transport, ascent, and eruption. *Elements*, Vol. 15, No. 6, pp. 405–410, http://dx.doi.org/10.2138/elements.15.6.405

Sharygin I.S., Litasov K.D., Shatskiy A., Safonov O.G., Golovin A.V., Ohtani E., Pokhilenko N.P. (2017) Experimental constraints on orthopyroxene dissolution in alkali-carbonate melts in the lithospheric mantle: Implications for kimberlite melt composition and magma ascent. *Chemical Geology*, Vol. 455, pp. 44–56, http://dx.doi.org/10.1016/j.chemgeo.2016.09.030

Stachel T., Chacko T., Luth R.W. (2017) Carbon isotope fractionation during diamond growth in depleted peridotite: Counterintuitive insights from modelling water-maximum CHO fluids as multi-component systems. *Earth and Planetary Science Letters*, Vol. 473, pp. 44–51, http://dx.doi.org/10.1016/j.epsl.2017.05.037

Stamm N., Schmidt M.W. (2017) Asthenospheric kimberlites: Volatile contents and bulk compositions at 7 GPa. *Earth and Planetary Science Letters*, Vol. 474, pp. 309–321, http://dx.doi.org/10.1016/j.epsl.2017.06.037

Tappert R., Tappert M.C. (2011) *Diamonds in Nature: A Guide to Rough Diamonds*. Springer, Berlin.

Timmerman S., Koornneef J.M., Chinn I.L., Davies G.R. (2017) Dated eclogitic diamond growth zones reveal variable recycling of crustal carbon through time. *Earth and Planetary Science Letters*, Vol. 463, pp. 178–188, http://dx.doi.org/10.1016/j.epsl.2017.02.001

Tolansky S. (1955) *The Microstructures of Diamond Surfaces.* NAG Press, London.

Tolansky S. (1960) *Surface Microtopography*. Longmans, London.

Westerlund K., Shirey S., Richardson S., Carlson R., Gurney J., Harris J. (2006) A subduction wedge origin for Paleoarchean peridotitic diamonds and harzburgites from the Panda kimberlite, Slave craton: Evidence from Re-Os isotope systematics. *Contributions to Mineralogy and Petrology*, Vol. 152, No. 3, pp. 275–294, http://dx.doi.org/10.1007/s00410-006-0101-8

Wiggers de Vries D.F., Bulanova G.P., de Corte K., Pearson D.G., Craven J.A., Davies G.R. (2013) Micron-scale coupled carbon isotope and nitrogen abundance variations in diamonds: Evidence for episodic diamond formation beneath the Siberian Craton. *Geochimica et Cosmochimica Acta*, Vol. 100, pp. 176–199, http://dx.doi.org/10.1016/j.gca.2012.08.034

Wilks E., Wilks J. (1991) *Properties and Application of Diamond*. Butterworth-Heinemann Ltd., London.

Zhang Z. (2016) Diamond resorption morphology as a fluid proxy in diamond-bearing environments: Constraints from empirical and experimental studies. PhD thesis, Dalhousie University, Halifax.

Zhang Z., Fedortchouk Y., Hanley J.J. (2015) Evolution of diamond resorption in a silicic aqueous fluid at 1-3 GPa: Application to kimberlite emplacement and mantle metasomatism. *Lithos*, Vol. 227, pp. 179–193, http://dx.doi.org/10.1016/j.lithos.2015.04.003

Gem News International

Contributing Editors

Emmanuel Fritsch, *University of Nantes, CNRS, Team 6502, Institut des Matériaux Jean Rouxel (IMN), Nantes, France* (fritsch@cnrs-imn.fr)

Gagan Choudhary, *Gem Testing Laboratory, Jaipur, India* (gagan@gjepcindia.com)

Christopher M. Breeding, *GIA, Carlsbad* (christopher.breeding@gia.edu)

TUCSON 2020

In early February, despite the early phase of the COVID-19 outbreak, the Tucson shows were well attended and sales were brisk. Several vendors indicated that they had their biggest single day of sales ever this year (figure 1). This anecdotal evidence was supported by the strong demand for identification and origin services reported by the GIA Show Service Lab. This year, it was hard to identify any one particular item leading demand or any game-changing new gem material finds. Instead, we found that vendors were carrying high-quality material in terms of color, clarity, and cut. In fact, many were carrying items that had been meticulously carved, fantasy-cut, or recut for ideal proportions (figure 2).

Surpassing its strong momentum from the past few years, teal blue sapphire from Montana was a prominent and well sought-after item (figure 3). Sapphire was doing very well at the shows, including parti-colored, fancy-colored (electric colors such as fuchsia and pinks as well as pastels such as lavender), and slabs displaying zoning or trapiche-like patterning (figure 4).

Emerald from around the world could be found, including some untreated smaller sizes from Russia (figure 5), melee and small-sized finished stones from Pakistan, attractive material from Ethiopia, and an abundance of material in a wide variety of color, clarity, and size from Colombia, Brazil, and Zambia.
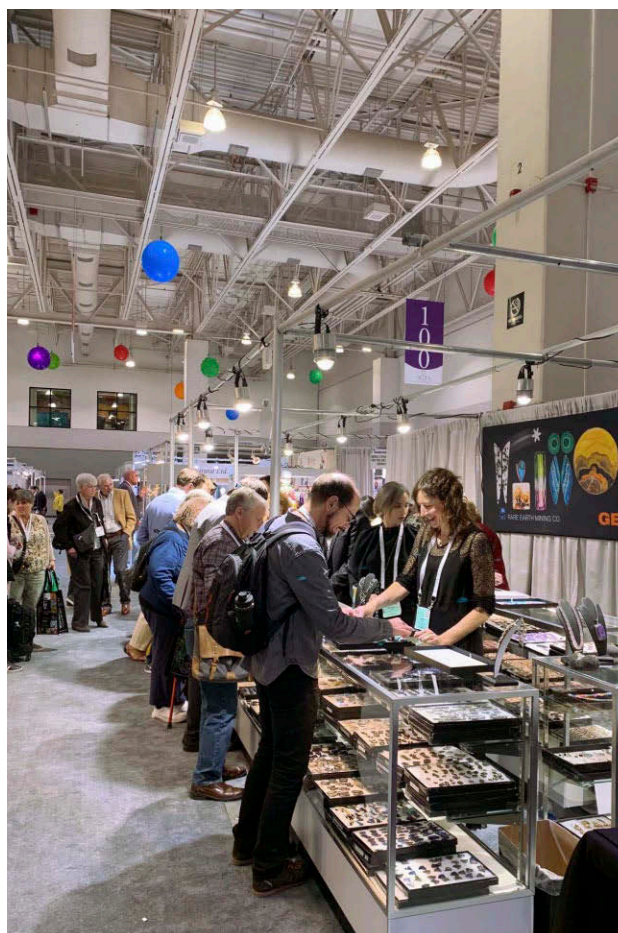
Figure 1. A busy booth on the first day of the AGTA show. Photo by Tao Hsu.

Outstanding brilliant green garnets in both demantoid and tsavorite varieties were available, including several larger-sized, ideally colored Russian demantoids (figure 6).

Figure 2. A 72 ct gem silica carving by Nick Alexander showing a highly desirable intense shade of blue. The material is from the Ray mine in Arizona. Photo by Kevin Schumacher; courtesy of Nick Alexander.

Figure 3. A suite of the popular teal blue Montana sapphires from Rock Creek. The center stone is 11.03 ct, and the other 14 stones total 8.38 carats. Photo by Jennifer Stone-Sundberg; courtesy of Pala International.

As "Classic Blue" is the Pantone color of the year and varieties of blue gemstones are very popular in general, gems prominently displaying a blue hue could be found throughout the shows. Along with sapphire, deep blue aquamarine from Nigeria (figure 7) was particularly popular, and many vendors displayed blue zircon, gem silica (again, see figure 2), apatite, cobalt spinel, blue topaz, haüyne, turquoise, blue moonstone, and lapis in their cases.

Electric-colored accent stones and melee in materials such as sapphire, spinel, apatite, and garnet varieties tsavorite and demantoid were easy to find both loose and in finished pieces (figure 8).

As has been the case for the past couple of years, gem slices in a variety of materials, shapes, and price points were very popular in both the AGTA and GJX shows. These are attractive to many designers, whether they are

Figure 4. Left: This set of 110 Australian sapphire "fancies" in 3 mm sizes was collected over several years. Right: A pair of trapiche-like Australian sapphire slices. Photos by Jennifer Stone-Sundberg; courtesy of Terry Coldham.

Figure 5. A 0.33 ct emerald from Malysheva, Russia, offered by Dudley Blauwet at the AGTA show. Photo by Kevin Schumacher.

Figure 7. Deep blue aquamarine from Nasarawa, Nigeria (left to right: 1.94, 2.84, and 1.84 ct). Photo by Emily Lane; courtesy of Jeff Hapeman.

working with higher-price-point material such as parti-colored sapphire (figure 9), diamond, and trapiche emerald, or more moderately priced material including amethyst, rhodochrosite, and petrified wood.

As always, Tucson was the place to find the unusual and phenomenal, with several vendors carrying exotic gem materials such as fluorescent hyalite opal (figure 10), star

Figure 6. A 6.73 ct round brilliant Russian demantoid of top quality showing a horsetail inclusion. Photo © Christian Wild.

peridot, brilliant green fluorite (figure 11, left), hackmanite, triphylite, grandidierite, axinite, and an array of bicolor stones in materials such as garnet, chrysoberyl (figure 11, right), tanzanite, and sphene.

Figure 8. Sea star pendant by Paula Crevoshay featuring 4.04 carats of ruby, 5.06 carats of lavender sapphire, 9.40 carats of purple sapphire, 3.87 carats of fuchsia sapphire, 6.79 carats of crystal spinel, and 0.43 carats of amethyst, set in 18K yellow gold. Photo by Emily Lane; courtesy of Paula Crevoshay.

Figure 9. Parti-colored sapphire slices from Montana (left) and Australia (right). Photos by Jennifer Stone-Sundberg; courtesy of Warren Boyd (left) and Terry Coldham (right).

Figure 10. Fluorescent hyalite opal flower pendant by Loretta Castoro, photographed in daylight-equivalent (left) and lower-power daylight-equivalent light with added short-wave UV light (right). The 12.63 ct fluorescent opal is from Zacatecas, Mexico. It is set in 18K yellow gold and has 48 yellow diamond accents (1.14 carats total) and 72 white diamond accents (1.27 carats total). Photos by Robert Weldon; courtesy of Loretta Castoro.

2020 also marked the first Tucson edition of the Ethical Gem Fair. The exhibitors showed a wide range of gemstones, prices, and origins. They were all united in their commitment to responsible sourcing, traceability, transparency, and social awareness. The variety of exhibitors reflected the different approaches taken to address these diverse challenges around the world. During its inaugural Tucson show, the Ethical Gem Fair mainly attracted young independent jewelry designers looking for gems with a transparent chain of custody from the mine to their use in finished jewelry.

*Duncan Pay, Jennifer Stone-Sundberg, Tao Hsu, Wim Vertriest, Aaron Palke, and Nathan Renfro*

Burmese star peridot. Asterism in peridot is a rare treat that has been reported on occasionally (S. Borg, "An unusual star peridot," *Journal of Gemmology*, Vol. 17, No. 1, 1980, pp. 1–4; Summer 2009 Lab Notes, pp. 138–139). In

January 2020, Tom Trozzo submitted to Stone Group Laboratories a 20.13 ct oval cabochon peridot (figure 12, left) that exhibited a soft yet prominent four-rayed star. Comparisons were made with an in-house lab sample that also exhibited reflection effects from tiny acicular inclusions. For purposes of this study, this comparison stone was recut to a 7.67 ct pear-shaped cabochon (figure 12, right) to enhance any potential asterism. However, the result appeared to be more of a cat's-eye effect, presumably due to the

Figure 11. An extremely diverse selection of unusual stones was on display at the GJX show. Left: Bright green fluorite offered by a European vendor; photo by Tao Hsu. Right: Bicolor chrysoberyl carried by United Colour Stone Co. from Bangkok; photo by Jennifer Stone-Sundberg.
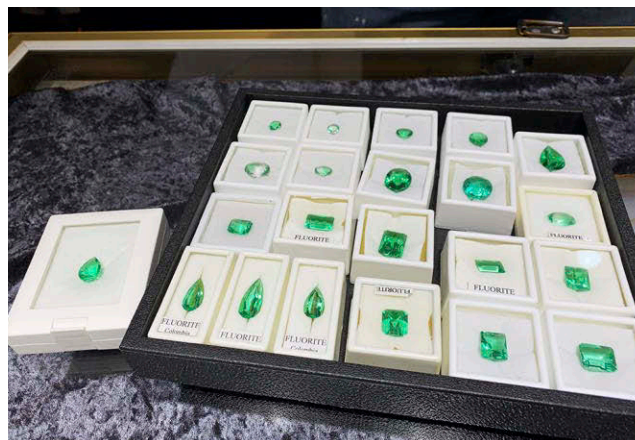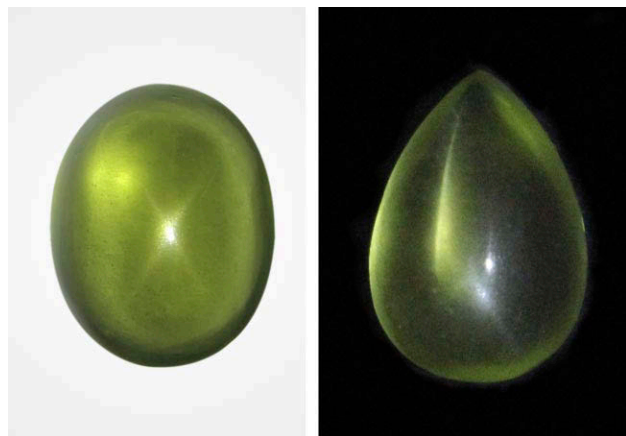
Figure 12. The 20.13 ct star peridot (left) and the 7.67 ct peridot exhibiting weak asterism with more prominent chatoyancy (right), presumably due to cutting style. Photos by Bear Williams.

Figure 14. A top-quality 9.49 ct Russian demantoid from the Korkodin mine. The horsetail inclusion under the table is the telltale signature of its origin. Photo by Kevin Schumacher; courtesy of Tsarina Jewels.

prominent keel from the original faceted pear shape. It is presumed that, based on the arrangement and concentration of inclusions, a more prominent asterism will be revealed upon further cutting. Apparent clarity was good on both stones, but with a slightly diffused effect; no large eye-visible inclusions were present. While the asterism was more pronounced on the oval, the acicular inclusions were more plentiful and of higher relief in the pear-shaped stone. Both stones had a yellowish green color, with the oval exhibiting a very slight grayish modifier.

Microscopic observation of the larger oval peridot revealed evenly distributed concentrations of extremely fine, short, brownish, acicular inclusions oriented in two directions (figure 13, left). In the pear shape, the needles were evenly dispersed throughout and oriented in three directions. The needles were also short and whitish to colorless (figure 13, right). Reflection effects in some materials may be difficult to define. There may be reflection effects from nonacicular inclusions, creating schiller as well as asterism. This was the case with the oval peridot, although asterism was clearly the dominant phenomenon.

The spot RI reading of approximately 1.65 and hydrostatic SG of 3.33 were consistent with peridot. The identification of both peridots was confirmed by GemmoRaman532-SG. Their provenance was reportedly Myanmar (Burma), and all tests were consistent with a Burmese origin. Interestingly, all known star peridots to date have been of Burmese origin. Although Pakistani peridot may often feature acicular inclusions of ludwigite, these are presumably protogenetic and not oriented consistently to the crystal structure of the host peridot.

Bear Williams and Cara Williams
Stone Group Labs
Jefferson City, Missouri

Large and fine demantoid from Russia. The green to yellowish green variety of andradite garnet was first found in the Ural Mountains. It was identified by Finnish mineralogist Nils von Nordensheld in 1864 and presented at the Ural Industrial Exhibition as a new mineral in 1887. Due to the garnet's high RI and dispersion, it was named demantoid, meaning "diamond-like."
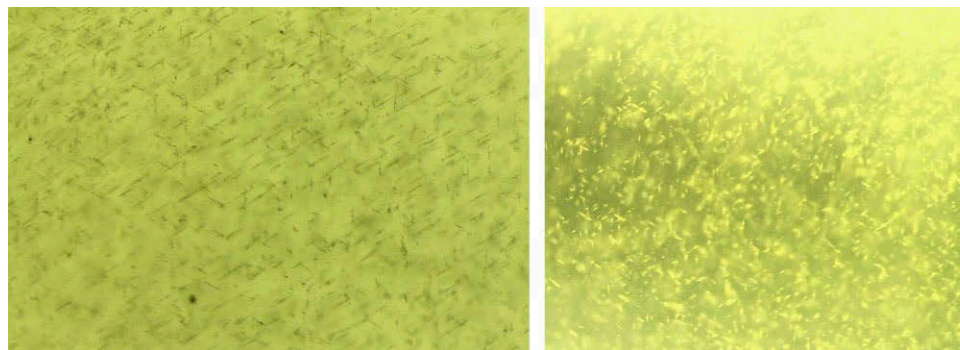

Figure 13. Brownish, acicular inclusions in the 20.13 ct star peridot (left, field of view 4 mm). Short, feathery, whitish needle-like inclusions in the 7.67 ct pear-shaped peridot (right, field of view 3.5 mm). Photomicrographs by Bear Williams.
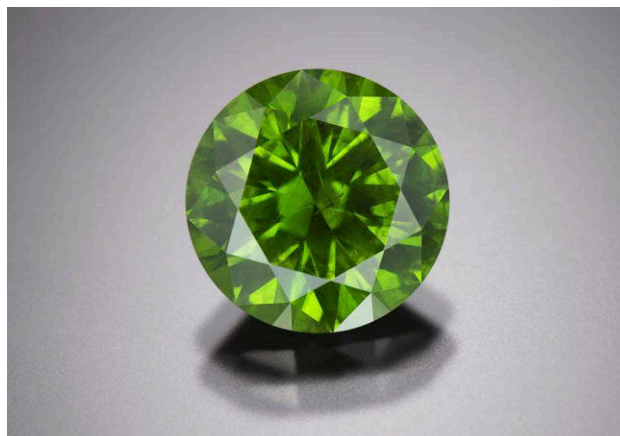
Figure 15. The Korkodin demantoid mine is an open-pit operation. Trucks transport the ore from the bottom of the pit to the nearby washing plant. Photo by Tao Hsu.

Russia remained the only source for demantoid until the mid-1990s, when the gem was discovered in Africa and later elsewhere. Today, Russian demantoid is still highly desired. At the GJX show, the authors saw an 8.49 ct fine-quality demantoid (figure 14) carried by Tsarina Jewels, the largest demantoid seen by the authors at this year's Tucson shows. It was from the Korkodin mine, located about 80 km south of Ekaterinburg, one of the two active mining operations in this area (figure 15). The Poldnevaya mine lies about 7 km to the north of Korkodin. Both operations are working on primary demantoid deposits with machinery. Together the two mines supply the majority of Russian demantoid.

Another impressive Russian demantoid was a 6.73 ct stone carried by Constantin Wild at the GJX show. This stone was also of top quality, showing high brilliance and fire. The owner informed the authors that the stone was cut from rough obtained in 2019 and possessed the best color he had seen in this material in decades (see figure 6 on p. 158).

Since Russian demantoid often occurs as small grains with no well-developed crystal forms in the matrix (figure 16), any finished stone above one carat is considered rare.

Illustrating the attention being given to this material, the 2019 AGTA Spectrum Award winner under the classical category featured a perfectly matched suite of 15 standard round brilliant cut Russian demantoid garnets. The bracelet by Jeffrey Bilgore included a 3.00 ct center Russian demantoid accented with 14 smaller Russian demantoids gradually decreasing in size (12.20 carats total) and 14 step-

Figure 16. Demantoid generally occurs as very small grains in the host rock (left). It is very difficult to find large size rough (right) of quality. This makes faceted stones over 1 ct very rare. Left photo by Tao Hsu; right photo courtesy of Constantin Wild.

2020 Tucson Photo Gallery
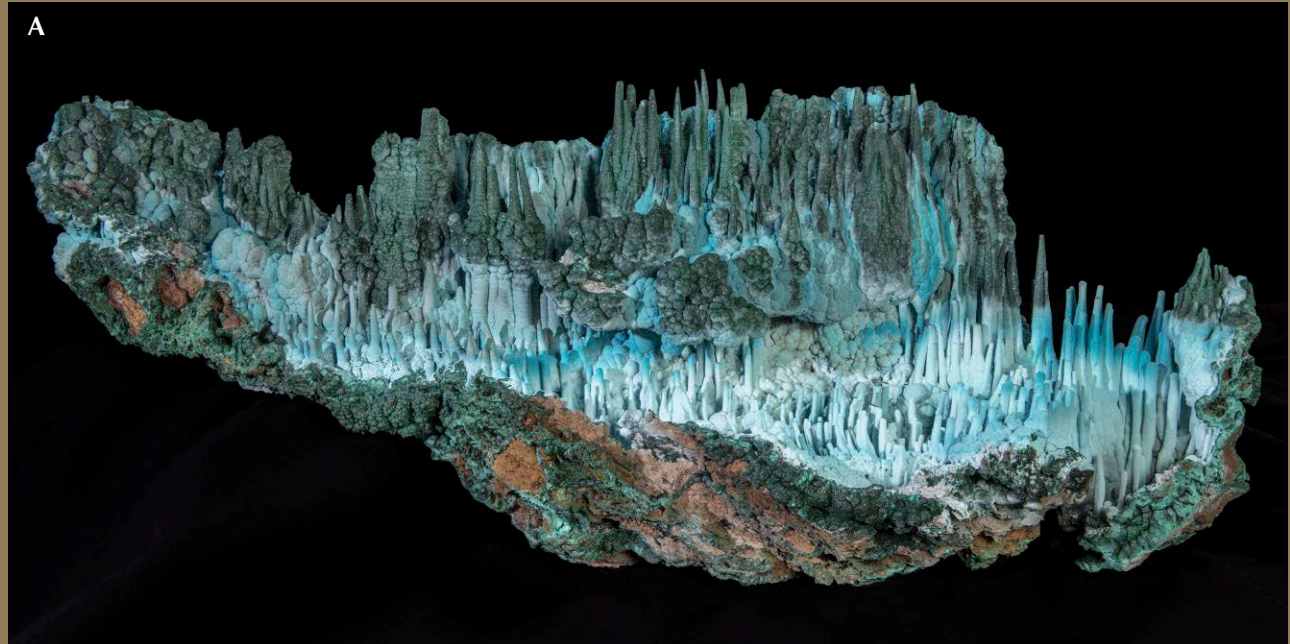
A: "Atlantis," a malachite and chrysocolla specimen from the Democratic Republic of the Congo measuring 70 × 25 cm. B: Lightning Ridge black opal and diamond ring, courtesy of The Gem Garden. C: Jellyfish design by Loretta Castoro displaying fluorescence, featuring a 49.37 ct moonstone and a Mexican hyalite opal. D: 5.74 ct cushion-cut spinel from Vietnam, shown in daylight and incandescent lighting, courtesy of Bryan Lichtenstein.

Photos by Robert Weldon (A, C, D), Emily Lane (B, E–H, J), and Kevin Schumacher (I).
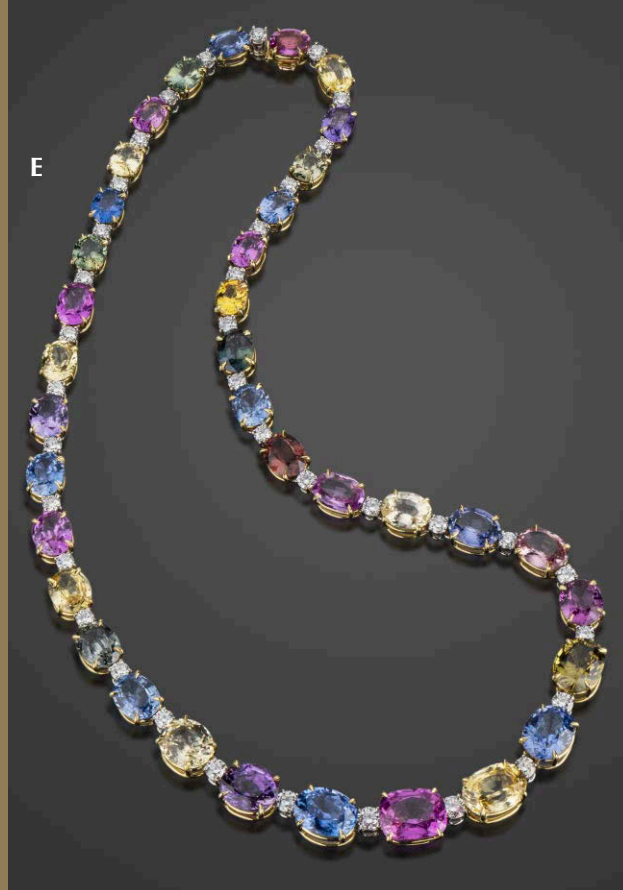
E: Bulgari multi-colored sapphire and diamond necklace with 36 sapphires totaling 72.29 carats, courtesy of M. Kantor & Associates. F: South Sea cultured pearl necklace, courtesy of Tara & Sons, Inc. G: Jadeite earrings, 16.77 carats total, courtesy of Jye's International. H: Paula Crevoshay brown-eyed Susan brooch featuring an orange Montana sapphire with multi-colored sapphires and diamonds. I: 7.35 ct Fantasy-cut heliodor carving by Nick Alexander. J: 1940s diamond and sapphire link bracelet by Oscar Heyman with 27 carats of blue sapphire, courtesy of M. Kantor & Associates.

Figure 17. Russian demantoid garnet and diamond bracelet set in platinum. The center stone is 3.00 ct, while the accent garnets total 12.20 carats and the accent diamonds 4.18 carats. Photos courtesy of Jeffrey Bilgore.

cut (4.18 carats total) diamonds all set in platinum (figure 17). Mr. Bilgore said he considers Russian demantoid to be on par with top gems such as Kashmir sapphire, Burmese ruby, and Colombian emerald. The suite came from the estate of a collector and attracted much attention from gem dealers familiar with Russian demantoids before ultimately being used in this award-winning piece of jewelry.

Tao Hsu, Jennifer Stone-Sundberg, and Aaron Palke
GIA, Carlsbad

Russian emerald. On the long list of emerald-producing countries, Russia is one of the more mysterious to the trade and consumers. Emerald was found in the Ural Mountains in the early nineteenth century. Malysheva was the most famous of these deposits and the world's largest emerald producer at the start of World War I. During the Soviet era, this deposit was nationalized and mined for beryllium instead of emerald. Today, underground mining is going strong and actively producing emeralds (figure 18).

Figure 18. The Malysheva emerald mine outside of Ekaterinburg, Russia. The giant open pit was originally mined for emerald and then beryllium. Now the mine operation is underground below the processing facility (the green building on the other side of the pit). Photo by Tao Hsu.

Figure 19. A collection of Russian emerald offered by Dudley Blauwet Gems. These stones range from about 0.1 to 3 ct. Photo by Tao Hsu.

At this year's show, the authors found two exhibitors with Russian emerald ranging in quality from commercial to fine without any treatment. Dudley Blauwet Gems offered Russian emeralds from 0.1 to about 3 ct at the AGTA show. The light to slightly dark green stones were offered as singles, pairs, and sets (see figure 19 and figure 5 on p. 158). Worth noting is that most of the Russian stones the authors saw showed bright colors and high clarity.

At the GJX show, Tsarina Jewels offered Russian emeralds of larger sizes and fine quality. This exhibitor carried stones as large as 8 ct or more (figure 20). These stones also displayed a wide range of various shades of green colors.

Figure 20. A selection of fine Russian emerald from Tsarina Jewels ranging from 1.27 to 8.38 ct. All stones are natural with no filling. Photo by Kevin Schumacher.
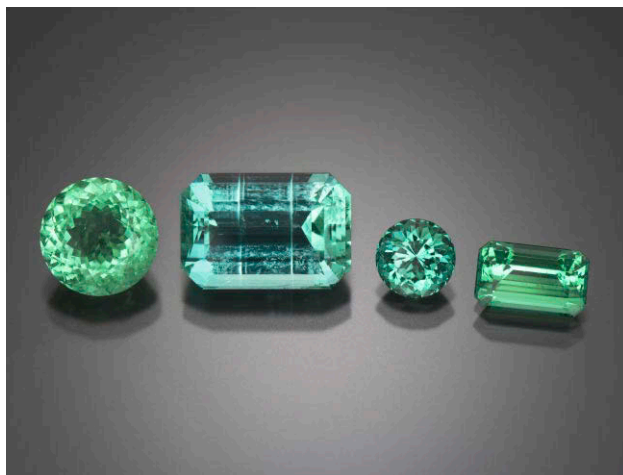
Figure 21. This bead strand is from Pakistan (9 mm beads), while the bead bracelet is from Siberia (20 mm beads). Green nephrite from Pakistan has a very similar appearance to material from British Columbia. The Siberian beads are much brighter. Photo by Kevin Schumacher.

The authors noticed that Russian emeralds are still quite rare to find on the market, while emeralds from Colombia and Zambia dominate the market.

Tao Hsu and Jennifer Stone-Sundberg

Nephrite jade from multiple sources. Green nephrite deposits are found at many locations around the globe, with British Columbia, Siberia, and northwestern China as the leading producers. Old and still active subduction zones with ophiolite have the potential to produce green nephrite. This is because green nephrite bodies are closely associated with their serpentinite host rocks, part of the ophiolite exposed on land when an ocean basin closes. All major green nephrite deposits cluster in this type of convergent-margin environment.

At the 2020 GJX show, Nikki Makepeace from Jade West in British Columbia showed the authors nephrite pieces from Pakistan, an emerging green nephrite source. The green to dark green appearance and the quality of these pieces (such as the bead strand in figure 21) are very similar to the production from British Columbia. In comparison, green nephrite from Siberia shows brighter colors (the bracelet in figure 21 and the pendant in figure 22). Ms.

Figure 22. High-quality nephrite from Siberia can sometimes show a color similar to that of green jadeite. Photo by Tao Hsu.

Makepeace informed the authors that the production from Pakistan is quite substantial.

The earliest report on Pakistan nephrite was published in 1963, with the positive identification of two pebbles collected in 1955 in the riverbed of the Teri Toi in Kohat District of Pakistan (B.C.M. Butler, "Nephrite jade in West Pakistan," *The Journal of the Royal Asiatic Society of Great Britain and Ireland*, No. 3/4, 1963, pp. 130–139). The geographical location of this deposit placed it in the collision belt along the Himalaya Mountains. This is the convergent margin between the Eurasian and Indian Plate when the Tethys Ocean closed about 50 million years ago, providing an ideal geological environment for nephrite formation.

In addition to the goods from Pakistan, the authors saw a large koru, a spiral shape often used in Maori art, made of nephrite from Afghanistan. Currently, Afghani materials are scarce on the international market. The only information the authors could find was that the rough comes from the Kohi-Safi District of central Parwan Province. This location is not far from the Pakistani deposit.

While buyers are still waiting to see more production from these emerging sources, green nephrite from British Columbia and Siberia still dominate the market. Siberian goods in general demand higher prices than materials from the rest of the world due to their brighter colors. British Columbian production is still high and can supply finished goods of all price ranges.

Tao Hsu and Jennifer Stone-Sundberg

Nigerian gems and jewelry. During the JCK show in Tucson, GIA had the opportunity to meet up with Amina Egwuatu, founder of Mina Stones. Mrs. Egwuatu, a GIA Graduate Gemologist from Abuja, Nigeria, started the company with the aim of promoting African culture through gems and jewelry. Mina Stones sources, cuts, designs, and manufactures everything in their workshops to keep as much value as possible in Africa. Mrs. Egwuatu works directly with the miners and has visited many of the sites where her stones are produced. This allows traceability throughout the entire supply chain. Mina Stones helped to establish the AGJES Sparkle Foundation, which supports miners through education about their stones, helps them with administration, and provides tools. By working this way, Mina Stones improves the conditions of its miners and suppliers.

Nigeria is known for tourmalines that possess a wide range of colors, rubellite being the most famous. A more recent rubellite discovery near Calabar, Cross River State, has produced higher volumes (though slightly lower quality) than the original find in Oyo State, which has not produced for a long time.

Apart from the red variety, this gem is also found in green, pink, and various combinations of these colors. About 20 years ago, there was even a discovery of cuprian tourmaline in western Nigeria that produced some fine material for a short period. According to various sources, a new pocket was discovered in early 2020 that made this material available in the market.

Another common stone from Nigeria is beryl. Various regions in the country produce fine aquamarine, morganite, heliodor, and green beryl (figure 23). While there are many emerald deposits known throughout the country, facet-grade material is limited to an area in Nasarawa State.

Sapphires are found throughout the eastern and central parts of Nigeria. In several areas such as Antang, Bauchi, Kaduna, and Gombe, the production is exclusively from artisanal miners. The better-known Mambilla

Figure 23. Strands of Nigerian beryl in assorted colors. Photo by Kevin Schumacher.

Figure 24. This necklace makes use of the Arewa knot, a symbol of unity. Photo by Kevin Schumacher.

Figure 25. This 16.23 mm, near-round 28.38 ct natural freshwater pearl was found along the banks of the Cumberland River in 2019. Photo by Emily Lane; courtesy of Gina Latendresse.

Plateau has a few larger operations, but small-scale mining is prevalent.

Nigerian sapphires are typically dark blue, although goods found in the southeastern part of the country tend to be lighter in color. Parti-colored, yellow, purplish, and green sapphires are also common.

Mina Stones' jewelry is inspired by Nigerian traditions. The country has long been known for its blacksmiths and goldsmiths, resulting in a strong jewelry culture. Mina Stones is trying to revive the skills, patterns, and heritage by making use of traditional alphabets and symbols. One example is a necklace featuring the Arewa knot (figure 24), a symbol that represents the unity of the different people in northern Nigeria.

Another collection draws inspiration from the city of Ife, in southwestern Nigeria. According to local beliefs, the city was found by a supreme deity and served as the seat for a long line of dynasties.

Mina Stones aims to represent Nigerian gems and jewelry. The country is an important supplier of many colored gemstones that have remained largely unknown to the general public.

Wim Vertriest
GIA, Bangkok

Exceptional natural freshwater pearl. At the AGTA show, we visited Gina Latendresse at the American Pearl Company of Tennessee booth to find out about anything new in the pearl industry. We were excited to learn that an exceptional pearl, both in size and quality, was discovered last year in the Cumberland River (figure 25). The pearl was found by a fisherman along the bank of the river in a "Pistol Grip" (*Tritogonia verrucosa*) mussel (figure 26). This 28.38 ct white pearl with natural color measured 16.23 mm in diameter and was near round with good luster. This was the first pearl of such size and quality found in the Ten-

Figure 26. The natural pearl from figure 25 shown in its shell (left), and the "Pistol Grip" shell exterior (right). Photos by Emily Lane; courtesy of Gina Latendresse.

Figure 27. Bicolor sapphires from the Rock Creek mine, Montana. Cutters took advantage of the color inhomogeneity of the rough to create these interesting color combinations. These stones range from 1.61 to 7.36 ct. Photo by Emily Lane; courtesy of Potentate Mining.

nessee region since the 1970s. The pearl is so unusual that Ms. Latendresse described it as either a collector specimen or suitable for museum display.

For context, the eastern portion of the United States was a source of many natural freshwater pearls to native Americans as evidenced by John Smith's 1608 writings noting the "many chains of great pearls about his [Chief Powhatan of the Powhatan Confederacy near present day Richmond, Virginia, also the father of Pocahontas] neck" (P.L. Barbour, Ed., *The Complete Works of John Smith (1580–1631)*, Vol. 1, University of North Carolina Press, Chapel Hill, 1983, p. 53). Two and a half centuries later, a pearl rush started with the discovery of pearls of notable size and quality by fishermen in New Jersey, which resulted in people searching streams and rivers throughout the country. In 1857, David Howell found a near-round 100 ct pearl in a fried mussel he fished from Notch Brook in New Jersey (which unfortunately had its luster destroyed by the frying process). Shortly thereafter, Jacob Quackenbush discovered a 23.34 ct pink baroque pearl of fine luster, later named the "Queen Pearl," that he sold to Charles Tiffany for $1,500. Good-quality pearls were found in the Cumberland, Tennessee, and Clinch Rivers in the state of Tennessee for many years thereafter (G.F. Kunz and C.H. Stevenson, *The Book of the Pearl: The History, Art, Science, and Industry of the Queen of Gems*, The Century Co., New York, 1908).

The recent discovery of such an extraordinary pearl proves that it is prudent to check the inside of mollusks known to produce pearls before consuming them!

Jennifer Stone-Sundberg and Tao Hsu

Interesting sapphires from Montana and Australia. While sapphire has always been popular at trade shows, occasionally the authors find some interesting stones with attractive color distribution or growth patterns that have a niche in the market.

At this year's AGTA show, Potentate Mining carried some spectacular bicolor faceted sapphires and a variety of slabs from its Rock Creek mine in Montana. The Rock Creek operation is one of four active sapphire mines in

Montana. Stones from this deposit tend to be flat, showing pastel colors, and many stones show bicolor or have an orange or yellow core called "yolk" by the local miners. Gem cutters and jewelry designers have been finding innovative ways to take advantage of these challenging attributes. Through careful design and cutting, some stones show attractive color combinations such as yellow/green, yellow/light blue, orange/blue, or simply different shades of yellow (figure 27). This type of bicolor is very characteristic of Rock Creek sapphires.

As for the flat rough, Potentate offers several categories based on color, pattern, and weight (figure 28). According to the company's marketing director, Warren Boyd, both cutters and designers have shown strong interest in these slabs, especially those weighing half a gram and above. Designers seem to prefer slabs with patterns while cutters or carvers prefer slabs with solid colors to make special cuts.

Figure 28. Flat rough sapphires from Rock Creek attract jewelry designers and cutters. The slabs are grouped and sold by their weight. Photo by Tao Hsu.
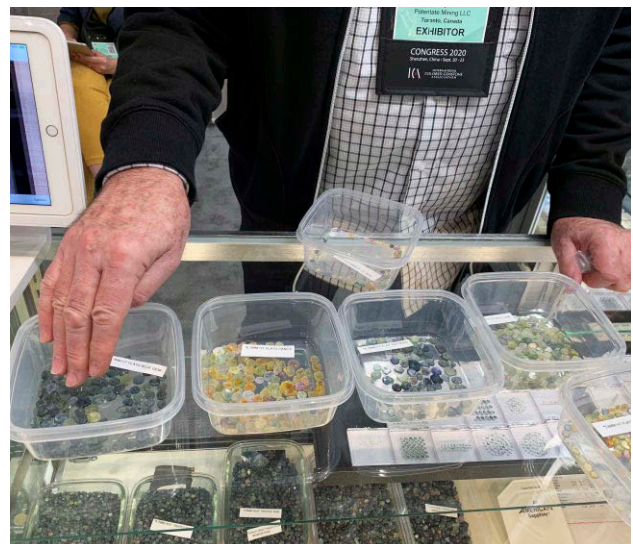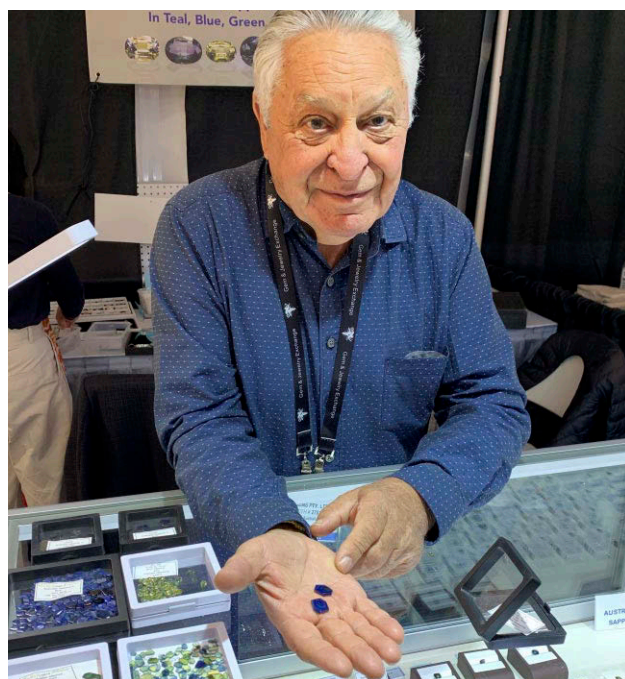
Figure 29. This pair of blue sapphire thin slabs displays a very attractive color. They were sliced off a dark blue sapphire crystal from Inverell, Australia. Mr. Coldham also offered thin slabs of blue and particolored sapphires from Australia. Photo by Tao Hsu.

At the GJX show, Terry Coldham from Intogems showed the authors a pair of thin blue sapphire slabs with characteristic hexagonal growth patterns. The pair in figure 29 is from the Inverell sapphire field of New South Wales, Australia. Blue sapphires from this area tend to show a very saturated and dark inky blue color. Slicing them into thin slabs makes the blue color much lighter and more desirable. However, the size and quality of this pair are extremely rare to find. Mr. Coldham also carries many parti-colored and fancy-color Australian sapphires (see figure 4 on p. 157), which also sold well at the show.

To watch videos of the sapphire slabs from Montana and Australia, go to https://www.gia.edu/gems-gemology/spring-2020-gemnews-sapphires-montana-australia.

Tao Hsu and Jennifer Stone-Sundberg

Exceptional rough and cut blue sapphire from Rock Creek, Montana. The Rock Creek sapphire deposit in Montana has been active since the 1890s and is known as the state's most fruitful deposit (T. Hsu et al., "Rock Creek Montana sapphires: A new age of mining begins," https://www.gia.edu/gia-news-research/rock-creek-montana-sapphires-new-age-mining-begins, August 29, 2016). This year in Tucson, Jeffrey Hapeman of Earth's Treasury showed the authors a very fine untreated blue sapphire rough with a yellow spot in the center, as well as a top-quality faceted light teal blue untreated stone with some yellow zoning (figure 30). Since

2014, Mr. Hapeman has been focusing on Rock Creek material in these nontraditional lighter blues to greens. They have proven to be very popular, as several AGTA vendors this year reported strong demand for these colors, not only in Montana sapphire but from other sources as well. When it comes to unheated material, only about 5% of the rough from Rock Creek is cut without treatment, and most of these are either fancy pinks, yellows, or lighter blues. In the past year Mr. Hapeman has seen a shift in demand to parti-colored and green sapphires, particularly deep bluish green.

Jennifer Stone-Sundberg, Tao Hsu, and Robert Weldon

New blue sapphire from Rakwana, Sri Lanka. The town of Rakwana, in southern Sri Lanka, has been known for decades as a premier source of royal blue sapphires. Often, a simple mention that a gemstone is from Rakwana will immediately explain the price and quality. In August 2019

Figure 30. The 17.65 ct "Lucky Sapphire" rough crystal and 3.92 ct oval cut using the custom "Helena" design, both from Rock Creek, Montana. Photo by Robert Weldon/GIA; courtesy of Jeffrey Hapeman.

Figure 31. A 49.99 ct rough sapphire crystal (5.8 cm in length) and a 33.16 ct cut stone with exceptional color from the 2019 Rakwana find. Photo by Robert Weldon/GIA.

a small pocket yielding numerous large sapphire crystals was discovered in the nearby Sinharaja Forest area of the Ratnapura District, Sabaragamuwa Province. What was unique about this find was the quality and size of the lustrous crystals. The 49.99 ct rough crystal in figure 31, measuring 5.8 cm in length and 1.6 cm at its widest point, was one of about 60 found in August 2019. It was also the largest complete crystal found. The beautiful 33.16 ct gem beside it was cut from a 207 ct piece of rough, the end of a large portion of a crystal. This crystal and cut gem rival the famous ones from Kataragama found four years ago.

Jennifer Stone-Sundberg, Tao Hsu, and Robert Weldon
Dudley Blauwet
Dudley Blauwet Gems
Louisville, Colorado

Trapiche gems. Jeffery Bergman is known in the trade as a collector of trapiche gems. These gems, characterized by their six-rayed patterns, are elusive and seldom found in high quality. Mr. Bergman believes people are attracted to the symmetrical pattern, which reflects a natural order in the chaotic world we live in. According to Bergman, trapiche gems are too rare to support a business, so he has also traded many other gemstones during his 50-year career.

As with most gemologists, the first trapiche gems he saw were Colombian emeralds. But it wasn't until 10 years after this initial encounter at the Tucson gem show that he purchased his first trapiche gemstone: a thick Colombian emerald weighing about 20 ct. Mr. Bergman sliced it in two, increasing the value after it became a matched pair of acceptable thickness.
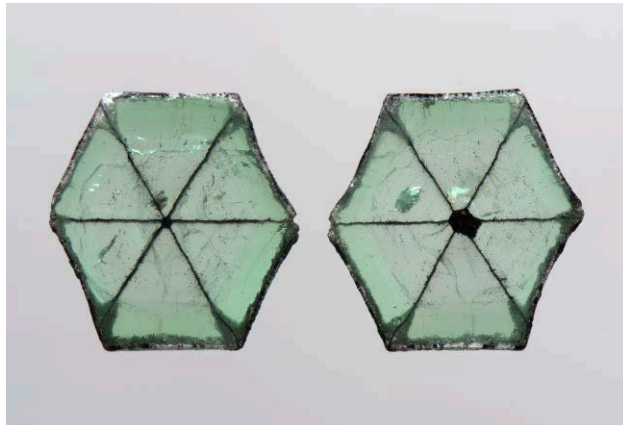
Figure 32. A pair of trapiche emerald slices from Colombia, 10.92 carats total. Photo by Kevin Schumacher; courtesy of Mayer & Watt.

He saw his first non-emerald trapiche gems at the Mae Sot gem market on the Thai-Burmese border in the early 2000s. Mr. Bergman was handed three Burmese trapiche sapphires from Mogok, something he never knew existed. Other collectors were equally surprised and paid high amounts for these stones, encouraging Mr. Bergman to expand his collection. During those days, many fine Burmese trapiche rubies came out of Mong Hsu while Mogok provided the trapiche sapphires.

Trapiche rough is extremely difficult to judge since the patterns often do not extend throughout the entire stone. In most cases, the most desirable pattern can only be found in the middle of the crystal length.

Trapiche and non-trapiche emerald evaluation are very similar, as the most important characteristics are always the color and transparency of the emerald itself (figure 32). The symmetry and shape of the pattern are only of secondary importance, followed by size and potential treatments.

Trapiche emeralds from Colombia are well known, with the Muzo mine producing the majority. The patterns can exhibit many variations, from perfect six-ray symmetry with high clarity to cloudy stones with broken or incomplete rays. Trapiche-like emeralds have recently been found in Swat, Pakistan, but they show a very different appearance and formation (Fall 2019 GNI, pp. 441–442). Beryls such as aquamarine and bixbite (red beryl) are known to exhibit trapiche or trapiche-like characteristics but they are even rarer than emeralds.

Trapiche corundum gems are mostly known from Myanmar. Trapiche ruby from Mong Hsu is often small. In his 20 years of trapiche experience, Mr. Bergman has only encountered two gem trapiche rubies from Mong Hsu that were over 1 carat. The material is fairly dark, which means it must be sliced thin to appreciate any color, thus reducing the weight of the stone drastically. Heat treatment rarely improves the appearance; it alters the trapiche pattern, making it chalkier and less pronounced.

The Tajik ruby mines have also produced trapiche rubies, as well as the mines in Nepal. Batakundi (Pakistan) and Orissa (India) are other sources of ruby with six-rayed patterns (Spring 2019 *G&G* Micro-World, p. 114).

Trapiche sapphires from Mogok (figure 33) are often dominated by gray tones or very saturated blues bordering black colors. Only the finest stones show a snow-white bodycolor with vivid blue arms. To date, these are the only true trapiche sapphires. Trapiche-like sapphires are much more common from basalt-related sources such as southern Vietnam, Australia, and even lesser-known areas such as Scotland.

Quartzes, including amethyst and smoky quartz, can exhibit trapiche patterns. A pocket of Zambian tourmalines and some extremely rare garnets also show a six-rayed pattern.

In Mr. Bergman's opinion, trapiche only applies when the symmetry is sixfold. This excludes more common materials with similar growth patterns like chiastolite. Asteriated diamonds, most often found in Zimbabwe,
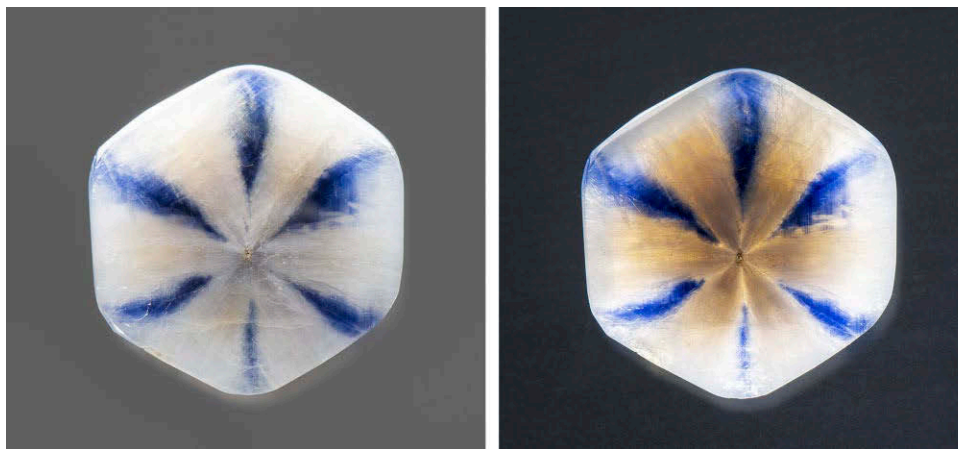

Figure 33. Trapiche sapphire from Mogok, Myanmar. This stone shows a regular pattern of snow white and blue zones. Photos by Kevin Schumacher.

Figure 34. These miniature opal carvings are favored by designers. They are hand-carved in Bali from different varieties of Australian opal. Photos by Tao Hsu and Jennifer Stone-Sundberg.

resemble trapiche when viewed in certain angles, but in reality they contain clouds extending in three dimensions at 90° angles.

In the last decades, knowledge and appreciation of these unique stones has spread and they are now actively sought after by collectors, bespoke designers, and gem enthusiasts. This increased demand and availability has driven gemologists to take a deeper look at these gems and their formation, but there remains much to be discovered.

Wim Vertriest

CUTS AND CUTTING

Carvings from Bali. Picturesque beaches and lush green jungles are not the only attractions that make Bali the most popular tourist destination in Indonesia. The local carving tradition, derived mostly from woodcarving, adds a layer of artistry and craftsmanship to this tropical paradise. Now many carvers there are also involved in different types of gem materials.

At the GJX show, the author found some authentic and attractive Balinese carvings of Australian opal, mammoth tusk, and bovine bone. Mr. Terry Coldham from Intogems brought opal carvings of pendant sizes, which are highly desired by jewelry designers (figure 34). Mr. Coldham utilizes rough from different Australian mining areas, primarily black and white opal, but some crystal opal as well. The carvings feature natural themes such as plants, flowers, and animals, as well as profiles of faces from different cultures. The carving style includes both relief panel and three-dimensional sculpture. Some pieces show color blocks being skillfully arranged, a technique commonly used by the Chinese in jade carving. The quality of the rough dictates the price, ranging from hundreds to thousands of dollars for each finished piece. According to Mr. Coldham, opal carvings have sold well over the past several years. He enjoys working with the Balinese carvers and added that after a couple of years of collaboration, the products have improved to better fit the international market.

Another exhibitor that caught the author's eye is Susan Tereba. Ms. Tereba moved to Bali over 30 years ago and still lives there today. She brought to the show amazing hand-carved mammoth tusk and bovine bone. Ms. Tereba appreciates the remarkable talent of the Balinese carvers, who are fast learners and can easily grasp themes that are not indigenous. These exquisite carvings also show a wide variety of motifs, with animals and goddesses the most popular and some pieces are gem studded (figure 35). The bovine bone carvings are dyed, and according to Ms. Tereba

Figure 35. Balinese carved mammoth tusk of a garden goddess. Photo by Tao Hsu.
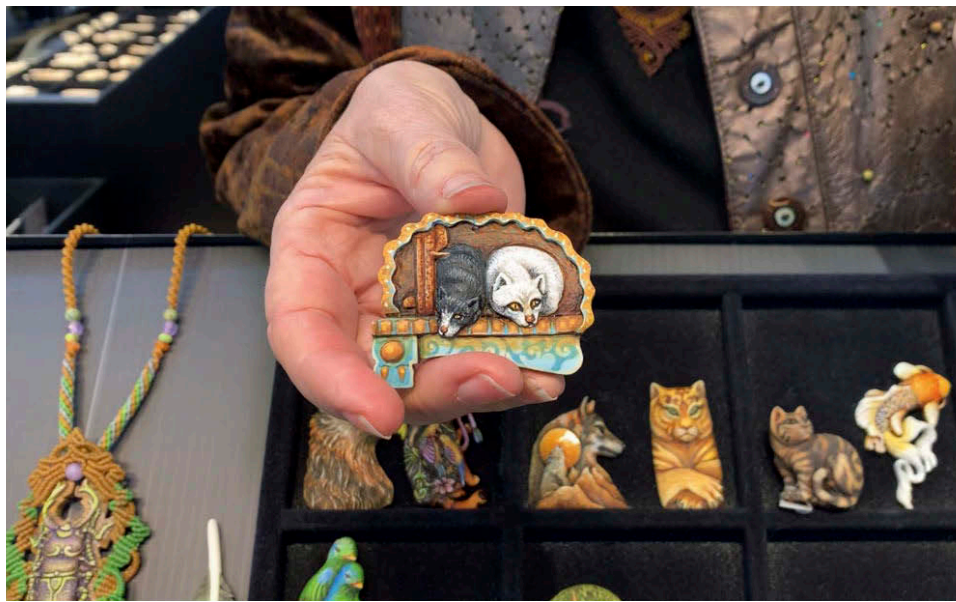
Figure 36. Bovine bone carvings are usually dyed to show vivid colors. The color is stable over many years. Photo by Tao Hsu.

the color is very durable and resistant to wear (figure 36). Jewelry designers and hobbyists are her main clients.

To watch videos of Terry Coldham and Susan Tereba displaying Balinese carvings, go to https://www.gia.edu/gems-gemology/spring-2020-gemnews-carvings-bali.

Tao Hsu

Gem carvings, fantasy cuts, and master recutting. This year at the AGTA show, the number of booths selling skillfully carved, fantasy cut, or expertly recut items was noticeably higher than in past years. These forms of working rough or previously cut material are a way to add significant value and desirability to material that might otherwise be cut into standard shapes or with the intent to maximize weight at the expense of beauty.

Nick Alexander (figure 37, left) of Alexanders Jewelers in Gilbert, Arizona, was exhibiting his work for the first time at the AGTA show. This year, Mr. Alexander won second place in the carving category of the AGTA Cutting Edge Awards with his 42.05 ct Oregon sunstone piece at the impressive age of 17. A favorite material of his is electric blue gem silica from the Ray mine in Arizona (see figure 2, p. 157). Mr. Alexander is also skilled at fantasy cutting with materials such as amethyst (figure 37, right) and beryl.

One of the carvers who has inspired Mr. Alexander, Glenn Lehrer of Larkspur, California (figure 38, right), was also at the AGTA show. Mr. Lehrer shared with us one of his newest works, an exquisite lotus flower carved out of a top-quality rose quartz from Madagascar (figure 38, left).

Figure 37. Left: Nick Alexander exhibits a selection of his work. Photo by Jennifer Stone-Sundberg. Right: A 64 ct fantasy cut amethyst from Bahia, Brazil. Photo by Kevin Schumacher; courtesy of Nick Alexander, Alexanders Jewelers.

Figure 38. A 322.72 ct Madagascar rose quartz lotus flower carving with grayish blue and padparadscha Montana sapphires in the center (5.56 and 0.65 ct, respectively), shown by the artist, Glenn Lehrer. Left photo by Robert Weldon/GIA, courtesy of Glenn Lehrer; right photo by Jennifer Stone-Sundberg.

This piece started as part of a museum collection project with designer Paula Crevoshay. It took two years to find the 3.8 kg rose quartz rough meeting his stringent demands: It had to be clean, clear, and with strong color. The finished carving measures 79.5 × 69.8 mm and weighs 322.72 ct. To complement the piece, the center features two sapphires from the Rock Creek area of Montana: a 5.56 ct grayish blue "torus ring" carving and a 0.65 ct padparadscha.

Master gem cutter David Nassi from New York City (figure 39, left) showed us an impressive set of unheated natural spinels and several other gems he had recut to maximize color and light return. Of particular interest was a phenomenal gem, a natural color-change cat's-eye alexandrite (figure 39, right) that was polished to a double-sided cabochon to display the cat's-eye effect on both sides of the stone. For videos of David Nassi displaying his work, go to https://www.gia.edu/gems-gemology/spring-2020-gemnews-carvings-fantasy-cuts-recutting.

Jennifer Stone-Sundberg, Tao Hsu, and Robert Weldon

JEWELRY DESIGN

Fine-quality jadeite jewelry. At this year's Pueblo Gem and Mineral Show, the authors met Frank Lau from Frank Lau
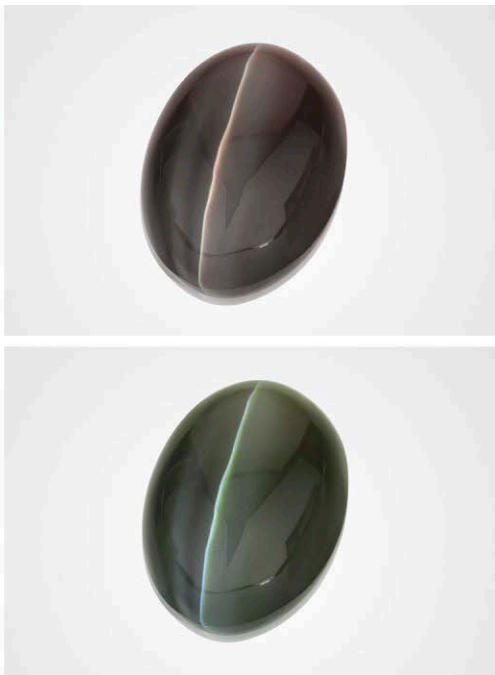

Figure 39. Left: David Nassi of 100% Natural, Ltd. showing a collection of unheated spinels he has recut, ranging in size from 7.10 to 18.53 ct. Photo by Jennifer Stone-Sundberg. Right: A 14.49 ct cat's-eye alexandrite from Sri Lanka cut by Nassi, showing reddish brown to green color change. Photos by Emily Lane; courtesy of David Nassi.

Figure 40. A selection of jewelry offered at Frank Lau's booth. Jadeite of fine quality is not commonly seen in Tucson. Photo by Tao Hsu.

Jewelry. What caught the authors' attention was the collection of fine-quality jadeite jewelry, which is predominantly found in the mainland China market but not in Tucson.

Mr. Lau's booth offered a wide variety of jadeite including green, colorless, lavender, and red ranging in quality from medium to fine (figure 40). The jadeites are polished and carved in Guangzhou, China, while the jewelry is manufactured either in China or Seattle, where the store is located. Clients of the jadeite jewelry include both Chinese and Americans, with many repeat customers.

While all of the jadeites are natural, Mr. Lau informed the authors that the reddish brown pendant is heated (figure 40). Reddish brown jadeite is extremely rare. This color is produced from a very thin layer of jadeite boulder (figure 41) leaving little material to make pieces of reasonable sizes. A good amount of reddish jadeite on the market is heated in

air to oxidize the Fe-containing minerals to make the stone look red. This treatment is extremely hard to identify.

The colorless jadeite pieces, also called "ice jade," are of very fine quality. This variety is popular with younger consumers. The exceptionally fine texture and relatively high transparency make it an alternative to the top-quality imperial green stones. When inclusions are present in the colorless jadeite, sellers describe them as "snowflakes" to attract buyers of different tastes (figure 42).

Figure 42. This colorless jadeite pendant is of very high transparency. Many sellers describe the whitish inclusions as "snowflakes." Photo by Tao Hsu.

Figure 41. A rough jadeite boulder shows a very thin layer of reddish brown skin. Red jadeite is even rarer than the green variety. This boulder was offered at the Myanmar Gem Emporium. Photo by Tao Hsu.

Figure 43. A cordierite Viking "sunstone" set in silver with the "vegvísir" compass symbol. Note that Mr. Berger's ring also features a cordierite cabochon set in silver. Photo by Jennifer Stone-Sundberg.

Figure 44. Examples of contemporary Scandinavian designs in silver containing thulite. Photo by Jennifer Stone-Sundberg; courtesy of Atle Berger.

Mr. Lau sources his rough materials from Myanmar, though the skyrocketing price of rough makes this business increasingly difficult. He looks forward to the availability of more consumer-oriented jadeite education so Western consumers can better appreciate this gem.

Tao Hsu and Jennifer Stone-Sundberg

Nordic gems and jewelry. At the JOGS show, Arctic Jewelry (Axvalla, Sweden) featured a variety of Nordic gemmy materials set mainly in silver using ancient, traditional, and contemporary Scandinavian designs. The pieces spoke to the mineral diversity, history, and artistry of the region.

The Vikings made navigation stones from locally sourced transparent crystals of minerals such as cordierite, a biaxial magnesium iron aluminum silicate, to help cross the seas under cloudy weather. These Viking "sunstones" are backed up by science, as cordierite and other materials such as calcite and tourmaline can be used to identify the position of the sun through even thick clouds. These stones visibly split sunlight into two images that when rotated to make equally bright, show rings of polarized light around the sun's position. Cordierite was found to be the most accurate navigation stone in simulated journeys from Bergen, Norway, to the Viking settlement of Hyarf in

Greenland (D. Száz and G. Horváth, "Success of sky-polarimetric Viking navigation: revealing the chance Viking sailors could reach Greenland from Norway," *Royal Society Open Science,* Vol. 5, 2018, No. 172187). An example of a silver pendant engraved with a vegvísir (a Nordic compass "wayfinder" symbol) and a cordierite center stone was shown to us by Atle Berger (figure 43).

Thulite, a manganese-containing pink variety of zoisite with some white calcite mottling, is the national gemstone of Norway, the country in which it was discovered by Anders Gustaf Ekeberg in 1820. The name comes from "Thule," the ancient name for the mythical island (believed to be modern-day Norway) that was considered the northernmost part of the world. At the Arctic Jewelry booth, contemporary Scandinavian designs in silver incorporating this stone were featured in jewelry ranging from rings to bracelets and necklaces (figure 44).

A bright and attractive blue material found at the booth is the slag byproduct of iron smelting in the Bergslagen region of central Sweden during the Middle Ages. This material was reported on previously in *G&G* (Winter 2006 GNI, p. 279) and characterized in the GIA lab. At that time, EDXRF was the method used for chemical analysis, but today with LA-ICP-MS we were able to more exactly determine the composition of this material from some rough

Figure 45. Rough "Swedish Blue" slag byproduct. Photo by Kevin Schumacher; courtesy of Atle Berger.

pieces given to us by Mr. Berger (figure 45). We identified it as a silica-rich glass with a composition of 56.35 wt.% SiO_2, 24.70 wt.% CaO, 7.68 wt.% MgO, 5.05 wt.% Al_2O_3, 2.23 wt.% FeO, 2.21 wt.% K_2O, 0.85 wt.% MnO, 0.27 wt.% Na_2O, and 0.65 wt.% other elements (average of 10 ICP spot analyses). This gave a calculated chemical formula of $(Na_{0.019}, Mg_{0.418}, Al_{0.217}, K_{0.103}, Mn_{0.026}, Fe^{2+}_{0.068},$ others$_{0.012})_{0.864} Si_{2.058} Ca_{0.967}O_6$, which is generally consistent with what was reported in 2006. The oxide components are fairly normal for iron foundry slag, but the silica-rich nature is what gives this material its fine glassy aspect compared to those slags that are more CaO-rich. The slightly greenish blue color comes from Fe^{2+} (FeO).

Jennifer Stone-Sundberg and Ziyin Sun

RESPONSIBLE PRACTICES

Ethical Gem Fair. Tucson's first Ethical Gem Fair, a platform for responsibly sourced gemstone suppliers to highlight their products and projects, was held February 3–6 at the Scottish Rite Cathedral. This was the first Ethical Gem Fair in the United States after being held in London and Edinburgh the last three years.

The Tucson event was a collaboration between suppliers Nineteen48, Capricorn Gems, Perpetuum Jewels, Nature's Geometry, Agere Treasures, Columbia Gem House,

and Anza Gems. They share a commitment to supply chain ethics, mine-to-market traceability, environmental and health and safety regulations, and supporting artisanal miners and communities.

Monica Stephenson, founder and president of Seattle-based Anza Gems, said her travels to East Africa to purchase rough have shown her that miners need to be educated about the value they bring to the supply chain. Ten percent of Anza's proceeds go to education at the mining communities.

Anza Gems is a partner of Moyo Gemstones, a responsibly sourced gemstone program that was sparked by GIA's artisanal mining education program. The pilot effort, a collaboration between GIA, Pact, and the Tanzania Women Miners Association (TAWOMA), focused on women miners in Tanga, Tanzania. After initial training, they were more knowledgeable about the mined gemstones but lacked a platform to bring them to the market. Stephenson saw potential here, and together with Pact and TAWOMA she founded Moyo Gemstones. The program provides a marketplace for gemstone transactions, offers free occupational health and safety training, and helps ensure that all miners are legally registered.

Stephenson said that before the program these miners would get a few dollars for gems from a broker, with no visibility into their value in the supply chain. Moyo has changed this through education. "For the miner to understand what she has and the value of those gems, and also to be taking home more like 95% of the export price, and pay her broker, is a complete reversal of the roles," Stephenson said. "This is truly a paradigm shift in this region. For her to have the income and financial sort of independence is enormous."

Each gem can be traced back to the miner, Stephenson said, and it's important to share that story with the consumer. "They need to know that what they're buying not only makes a difference, and not only does it not cause harm, but it actually is beneficial."

Anza Gems' offerings (figure 46) included sapphire, multiple colors of garnet, tourmaline, citrine, amethyst, zircon, and Mahenge spinel.

Brian Cook, owner of Nature's Geometry (Tucson), began selling crystals as a geology student almost 30 years ago. This took him to a remote area of Bahia, Brazil, where rutilated quartz is mined. He felt a strong connection to the place and made it his second home. Since then he has advocated for the development of resources more sustainable than mining so the community can rely on them when mining ends.

Cook told us about their project in Bahia to benefit the artisanal mining community. The first initiative will raise funds for dust masks for the miners, at least half of whom have no dust protection for underground mining. Second, he envisions a model of investment in regenerative agriculture to create food security, improve nutrition, and implement carbon sequestration. The area's soil is so rich that it allows

Figure 46. A selection of gemstones from Anza Gems. All of these stones were sourced in Tanzania, including the set of rough sapphires that was mined in Tanga province. Each stone can be traced back to the individual miner who unearthed the gem. Photo by Kevin Schumacher.

for farming of crops such as cacao, coffee, acai, and many others. The third component will be teaching lapidary skills.

Eighty percent of colored gemstones are mined by small-scale and artisanal miners, according to Cook. "This project could serve as a model for our industry at large," he said. While he recognizes that every situation is different, food, water, and energy will always be the basic needs of every being, and guaranteeing them can uplift a community.

Cook showed us several pieces of rutilated quartz from Bahia, including a sizable piece of rough (figure 47). Na-

Figure 47. Rough rutilated quartz from Bahia, Brazil. Photo by Kevin Schumacher.

ture's Geometry has been cutting the material since 1989. Each piece is unique, which Cook said is something the younger generation likes.

Cook said the response to the fair has been "phenomenal." He predicts it will grow in future years, with more vendors and a greater variety of stones.

Ian Bone, manager of Capricorn Gems (Central Queensland, Australia) said the Ethical Gem Fair was created to meet the needs of designers and customers who want a gemstone's mine-to-market story. "There's undoubtedly a generational shift happening," he said. "Customers want to know that the pieces are brought to market in the most responsible manner possible. We see this as the cutting edge of jewelry design and in fact the future of the jewelry industry."

Bone said that because Australia's mining industry already has strong regulations for safety, the environment, energy, and land reclamation, it could serve as an example for other mining communities around the world.

Bone, a Central Queensland native, has built his business around local gemstones: boulder opal, chrysoprase, zircon, and sapphire. He is able to witness the entire process, from mining to cutting to consumer sales. He showed us a selection of chrysoprase from Marlborough, Central Queensland (figure 48). "Marlborough has some of the best chrysoprase in the world," he said. "Chrysoprase is an unusual gem because you can get a whole set of qualities of that stone, from dollars a pound up to dollars a carat."

Bone said Capricorn Gems is breaking down boundaries between sourcing, production, and sales. They share their images, videos, and stories of mining with designers for use in their own marketing. One example is a booklet showcasing the works of designers around the world who

Figure 48. Capricorn Gems' chrysoprase from Marlborough, Central Queensland. Photo by Kevin Schumacher.

use stones from Capricorn Gems. "The client knows that their designer knows and trusts the gem supplier and knows where that material comes from," he said.

Hewan Zewdi, founder of Agere Treasures (Lynnwood, Washington), was born and raised in Ethiopia and moved to Seattle 14 years ago. There she earned her G.G. through GIA Distance Education. When Ethiopian opal (figure 49) was discovered in 2008–2009, people began calling from home to ask if she had a market for them. "That's what I study—that's what I want to do," she told them.

Figure 49. Ethiopian opal from Agere Treasures. Photo by Kevin Schumacher.

At the Denver Gem & Mineral Show, Zewdi's first trade show, she saw Ethiopian opal dealers undervaluing their material and advised them to increase their prices. She also began buying stones from them to sell in her local market in Washington. Her commitment increased when emeralds were discovered in southern Ethiopia. Agere Treasures now offers opal, emerald, amazonite, yellow labradorite, garnet, zircon, tourmaline, and sapphire.

Part of Zewdi's profits go to a new project to train young women in basic gemology and jewelry design. She also donates books on rocks and gems to the Ethiopian Ministry of Mining, and she assists the organization in obtaining gemstone identification at GIA so the stones can be priced accordingly by exporters in Ethiopia.

"Here everybody has the same mission, the same vision," Zewdi said of the Ethical Gem Fair. "To give back and get the material traceably and responsibly, without hurting the environment or the artisanal miner, by creating a fair trade and a fair price."

Buyers at the Ethical Gem Fair were younger people and designers looking for a stone with a story. They want to know about the supply chain for almost every product they use, including jewelry. The show's suppliers offer as much transparency as possible to their customers, often providing supporting information about the stones, such as images from the mines and cutting factories. Everyone involved in the show sees a growing demand for responsibly sourced gemstones.

Articles on two other exhibitors, Perpetuum Jewels and Columbia Gem House, can be found in the Spring 2019 *G&G*.

Wim Vertriest and Erin Hogarth

Figure 50. Split boules of bicolor synthetic sapphire grown by flame fusion. Photo by Jennifer Stone-Sundberg; courtesy of RusGems.

SYNTHETICS AND SIMULANTS

Bicolor synthetic sapphire. At the JOGS show, a wide selection of synthetic gem materials was offered by the Bangkok office of RusGems, a synthetic crystal growth company out of Russia. Olga Tanskaia showed us their extensive color range of synthetic sapphire, spinel, beryl, garnet, and other lab-grown crystals produced using a variety of crystal growth methods. She noted that blue and red synthetic gems are always their best sellers.

As we found with natural sapphire this year, bicolor synthetic sapphire, both rough and cut, was also available

and popular (figure 50). This material is grown by flame fusion, and the chromophore component of the powder composition is altered during the growth process at the desired length. Many different color combinations were available, including some with the popular teal blue and purple hues (figure 51, left). The inspiration for applying this method of color zoning to these flame-fusion grown crystals came from historical work on synthetic ruby laser rods where colorless (or "undoped") regions were desired for the ends of the rods (figure 52). A process to grow a single crystal having pure aluminum oxide for a certain length, then adding the desired level of chromium to the growth for the laser rod portion of the length, and then returning to pure aluminum oxide was developed to achieve this.

We took the step-cut bicolor synthetic sapphire in figure 51 back to the GIA lab to determine the trace element chemistry responsible for generating the teal and purple hues. Using laser ablation–inductively coupled plasma–mass spectrometry (LA-ICP-MS), we found that the teal end contained no Be, Mg, Ti, V, Mn, Fe, or Ni but did contain small amounts of Cr and Ga (approximately 4 ppma and 0.5 ppma, respectively) and a substantial amount of Co (approximately 140 ppma). The purple end similarly contained no Be, Mg, V, Mn, Fe, or Ni but did contain small amounts of Ti (0.6 ppma) and Ga (0.4 ppma), with substantial amounts of Co (120 ppma), and Cr (470 ppma). Cobalt is giving this crystal the greenish blue component of its color, and chromium is modifying the hue to purple. We used UV-Vis spectroscopy to detect absorption peaks that could be used with the trace element chemistry to explain the two differently colored regions. We identified chromium peaks at approximately 400 and 560 nm responsible for the red color component in the purple half. We also identified an additional peak in the purple half at around 640 nm, likely due to Co^{3+}. In the teal half, we did not find the Cr^{3+} peaks but did identify Co^{3+} peaks at 640 nm and at around 440 nm, and a peak around 600 nm due to Co^{2+} (K. Schmetzer and A. Peretti, "Characterization of a group of experimental Russian hydrothermal synthetic sapphires," *Journal of Gemmology*, Vol. 27, No. 1, 2000, pp. 1–7).

In inspecting the inclusions at the boundary between the two differently colored portions, we discovered bright
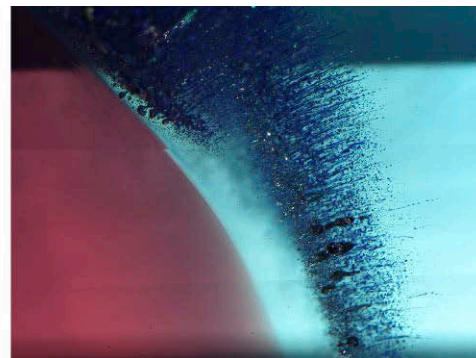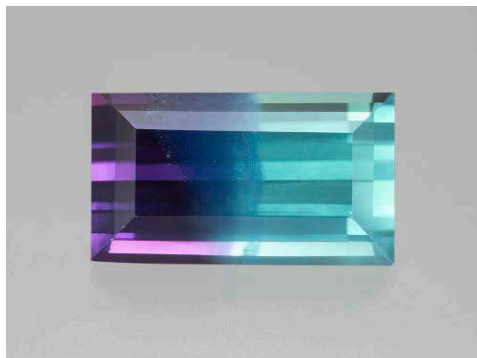

Figure 51. Left: Bicolor 14.83 ct synthetic sapphire showing popular teal blue and purple colors. Photo by Kevin Schumacher; courtesy of RusGems. Right: Wisps of presumably $CoAl_2O_4$ at the boundary of the teal and purple colors in the crystal. Photomicrograph by Nathan Renfro; field of view 7.05 mm.

Figure 52. Synthetic ruby rod grown by the flame-fusion technique showing chromium-free ends. Photo by Jennifer Stone-Sundberg; courtesy of RusGems.

blue wisps of what we believe to be $CoAl_2O_4$ (figure 51, right), a spinel-structure material referred to as "cobalt blue" that is used to impart a blue color to glass, ceramics, and plastics.

The ability to generate just about any hue in sapphire, including color zoning, was readily apparent when looking through the offerings of RusGems. It was fascinating to see evidence of the direct influence of the high-tech laser industry on these synthetic gems.

Jennifer Stone-Sundberg, Ziyin Sun, Nichole Ahline, and Nathan Renfro

ANNOUNCEMENTS

Third annual Gianmaria Buccellati Foundation Award winner. Yi-Hsuan Chiang, a graduate of GIA's Jewelry Design program in Taiwan, received the third annual Gianmaria Buccellati Foundation Award for Excellence in Jewelry Design during the Tucson shows. More than 200 students competed this year, and Chiang was one of 18 finalists from seven GIA campuses. Her winning design, of a necklace depicting a butterfly that has fallen into a spider's web, featured amethyst, diamond, moonstone, conch pearls, coral, black opal, and baroque pearl (figure 53).

Chiang will travel to Italy to meet Rosa Maria Bresciani Buccellati, president of the foundation, and visit its collection.

Larry French of the foundation said, "The designs that were selected as the 18 finalists and exhibited in Tucson beautifully illustrate the passion and dedication of those

who created them. It is in honor of Gianmaria Buccellati's name that we will welcome, as our guest, Ms. Chiang to Italy."

Figure 53. Yi-Hsuan Chiang's amethyst, diamond, moonstone, conch pearl, coral, black opal, and baroque pearl necklace design won the third annual Gianmaria Buccellati Foundation Award. Chiang is a graduate of the Jewelry Design program at GIA in Taiwan.
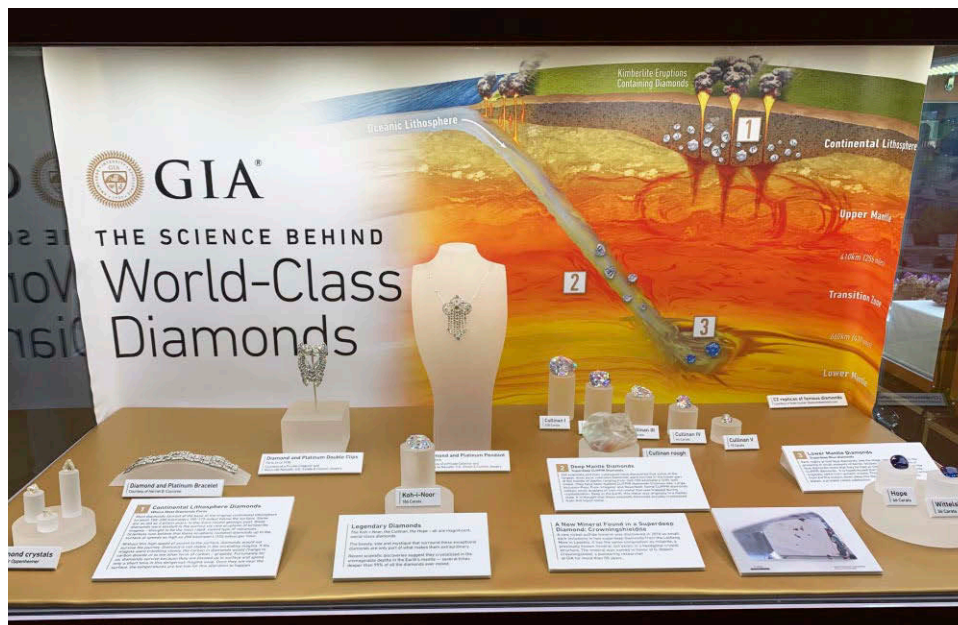
Figure 54. This exhibit highlighted GIA's research into the origin of several of the most famous diamonds. Photo by McKenzie Santimer.

The 2020 Gianmaria Buccellati Foundation Award for Excellence in Jewelry Design competition is underway and open to students in GIA's Jewelry Design courses who meet the eligibility requirements. For more information, visit gia.edu/buccellati-foundation-award-jewelry-design.

GIA Museum's Tucson exhibit receives two awards. The GIA Museum received two awards for its exhibit at the 2020 Tucson Gem and Mineral Show. "The Science Behind World-Class Diamonds" (figure 54) won Best Museum Exhibit from the Tucson Gem & Mineral Society and Best Institutional Educational Award from the Friends of Mineralogy. The exhibit demonstrated how famous diamonds such as the Hope and the Cullinan originated in extreme depths of the earth's lower mantle. The showcase featured extraordinary diamond jewelry and diamond replicas.

More than 30 cases were displayed by renowned museums including the Smithsonian Institution, LA County Museum of Natural History, and the Royal Ontario Museum. This is the second time GIA has won the award for Best Museum Exhibit, having won previously in 2016.

Robert Weldon receives Bonanno Award. Longtime *Gems & Gemology* author and photographer Robert Weldon (figure 55) has received the Accredited Gemologists Association's 2020 Antonio C. Bonanno Award for Excellence in Gemology. The award was presented during AGA's annual gala in Tucson on February 5.

During his more than 30-year career, Weldon has contributed scores of publications, serving as colored gemstone editor at *JCK* and senior writer at *Professional Jeweler*. His photography has appeared on more than 30 *G&G* covers, and he has written numerous feature articles for the journal. He coauthored, with Dona Dirlam, *Splendour & Science of Pearls* (2013). Since 2017, Weldon has been director

of GIA's Richard T. Liddicoat Gemological Library and Information Center. In recent years he has also been closely involved in providing gemological training to independent African miners.

Figure 55. G&G contributor Robert Weldon received the 2020 Bonanno Award for Excellence in Gemology.

COLORED STONES AND ORGANIC MATERIALS

DNA barcoding and next-generation sequencing (NGS) of freshwater pearls. Research efforts on the deoxyribonucleic acid (DNA) species identification of biogenic materials, in particular pearls, have been the focus of some gemological laboratories, including GIA's, for several years (J.B. Meyer et al., "DNA fingerprinting of pearls to determine their origins," *PLOS ONE*, Vol. 8, No. 10, 2013, e75606; K. Saruwatari et al., "DNA techniques applied to the identification of *Pinctada fucata* pearls from Uwajima, Ehime Prefecture, Japan," Spring 2018 *G&G*, pp. 40–50; K. Scarratt, *CIBJO Special Pearl Report*, 2019). Here we report on the findings of a study on the DNA analysis of cultured and natural freshwater pearls originating from both North America and China using the next-generation sequencing (NGS) technique, in collaboration with the Canadian Centre for DNA Barcoding at the University of Guelph.

A total of 22 freshwater pearl samples were subjected to DNA barcode analysis (figure 56). Nine American freshwater natural pearls (sample numbers 1, 2, 8, 12, 13, 15, 16, 17, and 18) and four American freshwater cultured pearls (sample numbers 3, 4, 9, and 10) from Gina Latendresse (American Pearl Company, Inc., Nashville, Tennessee), and nine Chinese freshwater cultured pearls (sample numbers 5, 6, 7, 11, 14, 19, 20, 21, and 22) from the GIA research collection were analyzed. The samples were either drilled with a hand drill using sterile techniques or crushed with a mortar and pestle using liquid nitrogen to obtain powder for analysis. Previously published DNA extraction protocols for pearls were modified to include newly designed primers for polymerase chain reaction (PCR) amplification and NGS. Only high-quality reads assigned to correct Ion Xpress MID (molecular identifier) tags were used in NGS data analysis. Negative PCR and negative extraction controls did not produce any valid sequencing data. Blast algorithms were utilized to match resulting operational taxonomic units to a reference library database for mitochondrial cytochrome c oxidase subunit I; results were imaged using MEGAN software. DNA sequences recovered from the unknown pearl samples were compared against the species sequence reference library in the Barcode of Life Data System, accessible at http://www.boldsystems.org, and compared against the National Center for Biotechnology Information database (https://www.ncbi.nlm.nih.gov).

DNA fragments from eight of the twenty-two samples were successfully recovered and identified. DNA-based species identification was highly consistent with the reported origin of the pearls (table 1). Results on the analyses of the 14 remaining samples were not successful, and no valid yield was recovered. This can be attributed to many factors, including insufficient DNA content due to limited sample size, or the elimination of trace DNA during the various routine pearl treatments known to be applied. While challenges remain on the extraction of DNA fragments from pearls, the results indicate that this technique can provide positive matches on individual pearls and prove which mollusk species they originated from, thus aiding in the identification of some challenging pearls or confirming mollusk origins in cases where greater detail may justify the time and expense of such analyses.

Figure 56. Twenty-two pearls of various kinds and species from various freshwater sources were used for the blind DNA study. Photo by Sood Oil (Judy) Chia.

Sample no.	Reported origin	DNA barcoding result
3	American freshwater cultured pearl (*Megalonaias nervosa*—Washboard)	*Megalonaias nervosa*
4	American freshwater cultured pearl (*Megalonaias nervosa*—Washboard)	*Megalonaias nervosa*
8	American freshwater natural pearl (*Potamilus alatus*—Pink Heelsplitter)	*Potamilus alatus/purpuratus*
9	American freshwater cultured pearl (*Megalonaias nervosa*—Washboard)	*Megalonaias nervosa*
10	American freshwater cultured pearl (*Megalonaias nervosa*—Washboard)	*Megalonaias nervosa*
15	American freshwater natural pearl (unknown)	*Megalonaias nervosa*
19	Chinese freshwater cultured pearl (*Hyriopsis* species)	*Hyriopsis cumingii/schlegelii*
22	Chinese freshwater cultured pearl (*Hyriopsis* species)	*Hyriopsis cumingii/schlegelii*

This joint research was previously presented at the 7th International Barcode of Life Conference (*Genome*, Vol. 60, No. 11, pp. 1003–1004). GIA will continue to investigate this field of research, which is proving to be a highly valuable supplementary technique in the gemological examination of pearls.

Chunhui Zhou
GIA, New York

Janet Topan and Evgeny V. Zakharov
Canadian Centre for DNA Barcoding
University of Guelph, Ontario, Canada

Sunstone plagioclase feldspar from Ethiopia. Ethiopia, traditionally known for opal, has become an important source for emerald and sapphire. After these significant discoveries, a new type of Cu-bearing sunstone feldspar, first shown in 2015 to Tewodros Sintayehu (Orbit Ethiopia Plc.), was discovered in the Afar region (L. Kiefert et al., "Sunstone labradorite-bytownite from Ethiopia," *Journal of Gemmology*, Vol. 36, No. 8, 2019, pp. 694–695). This material made its way to the jewelry market last year in Tucson.

To fully characterize this new production, GIA obtained 48 Ethiopian sunstones for scientific examination. Among them, 44 rough stones (figure 57, left) were borrowed from

Stephen Challener (Angry Turtle Jewelry), who acquired them from an Ethiopian gem dealer in Tucson in February 2019. Another four rough stones (figure 57, right) were purchased by author YK from Amde Zewdalem (Ethiopian Opal and Minerals) and Benyam Mengistu, who facilitates mining and exporting samples from Ethiopia, at the Tokyo International Mineral Association show in June 2019. Prior to this discovery, the only verified occurrences of Cu-bearing feldspar were from Lake and Harney Counties in Oregon (e.g., the Dust Devil and Ponderosa mines). However, more than a decade ago there was a controversy about Cu-bearing feldspar on the market purportedly from Asia or Africa with an undetermined color origin, presumably Cu-diffused (G.R. Rossman, "The Chinese red feldspar controversy: Chronology of research through July 2009," Spring 2011 *G&G*, pp. 16–30; A. Abduriyim et al., "Research on gem feldspar from the Shigatse region of Tibet," Summer 2011 *G&G*, pp. 167–180). Gemological testing and advanced analytical methods helped distinguish this new Ethiopian material from the Oregon material and the controversial feldspar of questionable color origin mentioned above in order to ensure GIA's accurate reporting of the natural origin of Cu-bearing feldspar.

Two polished rough Ethiopian samples gave RI readings of $n_\alpha = 1.562$ and $n_\gamma = 1.571$ and birefringence of 0.009. Optic

Figure 57. Left: Forty-four Ethiopian rough sunstones exhibiting different colors and clarities. The largest stone weighs 54.41 ct. Right: Four Ethiopian rough sunstones ranging from 9.92 to 35.42 ct. All 48 rough stones were identified as labradorite by LA-ICP-MS, except for one spot as bytownite. Photos by Diego Sanchez (left) and Shunsuke Nagai (right).
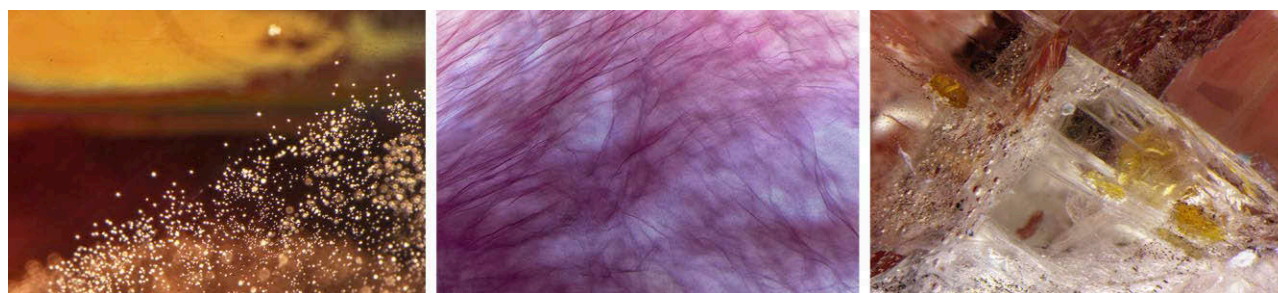
Figure 58. Left: Clouds of copper platelets were observed in numerous Ethiopian sunstones. Field of view 3.13 mm. Center: Dense networks of reddish wispy dislocations were seen in some Ethiopian sunstones, along with a slightly greenish blue bodycolor. Field of view 2.72 mm. Right: Yellowish crystals of what are likely fayalite were seen in one Ethiopian feldspar. These inclusions have also been documented in Oregon sunstone. Field of view 2.82 mm. Photomicrographs by Nathan Renfro.

signs were biaxial positive. Hydrostatic SG measurements were 2.70 and 2.72. These RI and SG ranges overlapped with Oregon sunstone (RI—n_α = 1.560–1.570, n_γ = 1.568–1.579; birefringence—0.006–0.012; SG—2.70–2.72) but were significantly higher than other Cu-bearing feldspars with undetermined natural or treated color origin (n_α = 1.551–1.559, n_γ = 1.559–1.566; birefringence—0.004–0.010; SG—2.68–2.69). A total of 18 Ethiopian sunstones were tested under a desktop UV lamp. Eleven showed very weak orange fluorescence, while seven were inert under long-wave UV. All showed very weak red fluorescence under short-wave UV. Under magnification, many showed dense clouds of reflec-

TABLE 1. Generalized trace element profiles of sunstone feldspar in parts per million weight (ppmw) and mol.% end members.

Ponderosa mine: Natural Oregon sunstone							
	Key trace element chemistry				Mol.% end members[a]		
	Mg	Cu	Ga	Sr	Ab	An	Or
Range	879–1110	3.78–179	12.0–14.0	437–485	28.1–32.4	67.3–71.6	0.27–0.37
Average	1050	58.2	12.8	452	29.9	69.8	0.29
Median	1060	27.1	12.7	450	29.8	69.9	0.29
Dust Devil mine: Natural Oregon sunstone							
	Key trace element chemistry				Mol.% end members[a]		
	Mg	Cu	Ga	Sr	Ab	An	Or
Range	810–1090	0.74–104	12.0–20.1	449–671	27.7–35.7	63.5–72.0	0.28–0.82
Average	920	25.0	16.4	580	32.2	67.2	0.62
Median	903	17.5	17.1	593	32.5	66.8	0.68
Natural Ethiopian sunstone							
	Key trace element chemistry				Mol.% end members[a]		
	Mg	Cu	Ga	Sr	Ab	An	Or
Range	261–686	0.51–115	16.5–25.3	283–781	29.7–39.4	60.1–69.9	0.37–1.42
Average	421	15.5	19.4	367	34.2	65.3	0.59
Median	411	7.54	19.2	328	34.4	65.0	0.49
Cu-bearing feldspar with undetermined color origin							
	Key trace element chemistry				Mol.% end members[a]		
	Mg	Cu	Ga	Sr	Ab	An	Or
Range	315–492	405–653	16.3–18.8	1120–1210	46.3–50.8	46.3–51.3	2.36–3.05
Average	423	499	17.6	1160	48.7	48.7	2.60
Median	420	481	17.7	1160	48.7	48.8	2.57

[a]*Abbreviations: Ab = albite, An = anorthite, Or = orthoclase*
Detection limits: 0.45–2.08 ppmw Na, 0.011–0.11 ppmw Mg, 0.26–0.59 ppmw K, 5.27–22.2 ppmw Ca, 0.014–0.050 ppmw Cu, 0.007–0.45 ppmw Ga, 0.002–0.008 ppmw Sr
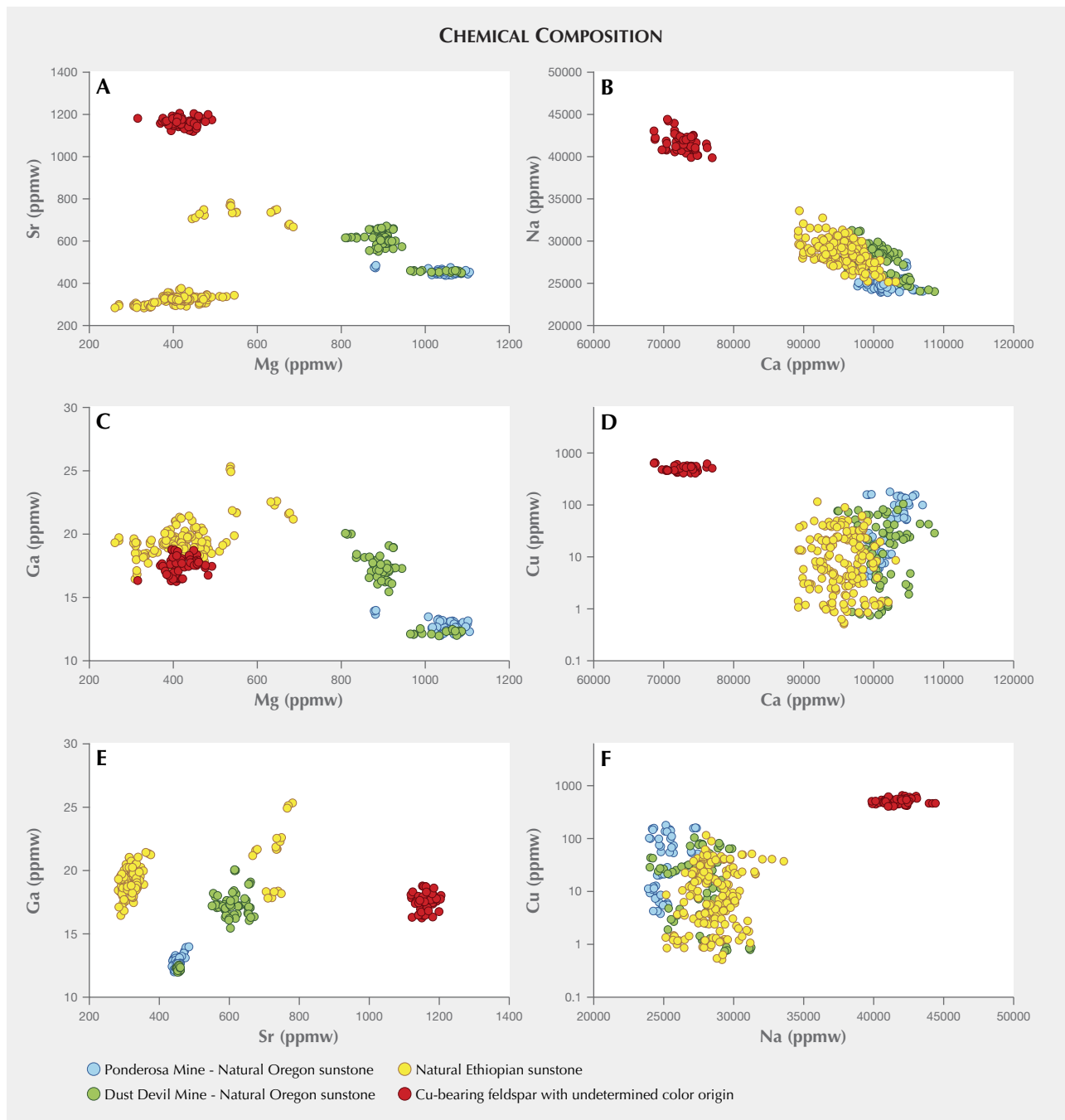
Figure 59. Chemical comparison of Oregon and Ethiopian sunstone and Cu-bearing feldspar with undetermined color origin. Mg (A and C) is the key trace element that separates Ethiopian from Oregon sunstone. The unknown Cu-bearing feldspar has a much higher Cu and Sr concentration than other natural untreated sunstones (A, D, E, and F). For major elements, Ethiopian sunstone overlaps with Oregon sunstone, with a slight lower Ca concentration (B and D). The unknown Cu-bearing feldspar contains more Na and less Ca than other natural untreated sunstones (B, D, and F).

tive copper platelets, much like those observed in material from Oregon (figure 58, left). Some stones also showed an interesting wispy network of reddish dislocation stringers with a greenish blue bodycolor in transmitted light (figure 58, center). Another example revealed several yellow crystals of what appeared to be fayalite, an inclusion also observed in Oregon sunstone (figure 58, right).

Laser ablation–inductively coupled plasma–mass spectrometry (LA-ICP-MS) was used to measure the chemistry of all 48 Ethiopian sunstones, 26 Dust Devil sunstones, 19
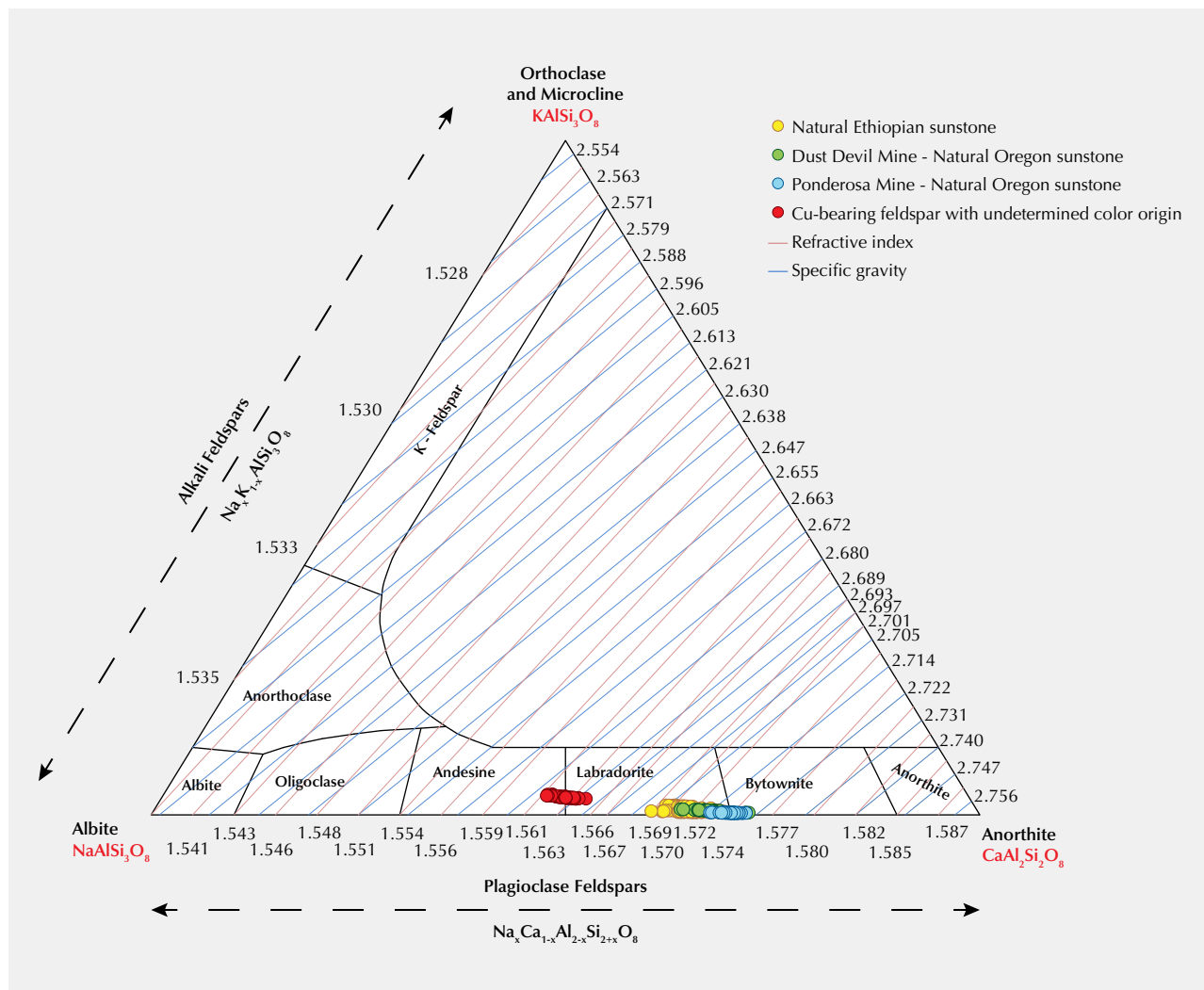
*Figure 60. Illustration of solid solution in the feldspars, modified after Deer et al. (*Rock-Forming Minerals, Volume 4: Framework Silicates, *1963). The nomenclature of the plagioclase series and the alkali feldspars is also shown. All 48 Ethiopian rough stones (yellow dots) were classified as labradorite except one bytownite. Forty-five Oregon sunstones (blue and green dots) were classified as labradorite-bytownite. Twenty Cu-bearing feldspars with undetermined color origin (red dots) were classified as andesine-labradorite. Ethiopian sunstones are less calcic than Oregon sunstones. Variation of refractive indices n_γ and specific gravity with composition of feldspars were plotted in the ternary plot as pink and blue straight lines, respectively. Note: n_γ = gamma, the highest RI of a biaxial crystal, light vibrating parallel to the Z optical direction.*

Ponderosa sunstones, and 20 Cu-bearing feldspars with undetermined color origin. NIST 610 and USGS GSD-1G and GSE-1G glasses were used as external standards. ^{29}Si was used as an internal standard. Ponderosa and Dust Devil sunstones yielded an end member composition of $Ab_{28-32}An_{67-72}Or_{0.3-0.4}$ and $Ab_{28-36}An_{64-72}Or_{0.3-0.8}$, respectively (table 1). They are classified as labradorite-bytownite using an albite-anorthite-orthoclase (Ab-An-Or) ternary diagram (figures 59B and 60, blue and green dots). Ethiopian sunstones yielded an end member composition of $Ab_{30-39}An_{60-70}Or_{0.4-1.4}$,

which is generally similar but less calcic than Oregon sunstones (table 1). All analyses of Ethiopian material indicated classification as labradorite except one spot that gave bytownite (figure 59B and figure 60, yellow dots). The Cu-bearing feldspar with undetermined color origin yielded an end member composition of $Ab_{46-51}An_{46-51}Or_{2-3}$ (table 1). They were classified as andesine-labradorite, distinct from the Oregon and Ethiopian material (figure 59B and figure 60, red dots). In addition to the differences with major elements Na, Ca, and K, the analyses revealed that the trace elements Mg,

Cu, Ga, and Sr were the four best discriminators providing clear separations among Oregon and Ethiopian sunstone and Cu-bearing feldspar with undetermined color origin. All Ethiopian sunstone had a lower Mg concentration (261–686 ppmw, table 1) than Oregon sunstone (>810 ppmw, table 1) (figure 59A). The Cu-bearing feldspar with undetermined color origin had a higher Cu (>405 ppmw) and Sr (>1120 ppmw) concentration than Oregon and Ethiopian sunstone (figure 59, A, D, E, and F). Interestingly, Ponderosa samples (figure 59, C and E) had a lower Ga concentration (<14.0 ppmw) than the Ethiopian sunstone and Cu-bearing feldspar with undetermined color origin. A group of Dust Devil stones with higher Mg, Ga, and Sr concentrations were separated from all other sources in figures 59A and 59C, further differentiating them from Ponderosa stones.

Copper-bearing sunstones from different sources are visually indistinguishable from one another. Gemological properties are usually sufficient to separate Ethiopian and Oregon sunstones from these Cu-bearing feldspars with undetermined color origin. However, accurate major and trace element chemical analysis obtained by methods such as LA-ICP-MS, XRF (Ga and Sr were first identified as reliable discriminators for separating Ethiopian from Oregon sunstones using XRF by author GRR before this work), or electron microprobe is critical to separating Ethiopian, Oregon, and Cu-bearing feldspar with undetermined color origin.

Ziyin Sun, Nathan D. Renfro, Aaron C. Palke,
Heidi Breitzmann, Jonathan Muyal, Dylan Hand,
Maxwell Hain, and Shane F. McClure
GIA Carlsbad

Yusuke Katsurada and Makoto Miura
GIA, Tokyo

George R. Rossman
California Institute of Technology, Pasadena

SYNTHETICS AND SIMULANTS

Dyed chalcedony imitation of chrysocolla-in-chalcedony. Chrysocolla-in-chalcedony, also known as gem silica or blue chalcedony in Taiwan, is the most valuable chalcedony variety on the Taiwanese market. The beautiful greenish blue color is derived from micro-inclusions of chrysocolla, which can be identified by observation of a peak at 3619 cm^{-1} in the Raman spectrum. This peak can be assigned to OH groups in chrysocolla. Therefore, the color origin for this material is fundamentally rooted in the presence of Cu^{2+} ions in the structure of the chrysocolla inclusions. In the past few years, a large number of dyed chalcedony imitations have appeared in Taiwan's market. The blue color of chalcedony dyed by copper salts, and that of natural specimens containing chrysocolla, is caused by Cu^{2+} ions.

Recently, a parcel of loose chalcedonies was sent to the Taiwan Union Lab of Gem Research (TULAB) for identification. These stones were submitted as natural blue chalcedony, but Raman spectroscopy later confirmed them as
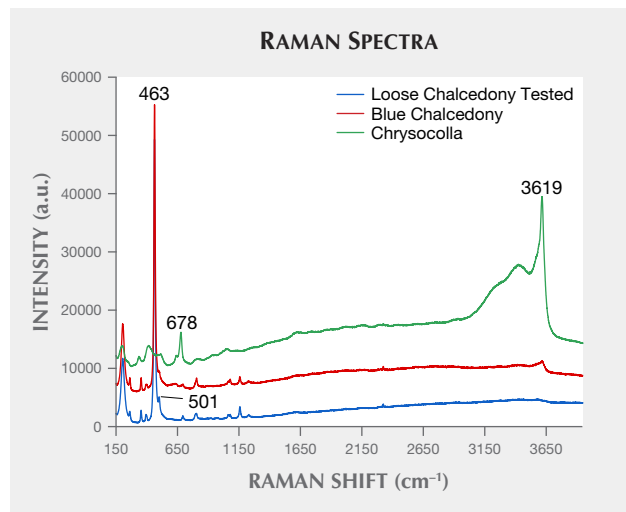

Figure 61. The Raman spectrum of the loose chalcedony compared to that of chrysocolla and blue chalcedony reveals a mineral composition of quartz (463 cm^{-1}) and moganite (501 cm^{-1}) but a lack of chrysocolla inclusions (3619 cm^{-1}).

chalcedony without the characteristic peaks of chrysocolla (figure 61).

With the owner's consent, we cut one cabochon and polished the cross section displaying a blue mantle zoning from surface to center parallel to its profile (figure 62). The sample was analyzed with EDXRF, and concentration mapping on the cross section confirmed that copper was concentrated on the surface and decreased toward the interior, which is strong evidence for dyeing with copper salts (figure 63).

Twenty pieces of chalcedony dyed with copper salts were further analyzed with EDXRF and compared to results from twenty pieces of natural blue chalcedony. EDXRF re-

Figure 62. A blue mantle zoning on the cross section of the loose chalcedony is due to the bath of copper dye. Photo by Shu-Hong Lin.
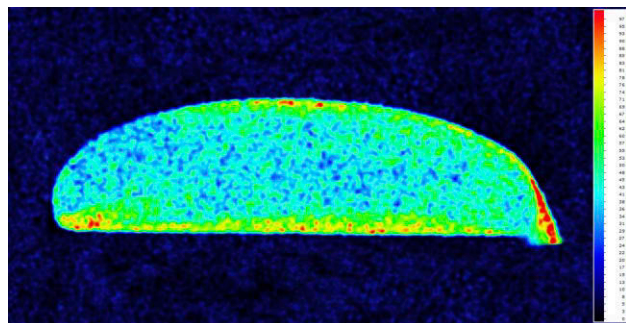
Figure 63. The concentration mapping for copper on the cross section of dyed chalcedony, which shows higher copper concentration in the periphery and lower in the interior; the different colors on the right represent the degree of relative concentration for copper from high to low.

sults indicated that the Si/Cu ratio of chalcedony dyed with copper salts was much higher than that of natural blue chalcedony (400–600 and 4–50, respectively). The content of Cu was relatively low in dyed chalcedonies tested.

There are many types of dye used for the color enhancement of chalcedony. Although a series of tests like those used above provide a comprehensive comparison between natural blue chalcedony and the dyed chalcedony analyzed in this research, it requires further verification whether these methods can be applied to other dyed chalcedonies.

Shu-Hong Lin
Institute of Earth Sciences, National Taiwan Ocean University, Keelung
Taiwan Union Lab of Gem Research, Taipei

Yu-Ho Li and Huei-Fen Chen
Institute of Earth Sciences, National Taiwan Ocean University

Jiann-Neng Fang
National Taiwan Museum, Taipei

Jadeite jade and serpentine doublet. The Lai Tai-An Gem Lab in Taipei recently received a carving presented as jadeite jade. The rectangular, uneven green piece, carved on one side but almost plain on the back and sides, weighed approximately 171.01 ct and measured approximately 50.4 × 39.9 × 7.4 mm (figure 64). Standard gemological testing revealed a spot RI of 1.66 on an area of the carved side, but surprisingly the smoother surfaces failed to yield clear readings. Microscopic observation revealed a coating in the areas where the failed RI attempts were made.

Subsequent infrared analysis proved the carved side was jadeite jade owing to the relevant absorption valleys observed at 1167, 1077, 962, 853, 665, 587, 529, 476, and 433 cm⁻¹. However, the four sides and base revealed valleys at 1001, 646, 557, and 460 cm⁻¹, characteristic of serpentine despite the surface coating observed (figure 65).

Figure 64. This "jadeite jade" carving submitted for identification proved to be a jadeite jade and serpentine doublet. Photo by Lai Tai-An Gem Lab.

The client granted us permission to remove the coating in order to analyze the item in more detail. After removal of the coating, the four sides and base showed a lighter saturation of green color separated by a visible horizontal line (figure 66, B and D). Before coating removal, the layering was not as obvious (figure 66, A and C). Magnification confirmed that the object was composed of two different materials. Standard gemological testing of the lighter colored material yielded RIs of 1.56, consistent with those expected

Figure 65. FTIR analysis revealed absorption valleys at 1167, 1077, 962, 853, 665, 587, 529, 476, and 433 cm⁻¹ in the jadeite jade portion (red spectrum) and valleys at 1001, 646, 557, and 460 cm⁻¹ in the serpentine portion (green spectrum).
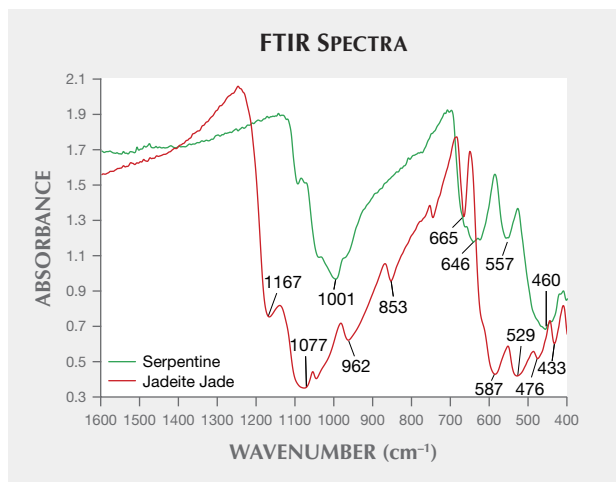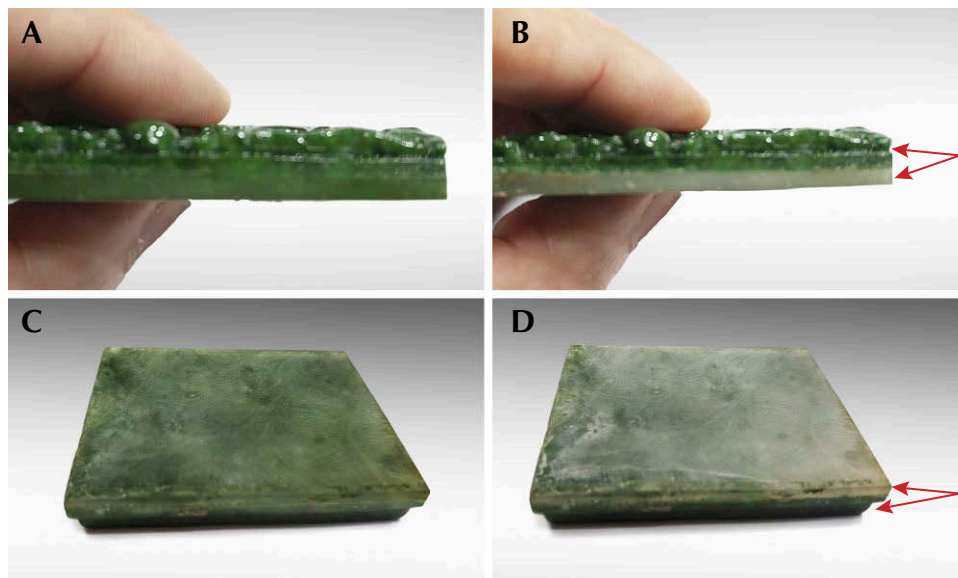
Figure 66. Removal of the coating from the four sides and base exposed a clear boundary between the two materials (B and D). Prior to the coating's removal (A and C), there were no indications the item was a doublet. Photos by Lai Tai-An Gem Lab.

for serpentine and supported by the FTIR and Raman analyses. Jadeite jade and serpentine can have a very similar appearance. The identification of this particular piece proved relatively straightforward, but if it were mounted in a closed-back setting with only the carved face visible, a costly identification error could easily result.

Larry Tai-An Lai (service@laitaian.com.tw)
Lai Tai-An Gem Laboratory
Taipei, Taiwan

MISCELLANEOUS

Television documentary series: "Beautiful Gem Stories." The unique allure of jewelry and the excitement of the global gem industry are captured in the Japanese documentary series "Beautiful Gem Stories." The program is broadcast on BS-TBS channel, a subsidiary of Tokyo Broadcasting System, and hosted by longtime *G&G* contributor and editorial board member Dr. Ahmadjan Abduriyim (Tokyo Gem Science, LLC and GSTV Gemological Laboratory). Hour-long episodes examine the growth of gemstones deep under the earth's surface and the mining methods to recover them, as well as the characteristics, craftsmanship, and cultural significance that make them special.

Since 2016, Dr. Abduriyim has filmed on location at important gem deposits in Madagascar, Mozambique (figure 67), Tanzania, Namibia, Sri Lanka (figure 68), Myanmar, Thailand, Vietnam, Brazil, Colombia, and other countries. He has also gone to natural and cultured pearl localities in Bahrain, the United Arab Emirates, Vietnam, and Japan, as well as global manufacturing centers, museums, and trade shows.

Figure 67. Dr. Ahmadjan Abduriyim hosts an episode of "Beautiful Gem Stories," filmed on location at the Montepuez ruby mine in northern Mozambique. Photo by Tomoaki Miyake.

Figure 68. In this episode, Dr. Abduriyim reports from the Bogawatalawa sapphire deposit in Sri Lanka. Photo by Tomoaki Miyake.

After monthly episodes from 2016 to 2018, four new episodes are broadcast per year now. With more than one million regular viewers, "Beautiful Gem Stories" has been warmly received.

"The financial crisis that hit the Japanese economy in 2008 took a heavy toll on consumer interest in jewelry," said Dr. Abduriyim. "But I am very grateful to contribute to restoring the jewelry industry in Japan and throughout the world with an enlightening look at gemstones."

ANNOUNCEMENTS

Dutrowite: New mineral species of tourmaline. A newly discovered mineral species of the tourmaline group has been named in honor of Dr. Barbara Dutrow (figure 69, left). Dutrowite (figure 69, right) was discovered in the Apuan Alps of Tuscany, Italy, and has been recognized by the International Mineralogical Association. The Austrian, Italian, and Swedish researchers who discovered the mineral named it in recognition of Dr. Dutrow's teaching and research contributions, particularly on tourmaline and its formation. She is the Gerald Cire and Lena Grand Williams Alumni Professor in the Department of Geology and Geophysics at Louisiana State University in Baton Rouge. In 2007, she was a coauthor of the 23rd edition of *Manual of Mineral Science*, a standard reference textbook for the study of minerals. Since 2016, Dr. Dutrow has served on the GIA Board of Governors.
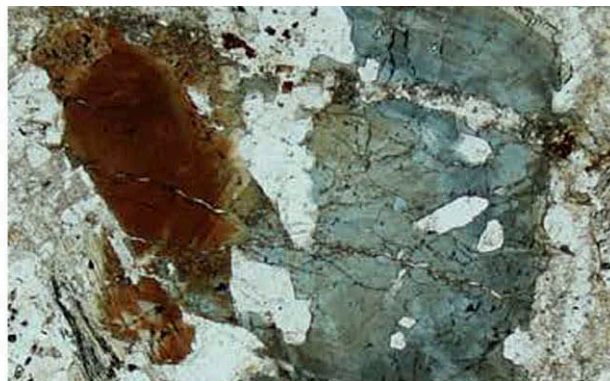

Figure 69. Left: Professor Barbara Dutrow has been honored with the naming of the new mineral dutrowite. Photo by Kevin Schumacher. Right: Sample of dutrowite (brown) and dravite (blue) tourmalines in meta-rhyolite from Italy. Courtesy of Cristian Biagioni.

G&G launches Facebook group. On February 5, 2020, *Gems & Gemology* launched a Facebook group dedicated to gemology and research published in the journal. The group has attracted jewelry professionals, researchers, students, and those with a general interest in gemology who want to share and expand their knowledge. With several dozen posts (figure 70), the *G&G* Facebook group has become a dedicated forum for the discussion of inclusions, treatments, field gemology and gemstone mining, and identification of laboratory-grown or cultured gemstones, including identification challenge quizzes. Some of the most popular posts to date have featured stunning photomicrographs of gersdorffite inclusions in quartz, diamonds with octahedral stellate cloud inclusions, mysterious sapphires from the Andes Mountains in South America, and the use of Google Earth for research in field gemology. The enthusiastic base of more than 7,000 members hails from all parts of the globe. To join, visit www.facebook.com/groups/giagemsgemology.

ERRATUM

In the Winter 2019 article "Geographic Origin Determination of Emerald," the figure 9 caption gave the source of the faceted emerald as Zarajet, Afghanistan. The correct location is Zarakhil, Afghanistan. We thank Ahmad Khaled for this correction.
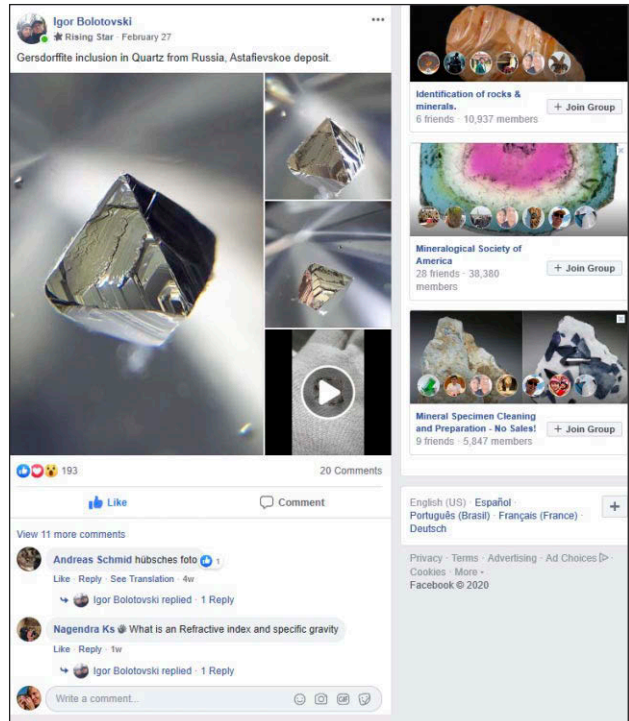

Figure 70. The G&G *Facebook group is a new community for all gem and jewelry enthusiasts.*

For online access to all issues of GEMS & GEMOLOGY from 1934 to the present, visit:

gia.edu/gems-gemology